New Theoretical Approaches to Atomic and Molecular Dynamics triggered by Ultrashort Light Pulses on the Atto- to Picosecond Time Scale

Dissertation zur Erlangung des Doktorgrades des Departments Physik der Universität Hamburg

vorgelegt von

Stefan Ulf Pabst

aus

Saalfeld/Saale

Hamburg

2012

Gutachter der Dissertation:	Prof. Dr. Robin Santra Prof. Dr. Lars Bjorn Madsen Prof. Dr. Eva Lindroth
Gutachter der Disputation:	Prof. Dr. Robin Santra Prof. Dr. Peter Schmelcher
Datum der Disputation:	17.12.2012
Vorsitzender des Prüfungsausscuhsses:	Dr. Alexander Chudnovskiy
Vorsitzender des Promotionsausscuhsses:	Prof. Dr. Peter Hauschildt
Leiterin des Department Physik:	Prof. Dr. Daniela Pfannkuche
Dekan der Fakultät für Mathematik, Informatik und Naturwissenschaften:	Prof. Dr. Heinrich Graener

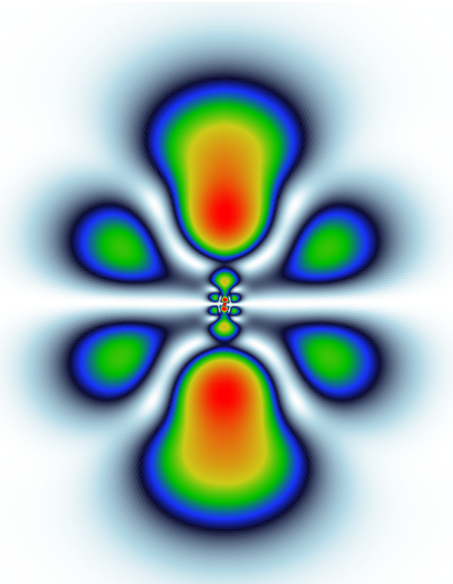

Ultrafast Ionization: Photoelectron density of an ionized electron originating from the $4d_0$ orbital of xenon, which has been exposed 100 as earlier to an 10 as long XUV pulse.

Zusammenfassung

Das Konzept der Atome als Grundbausteine der Materie existiert schon seit über 3000 Jahren. Eine Revolution im Verständnis von Atomen und Molekülen ereignete sich im letzten Jahrhundert mit der Geburt der Quantenmechanik. Nachdem die elektronische Struktur verstanden war, stieg das Interesse die Dynamik von Elektronen, Atomen und Molekülen zu studieren. Aus technischen Gründen war es bis vor Kurzem nur schwer möglich, diese ultraschnellen Prozesse zeitaufgelöst zu untersuchen. Die typische Zeitskala von atomaren und molekularen Prozessen liegt im Piko- bis Attosekundenbereich. Der enorme technische Fortschritt in den letzten Jahren ermöglicht es heutzutage Lichtpulse auf diesen Zeitskalen zu erzeugen. Mit diesen ultrakurzen Pulsen können atomare und molekulare Dynamiken generiert, beobachtet und kontrolliert werden. Mit dem technischen Fortschritt steigt auch der Bedarf an theoretischen Modellen, die die zugrunde liegenden Mechanismen erklären.

Diese Doktorarbeit beschäftigt sich mit der Entwicklung von theoretischen Modellen, mit denen das zeitliche Verhalten von Elektronen, Atomen und Molekülen in der Gegenwart von kurzen Lichtpulsen studiert werden kann. Mehrere Beispiele, wie Lichtpulse gezielt elektronische, atomare und molekulare Bewegungen auslösen und kontrollieren können, werden diskutiert.

Im ersten Teil dieser Arbeit liegt der Fokus auf der Rotationsdynamik von asymmetrischen Molekülen, welche im Bereich von hunderten von Femtosekunden bis hunderten von Pikosekunden liegt. Dabei ist das Ziel alle drei Achsen des Moleküles so gut wie möglich auszurichten. Um dies theoretisch zu studieren, entwickelte ich ein Programm, dass adiabatische und nicht-adiabatische Ausrichtungsdynamiken beschreiben kann. Anhand von SO_2 werden Strategien diskutiert, um eine optimale 3D-Ausrichtung in Abwesenheit eines Feldes zu erreichen, sodass nachfolgende Experimente nicht von dem ausrichtenden Feld gestört werden. Moleküle in der Gasphase mit einem hohen Grad an Ausrichtung sind ideal für Streuexperimente. Das Streubild enthält Informationen über die molekulare Struktur, die durch geeignete Verfahren aus dem Streubild extrahiert werden kann. Dies wird am Beispiel von laser-ausgerichtetem Naphthalin-Molekülen ($C_{10}H_8$) demonstriert. Die Qualität der Ausrichtung der Naphthalinmoleküle ist entscheidend für die Rekonstruktion der molekularen Struktur.

Im zweiten Teil werden Ionisierungsdynamiken von Atomen untersucht. Die charakteristische Zeitskala liegt hier im Attosekunden- bis Femtosekundenbereich. Obwohl viele Ionisierungsprozesse mit einem Ein-Teilchenbild beschrieben werden können, treten immer wieder interessante Multielektroneffekte auf. Basierend auf einem zeitabhängigen *configuration-interaction singles* (TDCIS) Ansatz studiere ich das zeitliche Verhalten solcher Multielektroneffekte. Bei der Photoionisierung von atomarem Xenon mit einem Attosekundenpuls treten unerwartete Korrelationen zwischen dem ionisierten Elektron und dem Ion auf. Diese Elektron-Ion-Verschränkung schlägt sich in Form einer reduzierten Kohährenz

in dem Ion nieder. Mittels Absorptionsspektroskopie kann die Population und die Kohärenz der ionischen Zustände mit einer Genauigkeit von wenigen Attosekunden ausgelesen werden. Sogar die Ionisierungsdynamik selbst kann beobachtet werden. Dabei treten feldgetriebene Wechselwirkungen zwischen dem Elektron und dem Ion auf, die sich deutlich in der Linienstruktur des transmittierten Spektrums erkennen lassen. Auch bei der Erzeugung von hohen Harmonischen (*high-harmonic generation* oder kurz HHG) kommt es zu Wechselwirkungen, die den Zustand des Ions verändern können. Solche Effekte werden Interkanalkopplungen genannt und sind im HHG-Spektrum sichtbar, wie meine Untersuchungen an Argon und Xenon zeigen.

All diese Beispiele demonstrieren auf der einen Seite, wie ultrakurze Pulse komplexe elektronische, atomare, und molekulare Bewegungen initiieren können. Auf der anderen Seite erlauben diese Pulse, die initiierten Bewgungen zu beobachten und zu kontrollieren.

Abstract

The concept of atoms as the building blocks of matter has existed for over 3000 years. A revolution in the understanding and the description of atoms and molecules has occurred in the last century with the birth of quantum mechanics. After the electronic structure was understood, interest in studying the dynamics of electrons, atoms, and molecules increased. However, time-resolved investigations of these ultrafast processes were not possible until recently. The typical time scale of atomic and molecular processes is in the picosecond to attosecond realm. Tremendous technological progress in recent years makes it possible to generate light pulses on these time scales. With such ultrashort pulses, atomic and molecular dynamics can be triggered, watched, and controlled. Simultaneously, the need rises for theoretical models describing the underlying mechanisms.

This doctoral thesis focuses on the development of theoretical models which can be used to study the dynamical behavior of electrons, atoms, and molecules in the presence of ultrashort light pulses. Several examples are discussed illustrating how light pulses can trigger and control electronic, atomic, and molecular motions.

In the first part of this work, I focus on the rotational motion of asymmetric molecules, which happens on picosecond and femtosecond time scales. Here, the aim is to align all three axes of the molecule as well as possible. To investigate theoretically alignment dynamics, I developed a program that can describe alignment motion ranging from the impulsive to the adiabatic regime. The asymmetric molecule SO_2 is taken as an example to discuss strategies of optimizing 3D alignment without the presence of an external field (i.e., field-free alignment). Field-free alignment is particularly advantageous because subsequent experiments on the aligned molecule are not perturbed by the aligning light pulse. Well-aligned molecules in the gas phase are suitable for diffraction experiments. From the diffraction pattern, information about the molecular structure can be gained. This is illustrated with the example of laser-aligned naphthalene molecules ($C_{10}H_8$). Furthermore, I demonstrate that the quality of the molecular alignment is essential for the reconstruction of the molecular structure.

In the second part of this work, the ionization dynamics of atoms is studied. The characteristic time scale lies, here, in the attosecond and the few-femtosecond regime. Although a one-particle picture has been successfully applied to many ionization processes, important many-body effects do constantly occur. Based on a time-dependent configuration-interaction singles (TDCIS) approach, I study the temporal behavior of these many-body effects. During the photoionization of atomic xenon, unexpected correlation effects between the ionized electron and the ion occur. This electron-ion entanglement results in a reduced coherence within the ion. Populations and coherences of the ionic states are probed with attosecond precision using transient absorption spectroscopy. Even the subcycle ionization dynamics can be studied with this technique. Here, field-driven dressing effects between the ion and the freed electron appear, which I investigate on atomic kryp-

ton. Interactions between the ion and the electron, which modify the ionic states, occur also in high-harmonic generation (HHG). They are visible in the HHG spectrum as my studies of argon and xenon show.

All these examples demonstrate on the one side, ultrashort pulses can be used to initiate complex electronic, atomic, and molecular motions. On the other side, it is also possible to probe and to control these dynamical processes with ultrashort pulses.

Contents

LIST OF PUBLICATIONS

2010 *"Computational Studies of X-ray Scattering From Three-Dimensionally-Aligned Asymmetric-Top Molecules"*
Stefan Pabst, Phay J. Ho, and Robin Santra
Phys. Rev. A **81**, 043425 (2010)

2010 *"Alignment of Asymmetric-Top Molecules Using Multiple-Pulse Trains"*
Stefan Pabst and Robin Santra
Phys. Rev. A **81**, 065401 (2010); Erratum: Phys. Rev. A **82**, 049901(E) (2010)

2010 *"Implementation of the time-dependent configuration-interaction singles method for atomic strong-field processes"*
L. Greenman, P. J. Ho, S. Pabst, E. Kamarchik, D. A. Mazziotti, and R. Santra
Phys. Rev. A **82**, 023406 (2010)

2011 *"Decoherence in Attosecond Photoionization"*
S. Pabst, L. Greenman, P. J. Ho, D. A. Mazziotti, and R. Santra
Phys. Rev. Lett. **106**, 053003 (2011)

2011 *"Synthesized Light Transients"*
A. Wirth, M. Th. Hassan, I. Grguraš, J. Gagnon, A. Moulet, T. T. Luu, S. Pabst, R. Santra, Z. A. Alahmed, A. M. Azzeer, V. S. Yakovlev, V. Pervak, F. Krausz, and E. Goulielmakis
Science **334**, 195 (2011)

2012 *"Impact of Multichannel and Multipole Effects on the Cooper Minimum in the High-Order-Harmonic Spectrum of Argon"*
Stefan Pabst, Loren Greenman, David A. Mazziotti, and Robin Santra
Phys. Rev. A **85**, 023411 (2012)

2012 *"Enhanced Nonlinear Response of Ne^{8+} to Intense Ultrafast X-rays"*
Arina Sytcheva, Stefan Pabst, Sang-Kil Son, and Robin Santra
Phys. Rev. A **85**, 023414 (2012)

2012 *"Theory of Attosecond Transient Absorption Spectroscopy of Krypton for Overlapping Pump and Probe Pulses"*
S. Pabst, A. Sytcheva, A. Moulet, A. Wirth, E. Goulielmakis, and R. Santra
Phys. Rev. A **86**, 063411 (2012)

LIST OF DEVELOPED PROGRAMS

XALMO X-ray Diffraction from Laser-Aligned Molecules

XCID Configuration-Interaction Dynamics Package

Part I

Introduction

Chapter 1

Overview

Rapid technological progress in generating shorter and shorter pulses has driven the interest in studying rotational, vibrational, and electronic excitations on their characteristic time scales[1]. I will start by giving an overview of two areas in atomic, molecular, and optical physics that have been the focus of my doctoral studies: (1) laser alignment of molecules and (2) ultrafast ionization dynamics. Both areas have in common that the dynamics of the system is induced by very short laser pulses. Due to the different characteristic time scales of rotational excitations (alignment) and electronic excitations (ionization), the duration of these pulses ranges from hundreds of picosecond (1 ps= 10^{-12} s) down to tens of attosecond (1 as= 10^{-18} s), respectively. Major parts of Part I of this dissertation will appear in European Physical Journal Special Topics **221**, 1 (2013).

In Chap. 2, I study the alignment dynamics of molecules. First, I give a review of what have been done in aligning and orienting molecules with optical laser fields. The underlying principle of laser alignment and orientation is presented in Sec. 2.1.1. In Sec. 2.1.2, I discuss the details of one-dimensional (1D) and three-dimensional (3D) alignment as well as what alignment and orientation means and how it can be measured. The ratio between the pulse duration and the rotational dynamics determines whether the alignment happens adiabatically or non-adiabatically. I discuss these dynamical aspects in Sec. 2.1.3. Schemes of achieving orientation rather than alignment are reviewed in Sec. 2.1.4.

In Sec. 2.2, I explain the program XALMO I have developed in order to calculate a wide range of 3D alignment dynamics ranging from adiabatic to non-adiabatic alignment. Due to the complexity of 3D alignment, I explain the symmetry considerations and specifics of the numerical implementation in order to make the program most efficient. In Sec 2.3, I focus applications of laser alignment. I discuss my publications about x-ray scattering from 3D laser-aligned molecules and the usage of multiple pulse scheme to achieve field-free 3D alignment. The publications resulting from these projects can be found in Chap. 4.

[1] N. Bloembergen, Rev. Mod. Phys. **71**, S283 (1999), A. H. Zewail, J. Phys. Chem. A **104**, 5660 (2000), and F. Krausz and M. Ivanov, Rev. Mod. Phys. **81**, 163 (2009)

In Chap. 3, I look into ultrafast ionization dynamics of noble gas atoms on the sub-femtosecond (1 fs= 10^{-15} s) time scale. Even though many processes and mechanisms can be well understood by focusing on a single electron, multi-electron effects can become important particularly for large atoms and molecules. The advantage of atomic systems is their small size and their high degree of symmetry. For ultrafast light-induced processes, this greatly helps to systematically study the importance of details in the electronic structure originating from electron-electron correlations. Before discussing the work I have done in this field, I start with a short review about the two most prominent mechanisms in ultrafast science: one-photon photoionization (in Sec. 3.1.2) and tunnel ionization (in Sec. 3.1.3). In Sec. 3.1.4, I discuss the high harmonic generation (HHG) process, which converts near-infrared (NIR) light with wavelengths of ~ 1 μm into UV and x-ray light with wavelengths in the 1–100 nm regime. Because of the coherence properties of this UV light, HHG is the most common method to generate pulses with durations in the sub-femtosecond regime and photon energies up to the extreme-ultraviolet (XUV).

The combination of NIR and XUV pulses offers a wide range of new possibilities. In the form of a pump-probe setup, where the pump pulse triggers the dynamics and the probe pulse detects the changes in the system, either pulse could be used as pump or probe. In Sec. 3.1.5, I discuss attosecond streaking experiments, where the XUV and the NIR pulses are used as pump and probe pulses, respectively. For attosecond transient absorption experiments discussed in Sec. 3.1.6 it is reversed and the NIR pulse is used as a pump and the XUV pulse is used as a probe.

In Sec. 3.2, I discuss numerical propagation schemes. In Sec. 3.2.1, I focus on the widely used single-active electron (SAE) model, where electron-electron correlations cannot appear, since only one specific electron is allowed to move and all others are frozen. The time-dependent configuration-interaction singles (TDCIS) approach I have developed generalizes the idea of the SAE model. Only one electron can be fully active in the TDCIS method as well. However, it can come from any occupied orbital. Furthermore, the ionic state can be changed by interactions between the active electron and the remaining electrons of the ion. The TDCIS approach is discussed in detail in Sec. 3.2.2.

I explain my contributions towards the TDCIS code I have developed with colleagues in Sec. 3.3. Furthermore, I discuss the XCID package, which is an optimized and further developed version of the initial TDCIS code. In Sec. 3.4, I present the projects I have worked on using the XCID package. My projects range from many-body correlation effects in attosecond photoionization (Sec. 3.4.1) to multi-orbital contributions in the HHG spectrum of argon (Sec. 3.4.2) to attosecond transient absorption spectroscopy with overlapping pump and probe pulses (Sec. 3.4.3). The publications resulting from these projects can be found in Chap. 5.

Atomic units ($\hbar = |e| = m_e = 1/(4\pi\epsilon_0) = 1$)[2] are used throughout if not explicitly mentioned otherwise.

[2] see http://physics.nist.gov/cuu/Constants or Mohr *et al.*, RMP **84**, 1527 (2012)

Chapter 2

Laser-Induced Molecular Alignment:
About Picosecond and Femtosecond Dynamics

2.1 Introduction

2.1.1 Principles of Molecular Orientation and Alignment

A wide range of processes in nature depend on the relative orientation of the objects involved. This is true in the macroscopic world (e.g., collisions of classical particles) and it is also true in the microscopic world of atoms and molecules (e.g., chemical reactions [1]). Therefore, the interest is high in controlling the directionality of single molecules [2]. A very elegant way to control the molecular motion is by using electric fields $\mathcal{E}$ [3–5] and magnetic fields $\mathcal{H}$ [6–9]. In the following I focus on electric fields, since they have become the common technique to orient and align molecules [10]. The strengths of magnetic interactions are generally three orders of magnitudes weaker than electronic interactions [11]. Magnetic moments of molecules are normally around a Bohr magneton ($1\,\mu_B = 0.5$ a.u.) and large magnetic fields of around 1 Tesla are needed to orient and to align molecules [6]. Static magnetic fields of this magnitude are quite difficult to generate than corresponding electric fields.

The underlying mechanism for orienting and aligning molecules with electric fields can be well understood by looking at the Taylor expansion of the vibronic (electronic + vibrational) energy levels E_i in terms of the applied electric field $\mathcal{E}(\omega)$ [12]

$$E_i = E_i^{(0)} + \sum_{n>0} E_i^{(n)}(\omega), \tag{2.1a}$$

$$E_i^{(n)}(\omega) = -\frac{1}{n!}\,\gamma_i^{(n)}(\omega) \cdot \mathcal{E}^n(\omega), \tag{2.1b}$$

where $E_i^{(0)}$ are the field-free energy levels and $\gamma_i^{(n)}(\omega)$ are the n-th order dipole response

functions depending on the laser frequency ω. The symbol $\cdot$ stands for the inner product between the two tensors $\gamma_i^{(n)}(\omega)$ and $\mathcal{E}^n(\omega)$. In Cartesian coordinates, the inner product of two tensors A and B of rank n reads $A \cdot B = \sum_{i_1,\cdots,i_n \in \{X,Y,Z\}} A_{i_1,\cdots,i_n} B_{i_1,\cdots,i_n}$. Note that the electric field $\mathcal{E}(\omega)$ is a vector (i.e., tensor of rank 1).

The homogeneous character of the electric field over the size of a molecule allows one to neglect contributions from quadrupole or even higher moments [13]. The first three dipole response functions appearing in Eq. (2.1b) are well known under the name permanent dipole moment $\mu := \gamma^{(1)}$, dipole polarizability tensor $\alpha(\omega) := \gamma^{(2)}(\omega)$, and hyperpolarizability tensor $\beta(\omega) := \gamma^{(3)}(\omega)$. Note, the permanent dipole moment is not ω-dependent. The field frequency ω is commonly much lower than any vibronic transition. Therefore, the ω-dependence of the response functions can be dropped and the static limit ($\omega \to 0$) can be used [14]. The Taylor expansions in Eq. (2.1a) is particularly powerful when relatively weak electric fields are applied such that the infinite sum converges quickly for small n.

Rotational Potential

For common alignment scenarios, the field intensity is in the range 10^{12}-10^{13} W/cm^2 [10] and lies in the perturbative regime such that it is sufficient to focus on the first three energy corrections in the infinite sum of Eq. (2.1a). The energy corrections $E_i^{(n)}$ of the vibronic states can be viewed as a potential,

$$\hat{U}_i = \sum_{n=1}^{3} E_i^{(n)}(\omega), \tag{2.2}$$

for the remaining rotational degrees of freedom. The corrections $E_i^{(n)}$ depend on the relative orientation of the molecule with respect to the polarization of the electric field, since $\gamma^{(n)}$ are defined in the body-fixed molecular frame. The orientation of any molecule can be characterized by the Euler angles φ, ϑ, and χ [15]. Therefore, all potentials $\hat{U}_i$ can be expressed in terms of the Euler angles. Geometrically, the Euler angles define three rotations, which transform the space-fixed laser frame defined by the axes X, Y, and Z into the body-fixed molecular frame defined by the axes a, b, and c. Figure 2.1 illustrates this 3D coordinate transformation. Commonly, the angle φ refers to the rotation around the space-fixed Z axis, the angle χ refers to a rotation around the body-fixed c axis, and ϑ defines the angle between the space-fixed Z and body-fixed c axes. In general, the angle between a body-fixed axis $g \in \{a, b, c\}$ and a space-fixed axis $F \in \{X, Y, Z\}$ is labeled ϑ_{Fg}. In Sec. 2.3.2, these angles are used to analyze the 3D alignment of naphthalene molecules.

In Sec. 2.1.2, the explicit form of the angle-dependence of $\hat{U}_i$ is discussed in detail for different types of molecules and laser fields. If U_i is energetically larger than the kinetic energy, the molecule becomes trapped in the potential and the orientation or alignment of the molecule becomes well-defined in the space-fixed coordinate system. If an entire ensemble of molecules is exposed to such an electric field, a collective (ensemble-averaged)

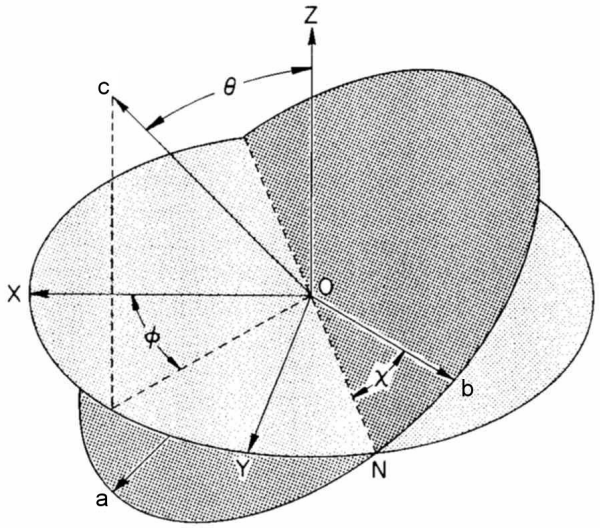

Figure 2.1: An illustration of a coordinate transformation from the space-fixed frame defined by the axes X, Y, Z into the body-fixed frame defined by the axes a, b, c. The rotations defined by the Euler angles φ, ϑ, χ are explicitly shown. The illustration is taken from Ref. [15]. Copyright © 1988 John Wiley & Sons, Inc.

orientation or alignment is observed, which is not random anymore. This is desirable, since the signal of a single molecule is generally too small to be statistically useful. A collective orientation or alignment increases the signal strength by the number of molecules in the ensemble, which can be easily of the order of 10^7 molecules [16].

Orientation and Alignment

Orientation and alignment refer both to the directionality of the molecule. However, there is a subtle difference between orientation and alignment. For orientation in 3D, all three Euler angles are uniquely defined. In the case of alignment, there exists a "head-tail" (C_2) symmetry around each symmetry axis–meaning an 180°-rotation of any symmetry axis does not matter. For perfect alignment, there exist 4 unique orientations that correspond to the same alignment [17]. The degree of orientation is measured by the quantity $\cos\vartheta$, where the sign indicates whether the molecules is oriented along or opposite to the desired orientation direction. The measure for alignment is $\cos^2\vartheta$, which is invariant under a 180°-rotation of the alignment axis (i.e., $\vartheta \to 180° + \vartheta$). For a randomly oriented (aligned) ensemble of molecules, the corresponding ensemble-averaged degree of orientation (alignment) is $\langle\cos\vartheta\rangle = 0$ $\left(\langle\cos^2\vartheta\rangle = \frac{1}{3}\right)$[1].

The measure for 3D orientation and 3D alignment requires at least 3 angles, one for each axis [18]. In the case of my studies on naphthalene (see Chap. 4.1/Ref. [19]), I used

[1] The angle ϑ_{Zc} is identical to the Euler angle ϑ.

the three measures $\cos^2\vartheta_{Xa}, \cos^2\vartheta_{Yb}$, and $\cos^2\vartheta_{Zc}$ to quantify 3D alignment. An average of these three angles can be also taken as a measure such that the 3D orientation/alignment is characterized by one quantity [20]. Orientation and alignment can be measured experimentally via the angular distribution of ion fragments of the aligned molecule [10, 21]. The ion fragments are produced by an intense second laser pulse, which forces the molecule to Coulomb explode. Fig. 2.2 illustrates how the degree of alignment is experimentally measured via Coulomb explosion. Recently, it has been shown that HHG can also be used to measure alignment dynamics [22].

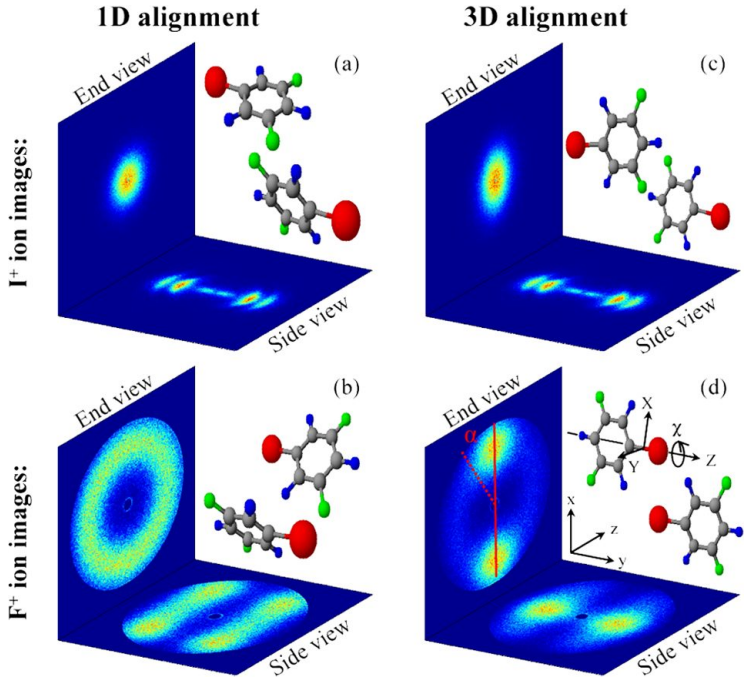

Figure 2.2: Illustration of measuring experimentally 3D alignment and/or orientation via the side view and end view detectors. The molecule shown is 3,5 difluoroiodobenzene, where the Iodine atom is depicted as red ball and the Fluorine atoms are depicted as green balls. Note, the space-fixed frame is labeled x, y, z and the body-fixed molecular frame is labeled X, Y, Z. The illustration is taken from Ref. [23]. Copyright © 2007 American Physical Society (APS).

The potential resulting from $E_i^{(2)}$ leads to aligned molecules, since inverting the direction of the electric field ($\mathcal{E} \to -\mathcal{E}$) does not affect the potential due to the quadratic field dependence [cf. Eq. (2.1b)]. The terms $E_i^{(1)}$ and $E_i^{(3)}$, which depend on odd powers of $\mathcal{E}$, change sign when the electric field is pointing in the opposite direction. Hence, the potential resulting from $E_i^{(1)}$ and $E_i^{(3)}$ leads to oriented molecules [24–27].

Structural Deformations

In most experiments the goal of applying an external field is to influence and to control only the rotational state while at the same time leaving the molecule in the vibronic ground state [10]. Common way to achieve orientation and alignment is with vibronically non-resonant optical fields alone [28, 29] and in combination with static electric fields [24, 27, 30]. However, alignment can be also achieved with resonant frequencies coupling two or several vibronic states with each other [31–34]. It has been shown that less intense electric fields are needed when resonant frequencies are used [35].

Structural deformations may also occur when static fields or non-resonant optical fields are used [36, 37]. Particularly for short laser pulses, where higher electric field strengths are needed to achieve the same degree of alignment [14], structural deformations start to appear [36, 38]. Nevertheless, the rigid-rotor approximation, where molecular deformations are ignored, is the most common model used [4, 10, 20, 29, 39, 40]. This model has been successful due to its great simplicity and explanatory power for many experimental results. Some works have been done to extend the rigid-rotor model in order to include centrifugal deformations in the rotational energies [41–44]. These deformations influence the rotational dynamics of the molecules, which becomes particularly prominent for linear molecules [45]. A complete description of rotational and vibronic dynamics, which may be even coupled to each other, is quite challenging.

In the following, the molecule is assumed to be in the vibronic ground state at all times[2]. Hence, I drop the vibronic index i. All energy corrections $E^{(n)}$, from now on, refer to the vibronic ground state of the molecule if not explicitly mentioned otherwise.

2.1.2 1D and 3D Alignment

Depending on the symmetry of the molecule and on the polarization of the electric field, molecules can be either aligned around one axis (1D alignment) or around all three axes (3D alignment) [10]. To understand under which conditions 1D or 3D alignment can be achieved, it is useful to consider the symmetries of the terms entering in the alignment potential.

For molecular alignment, only the term $E^{(2)}$ needs to be considered. Aligning molecules has several practical advantages in comparison to orienting them. First, not all molecules have permanent dipole moments ($\mu = 0 \Rightarrow E^{(1)} = 0$) and the third-order term $E^{(3)}$ has to be exploited, which requires large electric field strengths. Since all molecules have a non-zero polarizability [4], there always exists an aligning potential $E^{(2)}$. Second, quasi-monochromatic optical pulses can only couple to even order response functions (i.e., $\gamma^{(2n)}$)

[2] To be more precise, only the electronic state is considered to be in the quantum mechanical ground state. The vibrational degrees of freedom are described classically and not quantum-mechanically–meaning the nuclei are classical objects with fixed, well-defined distances between each other.

and, therefore, generate aligning potentials.

The tensors $\mathcal{E}^{2n+1}(t)$ vanish for optical monochromatic fields, since the cycle-averaged quantities of $\mathcal{E}^n(t)$ only survive for even n. Cycle-averaging of $\mathcal{E}^n(t)$ is justified when the field period is much smaller than the rotation dynamics of the molecule [38]. This is the case for typical alignment pulses (e.g., wavelength of 800 nm) with cycle periods in the few femtosecond regime. The typical time scale of rotational excitations is picoseconds (see Sec. 2.1.3).

As already mentioned, the energy correction of the vibronic ground state is an effective potential for the rotational degrees of freedom [cf. Eq. (2.2)]. The rotational Hamiltonian, where an optical pulse couples only to the polarizability α, is given by [19, 39]

$$\hat{H}(t) = \underbrace{A\,\hat{J}_a^2 + B\,\hat{J}_b^2 + C\,\hat{J}_c^2}_{\hat{H}_{\mathrm{rot}}} \underbrace{- \frac{1}{2}\sum_{LM}(-1)^{L+M}\hat{\alpha}_M^{[L]}\; F_{-M,\mathrm{avg}}^{[L]}(t)}_{-\hat{U}(t)}, \tag{2.3}$$

where $\hat{H}_{\mathrm{rot}}$ is the kinetic operator for molecular rotations, and $\hat{U}(t)$ is the effective aligning potential induced by the electric field, $\mathcal{E}(t)$. The rotational constants A, B, C of the molecular axes a, b, and c diagonalize the moment of inertia tensor. The angular momentum operators are given by $\hat{J}_g$ with $g \in \{a, b, c\}$. The potential $\hat{U}(t)$ is expressed via spherical tensor products [15], where $F_M^{[L]}(t) = [\mathcal{E}(t) \otimes \mathcal{E}(t)]_{M,\mathrm{avg}}^{[L]}$ is the spherical tensor of rank 2 with angular momentum L. M is the angular momentum projection onto the space-fixed Z axis. The subscript "avg" stands for the cycle-averaged quantity. Spherical tensors with $L = 1$ do not appear for α and $F(t)$, since both tensors are symmetric.

The electric field tensor $F(t)$ is "well-defined" in the space-fixed laser frame whereas the polarizability tensor α is "well-defined" in the molecular frame. Since the space-fixed Z axis is the quantization axis in the tensor product of Eq. (2.3), it is necessary to transform the known body-fixed spherical tensor components $\alpha_K^{[L]}$ (with the quantization axis c) into the space-fixed laser frame, which read [19, 39].

$$\alpha_M^{[L]}(\Omega) = \sum_K D_{M,K}^{*[L]}(\Omega)\,\alpha_K^{[L]}, \tag{2.4}$$

where $D_{M,K}^{*[L]}(\Omega)$ are the Wigner-D matrices connecting both frames with each other [15]. The three Euler angles are combined into $\Omega = (\varphi, \vartheta, \chi)$. It is exactly through this coordinate transformation that the alignment potential becomes angle-dependent $\hat{U}(t) \to \hat{U}(\Omega, t)$.

The quantum number K refers to the angular momentum projection onto the molecular c axis. The polarizability tensor α in the Cartesian representation is diagonal in the molecular frame with the values $\alpha_{a,a}, \alpha_{b,b}$, and $\alpha_{c,c}$. Note, the body-fixed frame that diagonalizes α is generally not the same frame that diagonalizes the moment of inertia tensor [46]. For small molecules (with a high symmetry), however, these two frames fall together. In the

following, I do not distinguish between these two molecular frames and focus on the case where they coincide.

Only terms in Eq (2.3) contribute to the aligning potential where both spherical tensor components, i.e., $\alpha_M^{[L]}$ and $F_{-M}^{[L]}(t)$, are non-zero. For example, $\alpha_0^{[0]}$ is the only non-zero component for a spherically symmetric molecule. Regardless of the complexity of $F(t)$ the resulting potential $\hat{U}(t)$ has no angle dependence, since only the Wigner-D matrix $D_{0,0}^{*[0]}(\Omega) = 1$ contributes. This angle-independent potential results in a global energy shift for all rotational states and, therefore, has no influence on the alignment process and can be neglected [47].

1D Alignment

The simplest alignment scenario is the 1D alignment of a linear ($A = B, C^{-1} = 0$) or symmetric-top ($A = B \neq C$) molecules with linearly polarized light. For linearly polarized fields, only the terms $F_0^{[0]}(t)$ and $F_0^{[2]}(t)$ are non-zero. The polarizability tensor in the Cartesian basis has the diagonal entries $\alpha_{aa} = \alpha_{bb} \neq \alpha_{cc}$ and, therefore, only the terms $\alpha_{K=0}^{[0]}$ and $\alpha_{K=0}^{[2]}$ are non-zero. By rotating from the molecular frame to the laser frame the Wigner-D matrix $D_{0,0}^{*[2]}(\Omega) = \frac{1}{2}(3\cos^2\vartheta - 1)$ enters. The resulting angle-dependent potential reads [4]

$$U_{1\mathrm{D}}(\vartheta, t) = -\frac{\alpha_{cc} - \alpha_{aa}}{2} \cos^2\vartheta \, [\mathcal{E}^2(t)]_{\mathrm{avg}}. \tag{2.5}$$

The cycle-average of a quasi-monochromatic pulse $\mathcal{E}(t) = \mathcal{E}_0(t)\sin(\omega t)$, where $\mathcal{E}_0(t)$ defines the pulse envelope, leads to the effective intensity $[\mathcal{E}^2(t)]_{\mathrm{avg}} = \mathcal{E}_0^2(t)/2$. For linear molecules, $\alpha_{cc} > \alpha_{aa}$ and the potential $U_{1\mathrm{D}}(\vartheta, t)$ has a minimum when the molecular c axis is aligned with the space-fixed Z axis ($\cos^2\vartheta = 1$). Depending on whether the symmetric-top molecule is prolate ($\alpha_{cc} > \alpha_{aa}$) or oblate ($\alpha_{cc} < \alpha_{aa}$), the molecular c axis is preferably aligned along ($\cos^2\vartheta = 1$) or perpendicular ($\cos^2\vartheta = 0$) to the field polarization axis Z.

In 1D alignment, only one molecular axis is fixed in space. Rotations around the axes c and Z are unaffected by $U_{1\mathrm{D}}(\vartheta, t)$, since no φ and χ dependencies exist in $U_{1\mathrm{D}}(\vartheta, t)$. As a consequence, the molecular axes a and b are aligned within a plane but it is not possible to hold either axis in a particular direction within this plane.

3D Alignment

3D alignment requires that all three molecular axes are fixed in space [20] (see Fig. 2.3). The potential $\hat{U}$ in Eq. (2.3) can only lead to 3D alignment, when $\hat{U}$ depends on all three Euler angels φ, ϑ, χ [40]. The ϑ dependence enters, since $F^{[L]}$ and $\alpha^{[L]}$ have non-zero components for $L > 0$, which influence the angular momentum J of the rotational states (for more details see Sec. 2.1.3). The φ and χ dependencies enter only when $F_{M=\pm 2}^{[2]} \neq 0$

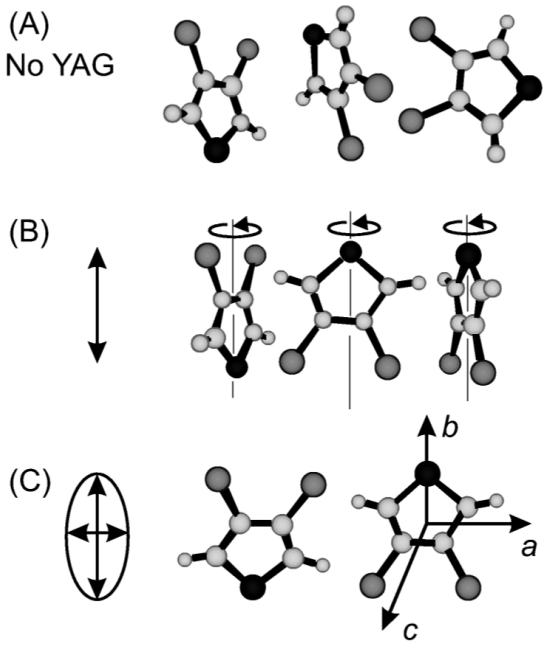

Figure 2.3: Illustration of non-aligned (A), 1D-aligned (B), and 3D-aligned (C) 3,4-dibromothiophene (black circles: sulfur, dark grey circles: bromine). For non-aligned molecules, all orientations are equally likely. 1D alignment is achieved with a linearly polarized pulse, and 3D alignment is accomplished with an elliptically polarized pulse. The illustration is taken from Ref. [48]. Copyright © 2000 American Physical Society (APS).

and $\alpha^{[2]}_{K=\pm 2} \neq 0$ are fulfilled, respectively. On the one side, $\alpha^{[2]}_{K=\pm 2} \neq 0$ is only possible for asymmetric-top molecules ($A < B < C$).

For symmetric-top and linear molecules, $\alpha_{aa} = \alpha_{cc}$ and, therefore, $\alpha^{[2]}_{K=\pm 2} = 0$. On the other side, $F^{[2]}_{M=\pm 2} \neq 0$ can be only achieved when elliptically polarized pulses or multiple pulses with different polarization directions are used. A schematic sketch of 3D alignment of two pulses with different linear polarizations is shown in Fig. 2.4.

If one of the two requirements for generating a φ- and χ-dependent potential is not fulfilled, only 1D alignment is possible. For instance, linearly polarized pulses (no φ-dependence) align asymmetric-top molecules (χ-dependence) only around the most polarizable axis [29, 49, 50] as for linear molecules. Panel (B) in Fig. 2.3 demonstrates this case. Elliptically polarized pulses (φ-dependence) used in combination with symmetric-top molecules (no χ-dependence) align only the symmetry axis c. However, this symmetry axis can be rotated in space, synchronized with the oscillating elliptically polarized field [45].

2.1.3 Alignment Dynamics

Dynamical states in quantum mechanics are coherent superpositions of eigenstates of the system (i.e., Hamiltonian). I start my discussion on symmetric-top rotors ($A = B$). Many effects can be understood in this case, while I also point out differences and similarities to asymmetric-top rotors. The rotational kinetic operator of a symmetric-top rotor is

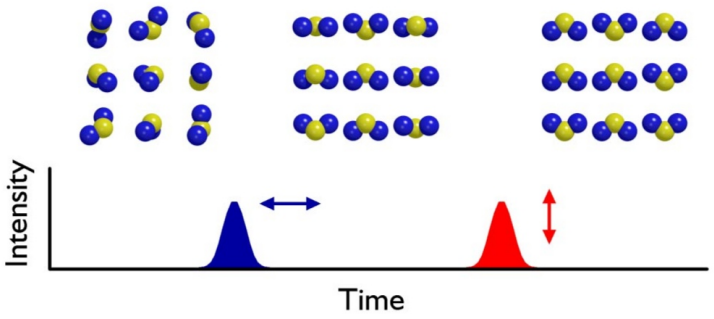

Figure 2.4: A schematic illustration of 3D alignment of SO_2 with two different linearly polarized pulses is shown. The first pulse aligns the randomly oriented molecules along the most polarizable axis. The second pulse aligns the second most polarizable axis leading to 3D alignment. This figure is taken from Ref. [51]. Copyright © 2006 American Physical Society (APS).

$\hat{H}_{\text{rot}} = A\,\hat{J}^2 + (C-A)\,\hat{J}_c^2$. Its rotational eigenstates are given by [15]

$$\langle \Omega |\, JKM \rangle = \sqrt{\frac{2J+1}{8\pi^2}}\, D^{*[J]}_{M,K}(\Omega), \tag{2.6a}$$

$$\hat{H}_{\text{rot}}\,|JKM\rangle = \underbrace{\left[A\,J(J+1) - (C-A)K^2\right]}_{E_{J,K}} |JKM\rangle\,, \tag{2.6b}$$

where $D^{*[J]}_{M,K}$ are the well-known Wigner-D matrices [15], and $E_{J,K}$ are the rotational energies. K and M are again the angular momentum projections onto the body-fixed c axis and the space-fixed Z axis, respectively. Since the rotation is defined in the molecular frame, the rotational energies are degenerate with respect to M. In the case of linear molecules ($C^{-1} = 0$), the rotation around the c axis is energetically not possible ($K = 0$) and the rotational energies simplify to $A\,J(J+1)$. For general asymmetric-top rotors, the kinetic operator

$$\hat{H}_{\text{rot}} = \frac{A+B}{2}\,\hat{J}^2 + \frac{2C-A-B}{2}\,\hat{J}_0^2 + \frac{A-B}{2}\left[\hat{J}_{+1}^2 + \hat{J}_{-1}^2\right], \tag{2.7a}$$

$$\hat{H}_{\text{rot}}\,|J\tau M\rangle = E_{J,\tau}\,|J\tau M\rangle\,, \tag{2.7b}$$

mixes different K states such that K is no longer a good quantum number. The rotational eigenstates $|J\tau M\rangle$ are superpositions of $|JKM\rangle$ [40]. It is not possible to give an analytic expression for the rotational energies $E_{J,\tau}$ in contrast to the rotational energies of symmetric-top rotors, $E_{J,K}$. The angular momentum operators are rewritten as spherical tensor operators $\hat{J}_{0,\pm1}$ in the body-fixed frame.

Similar to the relation between $\hat{x}$ and $\hat{p}_x$, where the localization of the wavefunction in real space requires the wavefunction to be delocalized (coherent superposition) in momen-

tum space, a localization of the rotational wavefunction at specific Euler angles requires a coherent superposition of rotational states, $|JKM\rangle$. Coherent superpositions of different J, K, and M states are needed to localize the rotational wavefunction in ϑ, χ, and φ, respectively. Rotational wavepackets of a symmetric-top rotor can be written as

$$|\Psi(t)\rangle = \sum_{J,K,M} c_{J,K,M}(t) e^{-i\,E_{J,K}\,t}\,|JKM\rangle\,. \tag{2.8}$$

The time evolution of the rotational wavepacket is determined by the time-dependent Schrödinger equation,

$$i\frac{\partial}{\partial t}\,|\Psi(t)\rangle = \hat{H}(t)\;|\Psi(t)\rangle\,, \tag{2.9}$$

where $\hat{H}(t)$ is defined in Eq. (2.3).

Alignment Revivals

The coefficients $c_{J,K,M}(t)$ do only change in time when an aligning potential is present. If no external field is present, $c_{J,K,M}(t)$ are time-independent constants. For linear molecules, all rotational energies $E_{J,K=0} = A\,J(J+1)$ are multiples of A. Hence, the rotational wavepacket shows a repeating pattern in time called *revivals*. The revival period is $T_{\text{rev}} = \pi/A$ [52]. Often the rotational period is given by $T_{\text{rev}} = \frac{1}{2A}$ [53], where A is given in Hz instead of energy units.

Additionally, there are features at $T_{\text{rev}}/2$ (half revivals) as shown in Fig. 2.5. At $T_{\text{rev}}/2$ neighboring rotational states swing out of phase leading to an antialignment of molecules. Quarter revivals at $T_{\text{rev}}/4$ do only occur for molecules with the appropriate spin statistics [41, 54]. For example, $^{16}O_2$ has two nuclear spins of $I = 0$. Due to the overall symmetry of the molecular wavefunction (vibronic + rotational + nuclear spin), only rotational states with an odd J are allowed and, therefore, quarter revivals can be seen [55]. In the molecule ^{79}Br-^{81}Br the two atoms are distinguishable and all rotational states have the same spin weight [44]. Hence, no quarter revivals are visible.

The revival features do also exist for symmetric-top molecules. The additional degree of freedom ($K \neq 0$ is possible) does not change the nature of these features. In asymmetric-top molecules no true revival structure can be found, since the rotational energies are non-commensurable [15]. However, revival-type behavior has been observed [53], which lasts only for a finite amount of time till the rotational states are totally dephased. The most common revival-like behaviors are C- and J-type revivals, where J-type revivals have a period of $1/(B+C)$ and occur for nearly symmetric-top molecules ($B \approx C$) [53, 56]. Revivals of the type J are common in planar molecules and have a period $1/(4C)$, where C is the rotational constant of the molecular c axis, which points perpendicular to the molecular plane [57].

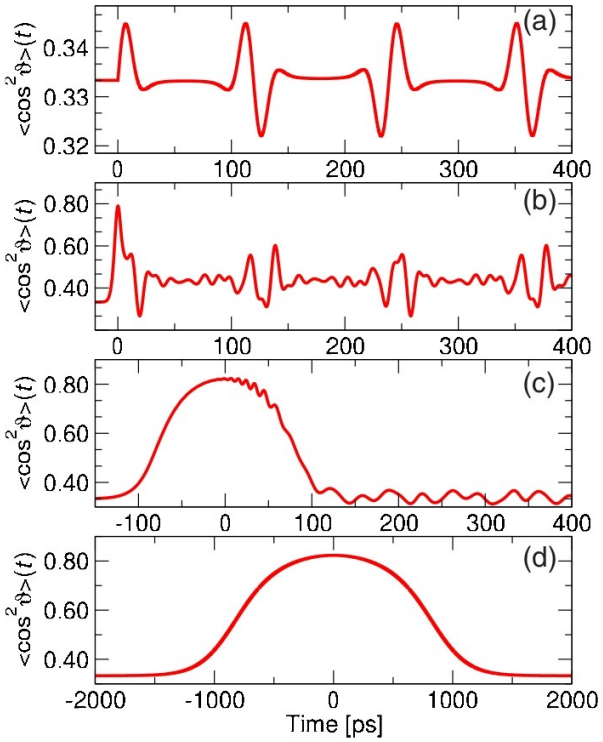

Figure 2.5: The degree of alignment $\langle \cos^2 \theta \rangle (t)$ is shown for the symmetric-top molecule CF_3Br. The different regimes of alignment dynamics are shown ranging from purely impulsive alignment (a) via mostly non-adiabatic (b) and quasi-adiabatic alignment (c) to perfectly adiabatic alignment (d). The pulse duration changes from 50 fs (a) over 10 ps (b) and 95 ps (c) to 1 ns (d). The revival period $1/(2A)$ of CF_3Br seen in (a) is close to 240 ps. This figure is taken from Ref. [14]. Copyright © 2008 American Institute of Physics (AIP).

The repeating revival behavior of symmetric-top molecules allows one to generate the alignment first and to use/probe the alignment at a later time [52, 58]. Revivals can be also used to increase the degree of alignment step-by-step by using several pulses separated by the revival period [45, 59]. Applying pulses at half or quarter revivals allows one to control the subsequent revival structure [55].

Adiabatic and Non-Adiabatic Alignment

To be able to generate and to use these revivals, it is necessary that the laser pulse kicking the molecule is short compared to T_{rev}. This type of alignment scheme is known as *impulsive* or *non-adiabatic* alignment [10, 60]. Since typical rotational periods are in the picosecond to nanosecond regime, impulsively aligning pulses are typically in the femtosecond regime. Pulses that are much longer than the rotational period lead to *adiabatic* alignment [35].

In the adiabatic regime, the alignment follows the envelope of the laser pulse and returns after the pulse to its initial state. Impulsive alignment gives the molecules a kick such that the molecular alignment dynamics persist after the pulse is over. Furthermore, impulsive alignment has been a very attractive technique to achieve alignment, since the molecule can be probed under field-free condition [49]. Figure 2.5 shows the different response behaviors of the symmetric-top molecule CF_3Br, which ranges from impulsive alignment in panel (a) to adiabatic alignment in panel (d).

Besides the laser pulse, the degree of alignment also depends on the rotational temperature of the molecules. As one may expect, with higher temperature the degree of alignment goes down [14]. This is true in the impulsive as well as in the adiabatic case. For both cases it is possible to derive an analytic expression for the maximum possible degree of alignment depending on the pulse parameters and the rotational temperature of the molecules [61]. The rotational temperature of the molecules also has an impact on the characteristic rotational period, which becomes shorter for increasing temperatures. Hence, higher temperatures lead to more adiabatic-like alignment behavior [14, 62].

Recently, quantum-state-selection techniques have been used to select only specific rotational states out of the thermally populated sea of rotational states [26, 63] in order to improve the alignment by minimizing the negative impact of temperature. An almost perfect 1D alignment of $\langle \cos^2 \vartheta_{2D} \rangle = 0.97$ was achieved with this scheme [26].

Very high degrees of alignment can be also reached with a combination of adiabatic and impulsive alignment [64]. A very popular technique is to use a long pulse, which is turned on adiabatically and turned off abruptly such that the molecule can be probed field-free [61, 65, 66]. Around the times of the turn-off, a second short pulse is used to "kick" the molecules into an even higher degree of alignment. This technique has become particularly popular to align asymmetric-top molecules in 3D under field-free conditions [23].

Non-adiabatic field-free 3D alignment via multiple femtosecond pulses is also possible [39, 51]. However, with such a pulse configuration it is much harder to achieve 3D alignment than 1D alignment [67]. I discuss field-free 3D alignment in Sec. 2.3.1. If it is not so important to get 3D alignment under field-free condition, adiabatic alignment schemes with an elliptically polarized pulse are quite powerful [48].

2.1.4 Molecular Orientation

For molecular orientation, it is necessary that the energy corrections $E^{(1)}(\omega)$ and $E^{(3)}(\omega)$ contribute to the potential $\hat{U}(\omega)$ [see Eq. (2.2)]. As discussed in Sec. 2.1.2, an optical monochromatic pulse cannot induce an orienting potential (i.e., $E^{(2n+1)}(\omega) = 0$). The reason is in the optical period, which is much shorter than the typical rotational time scale. For static electric fields $\mathcal{E}_{\text{static}}$, where the period goes to infinity, this is not true anymore, and the coupling to the permanent dipole moment μ leads to an orienting potential

$$U(\vartheta, t) = \mathcal{E}_{\text{static}}\, \mu \cos \vartheta. \tag{2.10}$$

Common static field strengths lie in the range of 10^2–10^5 V/cm ($\approx 10^{-8}$–10^{-5} a.u.) [68, 69]. Such weak fields only affect the rotational states when coupled to μ leading to the energy correction $E^{(1)}(\omega)$ [70]. Since optical laser pulses have been proven to be very successful in aligning molecules, several groups have worked on orienting molecules by combining static electric fields with optical laser pulses [68, 71, 72]. A schematic illustration of this technique is shown Fig. 2.6.

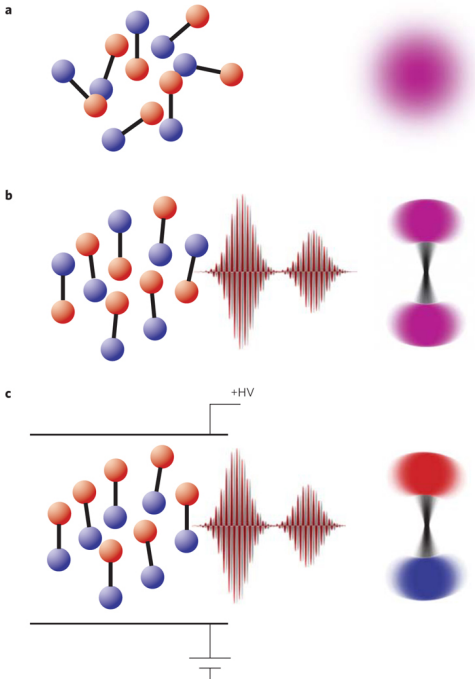

Figure 2.6: A schematic illustration of 1D orientation of a linear molecule by means of a combination of a weak static electric field and optical laser pulses. The coupling of the dc field to the permanent dipole moment of the diatomic molecule orients the molecule. Without any field the molecules are randomly oriented (a). Applying optical laser pulses aligns the molecules (b). The combination of static and optical fields (c) can be used to achieve high degrees of orientation. This figure is taken from Ref. [73]. Copyright © 2009 Nature Publishing Group (NPG).

For non-polar molecules ($\mu = 0$), multi-color pulses have to be used in order to orient molecules [18, 74, 75]. In this case, the orientation is accomplished through the coupling of the electric field to the hyperpolarizability tensor β (i.e., $E^{(3)}$ energy correction). Particularly for short pulses with high electric field strengths, it was shown that it is possible to achieve orientation via the hyperpolarizability [25, 74, 76]. In recent experiments, it has been seen that orientation substantially enhances when ionizing intensities are reached [77]. Similar to the case of alignment, earlier works have focused first on accomplishing field-free 1D orientation [71] and later 3D orientation [78].

The quality of orientation depends highly on the rotational temperature [76, 79, 80]. Many systematic studies have been performed to find the optimal setup for maximizing the orientation in a given molecule [74, 80, 81]. Very high degrees of orientation can be reached when quantum-state-selection techniques are combined with orienting static fields and impulsively aligning femtosecond pulses. This has been demonstrated with NO molecules, where an observed degree of orientation of $\langle \cos \vartheta \rangle = -0.74$ has been seen [82].

Recently, progress has been made in using terahertz (THz) pulses to orient molecules. The cycle periods is now in the picosecond regime and becomes comparable to the characteristic rotational time scale [80, 83–86]. As a consequence, the requirement for averaging the pulse over a period is not fulfilled anymore. The instantaneous electric field can, now, successfully couple to the permanent dipole moment. In contrast to static fields, the orienting potential becomes time-dependent. Interesting new rotational motions may appear by using THz pulses together with optical pulses, which lead to high degrees of orientation.

2.2 My Developments

2.2.1 XALMO

In this section, I discuss in more detail the 3D alignment package XALMO (X-ray Scattering of laser-aligned Molecules) I have developed. It is a generalization of earlier works [87], which was limited to linear and symmetric-top rotors. Most physical ideas and concepts implemented in the program are already presented in my publication [67] presented in Sec. 4.1. The scope of XALMO ranges

- from linear molecules to asymmetric-top molecules,
- from linearly polarized pulses to elliptically polarized pulses,
- and from non-adiabatic alignment to adiabatic alignment.

For each possible alignment scenario, all available symmetries are exploited. The angular momentum projection M is a conserved quantity for linearly polarized light but not for elliptically polarized light. The quantum number K is a conserved quantity for linear and symmetric-top molecules but not for asymmetric-top molecules. More details of the symmetry considerations are discussed at the end of this section. The XALMO package consists of three main program parts:

1. alignment propagation
2. temperature extrapolation
3. 3D x-ray scattering pattern.

In part (1) of XALMO, the time propagation of the rotational wavepacket is performed. The program is able to simulate impulsive and adiabatic alignment dynamics as well as everything in between. This wide dynamical range requires a numerical propagation of Eq. (2.9). In this way the laser-matter interaction is treated non-perturbatively and any kind of alignment pulse or pulse train can be simulated (as long as the criterion for cycle-averaging holds). Besides the calculation of time-dependent alignment signals like $\langle \cos^2 \theta_{Fg} \rangle (t)$, alignment probability distributions can be calculated. In part (3) of XALMO, these alignment probability distributions are used to calculate x-ray diffraction patterns for a given x-ray pulse. The impact of non-perfect alignment on the x-ray diffraction pattern is discussed in more detail in Sec. 2.3.2.

Part (2) of XALMO extrapolates the alignment dynamics to other (mostly lower) rotational temperatures, T. This is possible, since the influence of T is partially factored out. The initially thermally populated rotational states are incoherent with each other. Hence,

each initial state can be separately propagated and the overall signal is built up at the end. Adjusting the thermal weights of each initial state allows one to quickly assemble the degree of alignment for any temperature provided all required contributions are already calculated. This implemented strategy is particularly favorable for studying temperature dependencies. Also the demand on later calculations at higher temperature is strongly reduced, since calculations of parts of the needed initial states are already preformed.

Efficiency Considerations

Time Propagation In the following, I focus on some details of my implementation of solving as efficiently as possible the time-dependent Schrödinger equation [cf. Eq. (2.9)] with the initial condition $|\Psi(-\infty)\rangle = |J\tau M\rangle$. For symmetric-top molecules, τ is substituted by K. By expressing the wavepacket in the basis of the rotational eigenstates, it is easy to transform $|\Psi(t)\rangle$ into the interaction picture, where the alignment potential reads $\hat{U}_I(t) = e^{+i\hat{H}_{\mathrm{rot}}t}\hat{U}(t)e^{-i\hat{H}_{\mathrm{rot}}t}$. Propagating in the interaction picture has the advantage that the time evolution is exact when the pulse is over. The kinetic operator $\hat{H}_{\mathrm{rot}}$ can be substituted by the rotational energies E_{JK} for symmetric-top or $E_{J\tau}$ for asymmetric-top molecules, since the rotational wavepacket is expressed in the basis of the rotational eigenstates [see Eqs. (2.6)–(2.7)]. In the following, I use $E_{J\tau}$ to indicate the rotational energies (for asymmetric-top and symmetric-top molecules). However, evaluating an exponential function is numerically more expensive than preforming an addition or multiplication.

To improve the efficiency I discretize the equation of motion in the interaction picture and transform it back into the Schrödinger picture. This has the consequences that instead of the terms $e^{\pm iE_{J\tau}t}$ only the term $e^{-iE_{J\tau}dt}$ appears in the equation of motion (for more details see my publication in Chap. 4.1/Ref. [19]). The term $e^{-iE_{J\tau}dt}$ has the advantage that it only depends on the time step dt and not on the overall time t. Therefore, it is sufficient to evaluate this phase factor only once at the beginning of the calculation and store it. At a later time, this phase factor needs to be only loaded instead of loading the rotational energies and calculating the phase factors for the overall time t. Only when dt changes the term $e^{-iE_{J\tau}dt}$ needs to be reevaluated. This implementation can speed up the calculations by a factor 2 or more. Additionally, I implemented an adjustable time step scheme, which is particularly advantageous when a substantial part of the propagation is done under field-free conditions.

Symmetry Aspects Solving the time-dependent Schrödinger equation for 3D alignment is much more demanding than for 1D alignment. The alignment potential $\hat{U}_{1D}(t)$ given by Eq. (2.5) depends only on ϑ—more specifically only on $D^{[2]}_{00}(\varphi,\vartheta,\chi)$. As a consequence, the matrix elements $\langle JKM|\,\hat{U}_{1D}(t)\,|J'K'M'\rangle \propto \delta_{K,K'}\delta_{M,M'}$ do not change K and M, which are preserved during the entire propagation. Furthermore, the odd or even character of the initial angular momentum J is preserved as well, since J can only change in steps of

2. Note, for an orienting potential even and odd J can occur at the same time. The size of the configuration space needed to describe $|\Psi(t)\rangle$ for 1D alignment with the initial state $|JKM\rangle$ is rather small with $|(J+2n)KM\rangle\,, n \in \mathbb{Z}$. It scales like $J_{\max}/2$, where $J_{\max}$ is the maximum angular momentum needed.

For 3D alignment, the potential $\hat{U}(t)$ has to change also the K and M states as discussed in Sec. 2.1.2. The size of the required configuration space is, therefore, proportional to $2J_{\max}^3$. For common alignment scenarios, $J_{\max}$ is around 50. Hence, the calculations are 10^4 times more expensive. The configuration space can be reduced by a factor 4 by considering that the Hamiltonian is invariant under the operations $M \to -M$ and $K \to -K$. By being aware that K and M can only change by 2, another factor 4 can be saved. It is also true for asymmetric-top molecules even though K is not a good quantum number. However, the rotational eigenstates of an asymmetric-top molecule separate into two classes with only even and only odd K numbers (for more details see Chap. 4.1/Ref. [19]). The XALMO package is written in a way such that all available symmetries in the molecular frame (K symmetry) and in the laser frame (M symmetry) are exploited independently.

Another time consuming factor is the calculation of the alignment probability distribution $\rho(\varphi, \vartheta, \chi)$ needed for the x-ray scattering pattern. Here, a factor 16 can be gained by exploiting 4 symmetries in the Euler angles, which correspond to C_2 rotations around two axes in the molecular frame and two axes in the laser frame.

2.2.2 The Measure $\langle \cos^4 \vartheta \rangle$

An alignment is commonly measured in terms of directional cosines $\langle \cos^2 \vartheta_{Fg} \rangle$, where $F \in \{X, Y, Z\}$ refers to a space-fixed axis and $g \in \{a, b, c\}$ refers to a molecular axis (see Sec. 2.1.1). Higher order moments in $\cos^2 \vartheta_{Fg}$ ($\cos \vartheta_{Fg}$) are needed to get more information about the detailed alignment (orientation) distribution than just the statistical mean. The uncertainty of an observable $\hat{O}$ is such a quantity that requires higher moments. It is defines by $(\Delta\hat{O})^2 = \langle \hat{O}^2 \rangle - \langle \hat{O} \rangle^2$. The uncertainty in the orientation is given by $(\Delta \cos \vartheta_{Fg})^2 = \langle \cos^2 \vartheta_{Fg} \rangle - \langle \cos \vartheta_{Fg} \rangle^2$. If orientation is not possible (i.e., $\langle \cos \vartheta_{Fg} \rangle = 0$) the uncertainty is directly given by $\langle \cos^2 \vartheta_{Fg} \rangle$, which is the observable of choice for alignment scenarios. The alignment uncertainty is, therefore, given by $(\Delta \cos^2 \vartheta_{Fg})^2 = \langle \cos^4 \vartheta_{Fg} \rangle - \langle \cos^2 \vartheta_{Fg} \rangle^2$. For studies comparing classical and quantum behaviors in the alignment dynamics, the uncertainty $\Delta \cos^2 \vartheta_{Fg}$ becomes a useful quantity to look at, since higher order moments in the observable (like $\cos^4 \vartheta_{Fg}$) are generally more sensitive to quantum behavior than the statistical mean (i.e., $\langle \cos^2 \vartheta_{Fg} \rangle$).

For structural reconstruction from x-ray scattering patterns from laser-aligned molecules (see Sec. 2.3.2), it could become helpful to have more information about the alignment distribution than the mean value, $\langle \cos^2 \vartheta_{Fg} \rangle$. Methods like phase-retrieval algorithms [88–90] are used to extract the molecular structure out of the diffraction pattern. Phase-retrieval techniques commonly assume that the diffraction pattern is one perfectly coherent scatter-

ing image. Imperfect alignment, however, leads to incoherent averaging. Not taking into account these incoherent effects significantly reduces the resolution of the reconstruction (see Sec. 2.3.2). Methods including incoherent contributions in the reconstruction algorithm have been demonstrated to be very successful in improving the resolution. These schemes are known as partial coherence schemes [91]. Knowing more about the imperfect alignment (e.g., via $\Delta\cos^2\vartheta_{Fg}$) can help in finding good discretization schemes for an incoherent averaging due to imperfect alignment.

To evaluate $\Delta\cos^2\vartheta_{Fg}$, the matrix elements $\langle JKM|\cos^4\vartheta_{Fg}\,|J'K'M'\rangle$ expressed in the basis of the rotational eigenstates $|JKM\rangle$ have to be derived. They can be easily calculated once the operator $\cos^4\vartheta_{Fg}$ is formulated in terms of Wigner-D matrices. The directional cosines $\cos\vartheta_{Fg} = \mathbf{e}_F^L\cdot\mathbf{e}_g^M$ can be written in terms of the Cartesian basis vectors $\mathbf{e}_F^L$ and $\mathbf{e}_g^M$ of the space-fixed (laser) and body-fixed (molecular) frame, respectively. $\cos\vartheta_{Fg}$ are also the matrix elements of the rotation matrix $R(\Omega)$, which connects the the two frames [15] (see Fig. 2.1). Note that $\Omega = (\varphi,\vartheta,\chi)$ represents the full set of Euler angles. The Wigner-D matrices $D^{[1]}_{M,K} := D^{[1]}_{M,K}(\Omega)$ are also matrix elements of the rotation matrix $R(\Omega)$. This is the case, when the spherical basis vectors $\mathbf{e}_M^L$ and $\mathbf{e}_K^M$ with $K,M\in\{0,\pm1\}$ are used to define the space-fixed frame and the body-fixed frame, respectively. In the spherical basis, the transformation between the body-fixed frame and the space-fixed frame is given by

$$\mathbf{e}_M^L = \sum_K D^{[1]}_{M,K}\;\mathbf{e}_K^M. \tag{2.11}$$

The orthogonality relation of (complex) spherical basis vectors reads,

$$\mathbf{e}_p^*\cdot\mathbf{e}_q = (-1)^p\,\mathbf{e}_{-p}\cdot\mathbf{e}_q = \delta_{p,q}, \qquad p,q\in\{\pm1,0\}. \tag{2.12}$$

After expressing the Cartesian vectors in the spherical basis,

$$\mathbf{e}^L_{X/Y} = \sqrt{\frac{\pm1}{2}}\left(\mathbf{e}^L_{-1}\mp\mathbf{e}^L_1\right), \qquad \mathbf{e}^L_Z = \mathbf{e}^L_0, \tag{2.13a}$$

$$\mathbf{e}^M_{a/b} = \sqrt{\frac{\pm1}{2}}\left(\mathbf{e}^M_{-1}\mp\mathbf{e}^M_1\right), \qquad \mathbf{e}^M_c = \mathbf{e}^M_0, \tag{2.13b}$$

the directional cosines can be expressed in terms of the Wigner-D matrices:

$$\cos\theta_{Zc} = \mathbf{e}^L_Z\cdot\mathbf{e}^M_c = \sum_K D^{[1]}_{0,K}\;\mathbf{e}^M_K\cdot\mathbf{e}^M_0 = D^{[1]}_{0,0}\;, \tag{2.14a}$$

$$\cos\theta_{Xc/Yc} = \sqrt{\frac{\pm1}{2}}\left(D^{[1]}_{-1,0}\mp D^{[1]}_{1,0}\right), \tag{2.14b}$$

$$\cos\theta_{Za/Zb} = -\sqrt{\frac{\pm1}{2}}\left(D^{[1]}_{0,1}\mp D^{[1]}_{0,-1}\right), \tag{2.14c}$$

$$\cos\theta_{Xa/Yb} = \frac{1}{2}\left[\left(D^{[1]}_{1,1}+D^{[1]}_{-1,-1}\right)\mp\left(D^{[1]}_{1,-1}+D^{[1]}_{-1,1}\right)\right], \tag{2.14d}$$

$$\cos\theta_{Ya/Xb} = \frac{1}{2i}\left[\left(D^{[1]}_{-1,1}-D^{[1]}_{1,-1}\right)\pm\left(D^{[1]}_{1,1}-D^{[1]}_{-1,-1}\right)\right]. \tag{2.14e}$$

The matrices $\cos^4\vartheta_{Fg}$ can now be easily calculated by using the relation [15]

$$D^{[J_1]}_{M_1,K_1} D^{[J_2]}_{M_2,K_2} = \sum_J \langle J_1 M_1; J_2 M_2 | JM \rangle \langle J_1 K_1; J_2 K_2 | JM \rangle D^{[J]}_{M,K}. \tag{2.15}$$

Finally, the matrix $\cos^4\vartheta_{Fg}$ can be expressed in terms of the Wigner-D matrices. Here, five out of the nine combinations of $\cos^4\vartheta_{Fg}$ are stated:

$$\cos^4\theta_{Zc} = \left[D^{[1]}_{0,0}\right]^4 = \left[\frac{1}{3}D^{[0]}_{0,0} + \frac{2}{3}D^{[2]}_{0,0}\right]^2 = \frac{1}{5}D^{[0]}_{0,0} + \frac{4}{7}D^{[2]}_{0,0} + \frac{8}{35}D^{[4]}_{0,0}, \tag{2.16a}$$

$$\cos^4\theta_{Xc/Yc} = \frac{1}{5}D^{[0]}_{0,0} - \frac{2}{7}D^{[2]}_{0,0} + \frac{3}{35}D^{[4]}_{0,0} + \sqrt{\frac{1}{70}}(D^{[4]}_{4,0})_s \pm \sqrt{\frac{6}{49}}(D^{[2]}_{2,0})_s \mp \sqrt{\frac{2}{245}}(D^{[4]}_{2,0})_s, \tag{2.16b}$$

$$\begin{aligned}\cos^4\theta_{Xa/Yb} = \frac{1}{16}\Bigg[&\frac{16}{5}D^{[0]}_{0,0} + \frac{16}{7}D^{[2]}_{0,0} \mp \frac{8}{7}\sqrt{6}(D^{[2]}_{2,0})_{ss} + \frac{24}{7}(D^{[2]}_{2,2})_s \\ &+ \frac{18}{35}D^{[4]}_{0,0} \mp \sqrt{\frac{72}{245}}(D^{[4]}_{2,0})_{ss} + \frac{4}{7}(D^{[4]}_{2,2})_s \\ &+ \sqrt{\frac{18}{35}}(D^{[4]}_{4,0})_{ss} \mp \sqrt{\frac{4}{7}}(D^{[4]}_{4,2})_{ss} + (D^{[4]}_{4,4})_s\Bigg].\end{aligned} \tag{2.16c}$$

To keep the equations reasonably short, the symbols

$$(D^{[L]}_{K,M})_s = \begin{cases} D^{[L]}_{K,M} + D^{[L]}_{-K,M} + D^{[L]}_{K,-M} + D^{[L]}_{-K,-M} & , K \neq 0 \neq M \\ D^{[L]}_{K,0} + D^{[L]}_{-K,0} & , K \neq 0 = M \\ D^{[L]}_{0,M} + D^{[L]}_{0,-M} & , M \neq 0 = K \end{cases} \tag{2.17}$$

and $(D^{[L]}_{K,M})_{ss} = (D^{[L]}_{K,M})_s + (D^{[L]}_{M,K})_s$ have been introduced.

2.3 Applications

In this section, I discuss two applications of molecular alignment I have worked on. One project discusses field-free 3D alignment with multiple pulses in Sec. 2.3.1. In Sec. 2.3.2, the possibility to use 3D aligned molecules to obtain x-ray diffraction patterns is investigated. These diffraction patterns are used to reconstruct the molecular structure. Both projects have led to publications, which are presented in Sec. 4.

Besides my two projects, there are of course many other applications of aligned molecules; also in combination with my second field of study: ionization dynamics. Tunnel ionization, for instance, can depend on the alignment or even on the orientation of molecules [92, 93]. In heteronuclear molecules like OCS, the ionization potential is angle-dependent. By using

circularly polarized light, it is possible to mark via the vector potential from which end of the molecule the ionized electron originated from [92]. This experiment is an example that shows how important it is to have a good control of the rotational degrees of freedom of the molecule.

Molecular alignment can also influence the photoabsorption cross section of a molecule. Particularly when the absorption is favored along one specific molecular axis, the cross section depends on the angle between the favored molecular axis and the polarization direction of the photon [47]. This has been experimentally demonstrated on CF_3Br, where the x-ray absorption cross section depends on the alignment of the C-Br molecular axis [16].

HHG is another mechanism where the alignment of molecules matters. The HHG process can be separated into 3 main parts: (1) an electron gets tunnel-ionized by a strong laser field, (2) the same field accelerates the electron first away and then back to the ion, (3) the electron recombines with the ionic hole state and emits a highly energetic photon (much higher than the photon energy of the driving laser pulse). In Chap. 3, the physics behind HHG is discussed in more detail.

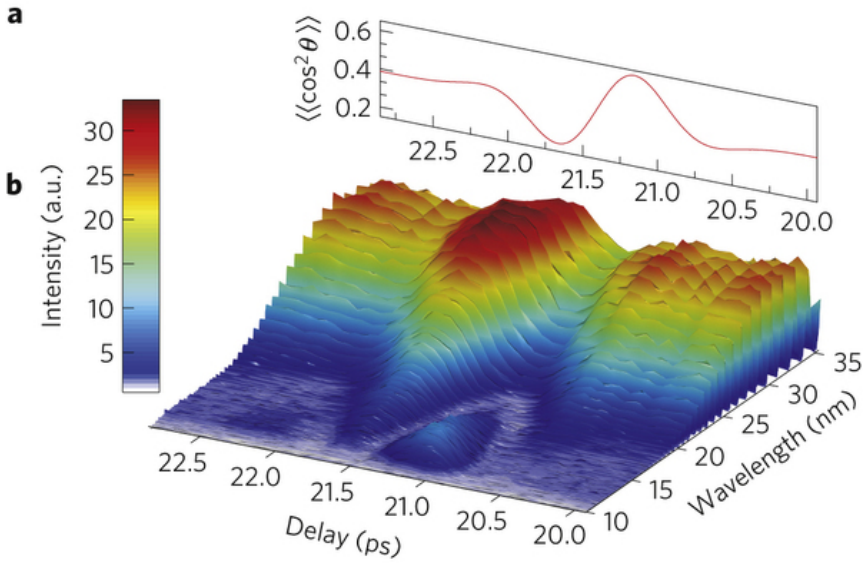

Figure 2.7: The HHG spectrum of CO_2 is shown as a function of pump-probe delay (and degree of alignment in panel a). The pump pulse aligns the molecule and the probe pulse drives the HHG process. The degree of alignment as a function of the pump-probe delay is shown in the background. Structural information about the molecular orbitals can be gained from these modifications of the HHG spectrum. This figure is taken from Ref. [94]. Copyright © 2011 Nature Publishing Group (NPG).

When molecules are used for the HHG process, it has been observed that the emitted HHG spectrum depends on the alignment of the molecule—specifically the alignment of the highest occupied molecular orbitals (HOMOs) with respect to the returning electron [95].

The angle dependence of the HHG spectrum is not just a scaling of the overall HHG yield. Changing the alignment direction of the molecule leads also to modification in the substructures of the HHG spectrum [94, 96, 97].

In Fig. 2.7 the HHG spectrum of CO_2 is shown as a function of alignment angle between the molecular symmetry axis and the polarization direction of the linearly polarized strong field pulse. It has been schown that structural informations about the HOMO orbitals can be extracted from the HHG spectrum [94, 98].

2.3.1 Using Multiple Pulses to 3D-Align SO_2 under Field-Free Conditions

As discussed in Sec. 2.1.2, the energy spacings between the rotational eigenstates of an asymmetric-top rotor are non-commensurable, and, therefore, no true revival pattern can be observed in contrast to linear and symmetric-top molecules. However, for a short time asymmetric-top molecules show revival features called A-, C-, and J-revivals [29].

In my publication [67] "Alignment of asymmetric-top molecules using multiple-pulse

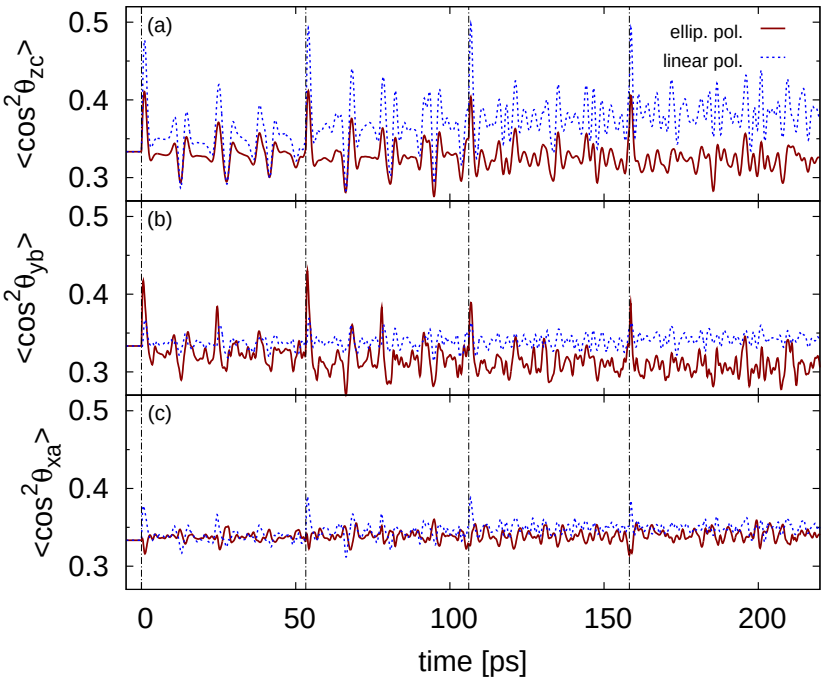

Figure 2.8: The alignment dynamics of all three molecular axes of SO_2 are shown. The short pulses (indicated by dashed lines) kick the molecules at the J revivals with linearly and with elliptically polarized pulses, respectively. This figure is taken from my publication [67].

trains" (see Sec. 4.2) I address the question whether or not it is possible to improve field-free 3D alignment of asymmetric molecules with multi-pulse schemes similar to those used for improving 1D alignment of linear molecules [45]. Field-free alignment can be only achieved with short femtosecond pulses such that the alignment dynamics is non-adiabatic. Specifically, I look at the asymmetric-top molecule SO_2, which is close to a symmetric-top molecule $A \approx B$. First, I investigated to which extent pulses equally spaced by $1/(A+B)$ (J revivals) improve the alignment.

In Fig. 2.8 the alignment dynamics of each molecular axis of SO_2 is shown for linearly and elliptically polarized pulses. As expected for linearly polarized pulses, only the most polarizable c axis gets aligned. With elliptically polarized pulses also the second most polarizable b axis can be aligned. However, the third molecular axis is counter-intuitively not aligned. This lack of alignment is classically not possible, since the alignment of two axes automatically aligns the third one as well. Here it is possible, since the degree of alignment is rather weak and a connection to a classical picture cannot be made.

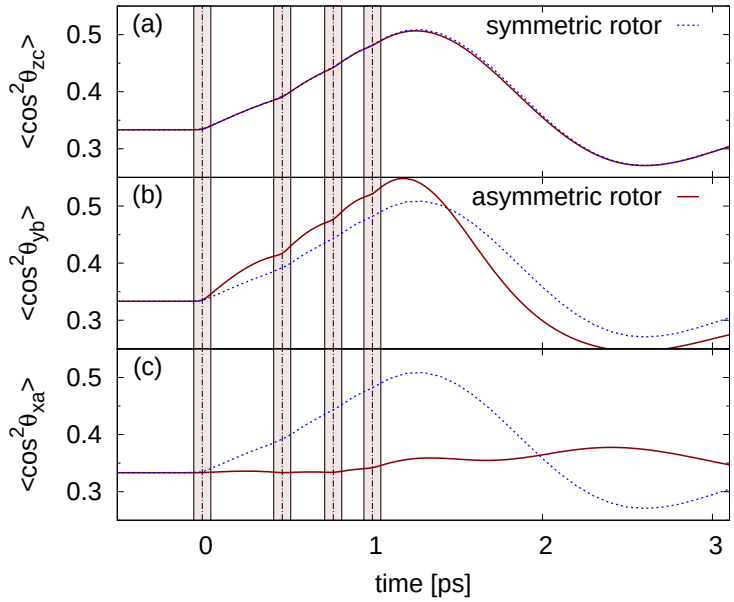

Figure 2.9: The alignment dynamics of all three molecular axes of SO_2 are shown. The short pulses kicking the molecules are highlighted (red shaded region). This figure is taken from my publication [67]. Copyright © 2010 American Physical Society (APS).

To improve on this technique, I proposed a new method of aligning asymmetric-top molecules with elliptically polarized pulses, which arrive directly after each other as discussed in Ref. [99] for linear molecules with linearly polarized light. The results I have obtained are shown in Fig. 2.9. The degree of alignment is significantly enhanced for the two most polarizable axes, whereas the least polarizable axis is almost not affected. Hence, SO_2 cannot be aligned in 3D with a sequence of short pulses.

Very recent studies on 3,5 difluoroiodobenzene improved on my idea by using a combination of linearly and elliptically polarized pulses. First results indicate it is possible to improve on 3D alignment; particularly when the molecule is oblate[3].

[3] private discussion at the GRC Multiphoton conference 2012

2.3.2 X-ray Scattering from 3D-Aligned Naphthalene Molecules

An interesting application of aligned molecules is electron [100, 101] or x-ray [87] diffraction. Particularly for single-molecule imaging [102, 103] it is favorable to know and to control the orientation of the molecule such that an entire 3D diffraction pattern can be collected. With the help of phase-retrieval algorithms it is possible to recover the phase information of the diffraction pattern, which was lost during the measurement [88–90, 104]. New approaches (namely multiwavelength anomalous diffraction) have also been developed to determine the phase directly from the measurement [105].

A large number of molecules contributing to the scattering signal is advantageous, since the scattering cross section is small—especially for large scattering angles [106]. When molecules are periodically ordered as in a crystal, Bragg peaks [107] occur and their scattering signal increases quadratically with the number of molecules. This quadratic increase is very favorable and it is at the heart of x-ray crystallography [107]. Periodic ordering is commonly exploited in order to determine the structure of macromolecules [107]. Unfortunately, not all molecules (like membrane proteins) can be grown in a large crystal.

Recent advances have shown it is also possible to recover the molecular structure from nanocrystals [108] (for a review see Ref. [109]). The high x-ray intensities are needed to collect enough signal destroy the molecules during the x-ray pulse [102]. This obstacle of molecular explosion can be overcome by making the x-ray pulse shorter than the time it takes for the molecule to explode [102, 110, 111].

Another approach for collecting x-ray diffraction patterns uses gas phase molecules, where up to 10^7 molecules can contribute to the scattering signal [16]. These molecules are randomly positioned (not randomly aligned) in space and, therefore, the diffraction pattern increases only linearly with the number of molecules. However, collecting signal over many x-ray shots reduces the required intensity such that common 3rd generation synchrotron sources like PETRA III at DESY[4] or the Advanced Photon Source at Argonne National Laboratory[5] can be used.

All molecules have to be oriented and/or aligned simultaneously to be able to record a single-molecule scattering pattern. Here is where laser alignment comes into play. Previous works have looked at x-ray scattering from 1D aligned symmetric molecules [87, 112]. In my publication [19] "Computational studies of x-ray scattering from three-dimensionally-aligned asymmetric-top molecules" (see Sec. 4.1) I present an extension of this scheme to x-ray scattering from 3D aligned asymmetric-top molecules. As an example molecule I used Naphthalene (see Fig. 2.10), which is a planar molecule with a head-tail symmetry such that orientation and alignment become indistinguishable. This is convenient, since different orientations add up incoherently and make it harder to reconstruct the molecular structure with phase-retrieval methods, which assume perfectly coherent diffraction patterns.

[4] http://hasylab.desy.de/facilities/petra_iii/index_eng.html
[5] http://www.aps.anl.gov

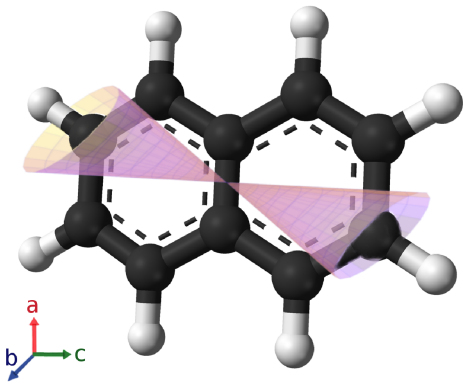

Figure 2.10: The structure of naphthalene ($C_{10}H_8$). All atoms lie in the *ac* molecular plane. The coordinate system is shown in the lower left corner. The cones symbolize the resolution limit of the carbon atoms due to imperfect alignment. This figure is taken from my publication [19]. Copyright © 2010 American Physical Society (APS).

The positions of the atoms in the laser frame are not well defined due to the imperfect alignment of the molecules (illustrated by the cones in Fig. 2.10). This uncertainty results in an incoherent average of different scattering patterns, which blurs out the scattering pattern for large scattering angles (i.e., large momentum transfer Q of the x-ray photon) as seen Fig. 2.11a. This has a direct consequence on the effective resolution in the corresponding reconstructions shown in Fig. 2.11b. The worse the alignment the smaller is the useful part of the diffraction patterns which can be fed into the phase-retrieval algorithm. Hence, the effective resolution decreases with less 3D-aligned molecules.

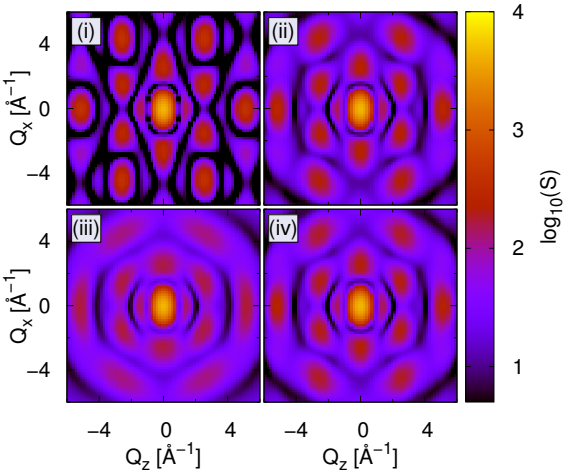

(a) X-ray diffraction patterns

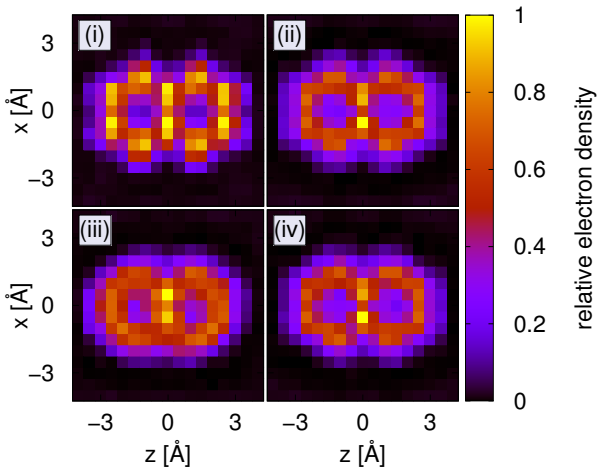

(b) Reconstructions

Figure 2.11: X-ray diffraction patterns (a) and their the corresponding reconstructed structure (b) are shown for different degrees of alignment: (i) perfect alignment, (ii) $T = 10$ mK and a 1 ps x-ray pulse, (iii) $T = 1$ K and a 100 ps x-ray pulse, and (iv) $T = 10$ mK and a 100 ps x-ray pulse. The aligning IR pulse is 100 ps long and aligns the molecule adiabatically. The figures are taken from my publication [19]. Copyright © 2010 American Physical Society (APS).

The main contribution to the imperfect alignment is the rotational temperature T [cf. panels (iii) and (iv) in Fig. 2.11]. The length of the x-ray pulse does not have a large influence as long as it is shorter or comparable with the adiabatic alignment pulse [cf. panels (ii) and (iv) in Fig. 2.11]. The effective resolution is only better than the typical distance between the atoms (~ 1.4 Å) when the rotational temperature is less than 10 mK. Quantum state selection techniques [26] could be used to improve the alignment but they result in less scattering signal.

Another approach to improve on the reconstruction uses partial-coherence schemes in the phase-retrieval algorithm [91]. It has been shown for partially coherent x-ray pulses that such schemes improve the quality of the reconstruction [113]. Partial-coherence schemes make explicit use of the fact that the final scattering pattern is an incoherent sum of coherent diffraction patterns. For x-ray scattering from 3D-aligned molecules, the incoherent sum enters due to the imperfect alignment. Similarly it is expected that partial-coherence schemes can be used to build in the effect of imperfect alignment.

2.4 Bibliography

[1] R. B. Bernstein, J. Chem. Phys. **82**, 3656 (1985).

[2] H. Loesch, Annu. Rev. Phys. Chem. **46**, 555 (1995).

[3] K. H. Kramer and R. B. Bernstein, J. Chem. Phys. **42**, 767 (1965).

[4] B. Friedrich and D. Herschbach, Phys. Rev. Lett. **74**, 4623 (1995).

[5] B. Friedrich and D. Herschbach, J. Phys. Chem. **99**, 15686 (1995).

[6] B. Friedrich and D. R. Herschbach, Z. Phys. D **24**, 25 (1992).

[7] A. Slenczka, B. Friedrich, and D. Herschbach, Phys. Rev. Lett. **72**, 1806 (1994).

[8] M. Auzinsh, A. V. Stolyarov, M. Tamanis, and R. Ferber, J. Chem. Phys. **105**, 37 (1996).

[9] S. Pelloni, I. García Cuesta, A. Sánchez de Merás, and P. Lazzeretti, J. Phys. Chem. Lett. **1**, 1463 (2010).

[10] H. Stapelfeldt and T. Seideman, Rev. Mod. Phys. **75**, 543 (2003).

[11] A. E. Siegman, *Lasers* (Univ Science Books, 1986).

[12] D. M. Bishop, Rev. Mod. Phys. **62**, 343 (1990).

[13] M. Medved, P. W. Fowler, and J. M. Hutson, Mol. Phys. **98**, 453 (2000).

[14] C. Buth and R. Santra, J. Chem. Phys. **129**, 134312 (2008).

[15] R. N. Zare, *Angular Momentum* (Wiley, New York, 1988).

[16] E. R. Peterson, C. Buth, D. A. Arms, *et al.*, Appl. Phys. Lett. **92**, 094106 (2008).

[17] J. C. H. Spence, K. Schmidt, J. S. Wu, G. Hembree, U. Weierstall, B. Doak, and P. Fromme, Acta Crystallogr A **61**, 237 (2005).

[18] T. Kanai and H. Sakai, J. Chem. Phys. **115**, 5492 (2001).

[19] S. Pabst, P. J. Ho, and R. Santra, Phys. Rev. A **81**, 043425 (2010).

[20] V. Makhija, X. Ren, and V. Kumarappan, Phys. Rev. A **85**, 033425 (2012).

[21] P. W. Dooley, I. V. Litvinyuk, K. F. Lee, D. M. Rayner, M. Spanner, D. M. Villeneuve, and P. B. Corkum, Phys. Rev. A **68**, 023406 (2003).

[22] R. M. Lock, S. Ramakrishna, X. Zhou, H. C. Kapteyn, M. M. Murnane, and T. Seideman, Phys. Rev. Lett. **108**, 133901 (2012).

[23] S. S. Viftrup, V. Kumarappan, S. Trippel, H. Stapelfeldt, E. Hamilton, and T. Seideman, Phys. Rev. Lett. **99**, 143602 (2007).

[24] B. Friedrich and D. Herschbach, J. Chem. Phys. **111**, 6157 (1999).

[25] S. De, I. Znakovskaya, D. Ray, *et al.*, Phys. Rev. Lett. **103**, 153002 (2009).

[26] L. Holmegaard, J. H. Nielsen, I. Nevo, H. Stapelfeldt, F. Filsinger, J. Küpper, and G. Meijer, Phys. Rev. Lett. **102**, 023001 (2009).

[27] H. Sakai, S. Minemoto, H. Nanjo, H. Tanji, and T. Suzuki, Phys. Rev. Lett. **90**, 083001 (2003).

[28] D. Daems, S. Guérin, E. Hertz, H. R. Jauslin, B. Lavorel, and O. Faucher, Phys. Rev. Lett. **95**, 063005 (2005).

[29] A. Rouzée, S. Guérin, V. Boudon, B. Lavorel, and O. Faucher, Phys. Rev. A **73**, 033418 (2006).

[30] L. Cai, J. Marango, and B. Friedrich, Phys. Rev. Lett. **86**, 775 (2001).

[31] M. J. Vrakking and S. Stolte, Chem. Phys. Lett. **271**, 209 (1997).

[32] G. Granucci, M. Persico, and P. V. Leuven, J. Chem. Phys. **120**, 7438 (2004).

[33] L. P. Yatsenko, S. Guerin, M. Amniat-Talab, and H. R. Jauslin, J. Chem. Phys. **126**, 034305 (2007).

[34] W.-H. Hu, C.-C. Shu, Y.-C. Han, K.-J. Yuan, and S.-L. Cong, Chem. Phys. Lett. **474**, 222 (2009).

[35] T. Seideman, J. Chem. Phys. **103**, 7887 (1995).

[36] M. Comstock, V. Senekerimyan, and M. Dantus, J. Phys. Chem. A **107**, 8271 (2003).

[37] C. B. Madsen, L. B. Madsen, S. S. Viftrup, *et al.*, Phys. Rev. Lett. **102**, 073007 (2009).

[38] C. M. Dion, A. Keller, O. Atabek, and A. D. Bandrauk, Phys. Rev. A **59**, 1382 (1999).

[39] J. G. Underwood, B. J. Sussman, and A. Stolow, Phys. Rev. Lett. **94**, 143002 (2005).

[40] M. Artamonov and T. Seideman, J. Chem. Phys. **128**, 154313 (2008).

[41] H. W. Kroto, *Molecular Rotation Spectra* (Dover Publications, Mineola, N.Y., 2003).

[42] V. Renard, M. Renard, S. Guérin, Y. T. Pashayan, B. Lavorel, O. Faucher, and H. R. Jauslin, Phys. Rev. Lett. **90**, 153601 (2003).

[43] R. de Nalda, C. Horn, M. Wollenhaupt, M. Krug, L. Bañares, and T. Baumert, J. Raman Spec. **38**, 543 (2007).

[44] P. J. Ho, M. R. Miller, and R. Santra, J. Chem. Phys. **130**, 154310 (2009).

[45] J. P. Cryan, P. H. Bucksbaum, and R. N. Coffee, Phys. Rev. A **80**, 063412 (2009).

[46] P. F. Bernath, *Spectra of Atoms and Molecules*, 2nd ed. (Oxford University Press, New York, 2005).

[47] C. Buth and R. Santra, Phys. Rev. A **77**, 013413 (2008).

[48] J. J. Larsen, K. Hald, N. Bjerre, H. Stapelfeldt, and T. Seideman, Phys. Rev. Lett. **85**, 2470 (2000).

[49] E. Péronne, M. D. Poulsen, C. Z. Bisgaard, H. Stapelfeldt, and T. Seideman, Phys. Rev. Lett. **91**, 043003 (2003).

[50] E. Péronne, M. D. Poulsen, H. Stapelfeldt, C. Z. Bisgaard, E. Hamilton, and T. Seideman, Phys. Rev. A **70**, 063410 (2004).

[51] K. F. Lee, D. M. Villeneuve, P. B. Corkum, A. Stolow, and J. G. Underwood, Phys. Rev. Lett. **97**, 173001 (2006).

[52] T. Seideman, Phys. Rev. Lett. **83**, 4971 (1999).

[53] L. Holmegaard, S. S. Viftrup, V. Kumarappan, C. Z. Bisgaard, H. Stapelfeldt, E. Hamilton, and T. Seideman, Phys. Rev. A **75**, 051403 (2007).

[54] P. R. Bunker and P. Jensen, *Molecular Symmetry and Spectroscopy*, 2nd ed. (National Research Council of Canada, 1998).

[55] K. F. Lee, D. M. Villeneuve, P. B. Corkum, and E. A. Shapiro, Phys. Rev. Lett. **93**, 233601 (2004).

[56] M. D. Poulsen, E. Péronne, H. Stapelfeldt, C. Z. Bisgaard, S. S. Viftrup, E. Hamilton, and T. Seideman, J. Chem. Phys. **121**, 783 (2004).

[57] P. M. Felker, J. Phys. Chem. **96**, 7844 (1992).

[58] F. Rosca-Pruna and M. J. J. Vrakking, J. Chem. Phys. **116**, 6567 (2002).

[59] M. Leibscher, I. S. Averbukh, and H. Rabitz, Phys. Rev. Lett. **90**, 213001 (2003).

[60] A. Keller, C. M. Dion, and O. Atabek, Phys. Rev. A **61**, 023409 (2000).

[61] T. Seideman, J. Chem. Phys. **115**, 5965 (2001).

[62] V. Kumarappan, C. Z. Bisgaard, S. S. Viftrup, L. Holmegaard, and H. Stapelfeldt, J. Chem. Phys. **125**, 194309 (2006).

[63] E. Gershnabel and I. S. Averbukh, J. Chem. Phys. **134**, 054304 (2011).

[64] S. Guérin, A. Rouzée, and E. Hertz, Phys. Rev. A **77**, 041404 (2008).

[65] J. G. Underwood, M. Spanner, M. Y. Ivanov, J. Mottershead, B. J. Sussman, and A. Stolow, Phys. Rev. Lett. **90**, 223001 (2003).

[66] M. D. Poulsen, T. Ejdrup, H. Stapelfeldt, E. Hamilton, and T. Seideman, Phys. Rev. A **73**, 033405 (2006).

[67] S. Pabst and R. Santra, Phys. Rev. A **81**, 065401 (2010).

[68] H. Tanji, S. Minemoto, and H. Sakai, Phys. Rev. A **72**, 063401 (2005).

[69] R. T. Jongma, G. von Helden, G. Berden, and G. Meijer, Chem. Phys. Lett. **270**, 304 (1997).

[70] B. Friedrich and Herschbach, J. Phys. Chem. A **103**, 10280 (1999).

[71] R. Baumfalk, N. H. Nahler, and U. Buck, J. Chem. Phys. **114**, 4755 (2001).

[72] Y. Sugawara, A. Goban, S. Minemoto, and H. Sakai, Phys. Rev. A **77**, 031403 (2008).

[73] J. G. Underwood, Nat. Phys. **5**, 253 (2009).

[74] R. Tehini and D. Sugny, Phys. Rev. A **77**, 023407 (2008).

[75] M. Muramatsu, M. Hita, S. Minemoto, and H. Sakai, Phys. Rev. A **79**, 011403 (2009).

[76] H. Yun, H. T. Kim, C. M. Kim, C. H. Nam, and J. Lee, Phys. Rev. A **84**, 065401 (2011).

[77] M. Spanner, S. Patchkovskii, E. Frumker, and P. Corkum, Phys. Rev. Lett. **109**, 113001 (2012).

[78] I. Nevo, L. Holmegaard, J. H. Nielsen, *et al.*, Phys. Chem. Chem. Phys. **11**, 9912 (2009).

[79] M. Machholm and N. E. Henriksen, Phys. Rev. Lett. **87**, 193001 (2001).

[80] M. Lapert and D. Sugny, Phys. Rev. A **85**, 063418 (2012).

[81] C. M. Dion, A. Ben Haj-Yedder, E. Cancès, C. Le Bris, A. Keller, and O. Atabek, Phys. Rev. A **65**, 063408 (2002).

[82] O. Ghafur, A. Rouzee, A. Gijsbertsen, W. K. Siu, S. Stolte, and M. J. J. Vrakking, Nat. Phys. **5**, 289 (2009).

[83] C.-C. Shu, K.-J. Yuan, W.-H. Hu, and S.-L. Cong, J. Chem. Phys. **132**, 244311 (2010).

[84] A. Fleischer, H. J. Wörner, L. Arissian, *et al.*, Phys. Rev. Lett. **107**, 113003 (2011).

[85] K. Kitano, N. Ishii, and J. Itatani, Phys. Rev. A **84**, 053408 (2011).

[86] C. Qin, Y. Tang, Y. Wang, and B. Zhang, Phys. Rev. A **85**, 053415 (2012).

[87] P. J. Ho and R. Santra, Phys. Rev. A **78**, 053409 (2008).

[88] J. Miao, D. Sayre, and H. N. Chapman, J. Opt. Soc. Am. A **15**, 1662 (1998).

[89] V. Elser, J. Opt. Soc. Am. A **20**, 40 (2003).

[90] V. Elser and R. P. Millane, Acta Crystallogr A **64**, 273 (2008).

[91] H. M. Quiney and K. A. Nugent, Nat. Phys. **7**, 142 (2011).

[92] L. Holmegaard, J. L. Hansen, L. Kalhoj, *et al.*, Nat. Phys. **6**, 428 (2010).

[93] J. L. Hansen, L. Holmegaard, J. H. Nielsen, H. Stapelfeldt, D. Dimitrovski, and L. B. Madsen, J. Phys. B **45**, 015101 (2012).

[94] C. Vozzi, M. Negro, F. Calegari, G. Sansone, M. Nisoli, S. De Silvestri, and S. Stagira, Nat. Phys. **7**, 822 (2011).

[95] T. Kanai, S. Minemoto, and H. Sakai, Nature **435**, 470 (2005).

[96] M. Meckel, D. Comtois, D. Zeidler, *et al.*, Science **320**, 1478 (2008).

[97] D. A. Telnov and S.-I. Chu, Phys. Rev. A **80**, 043412 (2009).

[98] J. Itatani, J. Levesque, D. Zeidler, *et al.*, Nature **432**, 867 (2004).

[99] I. S. Averbukh and R. Arvieu, Phys. Rev. Lett. **87**, 163601 (2001).

[100] C. I. Blaga, J. Xu, A. D. DiChiara, *et al.*, Nature **483**, 194 (2012).

[101] C. J. Hensley, J. Yang, and M. Centurion, Phys. Rev. Lett. **109**, 133202 (2012).

[102] R. Neutze, R. Wouts, D. van der Spoel, E. Weckert, and J. Hajdu, Nature **406**, 752 (2000).

[103] G. Huldt, A. Szoke, and J. Hajdu, Journal of Structural Biology **144**, 219 (2003).

[104] R. H. T. Bates, Optik **61**, 247 (1982).

[105] S.-K. Son, H. N. Chapman, and R. Santra, Phys. Rev. Lett. **107**, 218102 (2011).

[106] R. Santra, J. Phys. B **42**, 023001 (2009).

[107] J. Als-Nielsen and D. McMorrow, *Elements of Modern X-ray Physics* (Wiley, Chichester, 2001).

[108] H. N. Chapman, P. Fromme, A. Barty, *et al.*, Nature **470**, 73 (2011).

[109] R. A. Kirian, J. Phys. B **45**, 223001 (2012).

[110] K. J. Gaffney and H. N. Chapman, Science **316**, 1444 (2007).

[111] S. Boutet, L. Lomb, G. J. Williams, *et al.*, Science **337**, 362 (2012).

[112] P. J. Ho, D. Starodub, D. K. Saldin, V. L. Shneerson, A. Ourmazd, and R. Santra, J. Chem. Phys. **131**, 131101 (2009).

[113] L. W. Whitehead, G. J. Williams, H. M. Quiney, *et al.*, Phys. Rev. Lett. **103**, 243902 (2009).

Chapter 3

Ultrafast Ionization Dynamics in Noble Gas Atoms:
About Femtosecond and Attosecond Dynamics

3.1 Introduction

3.1.1 Description of Light-Matter Interaction

Electron excitations and ionizations induced by ultrashort laser pulses are key mechanisms in attosecond physics [1]. The energy difference between electronic states determines the time scale of the corresponding electronic motion. Typical energy differences between electronic states of molecules and atoms lie within $0.1 - 100$ eV. The corresponding time scales are 50 as to 50 fs. The rapid technological progress in building lasers with sub-femtosecond pulses [2, 3] makes it possible to study fundamental mechanisms in chemical and physical processes in a time-resolved fashion [4]. The attosecond physics community is closely tied to the strong-field physics community since, in one way or another, intense laser pulses are involved (at least in the generation of attosecond pulses). Due to the wide interest in these fields, several review articles have been written in strong-field physics [2, 5–9] and attosecond physics [1, 10–13], which focus more on ionization processes and system dynamics, respectively.

Pump-probe approaches are particularly advantageous for time-resolved studies [14]. Each pump-probe configuration corresponds to a snapshot and a sequence of snapshots corresponds to a movie. The time resolution is determined by the ability to accurately control the pump-probe delay τ, which can be already measured to subattosecond (zeptosecond) precision [15]. Many attosecond pump-probe experiments use a femtosecond near-infrared (NIR) pulse and an attosecond ultraviolet (UV) pulse [1]. Either pulse can be used as a pump or as a probe pulse (see Sec. 3.1.5 and Sec. 3.1.6). On the one hand,

NIR pulses are usually strong-field pulses, which lead to non-perturbative tunnel ionization. UV pulses, on the other hand, generally lead to electronic excitation and to perturbative multiphoton ionization.

Pump-probe experiments can also be done with two UV pulses [16]. It is, however, experimentally challenging if both UV pulses have low intensity, since the final signal strength would be quite weak. This is not the case for UV pulses generated by free-electron lasers (FELs) such as FLASH [17]. Here, the number of photons per pulse is quite high and UV-UV pump-probe experiments do not suffer from low statistics [16, 18]. All these different types of pump-probe schemes are complementary to each other and enable us to investigate many different aspects in the ultrafast world [1].

Keldysh Parameter

A common measure for characterizing the nature of field-induced ionization is the Keldysh parameter γ, which is given by [19]

$$\gamma = \sqrt{\frac{I_p}{2U_p}}, \tag{3.1}$$

where I_p is the ionization potential of the electronic state and $U_p = \frac{E^2}{4\omega^2}$ is the ponderomotive potential, which is the average energy of a free electron oscillating in the electric field with amplitude E and frequency ω. The Keldysh parameter distinguishes between two ionization regimes: perturbative ($\gamma \gg 1$) and non-perturbative ($\gamma \ll 1$) multiphoton ionization. Figure 3.1 illustrates the physical pictures behind these two regimes.

However, recent studies [20] have found that γ alone is not always a rigorous measure to decide whether or not the ionization is perturbative or non-perturbative. Particularly for $\gamma < 1$ and photon energies comparable or larger than the ionization potential ($\omega \gtrsim I_p$) the ionization process becomes more and more perturbative (contrary to what the Keldysh parameter would suggest).

In the case of $\gamma \gg 1$, the ionization lies in the perturbative multiphoton (or few-photon) regime. The light-matter interaction can be seen as a correction to the field-free system. The system gets ionized by absorbing a certain number of photons (see Fig. 3.1(a)). In other words, the final state of the system is a result of a well-defined (and countable) number n of light-matter interactions. These n light-matter interactions are exactly captured by the n^{th}-order perturbation correction. Therefore, this regime is the perturbative multiphoton regime.

The ionization is considered to be in the non-perturbative multiphoton (or tunneling) regime[1] for $\gamma \ll 1$. Here, the Coulomb potential of the system rather than the field is

[1] $\gamma \ll 1$ is also commonly referred to as the quasistatic limit, since γ goes to zero for a given field strength and $\omega \to 0$.

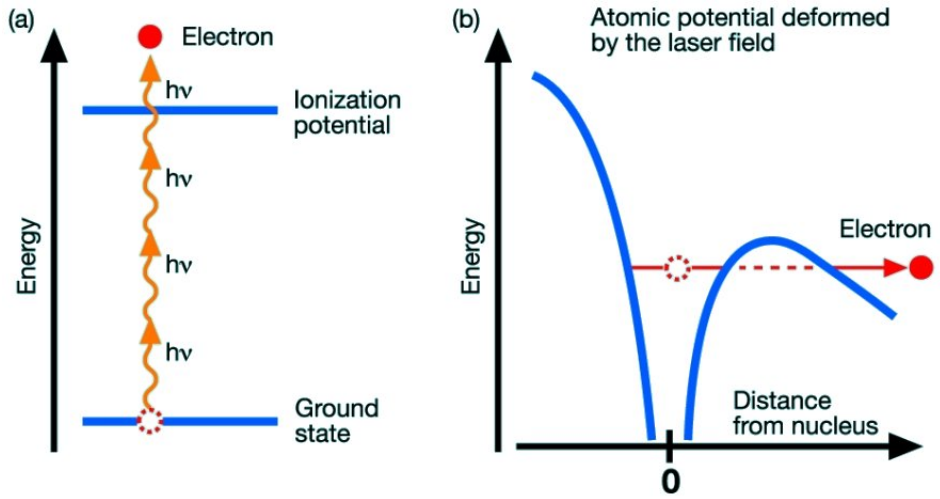

Figure 3.1: The perturbative (a) and the non-perturbative (b) multiphoton regimes are illustrated. This figure is taken from http://www.desy.de. Copyright © 2007 DESY.

considered to be the perturbation. Furthermore, the light-matter interaction is pictured as a local potential that strongly distorts the Coulomb potential, and already after a few Bohr radii the field-induced potential starts to dominate the motion of the electron (see Fig. 3.1(b)). This distortion creates a potential barrier, which can be overcome by the electron by *tunneling* through this barrier and, consequently, out of the system. Once the electron is tunneled to the outer side of the barrier, the Coulomb potential becomes negligible and the dynamics is govern by the field-induced potential. Note, not just quantized photon picture has been dropped but also the number of photons an electron absorbs during ionization becomes an ill-defined quantity due to the non-perturbative nature of tunnel ionization.

To distinguish experimentally these two ionization regimes, it is quite convenient to study the photoelectron spectrum, specifically the energy distribution [20]. In the tunneling limit, no characteristic photoelectron energies are observed whereas in the perturbative regime the photoelectron spectrum becomes discrete and the positions of the energy peaks reveal directly the number of photons the electron has absorbed during ionization.

Minimal Coupling Hamiltonian

By solving the full time-dependent Schrödinger equation (TDSE),

$$i\frac{\partial}{\partial t}\left|\Psi(t)\right\rangle = \hat{H}(t)\ \ \left|\Psi(t)\right\rangle, \tag{3.2a}$$

both ionization limits as well as everything in between can be fully described. However, making approximation to the Hamiltonian often helps to understand/identify better

the dominant processes (e.g., see Sec. 3.1.3). Following the principle of *minimal coupling* [21, 22], the interaction between light and matter is captured by replacing the canonical momentum $\hat{\mathbf{p}}$ by the kinetic momentum $\hat{\mathbf{v}}(t) := \hat{\mathbf{p}} - \alpha\, q_e\, \mathbf{A}(\mathbf{r}, t)$ and adding a scalar potential $q_e\, \phi(\mathbf{r}, t)$ to the Hamiltonian of field-free, non-interaction particles, i.e., $\hat{H} = \sum_n \hat{\mathbf{p}}_n^2/2$. Here, q_e is the charge of the electron and the speed of light in atomic units is given by $c = \alpha^{-1} \approx \frac{1}{137}$, where α is the fine-structure constant.

In the Coulomb gauge, $\hat{\nabla} \cdot \mathbf{A}(\mathbf{r}, t) = 0$, the scalar potential $\phi(\mathbf{r})$ represents the instantaneous Coulomb potential generated by the charged particles, and the vector potential $\mathbf{A}(\mathbf{r}, t)$ represents the propagating light field. The minimal coupling Hamiltonian for the electronic system reads

$$\hat{H}(t) = \sum_n \frac{\left[\hat{\mathbf{p}}_n - \alpha\, q_e\, \mathbf{A}(\hat{\mathbf{r}}_n, t)\right]^2}{2} + \sum_n \frac{Z\, q_e}{\hat{\mathbf{r}}_n} + \sum_{n \neq m} \frac{q_e^2}{|\hat{\mathbf{r}}_n - \hat{\mathbf{r}}_m|}, \tag{3.3}$$

where n runs over all electrons in the system, and Z is the nuclear charge. The Coulomb interaction between the charged particles, which is due to the exchange of virtual photons, is commonly not considered as a part of the light-matter interaction. Here, there term light-matter interaction refers to the interaction with external light fields—specifically the electric field component. Consequently, the terms describing the light-matter interaction are

$$\hat{H}_{\text{int}}(t) = -\alpha\, q_e \sum_n \mathbf{A}(\hat{\mathbf{r}}_n, t) \cdot \hat{\mathbf{p}}_n + \sum_n \frac{\alpha^2\, q_e^2}{2}\, \mathbf{A}^2(\hat{\mathbf{r}}_n, t), \tag{3.4}$$

where we have used the Coulomb gauge to rewrite the first term in Eq. (3.4). Often the space dependence of the light pulse can be dropped. This is known as the dipole approximation, i.e., $\mathbf{A}(\mathbf{r}, t) \to \mathbf{A}(t)$. This approximation is valid as long as the wavelength is large compared to the system size. Typical wavelengths in strong-field and ultrashort pulses lie within tens to thousands of nanometers (UV to IR light) which are large compared to the size of atoms and molecules (sub-Ångström to a few nanometers).

The $\mathbf{A}^2(t)$ term is a global energy shift and is normally dropped, since it has no affect on the electronic dynamics (as long as the dipole approximation is valid). For scattering experiments, where the wavelength is smaller than the object size, the dipole approximation cannot be made. In fact, the non-dipole terms of $\mathbf{A}^2(\mathbf{r}, t)$ are essential for describing (x-ray) scattering [23]. Without them no scattering pattern would occur.

Equivalent Forms of the Light-Matter Interaction

By performing a unitary transformation of the the wavefunction, alternative forms of the Hamiltonian can be obtained, which are all equivalent to each other [24]. The transformed

wavefunction and the transformed Hamiltonian read

$$\Psi(\mathbf{r},t) \to e^{-i\chi(\mathbf{r},\mathbf{p},t)}\,\Psi(\mathbf{r},t), \tag{3.5a}$$

$$\hat{H}(t) \to e^{i\chi(\mathbf{r},\mathbf{p},t)}\hat{H}(t)e^{-i\chi(\mathbf{r},\mathbf{p},t)} - \frac{\partial\,\chi(\mathbf{r},\mathbf{p},t)}{\partial t}, \tag{3.5b}$$

where $\chi(\mathbf{r},\mathbf{p},t)$ can be any real function. Hence, there exist an infinite number of possibilities [24]. These transformations are often called gauge transformations as well [24, 25]. However, we will refer to these different forms as *frames* so that we do not confuse them with the gauge transformations (like the Coulomb gauge) that are based on fundamental invariances of nature[2].

Rather than just dropping the $\mathbf{A}^2(t)$ in Eq. (3.4) it can be also transformed away with $\chi_A(t) = \frac{\alpha^2 q_e^2}{2}\int_{-\infty}^{t} dt'\,\mathbf{A}^2(t')$. There are three popular choices for representing the light-matter interaction. The light-matter interaction in the *velocity* frame with $\chi_V(\mathbf{r},t) = 0$ $[+\chi_A(t)]$ is already shown in Eq. (3.4). The light-matter interaction in the *length* frame [26] and the *Kramers-Henneberger* (or acceleration) frame [27, 28] is given by

$$\hat{H}_{\text{int}}(t) = -q_e\,\mathbf{E}(t)\cdot\sum_n \hat{\mathbf{r}}_n \qquad \text{with} \qquad \chi_L = -\alpha\,q_e\,\mathbf{A}(t)\cdot\sum_n \hat{\mathbf{r}}_n + \chi_A, \tag{3.6a}$$

$$\hat{H}_{\text{int}}(t) = \sum_n \frac{Z\,q_e}{|\hat{\mathbf{r}}_n - \mathbf{a}(t)|} - \frac{Z\,q_e}{|\hat{\mathbf{r}}_n|} \qquad \text{with} \qquad \chi_{\text{KH}} = -\alpha\,q_e\int_{-\infty}^{t} dt'\,\mathbf{A}(t')\cdot\sum_n \hat{\mathbf{p}}_n + \chi_A. \tag{3.6b}$$

The Kramers-Henneberger frame [see Eq. (3.6b)] corresponds to a coordinate transformation into the acceleration frame of the electron, where the electronic position is displaced by $\mathbf{a}(t) = -\alpha\,q_e\int_{-\infty}^{t} dt'\,\mathbf{A}(t')$. The subtraction of the field-free nuclear potential in Eq. (3.6b) means the resulting overall Hamiltonian is identical to the field-free Hamiltonian just with a time-dependent nuclear potential $\sum_i \frac{Z\,q_e}{|\hat{\mathbf{r}}_i - \mathbf{a}(t)|}$. The electron-electron interaction is not affected by this transformation, since the relative distances between electrons is unchanged by this transformation. In the Kramers-Henneberger frame, the coordinates are transformed such that one would stay in the rest frame of the electron if it is freely moving in the field (without any Coulomb potentials). As a result, the nuclei are moving and not the electrons as in the other two frames. Therefore, the Kramers-Henneberger frame is also known as the acceleration frame.

Equation (3.6a) is the most popular choice for the light-matter interaction, where $\mathbf{E}(t) = -\alpha\partial_t\mathbf{A}(t)$ is the electric field. The intuitive picture that comes with treating the light-matter interaction as a local potential, $\mathbf{E}(t)\cdot\hat{\mathbf{r}}$, is one reason for its popularity.

From now on, we explicitly set the electronic charge $q_e = -1$.

[2] Here χ is only a function of time and space and transforms also the vector potential $\mathbf{A} \to \mathbf{A} + \alpha^{-1}\nabla\chi$ and the scalar potential $\phi \to \phi - \partial_t\chi$ such that the minimal coupling Hamiltonian stays invariant [22].

3.1.2 Photoionization

One of the best studied light-matter interaction processes is one-photon ionization or simply photoionization [29, 30]. Photoionization is often discussed in terms of cross sections, which are measures of how likely a photon interacts with the object. The photoionization cross section of an N-electron system in the dipole approximation is given by [23, 31]

$$\sigma(\omega) = \frac{4\pi^2\,\alpha}{\omega} \sum_F \left| \sum_{n=1}^{N} \langle \Psi_F | \, \boldsymbol{\epsilon} \cdot \hat{\mathbf{p}}_n \, | \Psi_I \rangle \right|^2 \delta(E_F - E_I - \omega), \tag{3.7}$$

where ω is the photon energy, E_I is the energy of the initial state Ψ_I, and E_F is the energy of the final state Ψ_F. The delta distribution enforces the condition $E_F - E_I = \omega$, which ensures energy conservation. The polarization direction of the absorbed photon is given by $\boldsymbol{\epsilon}$. The continuum states Ψ_F are energy normalized, i.e., $\langle \Psi_F | \, \Psi_G \rangle = \delta(E_F - E_G)$. Equation (3.7) characterizes the absorption of one photon and can be derived from 1$^{\text{st}}$-order perturbation theory.

The photoionization cross section in Eq. (3.7) is given in terms of the momentum operator, $\hat{\mathbf{p}}_n$. Alternative and equally exact expressions for the electronic dipole transitions can be found. In order to do so, the following commutator relations involving the exact Hamiltonian are used:

$$\hat{\mathbf{p}}_n = -i[\hat{\mathbf{r}}_n, \hat{H}], \tag{3.8a}$$

$$[\hat{\mathbf{p}}_n, \hat{H}] = -i(\hat{\nabla}_n \hat{V}) = -i\,Z\,\frac{\hat{\mathbf{r}}_n}{|\hat{r}_n|^3}, \tag{3.8b}$$

with $\hat{V} = -\sum_n Z/|\hat{\mathbf{r}}_n| + \sum_{n\neq m} 1/|\hat{\mathbf{r}}_n - \hat{\mathbf{r}}_m|$ being the exact electronic potential consisting of the nuclear-electron and electron-electron Coulomb interactions. If the initial and the final states are energy eigenstates, the commutators in Eqs. (3.8) can be easily evaluated. The relationship between the corresponding matrix elements are

$$(E_F - E_I) \, \langle \Psi_F | \sum_n \hat{\mathbf{p}}_n \, | \Psi_I \rangle = i \, \langle \Psi_F | \, Z \sum_n \frac{\hat{\mathbf{r}}_n}{|\hat{r}_n|^3} \, | \Psi_I \rangle \,, \tag{3.9a}$$

$$\langle \Psi_F | \sum_n \hat{\mathbf{p}}_n \, | \Psi_I \rangle = i(E_F - E_I) \, \langle \Psi_F | \sum_n \hat{\mathbf{r}}_n \, | \Psi_I \rangle \,. \tag{3.9b}$$

The expressions involving the matrix elements of $\hat{\mathbf{r}}_n$, $\hat{\mathbf{p}}_n$, and $Z\,\hat{\mathbf{r}}_n/r_n^3$ are known as *length*, *velocity*, and *acceleration* forms of the electric dipole matrix [30, 31]. The equality of the different expressions for the electronic dipole matrix has been first discussed by Chandrasekhar [32]. For approximations to the exact eigenstates of the system, these forms start to differ and tend to emphasize different spatial parts of the wavefunction. The length form stresses the large distances, the velocity form stresses the intermediate ones, and the acceleration form stresses the short distances (for more details see Refs. [33, 34]).

Independent Particle Picture

It is not possible to determine the exact states Ψ_I and Ψ_F for many-electron systems due to the Coulomb interaction between the electrons [35]. Even the exact ground state of Helium, a two-electron atom, has not yet been found [36]. My studies focus on noble gas atoms, which have a closed-shell electronic structure. The big advantage of closed-shell atoms is that their electronic ground state Ψ_0 can be well approximated by the Hartree-Fock (HF) ground state Φ_0,

$$|\Psi_0\rangle \approx |\Phi_0\rangle = \prod_{n=1}^{N} \hat{c}_i^\dagger \,|\text{vacuum}\rangle\,, \tag{3.10}$$

where the operator $\hat{c}_i^\dagger$ creates an electron in orbital φ_i and $\hat{c}_i$ destroys it [37]. A very nice side effect of HF, the $(N-1)$-electron states, $|\Phi_i\rangle = \hat{c}_i\,|\Phi_0\rangle$, with a missing electron in orbital φ_i correspond quite well to the eigenstates of the ionic system. Hence, the ionization potential of an electron in orbital φ_i is given by $-\varepsilon_i$, where ε_i is the corresponding HF orbital energy. This statement is known as Koopmans' theorem [35].

Assuming the absorbed photon affects only one electron (active electron) and all the other electrons are spectators (passive electrons), the final N-body state can be simplified to $|\Psi_F\rangle \approx |\Phi_i^a\rangle = \hat{c}_a^\dagger \hat{c}_i\,|\Phi_0\rangle$, where the index i refers to occupied orbitals and a refers to unoccupied orbitals in the HF ground state. This assumption holds when the relaxation process of the remaining electrons is slow compared to the ionization dynamics. Hence, the electronic transition elements in Eq. (3.7) reduce to one-body transition elements

$$\sum_{n=1}^{N} \langle\Psi_F|\,\boldsymbol{\epsilon}\cdot\hat{\mathbf{p}}_n\,|\Psi_I\rangle = \langle\varphi_a|\,\boldsymbol{\epsilon}\cdot\hat{\mathbf{p}}\,|\varphi_i\rangle \underbrace{\langle\Phi_i|\,\Phi_i\rangle}_{=1}, \tag{3.11}$$

where the initial state is the Hartree-Fock ground state Φ_0. The photoionization cross section simplifies to [23]

$$\sigma(\omega) = \frac{4\pi^2\,\alpha}{\omega} \sum_a \left|\langle\varphi_a|\,\boldsymbol{\epsilon}\cdot\hat{\mathbf{p}}\,|\varphi_i\rangle\right|^2 \delta(\varepsilon_a - \varepsilon_i - \omega). \tag{3.12}$$

From $\sigma(\omega)$ the ionization rate Γ of an atom can be easily calculated by $\Gamma = J_{\text{EM}}\,\sigma(\omega)$, where J_{EM} is the photon flux of the ionizing pulse hitting the atom. Note that the cross section itself is not field-dependent. The photoionization rate increases linearly with the photon flux (intensity) for a fixed photon energy. For tunnel ionization, the ionization rate does not follow a power law and depends rather exponentially on the intensity (for details see Sec. 3.1.3).

Structural Information in Photoionization Cross Sections

The cross section also contains a wide range of electronic structural information about the system. A typical cross section behavior as a function of photon energy is shown in Fig. 3.2,

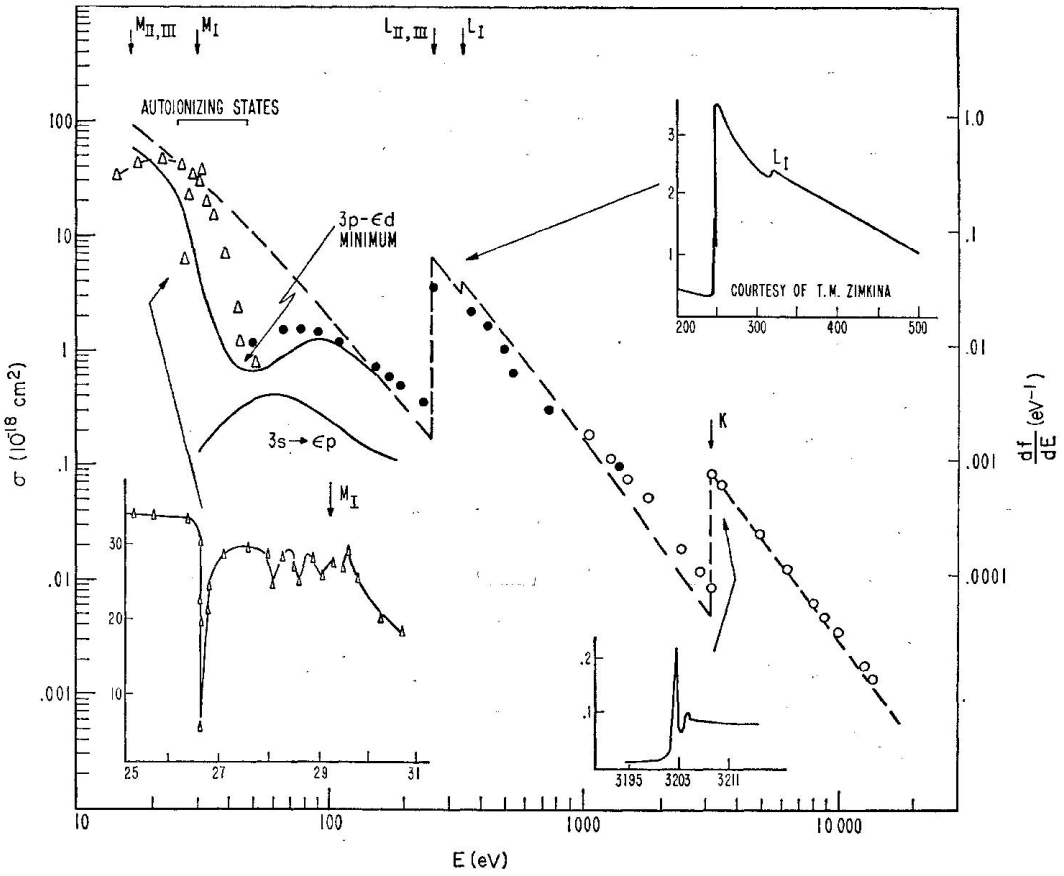

Figure 3.2: The total cross sections $\sigma(\omega)$ for argon: hydrogenic approximation (dashed line), one-electron model (solid line), experimental data (points). Insets show details of $\sigma(\omega)$ around certain energy regions. This figure is taken from Ref. [30]. Copyright © 1968 American Physical Society (APS).

where experimental values (points) as well as theoretical predictions (lines) for argon are shown. Very distinct jumps in $\sigma(\omega)$ occur when new ionization channels open, i.e., when the photon energy is high enough to ionize electrons out of the next energetically deeper lying subshell. In Fig. 3.2 the K ($1s$ shell) and L ($2s, 2p$ shells) edges are clearly visible at 3200 eV and 250 eV, respectively. The L edge consists actually of 3 edges corresponding to the subshells $2p_{1/2}, 2p_{3/2}$ and $2s$. The energy difference between $2p_{1/2}$ (L_{II} edge) and $2p_{3/2}$ (L_{III} edge) is ≈ 2 eV [38] and, therefore, not visible in Fig. 3.2. The $2s$ (L_{I}) edge can be singled out, since it is ≈ 25 eV [38] apart (see upper right inset in Fig. 3.2).

Another interesting feature appears shortly before the ionization edges and is called XANES (x-ray absorption near edges structure) [39]. A typical XANES profile is shown in the lower right inset in Fig. 3.2. The peak structure around the edge corresponds to electron excitations; more specifically, excitations into the Rydberg states of the atom.

With increasing energies the spacing becomes smaller between the Rydberg peaks, which are broadened by the lifetime of the corresponding state. When the spacing is smaller than their line widths, individual peaks are no longer visible and the cross section goes smoothly over into a continuum structure [39].

Above the ionization threshold, the XANES features slowly transform into EXAFS (extended x-ray absorption fine structure) features [40]. EXAFS originates from the interference with the photoelectron that has been backscattered by neighboring atoms [39, 41]. Hence, EXAFS can be used as a probe to study the vicinity of specific atoms, which can be chosen by tuning the photon energy close to an atom-specific absorption edge [23]. In Fig. 3.3 the XANES and EXAFS regions are shown for the K-edge of iron.

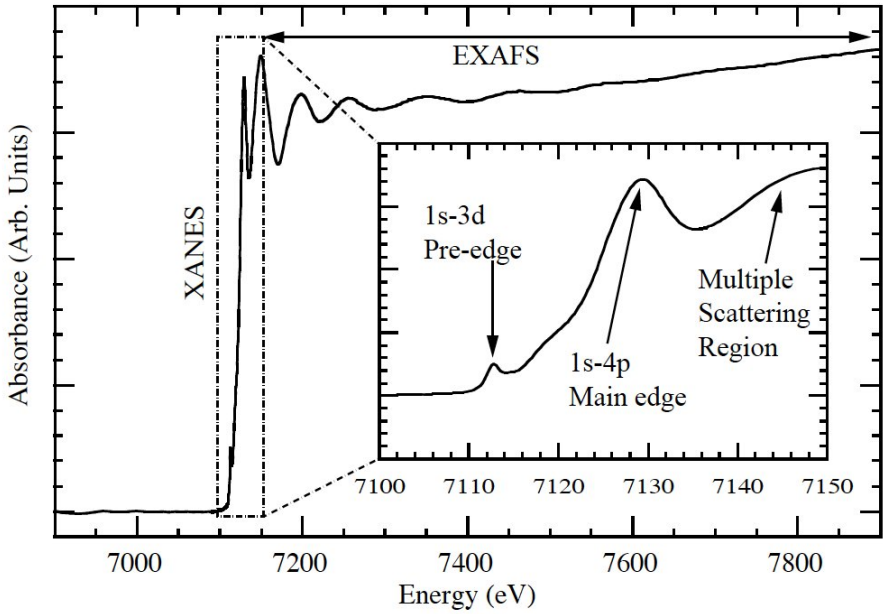

Figure 3.3: The cross section around the K-edge of Fe is shown. The XANES and EXAFS regions are highlighted. This figure is taken from Ref. [42]. © 2010 Matthew H. Carpenter.

Besides the characteristic absorption edges, the cross section contains more information about the electronic structure, particularly about the continuum structure [31]. A famous example is the Cooper minimum [43], which appears at 48 eV in argon [44] (see Fig. 3.2). It is a consequence of a sign change in the transition elements $\langle\varphi_{3p}|\, r\, |\varepsilon d\rangle$ from negative ($\omega < 48$ eV) to positive ($\omega > 48$ eV). The term ε is the energy of the ionized electron. This sign change results in a vanishing contribution from the $3p \to \varepsilon d$ ionization channel. The total cross section is, however, not really zero, since the much weaker $3p \to \varepsilon s$ and $3s \to \varepsilon p$ ionization channels have nonzero contributions [44]. Note that the channel $nl \to \varepsilon(l+1)$ is usually the dominant signal and much larger than $nl \to \varepsilon(l-1)$ [30], where n is the principal quantum number of the orbital. Cooper and Fano [30] have given a rule determining when

a Cooper minimum can occur in the photoionization cross section of a subshell. The rule excludes a Cooper minimum in the noodless subshells $1s, 2p, 3d$, and $4f$ as well as in the transitions $nl \to \varepsilon(l-1)$.

The occurrence of a Cooper minimum can be well-explained with a one-particle picture. However, the details like the exact position and the form of the minimum does depend on many-body physics [45]. For the Cooper minimum in Ar, doubly excited configuration corrections to the ground state, as included in the random phase approximation (RPA), are needed to predict the correct position [45].

In Fig. 3.4, the total photoionization cross sections of Ar and Xe are shown for the Hartree-Fock-Slater (HS) model [46, 47], an intrachannel CIS model, and an interchannel CIS model (explained below). CIS stands for the configuration-interaction singles method described in Sec. 3.2.2. All CIS results presented in this section are calculated with the XCID package I have developed (see Sec. 3.3). The basic differences between the models lie in the approximations made to the Hamiltonian and to the wavefunction. In HS, a single Slater determinant is used for the wavefunction as in HF whereas the CIS wavefunction is a sum of Slater determinants containing the HF ground state and all singly-excited (one-particle-one-hole) configurations Φ_i^a.

For HS, a spherical model potential is used, where the exchange potential between electrons is approximated by a free electron gas model [47] and the long range $1/r$ potential is enforced via the Latter-type correction [48]. The adjectives *interchannel* and *intrachannel* in the CIS model refer to the allowed electron-electron interaction. Intrachannel coupling considers only electron-electron interactions where the ionic state does not change. In this

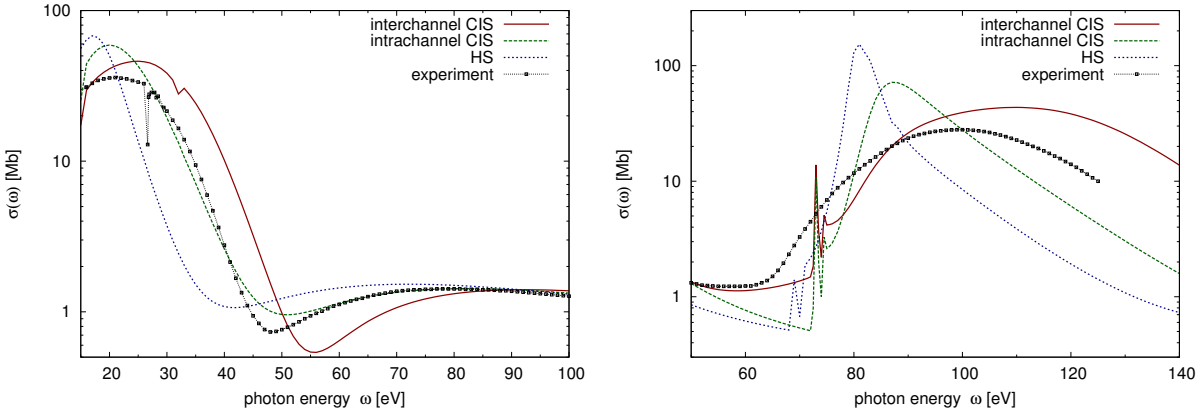

(a) Argon (b) Xenon

Figure 3.4: The absorption cross sections of Ar (a) and Xe (b) are shown for the Hartree-Fock-Slater (blue), the interchannel CIS (red), and the intrachannel CIS (green) models. Note that the interchannel CIS model also includes intrachannel interactions. The experimental data (line and points) are taken from Ref. [44].

case, the ionization channels are independent of each other. The intrachannel CIS model includes only intrachannel interactions. Interchannel coupling refers to electron-electron interactions where the excited/ionized electron changes the ionic state. The interchannel CIS model includes both intrachannel and interchannel interactions.

In Fig. 3.4, the total cross sections of argon (a) and xenon (b) are shown for different theoretical models. The Cooper minimum in Ar and the giant dipole resonance in Xe do exist in $\sigma(\omega)$ for all three models. It shows that the Cooper minimum as well as the giant dipole resonance are not results of many-body effects. They can be solely explained by one-particle physics. The position as well as the form of these features do, however, strongly differ between the different models.

In the HS model, these features occur at too low photon energies and are too narrow and too high in their shape. The potential resulting from intrachannel and interchannel interactions, which are large and repulsive, corrects the HS model too much and shifts the features to too high energies. Nevertheless, models including interchannel and intrachannel interactions generally yield results that are closer to the experimental values. Particularly in xenon, the shape and the position of the giant dipole resonance changes significantly when intrachannel and interchannel interactions are included (see Fig. 3.4b).

Interchannel coupling is particularly important for partial cross sections of deeper lying subshells. In Fig. 3.5, the photoionization cross sections of the $3s$ and $5s$ subshells of Ar and Xe, respectively, are shown. For argon, the Cooper minimum of the $3p \rightarrow \varepsilon d$ ionization channel affects the $3s$ cross section. Without interchannel interactions the effect is gone. Similarly for Xe, the giant dipole resonance in the $4d$ cross section at 100 eV also affects the cross section of the $5s$ (shown) and $5p$ (not shown) subshells. Switching off interchannel interactions leads to a dramatic change in the $5s$ cross section shown in Fig. 3.5b. Intrachannel interactions alone only slightly affect the cross sections.

Angular Distribution

The electronic structure features are also imprinted in the angular distribution of the differential cross section, $\frac{d\sigma}{d\Omega}$ [49, 50]. Studying the angular distribution of the photoionized electron is known as angle-resolved photoemission spectroscopy (ARPES) [51]. Changes in the angular distribution contain a wide range of information about the interaction between the electron and the ion, and about the orbital structure from which the electron came [50, 52]. This is particularly interesting in molecules [53–55] and solids [56, 57]. In atomic systems, the differential photoionization cross section averaged over all initial magnetic quantum numbers m_i reduces to [58]

$$\frac{d\sigma_i(\omega)}{d\Omega} = \frac{\sigma_i(\omega)}{4\pi}\left[1 + \beta(\omega)\, P_2(\cos\vartheta)\right], \tag{3.13}$$

where $P_2(x) = \frac{3}{2}x^2 - \frac{1}{2}$ is the 2^{nd}-Legendre polynomial, and ϑ is the angle between the photoelectron and the polarization direction of the light. The term $\sigma_i(\omega)$ is the partial

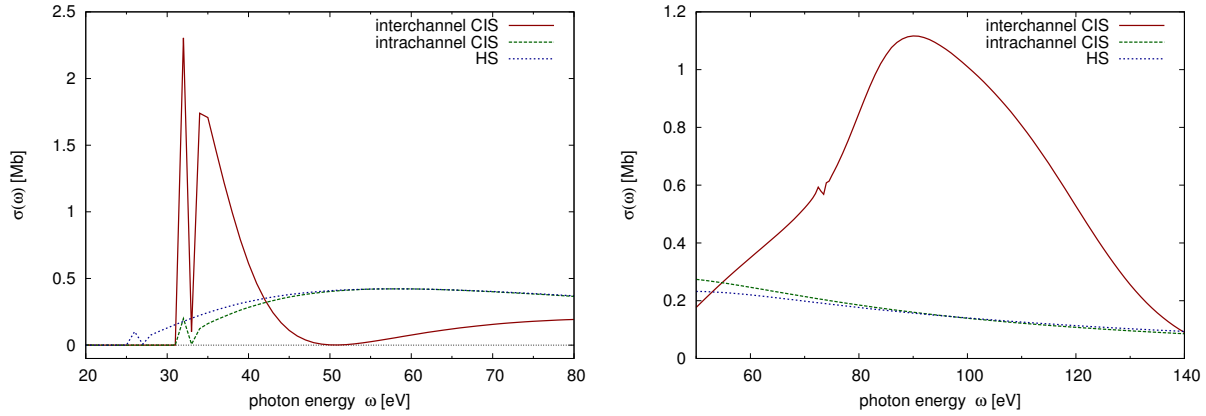

(a) Argon (b) Xenon

Figure 3.5: The absorption cross sections of Ar (a) and Xe (b) of the subshells $3s$ and $5s$, respectively, are shown for the Hartree-Fock-Slater (blue), the interchannel CIS (red), and the intrachannel CIS (green) models. Note that the interchannel CIS model also includes intrachannel interactions.

photoionization cross section of the subshell $n_i l_i$, where n_i is the principal quantum number and l_i is the angular momentum quantum number.

The angular distribution of $\frac{d\sigma_i}{d\Omega}$ is characterized by a single quantity: the β parameter [58]. Since $\frac{d\sigma_i}{d\Omega}$ must be positive, the range of β is restricted to $-1 \leq \beta \leq 2$. In Fig. 3.6, the beta parameter is shown for the $5s$ (Fig. 3.6a) and the $5p$ (Fig. 3.6b) subshells of Xe with and without various interchannel interactions to neighboring orbitals. In both cases, the behavior of β is significantly altered when interactions with other subshells are ignored. Hence, β is an ideal quantity for studying these interchannel effects [59].

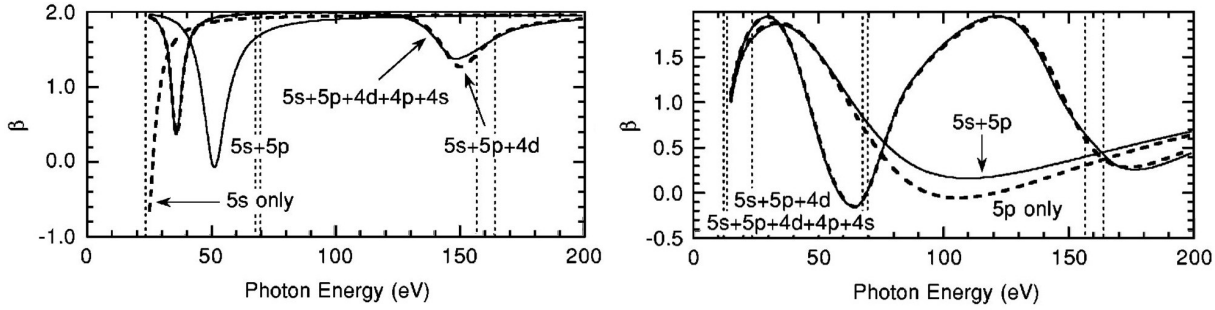

(a) Xenon $5s$ (b) Xenon $5p$

Figure 3.6: The $\beta(\omega)$ parameter is shown for the $5s$ subshell (a) and the $5p$ subshell (b) of Xe including various interactionss with other orbitals (see labels in the figures). The figures are taken from Ref. [60]. Copyright © 2001 American Physical Society (APS).

Perturbative Few-Photon Ionization

The probability of absorbing a second or even a third photon increases with higher intensities. Recent experiments [61] at the LCLS in the x-ray regime have impressively shown that up to eight photons can be easily absorbed by neon producing Ne^{+8}. In the x-ray regime, multiphoton ionization is dominated by *sequential* photoionization meaning one photon is absorbed at a time (i.e., multiple one-photon ionizations). This can be well understood by looking at the Keldysh parameter γ defined in Eq. (3.1). The high photon energy of x-rays leads to very small ponderomotive potentials and, therefore, to very large γ values indicating that x-ray ionization is far in the perturbative regime.

The ionization of an electron by simultaneously absorbing two photons is the simplest "true" multiphoton step. The absorption of several photons at the same time is also called *non-sequential* multiphoton ionization (see Fig. 3.1). It is particularly favored if the photon energy is close to a resonance. Non-sequential two-photon absorption is characterized by the two-photon ionization cross section $\sigma^{(2)}(\omega)$, which reads in the length form in lowest-order perturbation theory [62, 63],

$$\sigma^{(2)}(\omega) = \pi(4\pi\,\alpha\,\omega)^2 \sum_F \left| \sum_{H\neq I} \sum_{n,n'} \frac{\langle\Psi_F|\,\boldsymbol{\epsilon}\cdot\hat{\mathbf{r}}_n\,|\Psi_H\rangle\,\langle\Psi_H|\,\boldsymbol{\epsilon}\cdot\hat{\mathbf{r}}_{n'}\,|\Psi_I\rangle}{E_H - E_I - \omega} \right|^2 \delta(E_F - E_I - 2\omega), \tag{3.14}$$

where E_H is the energy of the intermediate state Ψ_H.

In another experiment [64] also performed on Ne at the LCLS, it has been seen that it was possible to produce Ne^{+9} even though it was energetically not possible to ionize Ne^{+8} further with a single photon. The ratio between the Ne^{+9} and Ne^{+8} productions showed a quadratic behavior in intensity pointing towards a two-photon ionization. Theoretical investigations showed that the production of Ne^{+9} is a combination of sequential and non-sequential two-photon ionization. To fully explain the production of Ne^{+9}, it is necessary to include coherence properties of the x-ray pulse [63].

3.1.3 Tunnel Ionization

For very high field strengths, the perturbative approach for describing multiphoton ionization breaks down. In the UV and x-ray regimes, it is quite difficult to reach the non-perturbative regime ($\gamma \ll 1$) with current light sources due to the high intensity needed. Since the Keldysh parameter goes linearly with ω at a given intensity, it is much easier to reach the non-perturbative regime with optical frequencies. In the non-perturbative multiphoton regime or strong-field regime, it is more favorable to picture the light-matter interaction in terms of a potential that distorts the electronic system (see Fig. 3.1). If the deformation of the Coulomb potential is large enough, the electron can tunnel out of the system into the continuum. This ionization process is, therefore, also known as tunnel

ionization. In the following, two prominent strong-field theories, i.e., the ADK and the SFA models, are discussed.

ADK Model

The pioneering work to describe tunnel ionization rates has been done by Landau and Lifshitz for the ground state of atomic hydrogen exposed to a static electric field [65]. Perelomov, Popov, and Terent'ev [66] extended the theory to any Coulomb wavefunction and to electromagnetic fields of low frequency (quasistatic limit). A generalized version, which can also describe many-electron atoms, is the popular Ammosov-Delone-Krainov (ADK) theory [67]. Recently, the ADK theory has been extended to molecular systems, where additionally the orientation of the molecule influences the ionization rates [68]. The molecular ADK model has become a quite popular tool for understanding strong-field ionization of molecules [69, 70]. The popularity is also supported by the fact that numerically solving the TDSE (even within the single-active-electron approximation) for molecular systems is very challenging.

The basic idea behind the ADK theory is that the solution of a pure Coulomb problem is matched to a semiclassical solution, which describes the electron in the classically forbidden

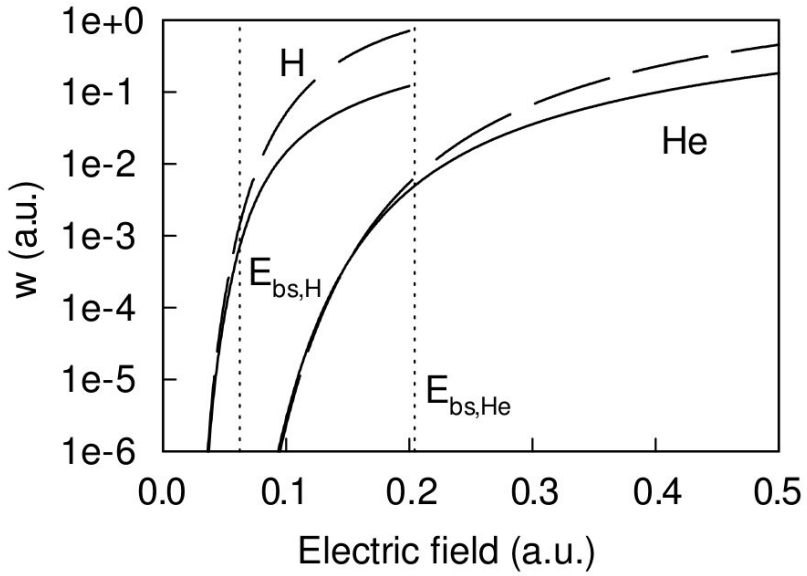

Figure 3.7: The static field ionization rates obtained with the ADK model (dashed) and numerically solving the Schrödinger equation (solid) are compared for H and He. The vertical dotted lines indicate the barrier suppression field strength for H and He beyond which ABI starts to arise. The figure is taken from Ref. [71]. Copyright © 1999 American Physical Society (APS).

region below the barrier and in the classically allowed region outside the barrier (for a review see Ref. [72]). It is assumed that the bound electronic state (near the nucleus) behaves under the barrier like a Coulomb wavefunction for large distances, which reads

$$\psi_c(r,\Omega) = D\, r^{Z/\kappa-1}\, e^{-\kappa r}\, Y_{l,m}(\Omega), \tag{3.15}$$

where r is the radius, $\Omega = (\theta,\phi)$ are the spherical angles, $Y_{l,m}(\Omega)$ are spherical harmonics [73] with the angular momentum l and its projection m, and Z is the nuclear charge. The ionization potential is given by $I_p = \kappa^2/2$. In the classically forbidden region under the barrier, the behavior of ψ_c has to be matched to a semiclassical. Ammosov, Delone, and Krainov [67] derived an analytical expression to match the Coulomb wavefunction to the semiclassical solution.

Note that the angular momentum l is not a conserved quantity anymore when an electric field is applied and the wavefunction does not factorize with respect to the spherical coordinates r,Ω as in the field-free case. The solution of the Hamiltonian including the electric field (within the dipole approximation) factorizes for parabolic coordinates: $\zeta = r+z$, $\eta = r-z$ and ϕ. Hence, the wavefunction reads $\psi = f_1(\zeta)\, f_2(\eta)\, e^{im\phi}/\sqrt{2\pi}$ [72].

For very strong fields, the Coulomb barrier is suppressed below the field-free binding energy. Consequently, the electron can be ionized directly over the barrier (above-barrier-ionization or ABI) without the need for tunneling [74]. In Fig. 3.7 the ADK tunnel ionization rates for H and He are compared to results obtained by numerically solving the Schrödinger equation (see Sec. 3.2.1). Up to the field strength E_{bs}, the ADK rates are identical to the numerical results. Above E_{bs} the ABI starts to kick in and the ADK model overestimates the ionization rate.

SFA Model — Path-Integral Approach

Another approach to describe tunnel ionization is based on path-integral techniques [75, 76] pioneered by Keldysh, Faisal, and Reiss [19, 77, 78] (also called the KFR theory). Since the impact of the atomic potential is neglected and only the influence of the strong laser field is considered, this approach is also referred to as the strong-field approximation (SFA) [6]. The formally exact solution of the TDSE [cf. Eq. (3.2a)] reads

$$|\Psi(t)\rangle = \mathcal{T}\left[\exp\left(-i\int_{t'}^{t} dt''\ \hat{H}(t'')\right)\right]|\Psi(t')\rangle = \hat{U}(t,t')\,|\Psi(t')\rangle\,, \tag{3.16}$$

where $\hat{U}(t,t')$ is the exact time propagator, and $\mathcal{T}$ stands for the time ordering of the operator. The probability of finding an electron with velocity $\mathbf{v}$ at time t is given by $|a_{\mathbf{v}}(t)|^2$ with

$$a_{\mathbf{v}}(t) = -i\int_{t'}^{t} dt''\ \langle \mathbf{v}(\mathbf{t})|\,\hat{U}(t,t'')\ \hat{H}_{\mathrm{int}}(t'')\ \hat{U}_{\mathrm{elec}}(t'',t')\,|\Psi_0\rangle\,. \tag{3.17}$$

$\hat{U}_{\text{elec}}(t'', t')$ is the field-free propagator, and $|\mathbf{v}\rangle$ describes the outgoing electron which turns asymptotically into a plane wave [8]. Physically, Eq. (3.17) means the electron starts in state Ψ_0. At time t'', the electron is promoted into a continuum state where it remains till the time t is reached.

In the SFA, several approximations are made to Eq. (3.17): (1) the final state $|\mathbf{v}\rangle$ is approximated by plane waves or Volkov states [79]; (2) the exact propagator $\hat{U}$ is approximated by $\hat{U}_{\text{SFA}}$, which is the time propagator of the simplified SFA Hamiltonian $\hat{H}_{\text{SFA}}(t) = [\hat{\mathbf{p}} + \alpha\mathbf{A}(t)]^2/2$, where all Coulomb interactions are neglected. The advantage of using Volkov states instead of plane waves is that Volkov states are the eigenstates of $\hat{H}_{\text{SFA}}(t)$. Since $\hat{H}_{\text{SFA}}(t)$ does not depend on the position $\hat{\mathbf{q}}$, the *canonical* momentum $\mathbf{p}$ is a conserved quantity. For any time t' the *kinetic* momentum (velocity) $\mathbf{v}(t') = \mathbf{p} + \alpha\mathbf{A}(t')$ is given by

$$\mathbf{v}(t') = \mathbf{v}(t) - \alpha\mathbf{A}(t) + \alpha\mathbf{A}(t'). \tag{3.18}$$

It is not surprising that the favorite form of the laser-matter interaction in the SFA theory is the velocity form[3].

Both propagators appearing in Eq. (3.17) can be analytically expressed and the resulting phase factor $S(t, t')$ reads [8]

$$S(t, t') = \frac{1}{2}\int_{t'}^{t} \left[v_z(t) - \alpha\, A(t) + \alpha\, A(t'')\right]^2 dt'' - I_p\, t' + \frac{v_\perp^2}{2}(t - t'), \tag{3.19}$$

where the vector potential is linearly polarized in the z direction. The terms v_z and $v_\perp$ are the velocity components along and perpendicular to the vector potential. Note that the initial ground state energy of Ψ_0 is the negative ionization potential $E_0 = -I_p$. It is used to evaluate the propagator $\hat{U}_{\text{elec}}(t'', t')$ in Eq. (3.17).

The main contribution to $a_{\mathbf{v}}(t)$ comes from the time $t' = t_0$, where $\partial_{t'}\, S(t, t')\Big|_{t'=t_0} = 0$. For other times t', the phase of $S(t, t')$ oscillates too rapidly such that these times do not contribute to the overall signal in first order [8]. This approach is known as the saddle point method. The derivative condition leads to an equation for t_0. It reads

$$\sin^2(\omega_L\, t_0) + \gamma^2 = 0, \tag{3.20}$$

where γ is the Keldysh parameter, and the final time has been conveniently set to $t = n\pi$ such that the vector potential vanishes. Any other final time is also possible, since the result should not depend on the final time, which may be defined by the measuring process.

The electric field is taken as a plane wave with frequency ω_L and amplitude E_0. Furthermore, setting $v_\perp = v_z = 0$ means the initial velocity of the electron after tunneling is 0. The time which solves Eq. (3.20) is pure imaginary $t_0 = i\tau$ indicating a classically forbidden

[3] In the length form, a potential energy shift appears whose physical meaning is not clear [80, 81].

region. For $\gamma \ll 1$, the relation $\gamma = \omega_L \tau$ emerges, which connects the Keldysh parameter with the so called tunneling time τ [8]. For $t_0 = i\tau$, the phase is purely imaginary as well and reads $S = -i2/3\, I_p \tau$. Hence, one finds the ionization rate

$$\Gamma \propto \left|e^{-i\,S}\right|^2 = e^{2\,\mathrm{Im}[S]} = e^{-2/3\sqrt{2I_p}^3/E_0} \tag{3.21}$$

decreases exponentially with a higher ionization potential and a weaker electric field. The prefactor of the ionization rate can be approximated by analytical results for a Coulomb barrier [65, 82].

In the perturbative multiphoton regime ($\gamma \gg 1$), Eq. (3.20) interestingly yields $\tau \approx \ln(2\gamma)/\omega_L$. Consequently, the ionization rate becomes proportional to the electric field, i.e.,

$$\Gamma \propto E_0^{2N} = I^N \quad \text{with} \quad N = I_p/\omega_L \tag{3.22}$$

and $I = E_0^2$ the field intensity. The exponent N gives rise to a photon order and is a good estimate how many photons are required to ionize the system.

Despite the success of the SFA, it is known that neglecting the long-range Coulomb potential leads to disagreement with experimental [83, 84] and numerical [85, 86] results in the total ionization rates and especially in the angular photoelectron distribution. Groups have worked on including Coulomb corrections by eikonal-like approximations for the Coulomb-Volkov continuum [87, 88] or by semiclassical perturbation theory [6]. The latter method is commonly called Coulomb-corrected SFA (CCSFA) [6, 89]. In Fig. 3.8, the angular photoelectron distributions are shown for the SFA (green line), the CCSFA (red line), the TDSE

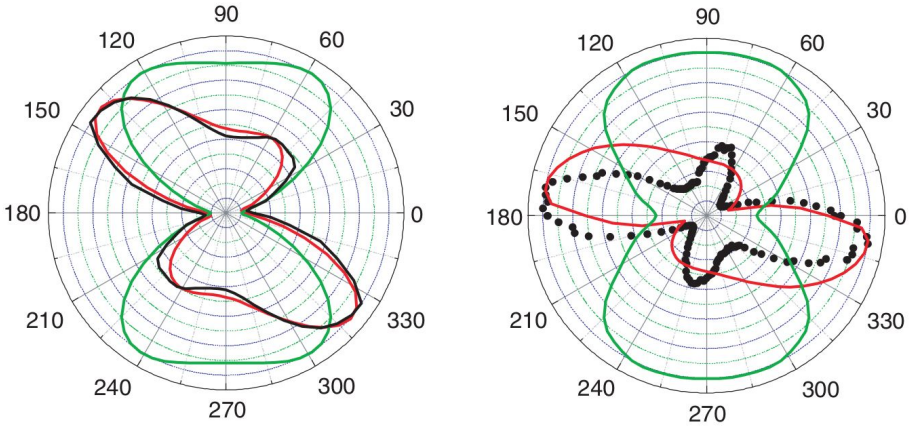

Figure 3.8: The angular momentum distributions of the photoelectron are shown for Ne (left) and Ar (right). The SFA model (green line), the CCSFA (red line), the TDSE results with SAE approximation (black line), and the experimental data (black dots) are compared. The figures are taken from Ref. [6]. Copyright © 2008 Taylor & Francis Group.

results with the single-active-electron (SAE) approximation (black line), and the experimental data (black dots). The SFA does not correctly describes the angular distribution. The CCSFA significantly improves the results towards the SAE and experimental results.

Other widely used techniques to determine the tunnel ionization rates are numerical based Floquet theory [90], complex scaling [91, 92], and explicit time integration methods [93–95] discussed in Sec. 3.2.

3.1.4 High Harmonic Generation

One of the most fundamental processes in attosecond physics is high harmonic generation (HHG) (for a review see Ref. [96]). HHG is used to generate sub-femtosecond pulses with photon energies in the EUV range from NIR femtosecond pulses. HHG was first observed in the late 1980s in rare gas atoms [97, 98]. Rapid developments have now made it possible to generate isolated attosecond pulses shorter than 100 as [99, 100], and with photon energies up to the x-ray regime [3]. These x-ray pulses can in principle be used to generate subattosecond (zeptosecond) pulses [101, 102].

The mechanism behind HHG is well explained by a semiclassical model called the three-step model [103, 104]. It factorizes the HHG mechanism into three separate steps. An illustration of the three-step process is shown in Fig. 3.9a. In the first step the outermost electron gets tunnel-ionized by the NIR field. In step two, the electron moves in the presence of the electric field and due to the short cycle period of the NIR pulse, the electric field drives the electron back towards the ion. In the third step, the electron can recombine with the ion via emitting a high energy photon. The photon energy is determined by the ionization potential I_p plus the amount of energy that the electron gained in the NIR field. The maximum emitted photon energy (commonly referred to as the cut-off energy) is given by [103]

$$E_{\text{cut off}} = I_p + 3.17\, U_p, \tag{3.23}$$

where $U_p = \frac{E^2}{4\omega^2}$ is the ponderomotive potential, i.e., the cycle-averaged quiver energy of a free electron in an electric field with amplitude E and frequency ω. Characteristic for HHG is the plateau region, where the harmonics extend up to the cut-off energy without decreasing in strength (see Fig. 3.9b).

A thorough theoretical discussion of HHG based on the SFA has been given in Ref. [106], which relates the analytically derived dipole moment, $\langle x \rangle (t)$, to the HHG spectrum. Particularly the saddle-point approximations, which are made in the derivation, provide a physical picture of the underlying process. Whereas in Sec. 3.1.3 the saddle-point approximation has been made only with respect to the tunneling time τ [cf. Eq. (3.20)], the saddle-point approximation of the classical action of $\langle x \rangle (t)$ is done in HHG with respect to three variables: (1) canonical momentum $\mathbf{p}$; (2) the tunneling time τ; and (3) the return

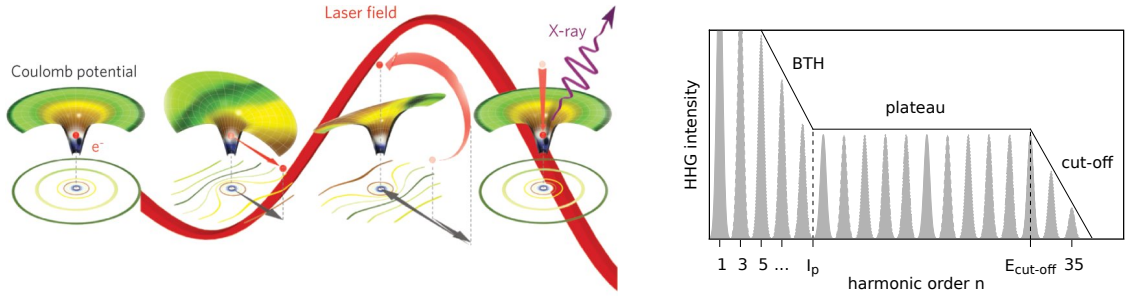

(a) Three-step model (b) HHG spectrum

Figure 3.9: (a) Illustration of the semiclassical three-step model for HHG. The figure is taken from Ref. [105]. Copyright © 2010 Nature Publishing Group (NPG). (b) A sketch of a typical HHG spectrum showing the below-threshold harmonics (BTH), the plateau region, and the cut-off region.

time t. As a result, three saddle-point equations appear: [106]

$$\partial_{\mathbf{p}} S(\mathbf{p}, t, \tau) = \mathbf{x}(t) - \mathbf{x}(\tau) = 0, \tag{3.24a}$$

$$\partial_{\tau} S(\mathbf{p}, t, \tau) = \frac{[\mathbf{p} + \alpha\, \mathbf{A}(t-\tau)]^2}{2} + I_p = 0, \tag{3.24b}$$

$$\partial_{t} S(\mathbf{p}, t, \tau) = \frac{[\mathbf{p} + \alpha\, \mathbf{A}(t)]^2}{2} + \frac{[\mathbf{p} + \alpha\, \mathbf{A}(t-\tau)]^2}{2} = 2N + 1, \tag{3.24c}$$

where S is the classical action, and N is a positive integer number. Each of these equations has a physical implication. Equation (3.24a) states that the returning electron recombines exactly at the same position where the electron has been initially ionized. Equation (3.24b) defines the tunnel time τ [cf. Eq. (3.20)]. Only imaginary τ can fulfill Eq. (3.24b). Equation (3.24c) in combination with Equation (3.24b) relates the photon energy of the emitted photon to the $(2N+1)$-th harmonic of the driving frequency ω.

HHG has also become very popular for molecular systems (for reviews see Refs. [96, 107, 108]). For molecular HHG spectra, the non-spherical Coulomb potential can no longer be ignored. It has been shown that SFA calculations miss several important features in the HHG spectrum [109, 110]. The quantitative rescattering theory (QRT) [111] has become a very prominent way to calculate HHG spectra for molecules. It relates the recombination step to inverse photoionization. Hence, in QRT the recombination cross section gets replaced with the well-studied photoionization cross section obtained from high-level calculations or experiments (see Sec. 3.1.2).

For time-dependent propagation methods as presented in Sec. 3.2, the Larmor formula has to be used to calculate HHG spectra. The Larmor formula connects the acceleration of a charged particle, $\langle \hat{\mathbf{a}}_{\mathbf{c}} \rangle (t)$, to the emitted radiation, $S(\omega)$ [21]. Just as the photoionization cross section can be described with a range of equivalent expressions [see discussion of

Eq. (3.7)], so too are there several equivalent ways to express the HHG spectrum,

$$S(\omega) \propto \left| \int_{-\infty}^{\infty} dt\ e^{-i\omega t} \langle \hat{\mathbf{a}}_c \rangle (t) \right|^2 = \left| \int_{-\infty}^{\infty} dt\ e^{-i\omega t} \left[\partial_t \langle \hat{\mathbf{v}} \rangle (t) \right] \right|^2 = \left| \int_{-\infty}^{\infty} dt\ e^{-i\omega t} \left[\partial_t^2 \langle \hat{\mathbf{r}} \rangle (t) \right] \right|^2 . \tag{3.25}$$

The acceleration $[\langle \hat{\mathbf{a}}_c \rangle (t)]$, the velocity $[\langle \hat{\mathbf{v}} \rangle (t)]$, and the length $[\langle \hat{\mathbf{r}} \rangle (t)]$ forms are shown in Eq. (3.25). As in the case of the photoionization cross section, all three expressions are only equivalent when the exact wavefunction is known. For atomic hydrogen, the equalities of the expressions in Eq. (3.25) have been confirmed numerically [112]. For multi-electron systems, approximations have to be made to the wavefunction and/or the Hamiltonian. Hence, the equalities in Eq. (3.25) do not strictly hold anymore. Results based on the TDCIS method (see Sec. 3.2.2) have shown that for larger atoms the discrepancy in the HHG spectrum increases between the length and the acceleration forms. This indicates that the approximations made in TDCIS (and even more for the SFA and SAE models) become less valid for heavier atoms. For the two lightest noble gas atoms helium and neon, both ways of calculating the HHG yield identical results.

Extending the Cut-Off Energy & Phase Matching

The attribute "high" in HHG is justified, since the harmonic order n can easily be a triple-digit number ($n \geq 100$). In a very recent experiment, harmonic orders of $n > 5000$ have been achieved [3]. Interestingly, Eq. (3.23) states that higher cut-off energies can be achieved with lower driving frequencies (longer wavelengths). The maximum harmonic order achievable goes with ω^{-3}. Long driving wavelengths have been proven to be a successful way to increase the cut-off energy into the water window ($\approx 300 - -500$ eV) [113] and even up into hard x-ray regime above 1 keV [3]. Equation (3.23) shows that increasing the wavelength is not the only way to increase the cut-off energy. Higher electric field strengths (or intensities) als move the cut-off energy into the keV regime [114].

Both approaches for extending the cut-off energy (using longer wavelengths or higher intensities) have drawbacks. High intensities automatically lead to higher ionization probabilities. Highly ionized media, however, are not wanted. They result in strong dispersion effects. As a consequence, the HHG spectrum significantly changes while traveling through the medium. Dispersion effects need to be minimized to ensure the HHG light is always in phase with the driving field such that the maximum gain in the HHG yield can be achieved (see Fig. 3.10). If the HHG light is out of phase with the driving field, the HHG light produced from different atoms no longer adds up constructively [115, 116].

The ionization potential is another knob that can be turned (by targeting the appropriate atom) to increase the cut-off energy. Large ionization potentials are favorable not just because of Eq. (3.23). They reduce the ionization probability and make it, therefore, easier to ensure phase-matching. Hence, the most ideal atoms are noble gas atoms, particularly He [117].

Locking of the phase velocities of the HHG field to that of the driving field is known as phase-matching (for a review see [118]). In Fig. 3.10(a) the idea of phase matching is illustrated. Figure 3.10(b) shows the Guoy phase [119], which changes mostly around the focus point of the laser field and arises due to geometrical reasons [120]. The correct Guoy phase is important for the HHG spectrum. This has been shown for Xe [121] where the overall HHG spectrum changes dramatically depending on the geometrical Guoy phase. The Guoy phase is controlled by the position of the laser focus relative to the gas medium (see Fig. 3.10).

Phase-matching is the main bottleneck for generating broad HHG spectra ranging into the x-ray regime [96, 122], since it is difficult to ensure phase matching over such a large energy range. Long wavelengths avoid high ionization rates but suffer low conversion efficiencies, which scale microscopically with $\lambda^{-6.5}$ [123–126].

Several novel ideas [127–133], which go beyond a single active electron [127] and a single driving frequency [128–133], have been proposed to extend the HHG energy cut-off. Unfortunately, the conversion efficiency is quite reduced compared to conventional HHG. Instead of ionizing just one electron, an idea was put forward [127] to ionize two electrons and let them recombine simultaneously. This leads to a second plateau region in the HHG spectrum. The efficiency is strongly reduced by up to 12 orders of magnitude. Multi-color driving fields [128] have been explored as well as combinations of an intense NIR pulse with an assisting non-resonant [129–131] or resonant [132, 133] UV/x-ray pulse.

Isolated Attosecond Pulses

The discrete harmonic peaks in the HHG spectrum (as in Fig. 3.9) lead to attosecond pulse trains rather than an isolated pulses. To generate isolated attosecond pulses [134], a frequency filter is used (often a thin metal foil) to filter out a continuous energy window of the HHG spectrum in the cut-off region [135]. Phase stability over the entire spectrum

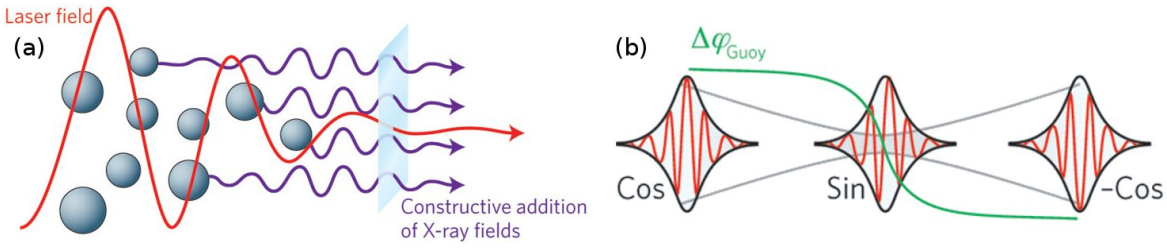

Figure 3.10: (a) The concept of phase matching and the coherent build up of the macroscopic HHG signal are illustrated. (b) The geometrical Guoy phase is shown. It changes particularly around the focal point of the NIR driving field. The Guoy phase has to be considered to ensure phase matching. The figure is taken from Ref. [105]. Copyright © 2010 Nature Publishing Group (NPG).

is important for generating pulses with a finite duration. Having control over the phase of each single frequency allows one to create pulses with arbitrary pulse shapes [136]. For Fourier-limited pulses, the pulse duration is inversely proportional to the bandwidth of the HHG spectrum, i.e., $\tau = 4\ln(2)/(d\omega)$, where τ and $d\omega$ are the FWHM-duration and FWHM-bandwidth, respectively, of the intensity profile. Hence, subfemtosecond pulses require bandwidths of a few eV whereas subattosecond pulses require bandwidths reaching into the keV regime [101].

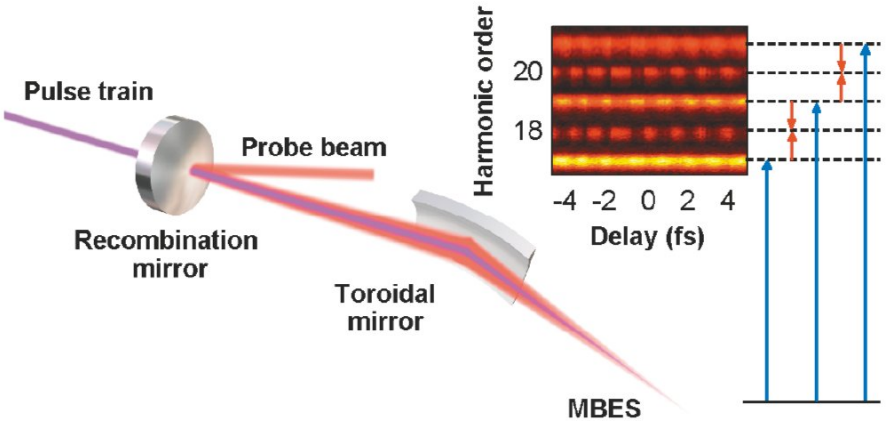

Figure 3.11: Illustration of a RABITT measurement. The overlap of HHG and driving fields leads to two ambiguous ionization pathways (right figure) The resulting interferences in the electron energy as a function of the time delay (upper right figure) contains information about the relative phases between neighboring harmonics in the HHG spectrum. The figure is taken from Ref. [115]. Copyright © 2005 American Physical Society (APS).

To experimentally prove that the generated HHG spectrum really leads to attosecond pulses, it is necessary to measure phase and amplitude of the frequency components of the HHG spectrum. There exist two main techniques to characterize attosecond pulses:

1. Reconstruction of attosecond beating by interference of two-photon transition (RABITT) [115, 137, 138],
2. Frequency-resolved optical gating (FROG) [139–141].

The pulse durations obtained by both methods agree within 10% [142]. RABITT can only be used to determine the pulse duration of attosecond pulses in pulse trains (not isolated attosecond pulses). RABITT (see Fig. 3.11) is based on interferences of two-photon-processes, which lead to photoelectron energies corresponding to even harmonics of the driving frequency ω. This is done by overlapping the attosecond pulse train with the driving NIR field. The interference appears due to two ionization pathways: (1) absorbing an UV photon and an NIR photon $[(2n-1)\omega + \omega]$, and (2) absorbing an UV photon and emission of an NIR photon $[(2n+1)\omega - \omega]$. The relative phase between the harmonics

$2n \pm 1$ can be measured by changing the time delay between the attosecond pulse train and the NIR driving field.

FROG is an auto-correlation technique. It is based on an iterative method to reconstruct the amplitude and the phase of the electric field [139]. FROG has been widely used for optical fields. A modified version of FROG called FROG-CRAB (Frequency-resolved optical gating for complete reconstruction of attosecond bursts) [140, 143] can characterize isolated attosecond pulses, and it is nowadays widely used experimentally [144, 145]. FROG-CRAB measures the FROG trace between a low-frequency field and the isolated attosecond pulse. To do so, the attosecond UV pulse ionizes the system with a one-photon step and the low-frequency field dresses the ionized electron in the continuum (like attosecond streaking discussed in Sec. 3.1.5). The FROG trace is, then, given by the spectrum of the ionized electron $|a(\mathbf{v}, \tau)|^2$, where $a(\mathbf{v}, \tau)$ is the transition amplitude to a final continuum state with velocity $\mathbf{v}$ [cf. Eq. (3.17)]. The term τ is the time delay between the two pulses. The low-frequency, dressing field is used like a temporal phase gate $e^{i\phi(\tau)}$, where $\phi(\tau)$ is the accumulated phase of the ionized electron in the dressing field.

Probing Electronic Structure and Dynamics

Up to now, HHG has been discussed as a tool to generate attosecond UV/x-ray pulses used for studying ultrafast processes. The popularity of HHG, however, does not stop here. HHG has become more and more a scientific tool in itself to study electronic structure and dynamics of atoms and molecules [108]. Particularly popular is tomographic imaging of the outer-most molecular orbitals (HOMOs) [147]. The idea behind this tomographic approach is that the HHG spectrum contains structural information of the orbitals. The HHG spectrum depends on the recombination matrix elements $\langle\varphi_i|\,\hat{\mathbf{r}}\,|\varphi_e\rangle$, where φ_i is the

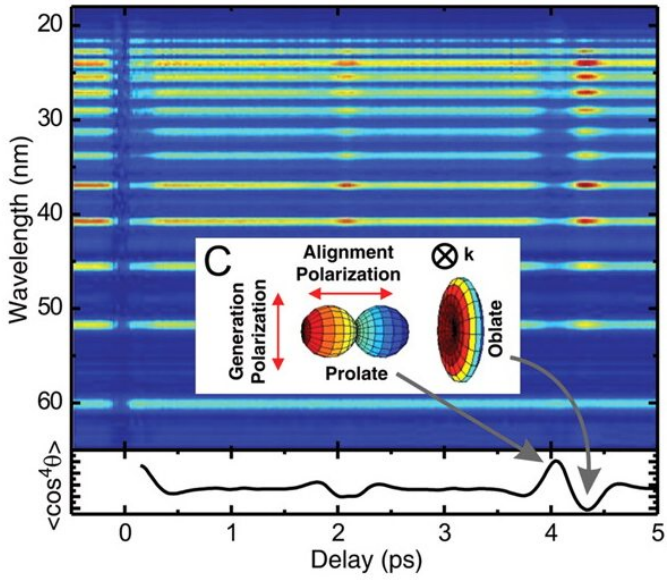

Figure 3.12: HHG spectrum of SO_2 is shown as function of pump-probe delay. With the help of impulsive alignment, HHG spectra from differently aligned molecules can be obtained. Particularly at pump-probe delays where the alignment is non-isotropic, new feature appear in the HHG spectrum. The figure is taken from Ref. [146]. Copyright © 2008 American Association for the Advancement of Science (AAAS).

hole wavefunction, φ_e is the wavefunction of the returning electron. Assuming that the returning electron can be approximated as a plane wave ($\varphi_e(\mathbf{r}) \approx e^{i\mathbf{k}\cdot\mathbf{r}}$) the HHG spectrum contains spatial Fourier components of φ_i, which can be used to reconstruct the hole orbital [147, 148].

It is even possible to apply this technique to HHG spectra with multiple orbital contributions [146]. Here the ability to laser-align molecules (see Chap. 2) is crucial, since tunnel ionization and recombination are highly angle-dependent processes. In Fig. 3.12, the HHG spectrum for laser-aligned SO_2 is shown. At pump-probe delays where the molecular alignment is non-isotropic (alignment or anti-alignment), new features appear in the HHG spectrum. Depending on whether molecules are aligned or anti-aligned, certain harmonics are suppressed or enhanced, indicating multi-orbital contributions.

Normally it is assumed that the HHG electron only comes from the most weakly bound (outer-most) orbital. This is not true anymore when the ionization potentials of neighboring states are quite similar. Consequently, the hole wavefunction of the ion is not stationary anymore, and can be written as a superposition of several ionic states. Correlation effects within the ion can also lead to additional hole motions [149, 150]. In SO_2 up to 3 orbitals (i.e., HOMO, HOMO-1, and HOMO-2) can contribute [151] to the HHG signal depending on the alignment of the molecule with respect to the strong field polarization direction. Ionizing along the molecular axis can lead to a coherent superposition of HOMO and HOMO-2. It has been even demonstrated that it is possible to retrieve the relative phase between the two orbitals at the time of tunnel ionization [151]. However, other experimental [148] and theoretical [107] studies seem to suggest that there is no strong HOMO-2 contribution in the HHG spectrum and that the HOMO orbital is sufficient to explain the HHG spectrum.

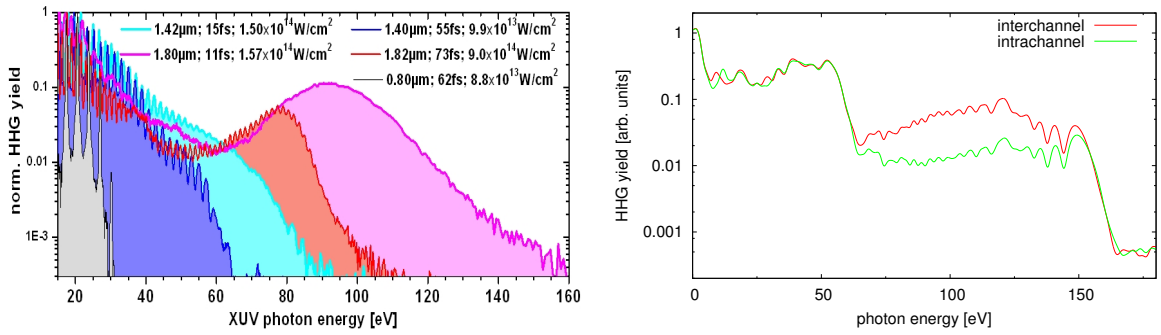

(a) Experimental spectrum (b) Theoretical spectrum

Figure 3.13: (a) The experimentally obtained HHG spectrum of Xe is shown for different driving pulses leading to different energy cut-offs. The figure is taken from Ref. [152]. Copyright © 2012 IOP Publishing. (b) The theoretical spectrum obtained with our TDCIS approach is shown with (red line) and without (green line) interchannel coupling.

Multi-orbital contributions can also play a role in atoms [153–155], but they are less prominent due to higher symmetries and larger energy differences between the orbitals. For larger atoms, multi-electron effects start to emerge. A very prominent example is the giant dipole resonance in Xe as discussed in Sec. 3.1.2 in terms of the photoionization cross section. The giant dipole resonance (originating from the $4d$ subshell) also affects the photoionization cross sections of the $5s$ and $5p$ subshells due to interchannel coupling. As a result, signatures of the giant dipole resonance appear in the recombination step ($\varepsilon l \to 5p$) and, therefore, also in the HHG spectrum, provided the cut-off energy is large enough to reveal this feature ($E_{\mathrm{cutoff}} > 100$ eV). This has been confirmed experimentally for the first time in Ref. [154]. Figure 3.13a shows the experimental HHG spectrum for different cut-off energies. The giant dipole resonance starts to appear with increasing E_{cutoff}. Results from theoretical *ab initio* calculations based on TDCIS (see Sec. 3.2.2) are shown in Fig. 3.13b. No giant dipole resonance can be seen in the HHG spectrum when interchannel interactions are ignored.

Also the Cooper minimum in Argon, which has been discussed in Sec. 3.1.2 in terms of the photoionization cross section, can be seen in the HHG spectrum [153, 156–158]. In Sec. 3.4.2 the influence of multiple orbitals on the location and shape of the Cooper minimum is discussed. Analogous to atoms, the Cooper minimum does also exist in molecules [159], and, therefore, also in the HHG spectrum of molecules. This has been recently experimentally demonstrated on N_2[160] and CS_2 [161].

3.1.5 Attosecond Streaking

After the discussion of photoionization and tunnel ionization—the two most important processes in attosecond physics—and how they are involved in generating attosecond pulses, the focus now shifts to applications and prominent attosecond techniques involving both types of ionization processes. Pump-probe experiments are an ideal tool to study fundamental physical mechanisms in a time-resolved fashion [1]. One popular pump-probe experiment is streaking [162] and has been used for atomic [163], molecular [164], and solid state [165] systems. As discussed in Sec. 3.1.3, the exact eigenstates of a free electron in the presence of an electric field are the Volkov states [79]. The instantaneous velocity $\mathbf{v}(t)$ at time t can be directly connected to the instantaneous velocity $\mathbf{v}(t')$ at any other time t' [see Eq. (3.18)]. Due to the importance of Eq. (3.18) for streaking, it is stated again: $\mathbf{v}(t) = \mathbf{v}(t') + \alpha\,\mathbf{A}(t') - \alpha\,\mathbf{A}(t)$.

When the electron hits the detector and its energy gets measured, no electric field is present such that $\mathbf{A}(t') = 0$. Additionally, when the initial velocity $\mathbf{v}(t)$ is known, it is possible to extract uniquely the time t from Eq. (3.18) for an appropriate shape of the streaking pulse. "Appropriate" means in this context that the vector potential $\mathbf{A}(t)$ changes over the period of interest such that $\mathbf{A}(t)$ can be mapped one-to-one to the time t. In Fig. 3.14, the principle idea of a streaking experiment is illustrated. Due to the time-dependent vector potential, the temporal structure of the electron wavepacket

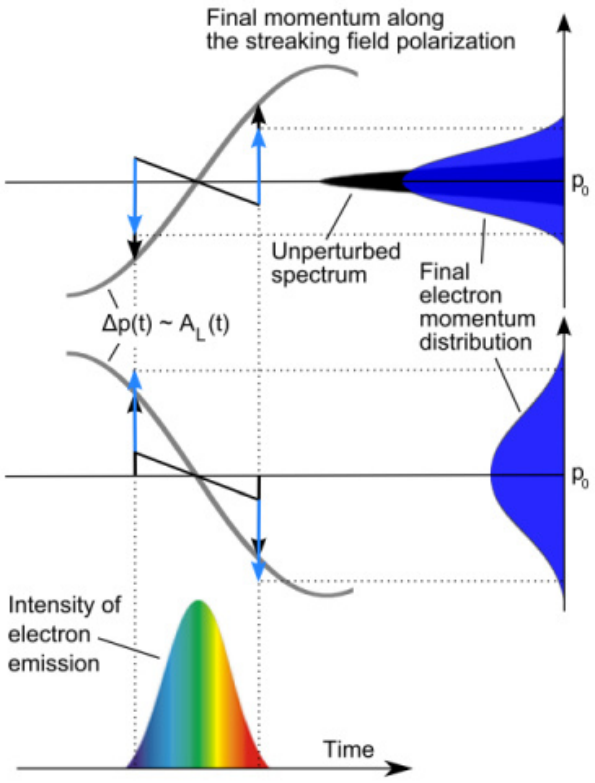

Figure 3.14: Illustration of a streaking measurement with a chirped electron wavepacket. Depending on the vector potential, the final electron momentum distribution is broadened or narrowed. The figure is taken from Ref. [169]. Copyright © 2011 Optical Society of America.

can be uniquely mapped onto the kinetic energy of the electron, which can be measured quite precisely. This makes it possible to measure the chirp of an electronic wavepacket as illustrated in Fig. 3.14. Depending on the energy resolution of the detector and the gradient of the vector potential $\partial_t \mathbf{A}(t)$, a time resolution on the attosecond scale can be easily achieved [166–168] and even zeptosecond resolution is feasible [15].

Streaking can be also used to determine the shape of the streaking pulse itself [170] or the shape of the photoionizing pulse [162, 169] (for a review see Ref. [171]). When the streaking pulse is well-known, photoionization directly connects the substructure of the electron momentum distribution to information about the chirp and pulse duration of the ionizing pulse. The shift of the center of the electron momentum distribution (p_0 in Fig. 3.14) is a direct measure of the vector potential. The entire vector potential $\mathbf{A}(t)$ can be measured by varying the pump-probe delay. The streaking pulse can vary from terahetz (THz) [167] to IR frequencies [170]. It is important that the jitter (i.e, fluctuation in the pump-probe delay) is small compared to the wavelength of the streaking field.

Studying Ultrafast Electron Motion

One of the first demonstrations of streaking has been done on atomic krypton [163]. After photoionizing the inner-shell $3d$ electron, the $3d^{-1}$ krypton ion decays further to Kr^{2+}

via the prominent MNN-Auger decay [172, 173]. The time at which each single Auger decay event happened was measured by streaking the Auger electron. From the resulting statistics, which show an exponential decay behavior ($\propto e^{-t/\tau_h}$), the lifetime of the $3d$ hole was found to be $\tau_h = 7.9 \pm 1.0$ fs. The corresponding linewidth of $\Gamma = 84 \pm 10$ meV agrees well with the 88 ± 4 meV energy-domain measurements [173]. The pump pulse, which defines the reference $t = 0$, must be short in comparison to the Auger decay; hence, it needs to be on the subfemtosecond scale.

Streaking measurements make it possible to study very fundamental questions about the dynamics of electrons that could not have been addressed before. For instance, when several subshells of an system (e.g., atom) can be directly ionized: Does the ionization happen in all subshells at the same time? Streaking measurements on neon showed that the $2p$ electron is ionized 21 as later than the more tightly bound $2s$ electron [168]. This finding sparked a wave of theoretical investigations [174–179] not just in neon but also in other noble gas atoms [176]. Time delays between different ionization channels have been measured in other atoms as well [180, 181]. Most theoretical studies [174, 175, 177] predict a time delay of no more than ≈ 10 as—half the experimental value. Some studies point towards an additional measurement-induced time delay originating from the IR streaking pulse [179]. For a review about attosecond delays in photoionization see Ref. [13].

With the high time resolution of streaking experiments it is possible to address whether tunneling takes a finite amount of time (i.e., tunneling time) or happens instantaneously [182, 183]. In the classically forbidden tunneling limit, the tunneling time is purely imaginary indicating that tunneling is an instantaneous process in real time. A recent experiment [184] on helium strengthens this statement by setting the upper limit for the tunneling time at 12 as due to experimental uncertainties. Experimentally it is quite difficult to define an initial time just before the electron tunnels and a final time when the electron appears outside the barrier.

The authors of Ref. [184] were able to do so by using elliptically polarized light. The maximum of the electric field defines the initial time of tunneling. The angular kick the electron experienced due to the elliptically polarized light determines the time the electron appears in the continuum [185]. The difference between these two times yields the tunneling time. In contrast to previous examples, the angular rather than the radial vector potential component is exploited. Another modification to common streaking experiments is that only one pulse has been used, which operates as pump and as probe. A separate pump pulse is not needed due to the highly non-linear tunnel ionization rate, which naturally selects time "zero" to be the time when the electric field reaches its maximum.

3.1.6 Attosecond Transient Absorption Spectroscopy

In the previous section, the strong-field pulse has been used to probe the ionized electron. In the following, another pump–probe setup is explored, where the longer pulse is used as

pump and the shorter (UV attosecond) pulse is used as probe. The longer pulse could be an NIR pulse, which tunnel-ionizes the system. The shorter UV attosecond pulse probes the system via 1-photon absorption. However, instead of probing the outgoing electron, as done in streaking, the attosecond pulse is used to probe the ionized system that is left behind. The discrete electronic excitation structure of an ion makes it possible to use resonances, which do not exist in a continuum-continuum transition. Resonant transitions have the advantage of possessing a strongly enhanced transition probability and being energetically localized. Both aspects make resonant transition features useful markers.

Since the electron is not probed, one does not look at electronic momentum distributions but rather at the transmitted/absorbed probe signal. Therefore, this technique is called (attosecond) transient absorption spectroscopy [186]. Transient absorption spectroscopy was not invented by the attosecond community, it has been already used on the femtosecond scale for probing chemical [187, 188] and solid state systems [189]. However, it has been recently extended into the attosecond regime [136, 186, 190]. The time resolution arises by systematically changing the pump-probe delay τ. The quality of the time resolution is determined on the one hand by the duration of the probe pulse and on the other hand by the jitter in the pump-probe delay.

The rapid progress in attosecond technology [1, 2], particularly, in controlling the phases of single frequency components in ultrashort pulses [136] decreased the jitter uncertainty to a few attoseconds. Beside the high attosecond resolution, there is a nice side effect that comes along with attosecond pulses. Due to their short durations, they provide a broad spectrum. With a broad spectrum, several ionic excitations can be accessed with a single pulse. This has the advantages that phase relations between different states can be probed. At first glance, the high temporal and the high spectral resolutions seem to contradict each other due to Heisenberg's uncertainty principle. This is, however, not the case. The high temporal confinement, due to the pulse duration, results in an excited electronic state which is not well-defined in energy. This has, however, no consequences for the high spectral resolution of the transmitted attosecond pulse at the detector. In a more technical language, the high temporal and the high spectral resolutions are not conjugated variables to each other and, therefore, can be independently measured from each other.

Studying Dynamical Processes in Ionic Systems

The first demonstration of attosecond transient absorption spectroscopy has been done with atomic krypton [186]. The NIR pump pulse tunnel-ionizes the atom by creating a hole in the $4p^{-1}$ manifold. The attosecond pulse probes the ionic states by exciting the ion into states with a hole in the $3d^{-1}$ manifold. In Fig. 3.15 a sketch the pump and probe steps (a) as well as the theoretically predicted (b) and experimentally measured (c) transient absorption spectrum are shown. Due to spin-orbit interaction, there are three transition lines instead of just one visible between the $4p^{-1}$ and $3d^{-1}$ manifolds. The corresponding transitions are $[4p^m_{3/2}]^{-1} \rightarrow [3d^m_{5/2}]^{-1}$,$[4p^m_{1/2}]^{-1} \rightarrow [3d^m_{3/2}]^{-1}$, and $[4p^m_{3/2}]^{-1} \rightarrow [3d^m_{3/2}]^{-1}$. The population

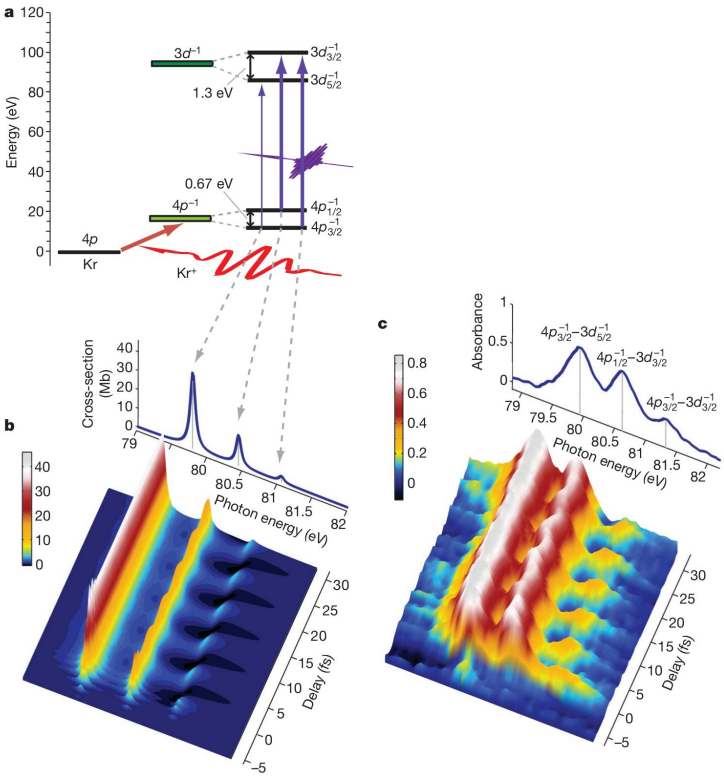

Figure 3.15: (a) Illustration of the attosecond transient absorption experiment with atomic krypton. The NIR pump pulse tunnel ionizes the atom and the EUV attosecond pulse probes the ion by resonantly exciting the ion further. The transition lines of the transient absorption spectrum contains population and coherence informations of ionic states. The theoretically predicted (b) and the experimentally measured (c) spectra are shown. The figure is taken from Ref. [186]. Copyright © 2010 Nature Publishing Group (NPG).

probabilities are directly proportional to the corresponding transition strengths [190]. Even coherence properties can be extracted from the spectrum via the shape of the transition lines. In Fig. 3.16(a), the influence of the line shape on the effective line strength is shown. It reveals the hole dynamics due to the coherence superposition between the ionic states $[4p_{3/2}^{\pm 1/2}]^{-1}$ and $[4p_{1/2}^{\pm 1/2}]^{-1}$. Consequently, the full state of the ionic system, which is given by the ion density matrix (IDM), can be measured.

An analytic expression has been derived in Ref. [190] which treats the probe pulse in 1st-order perturbation theory. By fitting the analytic expression to the experimental data, all entries of the IDM (within the $4p^{-1}$ manifold) can be extracted. After doing this for many pump-probe delays τ, the entire hole dynamics of Kr^+ is reconstructed. The relative phase between the ionic states $[4p_{3/2}^{\pm 1/2}]^{-1}$ and $[4p_{1/2}^{\pm 1/2}]^{-1}$ and the resulting spatial motion of the hole state are shown in Fig. 3.16(b). Furthermore, even traces of doubly ionized krypton states have been seen. This makes it possible to directly test many-body physics of multielectron ionization dynamics with transient absorption spectroscopy [191].

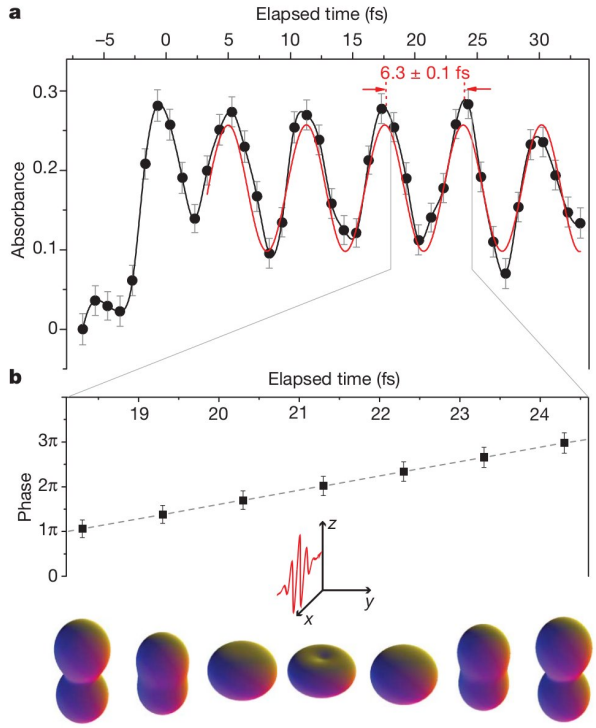

Figure 3.16: (a) The beating of the $[4p^m_{3/2}]^{-1} \rightarrow [3d^m_{3/2}]^{-1}$ transition line is shown. This beating gives a direct measure for the coherence between the $[4p^{\pm 1/2}_{3/2}]^{-1}$ and $[4p^{\pm 1/2}_{1/2}]^{-1}$ ionic states. (b) The reconstructed phase between the two ionic states is shown. After having determined the populations and phase between ionic state, the full hole dynamics, which is shown at the bottom, can be reconstructed. The figure is taken from Ref. [186]. Copyright © 2010 Nature Publishing Group (NPG).

An important assumption in the above discussion is that the ion is an isolated system meaning the ionized electron is far away and cannot influence the ion anymore. When pump and probe pulses do overlap, this assumption does not hold anymore. It is, therefore, not clear to which extent the transient absorption signal can be still related to the instantaneous IDM. However, it turns out that transient absorption spectroscopy can even offer insight into laser-induced electron-ion interactions. This becomes particularly important when sub-cycle ionization dynamics are studied. This aspect is one of the projects I have worked on and is discussed in more detail in Sec. 3.4.3.

Studying Excited Electronic States

Attosecond transient absorption spectroscopy refers only to how the system gets probed. Therefore, there are many ways the system can be prepared (by the pump pulse). Instead of ionizing krypton with an intense NIR pulse, another attosecond pulse can be used to

initially ionize krypton [192]. Helium is another popular system that has been studied by transient absorption spectroscopy [193–197]. The pump step here is an excitation to Rydberg states rather than tunnel or photoionization. Many phenomena can be observed with such pump schemes. If the excited state is a metastable state, the autoionization dynamics can be studied [195, 198]. The Autler-Townes splitting of the excited states can also be probed by applying an additional NIR pulse that induces a coupling to nearby Rydberg states [193, 195–197]. A sub-cycle Stark-shift driven by an NIR pulse has also been observed in an excited helium atom [194].

It is also possible to probe the recombination dynamics of HHG mechanism by transient absorption [199]. Here, an attosecond pulse train rather than an isolated attosecond pulse is used as probe. First, one attosecond pulse excites the electron into a Rydberg state. The NIR pulse drives this electron away and back to the ion (as in HHG). When the electron returns, the subsequent attosecond pulse excites another electron. This leads to inferences in the HHG spectrum, which can be used to study the underlying electronic dynamics.

3.2 Numerical Methods In Strong-Field Physics

There exist two major theoretical approaches for describing the underlying ultrafast processes. One approach is based more on analytical expressions (like the SFA). Many simplifications have to be made in order to arrive at these analytical expressions, limiting applicability. More general approaches are no longer analytically solvable and require computational help. This means numerically solving the time-dependent Schrödinger equation (TDSE) [cf. Eq. (3.2a)]. However, even the TDSE cannot be solved numerically for many-electron systems without making some approximations [200].

For systems that are not highly correlated such as noble gas atoms, it is useful to exploit an independent particle picture, where the N electrons only interact indirectly with each other via a mean-field potential created commonly by all N electrons. The most common mean-field theory is Hartree-Fock (HF) [35, 201], which approximates the full N-electron wavefunction $|\Psi\rangle$ by a single Slater determinant $|\Phi_0\rangle$ as described in Sec. 3.1.2. Most many-body theories [202] (e.g., configuration-interaction or couple-cluster) use the HF state as a reference state to build up a multi-configuration wavefunction consisting of several Slater determinants, which is able to capture correlation effects going beyond the independent particle picture. However, these many-body theories have the disadvantage that they quickly become numerically costly. Hence, they are mainly used for ground state properties of molecular systems.

In strong-field calculations, it is necessary to describe a wide range of continuum states, since an electron can be freed from the system and may even return to it at a later time. The highly delocalized continuum states required in the calculations do not favor an orbital description based on Gaussian-type functions as done in most quantum chemistry

approaches [94]. The non-adiabatic character of the electronic motion makes it quite challenging to exploit many-body theories including a high degree of correlations.

For multi-cycle pulses, it is advantageous to exploit the periodicity of the pulse by using Floquet theory [90, 203]. The time-dependent Hamiltonian is transformed into a time-independent, block-trigonal Hamiltonian, where the diagonal blocks correspond to the number of photons that have been absorbed or emitted.

Many ultrafast processes in closed-shell systems are dominated by a single particle. Adapting the theoretical approach by incorporating a single-active-electron (SAE) picture is quite advantageous. A single-active electron (SAE) picture means only one electron is involved in the process (active electron) whereas all other electrons are just spectators (passive electrons) and are not affected by the dynamics of the active electron or the external field. On the one side, it dramatically reduces the numerical challenges (see Sec. 3.2.1). On the other side, it also favors a more intuitive physical picture.

However, many-body effects going beyond the SAE picture do exist and indeed become even very important for larger atoms and molecular systems as discussed in Sec. 3.1.4. A time-dependent configuration-interaction singles (TDCIS) approach makes use of a single-active electron picture. However, it does not restrict from which orbital the electron gets ionized. It is also possible for the active electron to modify the ionic state after it has been ionized (i.e., interchannel interactions). In Sec. 3.2.2, the basic aspects of TDCIS are discussed. In Sec. 3.4, I discuss ultrafast phenomena that require many-body theories like TDCIS and cannot be explained by a SAE picture. First, however, I discuss briefly the SAE approach with its advantages and disadvantages.

3.2.1 Single-Active-Electron Models

The most common numerical approach to tackle strong-field problems is solving the TDSE [cf. Eq. (3.2a)] with the SAE approximation. The SAE reduces the Hamiltonian to a one-particle Hamiltonian

$$\hat{H} = \frac{\hat{p}^2}{2} + \hat{V}, \tag{3.26}$$

where $\hat{V}$ is a one-particle potential resulting from the interaction with the remaining electrons. In the SAE, $\hat{V}$ is commonly described by a local model potential [157]. For atomic systems, the model potential is also assumed to be spherically symmetric. In the limit of very short and very large distances, the behavior of $\hat{V}$ is known: $\lim_{r\to 0} V(r) = -Z/r$ and $\lim_{r\to\infty} V(r) = -1/r$. Very close to the atomic core, the electronic potential is dominated by the nuclear potential (i.e., $-Z/r$). Far away from the atom, the nuclear potential is screened by the remaining $N-1$ electrons and the ionized electron feels an attractive potential of a singly-charged point-particle (i.e., $-1/r$). Between these two limits, the model potential is constructed such that the ionization potential and excitation energies are well

reproduced [204]. A common example of a model potential looks like [157]

$$V(r) = -\frac{1 + Ae^{-Br} + (Z - 1 - A)e^{-Cr}}{r}, \tag{3.27}$$

where A, B and C are the coefficients adjusting the potential. Despite the simplicity of such model potentials, they can explain and reproduce quite well experimental observations like ATI and HHG spectra [204]. The success of SAE models confirms that a wide range of strong-field and attosecond processes are mainly one-electron processes. This is particularly true for noble gas atoms, specifically the lighter ones. For heavier noble gas atoms [154] or molecules [205] many-electron effects and the interaction of several orbitals start to emerge. In this case, it is not possible to capture the dynamics with the SAE approximation, since SAE assumes that all other electrons are frozen.

The SAE approximation does also imply that the remaining ion can only be in one specific state, normally the ionic ground state. SAE is a single-channel theory, where the term "channel" refers to the state of the $N-1$ electrons. It is necessary to use multi-channel theories when studying ionic excitations and superpositions of several ionic states.

The spherically symmetric character of the ionic potential is strictly speaking not true, since mostly the outer-most p_0 orbital gets ionized by linearly polarized light. Hence, the electron distribution in the ion is not spherical and, therefore, also the resulting potential is not spherical. For atomic systems, that may not be so critical. For molecular systems, however, the potential is obviously non-spherical and also electron-electron interactions become more important.

One way to construct a molecular SAE potential is by following the spirit of density functional theory (DFT) [94, 206]. Here, a one-particle potential is reconstructed from the electron density of the neutral ground state calculated with standard quantum chemistry codes (e.g., DALTON [207]). The overall SAE potential can be written as [94]

$$V(\mathbf{r}) = V_{ee}^{x}(\mathbf{r}) + V_{en}(\mathbf{r}) + V_{ee}^{d}(\mathbf{r}) + G_c(\mathbf{r}), \tag{3.28}$$

where $V_{ee}^{d/x}(\mathbf{r})$ is the direct and exchange contribution of the electron electron interaction, respectively, $V_{en}(\mathbf{r})$ is the attractive electron-nuclei interaction, and $G_c(\mathbf{r})$ is a long-range correction in order to obtain the right $-1/r$ long-range behavior. The exchange term V_{ee}^{x} is generally non-local. The local density approximation (LDA) [208] is, however, a common way to make the potential local by expressing V_{ee}^{x} in terms of the local electron density $\rho(\mathbf{r})$. Other DFT approximations have also been considered to improve the SAE potential for molecules [209]. The quantity that determines the success of these potentials is the angle-dependent ionization rate [94, 210] (see Fig. 3.8 and discussion in Sec. 3.1.3). The correct angle dependence is particularly important for imaging molecular orbitals [210].

3.2.2 Time-dependent Configuration-Interaction Singles (TDCIS)

A common post-Hartree-Fock method is configuration-interaction (CI), which adds systematically higher excitation classes to the wavefunction i.e.,

$$\begin{aligned}|\Psi\rangle &= \alpha_0\ |\Phi_0\rangle + \sum_{n=1}^{N} \sum_{\substack{a_1,\dots,a_n \\ i_1,\dots i_n}} \alpha_{i_1,\dots,i_n}^{a_1,\dots,a_n} \underbrace{\prod_{h=1}^{n} \hat{c}_{a_h}^\dagger \hat{c}_{i_h}\ |\Phi_0\rangle}_{\left|\Phi_{i_1,\dots,i_n}^{a_1,\dots,a_n}\right\rangle} \\ &= \alpha_0\ |\Phi_0\rangle + \sum_{a_1,i_1} \alpha_{i_1}^{a_1}\ \left|\Phi_{i_1}^{a_1}\right\rangle + \sum_{a_1,a_2,i_1,i_2} \alpha_{i_1,i_2}^{a_1,a_2}\ \left|\Phi_{i_1,i_2}^{a_1,a_2}\right\rangle + \dots,\end{aligned} \tag{3.29}$$

where Φ_0 is the HF ground state and $\left|\Phi_{i_1,\dots,i_n}^{a_1,\dots,a_n}\right\rangle$ are n-particle-n-hole (np-nh) configurations with $\hat{c}_a^\dagger, \hat{c}_i$ being creation and annihilation operators of the corresponding orbitals. The HF ground state is used as reference state from which all np-nh configurations are defined. The indicies a and i refer to unoccupied (virtual) and occupied orbitals in Φ_0, respectively. The indicies p, q, r, s are used to refer to all orbitals (occupied + unoccupied). If n goes up to the total number of electrons, one speaks of full CI (FCI). Including only singly excited configurations is called CI-Singles (CIS). Similarly, including only doubly excited configurations is called CI-Doubles (CID), and including singly and doubly excited configurations is called CI-Singles-Doubles (CISD).

The size of the np-nh-configuration space is $(N_a N_i)^n$, where N_a and N_i are the numbers of unoccupied and occupied orbitals, respectively. Since N_a is quite large (in principle infinitely large) it is computationally not feasible to go to very high excitation classes. To calculate exact ground state properties (e.g., response functions), it not necessary to include states that are very delocalized and extend far from the atom/molecule. Hence, N_a is relatively small and higher np-nh-excitations classes and, therefore, higher-order correlations can be included in the calculations. In strong-field physics, where it is important to describe a wide range of the continuum states, N_a can easily be a 5-digit number. Including, therefore, doubly or triply excited configurations quickly becomes infeasible.

Time-dependent configuration-interaction singles (TDCIS), with time-dependent coefficients $\alpha_i^a(t)$, seems to be an ideal extension to the SAE model for investigating strong-field and attosecond phenomena. The TDCIS wavefunction reads

$$|\Psi(t)\rangle = \alpha_0(t)\ |\Phi_0\rangle + \sum_{a,i} \alpha_i^a(t)\ |\Phi_i^a\rangle\,. \tag{3.30}$$

This wavefunction ansatz still makes use of the fact that most strong-field processes in atoms are one-electron processes but it also acknowledges that the active electron may not just come from the least weakly bound (outer-most) occupied orbital. TDCIS also takes into account that the active electron can influence the state of the parent ion.

The TDCIS method I discuss here was first presented by Rohringer *et al.* [211] for atomic systems and has been later extended to include spin-orbit splitting for the occupied

orbitals [212] and the inclusion of the exact residual Coulomb interaction $\hat{H}_1$ [213]. During my studies, I have combined both extensions in order to study electron-ion correlation effects on orbitals that are split due to spin-orbit interaction [214]. The Hamiltonian[4]

$$\hat{H}(t) = \hat{H}_0 + \hat{H}_1 + E(t)\,\hat{z} \tag{3.31}$$

is preferably partitioned into three parts:

- $\hat{H}_0$ is the Fock operator defining the HF ground state Φ_0 and the one-particle orbitals φ_p with their orbital energies ε_p ($\hat{H}_0\,|\varphi_p\rangle = \varepsilon_p\,|\varphi_p\rangle$).
- $\hat{H}_1$ is the residual electron-electron interaction that cannot be captured by the mean-field potential that is included in $\hat{H}_0$.
- The light-matter interaction $E(t)\,\hat{z}$, expressed in the length form after the dipole approximation is made (no space dependence of E).

The residual Coulomb interaction $\hat{H}_1$ is the only two-body operator in Eq. (3.31) and captures all effects beyond an independent particle picture. The detailed expression reads $\hat{H}_1 = \hat{V}_c - \hat{V}_{\mathrm{HF}} - E_{\mathrm{HF}}$, where $\hat{V}_c = \frac{1}{2}\sum_{i\neq j}\frac{1}{|\hat{\mathbf{r}}_i - \hat{\mathbf{r}}_j|}$ is the exact electron-electron interaction, $\hat{V}_{\mathrm{HF}}$ is the HF mean-field potential, and E_{HF} is the HF ground state energy. Subtracting E_{HF} is only been done out of convenience, shifting all energies such that the HF ground state has zero energy. Inserting Eq. (3.30) in Eq. (3.2a), the equations of motion for the CI-coefficients emerge, which read

$$i\alpha_0(t) = E(t)\sum_{a,i}\langle\Phi_0|\,\hat{z}\,|\Phi_i^a\rangle\,\alpha_i^a(t), \tag{3.32a}$$

$$\begin{aligned} i\alpha_i^a(t) = {} & (\varepsilon_a - \varepsilon_i)\,\alpha_i^a(t) + E(t)\left[\langle\Phi_i^a|\,\hat{z}\,|\Phi_0\rangle\;\alpha_0(t) + \sum_{b,j}\langle\Phi_i^a|\,\hat{z}\,\big|\Phi_j^b\big\rangle\;\alpha_j^b(t)\right] \\ & + \sum_{b,j}\langle\Phi_i^a|\,\hat{H}_1\,\big|\Phi_j^b\big\rangle\;\alpha_j^b(t). \end{aligned} \tag{3.32b}$$

The terms $\langle\Phi_0|\,\hat{z}\,|\Phi_i^a\rangle$ and $\langle\Phi_i^a|\,\hat{z}\,|\Phi_0\rangle$ describe the light-matter interaction that couples the neutral ground state to the singly-excited states. Note that $\hat{H}_1$ does not lead to couplings between the ground state and the singly-excited states. Hence, without any external field the atom remains in the ground state.

By setting the matrix elements $\langle\Phi_i^a|\,\hat{H}_1\,\big|\Phi_j^b\big\rangle$ with $i \neq j$ to zero, the interchannel interaction can be switched off in the TDCIS model. When $\hat{H}_1$ is switched off the intrachannel interactions are also ignored. This makes it possible to systematically study dynamical effects that go beyond an independent particle picture. The transition matrix

[4] In Ref. [63, 158, 213–215] the charge of the electron is $q_e = 1$ such that $-E(t)$ rather than $E(t)$ appears.

elements $\langle\Phi_i^a|\,\hat{z}\,|\Phi_j^b\rangle$ separate into two independent single-particle transitions [cf. Eq. (4) in Chap. 5.5], one between occupied orbitals (ionic transition) and one between virtual orbitals (electronic transition).

The calculated photoelectron wavepacket after ultrafast UV photoionization (10 as pulse) is shown for the $5s$ and the $4d_0$ ionization channels in Fig. 3.17. The $l = 1$ and the $l = 3$ characteristics of the electron wavepackets are clearly visible. As noted in Sec. 3.1.2 the photoelectron prefers to increase its angular momentum rather than to decrease it when absorbing the photon. Therefore, the photoelectron of the $4d_0$ channel possesses mainly $l = 3$ character.

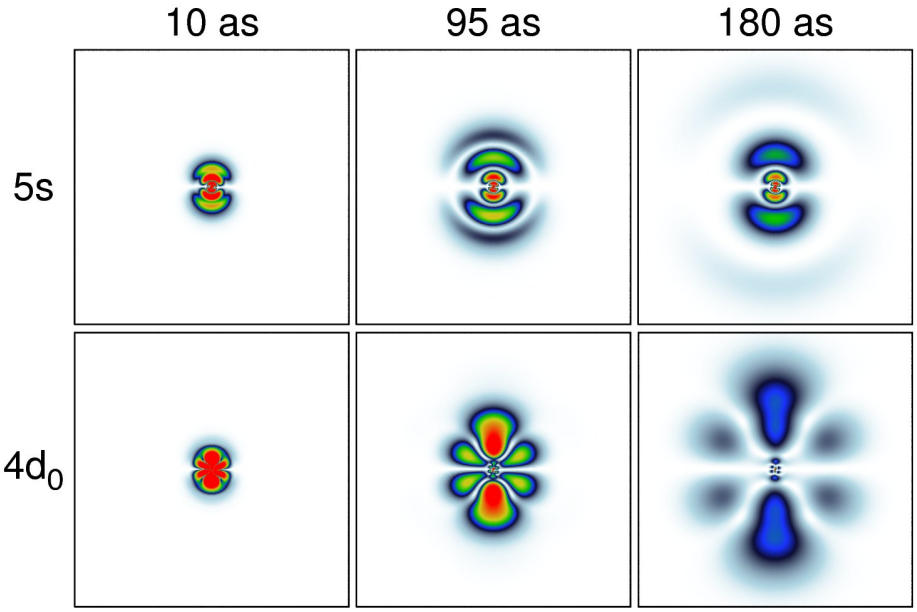

Figure 3.17: Photoelectron wavepackets originating from the $4d_0$ and $5s$ orbitals are shown for several time delays after the ionizing UV attosecond pulse has hit the atom. The mean photon energy is 136 eV and the pulse duration is 10 as.

The residual Coulomb interaction within each channel ($\langle\Phi_i^a|\,\hat{H}_1\,|\Phi_i^b\rangle$) is generally not local and not spherically symmetric—approximations that are normally made in SAE models. Interchannel interactions ($\langle\Phi_i^a|\,\hat{H}_1\,|\Phi_j^b\rangle$ with $i \neq j$) do fulfill this assumption even less. Only asymptotically do they hold. In Sec. 3.4.2, the effect of these approximations are discussed in terms of the HHG spectrum of argon.

Ion Density Matrix

TDCIS describes two subsystems, the active electron and the parent ion. In Chaps. 3.4.1 and 3.4.3, I discuss situations, where the interaction between these two subsystems leads to measurable effects in the ionic state. To extract information about the ionic sub-

system from the full N-body system, the trace of the full N-electron density matrix $\hat{\rho}(t) = |\Psi(t)\rangle\langle\Psi(t)|$ [216] over the other subsystems (i.e., the electron) has to be performed [217, 218]. As a result, one obtains the reduced density matrix of the ionic subsystem

$$\hat{\rho}^{\mathrm{IDM}}(t) = \mathrm{Tr}_a\left[\hat{\rho}(t)\right], \tag{3.33a}$$

$$\rho^{\mathrm{IDM}}_{i,j}(t) = \sum_a \left\langle \Phi^a_i \middle| \Psi(t)\right\rangle \left\langle \Psi(t) \middle| \Phi^a_j\right\rangle. \tag{3.33b}$$

also called ion density matrix (IDM). This IDM uniquely characterizes the state of the ion. Since more than one occupied orbital (channel) can be ionized, it is possible to create a superposition of ionic eigenstates. Figure 3.16 shows the hole motion in singly-ionized krypton. The IDM is also an ideal quantity to study coherences in the ionic subsystem. After the atom has been ionized, the parent ion does not need to be in a coherent state as the discussion of Sec. 3.4.1 shows.

Orbital Representation

For atomic systems, it is convenient to use spherical coordinates, where the field-free one-particle orbitals can be factorized into a radial and an angular part, i.e.,

$$\langle \mathbf{r}|\,\varphi_p\rangle = \varphi_p(\mathbf{r}) = \frac{u_{n_p,l_p}(r)}{r}\, Y_{l_p,m_p}(\Omega), \tag{3.34}$$

where n_p, l_p and m_p are the radial, the angular momentum, and the magnetic quantum numbers of the orbital φ_p, respectively. $Y_{l,m}(\Omega)$ are spherical harmonics [73], where $\Omega = (\vartheta, \varphi)$ stands for the two angular coordinates. The factorization between radial and angular parts has several advantages. First, the 3D-integrals needed for evaluating the matrix elements in Eq. (3.32b) factorize into three 1D-integrals, where the two angular integrals can be solved analytically (in the form of Clebsch-Gordan coefficients). Furthermore, the magnetic quantum number of the full N-electron state, $\Psi(t)$, is conserved ($M = 0$) for linearly polarized light[5] . For TDCIS, this has the consequence that the magnetic quantum number of the active electron cannot be changed ($m_a = m_i$). This restriction in m is quite advantageous for numerical purposes.

The underlying radial grid is chosen to be nonlinear such that more grid points are closer to the origin (i.e., the atomic nucleus). In particular, the Möbius transformation $x \longmapsto r(x) = r_{\max}\zeta/2\,(1+x)(1-x+\zeta)^{-1}$ is exploited [213, 219] with $x \in [-1, 1]$. The nonlinearity of the mapping and the usage of pseudo-spectral techniques [219] significantly reduce the number of grid points needed to a few hundreds for system sizes of around 100 a_0 ($a_0 = 5.29 \cdot 10^{-11}$ m).

[5] Circularly or elliptically polarized light breaks this symmetry.

Complex Absorbing Potential

For ionization scenarios, it is common that the ionized electron separates from the ion with great speed. Before the pulse is over, the electron may have traveled several hundreds or thousands of a_0. Such large grids are computationally not feasible. To avoid artificial reflections from the grid boundary, a complex absorbing potential (CAP) is introduced [91], which absorbs the outgoing electron just before the grid ends. By putting the absorbing potential at the end of the grid, the absorbed electron is far enough away such that it does not influence the ion anymore. Hence, the absorbing potential does not influence the physics near the atom/ion.

Unfortunately, introducing a CAP results in a non-hermitian Hamiltonian ($\hat{H} \to \hat{H} - i\eta\hat{W}$). Hence, the norm of the wavefunction is not conserved anymore. The specific shape of the absorbing potential used in all examples presented in Sec. 3.4 is given by $W(r) = (r - r_c)^2\,\Theta(r - r_c)$ [213], where $\Theta(x)$ is the Heaviside function. Having a non-hermitian $\hat{H}_0$ also means that the orbital energies ε_p become complex.

If the CAP is chosen correctly, the imaginary part of ε_p can be directly related to the lifetime of the orbital [91]. This is particularly interesting for autoionizing states [220]. An alternative method is exterior complex scaling (ECS), where the radius r is replaced by a complex radius $R(r)$ [91]. ECS is formally an exact method, which make an analytical continuation of the Hamiltonian into the complex plane [91]. However, the scaled Hamiltonian can also be separated into an unscaled and a scaled part. The scaled part can then be treated as a CAP, which is now non-local.

Absorbing the electron results in a reduced norm in the ionic subsystem. To restore the norm, at least for the ionic subsystem, which should not be affected by the CAP, a correction term for $\hat{\rho}^{\mathrm{IDM}}$ has been derived. An explicit derivation is given in Sec. II.D of Ref. [213]/Chap. 5.1. The CAP correction can be also used to determine the ionization rate or the ionization cross section [63], since each ionized electron has to hit the CAP eventually. One has to be careful when the electron is only excited and still bound. In this case the CAP correction cannot be used as a measure of ionization.

A more efficient way to determine the photoionization cross section is by using the autocorrelation function $g(t_1 - t_0) = \langle \Psi(t_1) | \Psi(t_0) \rangle$ with the initial state $|\Psi(t_0)\rangle = \hat{p}\,|\Phi_0\rangle$ [30, 221]. Here, one assumes a delta-like kick at time t_0 such that all frequency components are equally included. Consequently, all energy eigenstates are involved in the system response. The photoionization cross section in terms of the correlation function reads

$$\sigma(\omega) = \frac{2\pi\,\alpha}{\omega} \int_{-\infty}^{\infty} dt\; g(t)\, e^{i\omega t} = \frac{4\pi\,\alpha}{\omega}\, \mathrm{Re}\left[\int_{0}^{\infty} dt\; g(t)\, e^{i\omega t} \right], \tag{3.35}$$

where in the second relation the property $g(t) = g^*(-t)$ has been used.

Limitations

TDCIS is a multi-channel theory, where only one electron can be ionized. Hence, multiple ionization processes cannot be described by TDCIS. Due to the residual Coulomb interaction, this outgoing electron can alter the ionic state. The degree of freedom of the ionic state is, however, quite limited. The only allowed ionic states are one-hole configurations $|\Phi_i\rangle = \hat{c}_i |\Phi_0\rangle$, where an electron is removed from the HF ground state. In these configurations, all other electrons are frozen. Hence, the only ionic motion allowed is the hopping of the hole between occupied orbitals. More complicated dynamics require at least one more electron to be non-frozen meaning 2p-2h configurations $\left|\Phi_{i_1,i_2}^{a_1,a_2}\right\rangle$ are needed.

The consequences of the CIS restriction for the ionic states have been discussed in my most recent project (see Chap. 5.5/Ref. [214]) in terms of the polarizability of the ion. The comparison with higher-order approaches like CASSCF[6] has shown that polarizability is underestimated by CIS. Particularly the rearrangement of the remaining electrons is crucial to obtain a more accurate picture of the ionic subsystem.

3.3 My Developments

3.3.1 XCID

In this section, I discuss in more detail XCID, a configuration-interaction dynamics package I have developed. It is based on the TDCIS model described in Sec. 3.2.2 and in more detail in Chap. 5.1/Ref. [213]. The first version was written by Loren Greenman with support from Phay Ho and myself. The current program uses the main logic of the first version. It is, however, a new program written in FORTRAN 95. It is written in a modular structure such that extensions can be easily incorporated. The efficiency has also been greatly improved by disentangling computational tasks, making use of reoccurring objects, and exploiting physical symmetries in the Hamiltonian. The current XCID package separates into four main subprograms:

- Calculating the Hartree-Fock orbitals,
- Generating all matrix elements in the HF-orbital representation,
- Propagating the TDCIS wavefunction in time,
- Post-processing of the data produced during the propagation.

A wikipage provides users with information about the structure and the usage of XCID. All parameters and how they can be specified are explained.

[6] CASSCF - Complete Active Space Self-Consistent Field Theory

Efficiency

An unwanted but unavoidable side effect of a more general (and complex) theoretical model is the increase in computational demand. Therefore, it is important to exploit as many symmetries as possible. Since there are no spin-dependent terms in the Hamiltonian, spin-up and spin-down electrons behave exactly the same and the spin-singlet character ($S = 0$) of the closed-shell HF ground state is preserved. Using only spin-singlet configurations results in a reduction by a factor of 2 of the number of configurations needed. Another not so general symmetry arises with the usage of linearly polarized light. The overall angular momentum L of the ground state of a closed-shell system is $L = 0$ and, therefore also the projection along the polarization direction, i.e., $M = 0$. For 1p-1h configurations, Φ_i^a, it means the magnetic quantum numbers of the active electron and the hole orbital are the same, i.e., $m_a = m_i$. Since the $M = 0$ character cannot be changed by linearly polarized light, there exists a symmetry between the coefficients $\alpha_i^a(t)$ with $m_a = m_i > 0$ and $m_a = m_i < 0$; to be more precise, they are the same. After transforming the configurations into symmetry-adapted configuration classes, one finds that only even parity configurations get populated, reducing the number of needed configurations by another factor of 2 (for details see Eqs. (4)-(5) in Chap. 5.4/Ref. [158]).

When spin-orbit effects are included, the spin $\hat{\mathbf{s}}$ and the orbital angular momentum $\hat{\mathbf{l}}$ are not decoupled. Now, the total angular momentum $\hat{\mathbf{j}} = \hat{\mathbf{l}} + \hat{\mathbf{s}}$ has to be considered. Similarly, the spin and the m symmetry, which have been discussed above, are not independent of each other anymore. The symmetry that remains of spin-orbit interactions is a new m symmetry but with respect to m_j (the projection of the total angular momentum) rather than to m_l (the projection of the orbital angular momentum). Since the spin and m_l symmetries are tied together, only one factor of 2 is saved, making the configuration space twice as large as before. A detailed description of the new m_j symmetry-adapted configuration classes and the resulting new matrix elements are given in Sec. II.B-II.C of Chap. 5.5/Ref. [214].

The terms $v_{pqrs} := \langle \varphi_p, \varphi_q | \, 1/\hat{\mathbf{r}}_{12} \, | \varphi_r, \varphi_s \rangle$ need to be evaluated for specific orbital combinations in order to calculate the residual Coulomb interaction, $\hat{H}_1$. Making use of the decomposition of angular and radial part of the orbitals φ_p, a multipole expansion of $1/\hat{\mathbf{r}}_{12}$ has to performed leading to an infinite sum. The integrals over the angular degrees of freedom can be performed analytically. The ordering of the 2 radial integrals affects the efficiency of the calculations. The radial integral with the smaller number of orbital combinations should always be preformed first. For instance, if the number of combinations for $\varphi_p^*(\mathbf{x}_1)\,\varphi_r(\mathbf{x}_1)$ is smaller than for $\varphi_q^*(\mathbf{x}_2)\,\varphi_s(\mathbf{x}_2)$, the radial integral of the coordinate $\mathbf{x}_1$ should be performed first.

The entire radial grid, which extends to 100 a_0 or more, is not needed to determine the occupied orbitals during the HF routine. Especially, large radii can be ignored for determining the occupied HF orbitals. In contrast, virtual states with large angular momenta experience a large repulsive potential, $l(l+1)/r^2$. Hence, these orbitals are basically zero near the origin. I have found that ignoring small distances for high angular momenta

increases the stability in the diagonalization of the Fock operator, $\hat{H}_0$. This eliminates the highest energy eigenstates; however, they are ignored in the time propagation anyway.

New Features

I have also extended the XCID package and included new features. The spin-orbit splitting in the occupied orbitals is fully implemented for the full TDCIS Hamiltonian including the residual Coulomb interaction $\hat{H}_1$. Several propagation methods are available ranging from the 2$^{\text{nd}}$-order time-differencing method to the forward Euler method and the modified Euler method (or midpoint method), to the Runge-Kutta-4 method [222, 223]. XCID can read the pulse shape from a file. In this way, any kind of pulse shapes can be used (e.g., experimentally measured pulses). The interface which reads the system parameters has been written in a user-friendly way. Parameters can be read in two ways: (1) a formatted input file using the FORTRAN-specific namelist feature or (2) via self-defined flag options ideal for command-line executions (e.g., shell scripts).

3.4 Applications

In this section, I discuss mainly three projects I have completed in the areas of strong-field and attosecond physics. All of them have been performed with the XCID package, which is based on the TDCIS approach described in Sec. 3.2.2 and Chap. 5.1/Ref. [213]. All projects focus on many-body and correlation effects that go beyond an independent particle picture. Already in a fundamental process like photoionization these effects are present. In Sec. 3.4.1, I present my studies on attosecond photoionization. There, a surprising phenomenon has been found in the parent ion resulting from interchannel coupling effects. The single-active-electron model is tested in Sec. 3.4.2, where I investigate the influence of multi-orbitals and multipole effects in terms of the HHG spectrum of argon. The state of the multi-level ion is uniquely defined by the ion density matrix (IDM). The IDM is experimentally accessible with transient absorption spectroscopy as discussed in Sec. 3.1.6. Even field-induced dynamics on a sub-cycle time scale can be studied with overlapping pump and probe pulses. In Sec. 3.4.3, I demonstrate this possibility on atomic krypton exposed to an intense NIR pulse.

3.4.1 Decoherence in Attosecond Photoionization

Correlation effects can appear in the most fundamental processes like photoionization. In my publication [215] "Decoherence in Attosecond Photoionization" (presented in Chap. 5.2) I investigate to which degree a coherent hole wavepacket can be initiated in the ion and how correlations between the photoelectron and the ion may affect the ionic state.

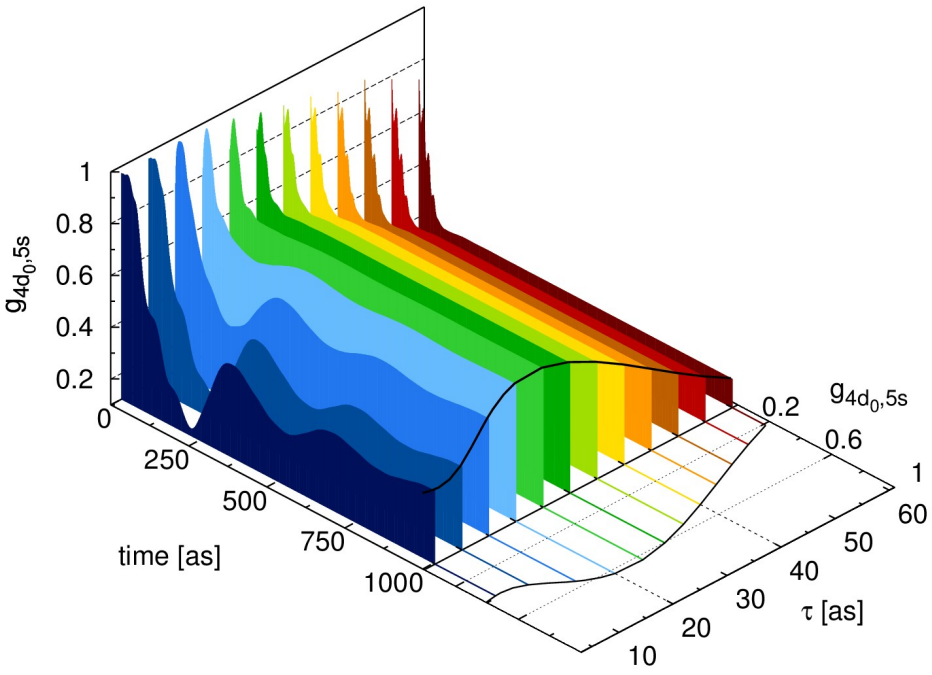

Figure 3.18: The dynamical behavior of the degree of coherence $g_{I,J}(t)$ between the ionic states $I = 4d_0^{-1}$ and $J = 5s^{-1}$ is shown for different pulse durations. The mean photon energy is kept fixed at 136 eV. The final degree of coherence at 1 fs after the pulse is projected onto a 2D graph shown on the right. The figure is taken from Ref. [215]. Copyright © 2011 American Physical Society (APS).

Ionization is not an instantaneous process and the photoelectron needs a finite amount of time to separate from the ion. During this finite time window, the electron is still close to the ion and via electron-electron interactions, the photoelectron can change the ionic state. Such an interaction entangles the electronic wavefunction with the ionic wavefunction. This ionization process can be also viewed in a system+bath picture, where the parent ion is the system and the ionized electron is the bath [218]. Note that the bath is in this case the smaller subsystem (contrary to common system-bath scenarios in chemistry where the bath is the chemical environment). It is well-known from system-bath models that the interaction between the two subsystems influences, or more precisely reduces, the coherent properties within each subsystem. Exactly the same is true for photoionization.

From a theoretical point of view, two common approximations have to be abandoned to be able to describe an entanglement between ion and photoelectron. First, the sudden approximation cannot be made, which assumes that the ionized electron is instantaneously removed from the ion and no interaction between the ionized electron and the ion is possible. Second, the remaining $N-1$ electrons in the ion cannot be assumed to be spectators which are frozen during the ionization process. The ion has to be described as a multi-level system such that the state of the ion is able to change due to the residual Coulomb interaction

with the photoelectron. The TDCIS approach is, here, ideal to describe these correlation dynamics. In photoionization, this change in the ionic state is known as interchannel coupling (see Sec. 3.1.2 for a detailed discussion). If the interaction with the photoelectron does not change the ionic state, the entanglement between the electron and the ion is strongly reduced and the coherence in the ionic subsystem is preserved.

Atomic xenon is chosen to demonstrate the importance of interchannel coupling effects in ultrafast photoionization. Here, the principal idea is to create a dynamical hole wavepacket in singly ionized xenon. The energetically most favorable option (ignoring spin-orbit splitting) for creating a coherent hole state via one-photon ionization with linearly polarized light is through a superposition of the ionic states $4d_0^{-1}$ and $5s^{-1}$, where $4d_0$ and $5s$ refer to the occupied orbitals the ionized electron originates from. The finale state of the photoelectron must be the same to be able to create a coherent hole wavepacket in the ion. This is necessary, since it must be impossible to tell from which orbital the electron came. Since linearly polarized light is used, the angular momentum projections m_l of both occupied orbitals must be the same. The angular momentum l of both orbitals must be the same or differ by 2, since photoionization always changes l of the electron by 1.

The final energy of the photoelectron must also be indistinguishable for the two channels. This is only possible when the spectral bandwidth of the pulse is larger than the energy difference between both ionic states. In xenon, the energy difference between the ionic states $4d_0^{-1}$ and $5s^{-1}$ is ≈ 50 eV. For a Fourier-limited Gaussian pulse that means a full-width-half-maximum (FWHM) duration of ≈ 36 as. To classify the entanglement between the parent ion and the photoelectron, the lack of coherence (i.e., decoherence) in the ionic subsystem is investigated. The degree of coherence $g_{I,J}(t)$ between the two ionic states I and J is given by

$$g_{I,J}(t) = \frac{\left|\rho_{I,J}^{\mathrm{IDM}}(t)\right|}{\sqrt{\rho_{I,I}^{\mathrm{IDM}}(t)\rho_{J,J}^{\mathrm{IDM}}(t)}}, \tag{3.36}$$

where $g_{I,J} = 1$ stands for perfect coherence and $g_{I,J} = 0$ stands for a perfectly incoherent system. In Fig. 3.18, the degree of coherence between the ionic states $4d_0^{-1}$ and $5s^{-1}$ is shown as a function of time for different pulse durations. The mean photon energy is kept constant at 136 eV, well above the ionization potential of the $4d_0$ and $5s$ orbital (75 eV and 25 eV, respectively).

There are several interesting aspects encoded in Fig. 3.18. First, the initial ($t = 0$) and the final ($t = 1\ fs$) degrees of coherence decrease for long pulse durations. This drop is well understood and is directly related to how well the spectral bandwidth of the pulse can cover the energy difference between $4d_0^{-1}$ and $5s^{-1}$. For longer pulses, the spectral bandwidth decreases such that it becomes possible to determine energetically from which orbital the photoelectron came.

Second, the initial degree of coherence at $t = 0$ increases monotonically with shorter pulses. When the spectral bandwidth becomes larger than the energy difference between

the ionic states, $g_{I,J}(0)$ approaches perfect coherence. Third, interchannel coupling destroys this initial coherence by entangling the photoelectron with the ion. When interchannel interactions are switched off, the high initial degree of coherence is preserved for later times (see Fig. 4 in Chap. 5.2/Ref. [215]). For very short pulses in particular, the ionization dynamics of the electron becomes strongly entangled with the ion. Consequently, the ionic coherence starts to drop directly after the pulse. The oscillations in $g_{I,J}(t)$ also indicate that there exists a strong, dynamic interaction between the ion and the photoelectron.

The reason why interchannel coupling increases in importance for ultrashort pulses lies in the nature of the broad spectrum. Even though the mean photon energy is sufficiently large, there exist many energetically lower photons in the broad spectrum, which result in a photoelectron with almost no kinetic energy. Thes low energy part of the photoelectron does strongly interact with the parent ion and leads to an enhanced entanglement. Our studies on the degree of coherence as a function of the mean photon energy with a fixed spectral bandwidth (see Fig. 3 in Chap. 5.2/Ref. [215]) confirm that the enhanced entanglement is due to the low rather than the high energy part of the photoelectron.

The lesson learned from this study is that the required spectral bandwidth needed to create a coherent superposition is not sufficient to ensure that the hole wavepacket in the ion is coherent. Besides the interest in understanding fundamental processes, the question whether or not it is possible to create a coherent hole wavepacket in an ion via photoionization is of wider interest.

In molecular systems, where the valence-shells are highly delocalized, the hole dynamics can be quite complex [224, 225]. Creating a coherent hole wavepacket is important for the subsequent dynamics. Without coherences (between the exact ionic eigenstates) no hole motion can exists. It has been shown that higher order correlation effects within the ion can also be a driver of hole dynamics [226]. Transient absorption spectroscopy is an ideal tool to study these hole motions. In combination with UV and even more so with x-ray light, it is possible to probe local, site-specific consequences of the delocalized electronic motion in molecules [227, 228].

3.4.2 Multiorbital and Multipole Effects in the HHG Spectrum of Argon

Multiorbital effects and particularly interchannel effects are well known in photoionization (cf. Sec. 3.1.2). They lead to strong modification in the partial cross sections of valence and inner-shell orbitals. The coherent properties of the ion are also influenced by interchannel interactions as discussed in Sec. 3.4.1. In the tunnel ionization regime, it has been shown that the electron can come from multiple orbitals [136, 186]. Tunnel ionization and recombination are the first and the last step of HHG, respectively. Therefore, it is quite natural to ask to which extent multiorbital effects have to be considered in HHG, where they are normally neglected (cf. Sec. 3.1.4).

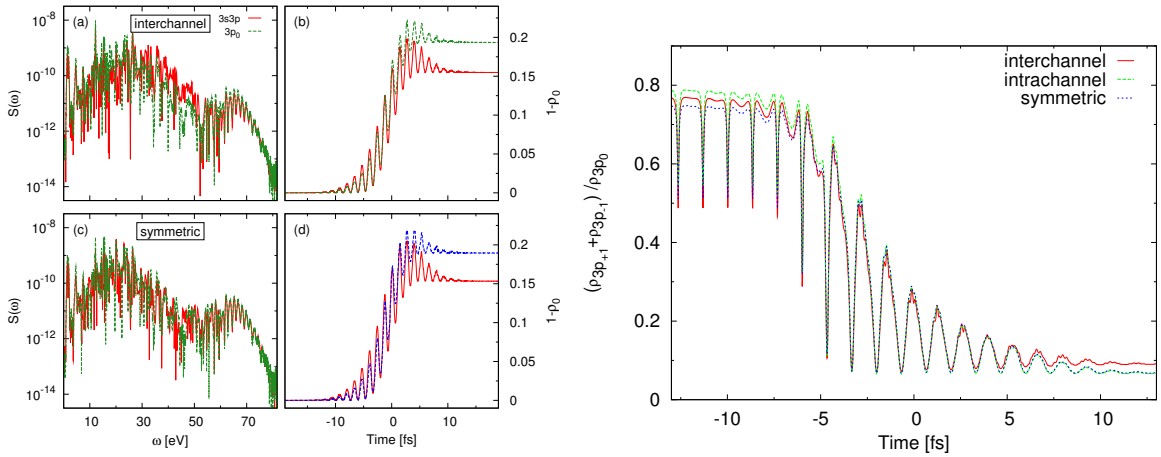

(a) HHG spectrum and depopulation (b) Population ratio

Figure 3.19: (a) The HHG spectrum $S(\omega)$ and the ground state depopulation $1-\rho_0$ of Ar are shown for different combinations of active occupied orbitals and approximations of the residual Coulomb interaction. Different sets of active occupied orbitals are compared for the full and the symmetrized version of $\hat{H}_1$. (b) The ratio of the hole populations $3p_0^{-1}$ and $3p_{-1}^{-1}+3p_1^{-1}$ is shown as a function of time. These figures are taken from Ref. [158]. Copyright © 2012 American Physical Society (APS).

In molecular systems, multi-orbital contributions to the HHG spectrum have been observed as a function of alignment angle [146]. In atomic systems, multiorbital effects are generally less important due to the higher orbital symmetries and the larger energy splittings between them. However, this does not mean they are absolutely absent, and the larger the atom the more prominent are multiorbital effects. For example, the HHG spectrum of xenon can only be understood when interchannel interactions between the $4d$ and $5p$ orbitals are taken into consideration (see Fig. 3.13).

In my publication [158] "Impact of Multichannel and Multipole Effects on the Cooper Minimum in the High-Order-Harmonic Spectrum of Argon" presented in Chap. 5.4, I investigate multiorbital as well as multipole effects in the HHG spectrum of argon. Argon is an ideal atom, since, with 18 electrons, it is not one of the lightest noble gas atoms [7]. Additionally, in the photoionization cross section and also in the HHG spectrum of argon there exists a special feature called the Cooper minimum, which can be used as a marker to help quantify differences between models. Note that the existence of the Cooper minimum is not a result of multiorbital effects but its position and shape are. Multipole effects are normally ignored in atoms, where the effective potential of the active electron is modeled as spherically symmetric [see Eq. (3.27)]. Since the electron gets mainly ionized out of the $m=0$ orbital, the remaining ion is predominantly in the $P_{m=0}$ state. Consequently, the resulting Coulomb potential of the ion has, at short range, a quadrupolar rather than a

[7] The calculations for heavier atoms, like krypton and xenon, are more costly, since for large HHG cut-off energies the $3d$ and $4d$ orbitals have to be considered, respectively.

spherically symmetric character. To simulate a spherically symmetric potential, the residual Coulomb interaction H_1 is averaged over all orbital magnetic quantum numbers (for details see Chap. 5.4/Ref. [158]). The spherical averaging has the additional consequence that interchannel interactions drop out of the spherically symmetrized $\hat{H}_1$. Hence, the symmetrized $\hat{H}_1$ includes only intrachannel interactions.

Both multiorbital and multipole effects are investigated separately. First, multi-orbital effects are studied by allowing ionization out of $3s$ and all $3p$ orbitals, out of all $3p$ only, or out of $3p_0$ only. Second, multipole effects are studied by using interchannel and intrachannel interactions, only intrachannel interactions, and the spherically symmetric intrachannel version of $\hat{H}_1$. In Fig. 3.19a, the HHG spectrum and the ground state depopulation are compared for a single-orbital ($3p_0$) and a multiorbital ($3s$ and all $3p$) model of argon. When the symmetrized residual Coulomb interaction is used, the differences in the HHG are very small indicating that the $3p_0$ orbital is the dominant contributer to the HHG spectrum. When interchannel interactions are included in the calculations, the HHG spectrum becomes sensitive to whether or not the orbitals $3p_{\pm1}$ are considered. The influence of $3s$ is minimal and can be ignored. The direct contributions of $3p_{\pm1}$ are negligible but their indirect influence on $3p_0$ is not. In the energy region of 30-50 eV, the HHG spectrum is enhanced by interchannel interactions by up to one order of magnitude.

In Fig. 3.19b, the population ratio between the orbitals $3p_{\pm1}$ and $3p_0$ is shown as a function of time during NIR driving field, which is centered around $t = 0$ and has a FWHM-width of 10 fs. Interestingly, the ratio decreases monotonically (up to the oscillations synchronized with the electric field). The low final ratio illustrates that mainly $3p_0$ gets ionized. Small final hole populations in $3p_{\pm1}$, which are often used as an argument to ignore these channels, are not as small during the pulse (relative to the $3p_0$ population) as shown in Fig. 3.19b. Taking additionally interchannel coupling effects into account shows that the population-based argumentation of excluding the $np_{\pm1}$ orbitals is not universally valid and has to be used with caution. Also in atomic xenon, it is due to the interchannel effects that the $4d$ orbitals cannot be neglected even though they are deeply bound and the direct contributions of $4d$ are negligible.

3.4.3 Attosecond Transient Absorption Spectroscopy for Overlapping Pump and Probe Pulses

In Sec. 3.1.6, the basic ideas of attosecond transient absorption spectroscopy (ATAS) have been discussed. ATAS is an ideal probe for studying the electronic dynamics in the parent ion. The high time resolution accompanying ATAS makes it possible to study ultrafast electronic motion on a subfemtosecond time scale. Since an optical cycle of 800 nm (NIR) is 2.6 fs long, subcycle ionization dynamics can be studied as demonstrated in Chap. 5.3/Ref. [136] with atomic krypton. The final degree of coherence of $g = 0.85 \pm 0.05$ that has been experimentally achieved agrees with the TDCIS predictions of $g = 0.82$ after

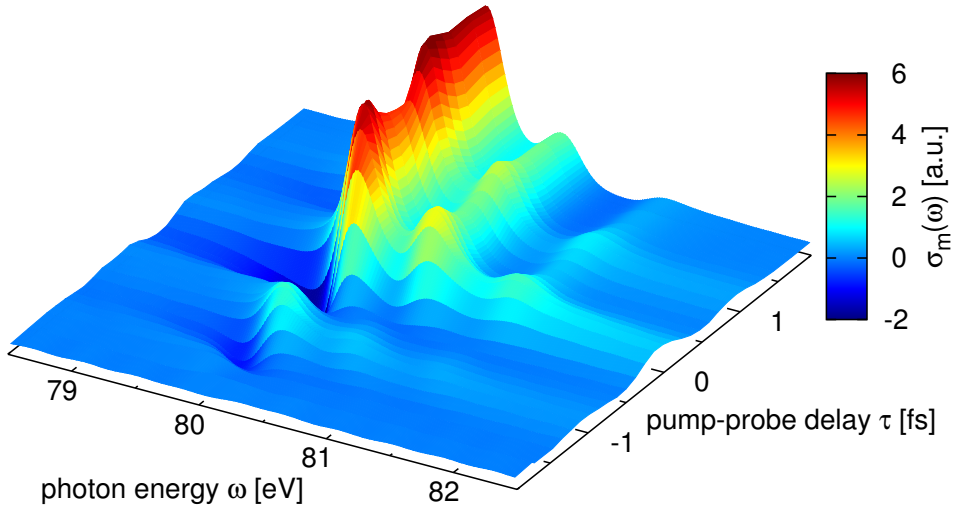

Figure 3.20: Attosecond transient absorption spectrum of krypton during tunnel ionization is shown as a function of photon energy ω and pump-probe delay τ. The figure is taken from Ref. [214]. Copyright © 2012 American Physical Society (APS).

taking into account propagation effects, which increase the degree of coherence measured at the detector by up to 14% ($g = 0.72$ before propagation effects). To study theoretically the coherence between the ionic states $[4p_{1/2}^{\pm 1/2}]^{-1}$ and $[4p_{3/2}^{\pm 1/2}]^{-1}$, the XCID package was extended to include spin-orbit effects in the occupied orbitals[8]. The residual Coulomb interaction, $\hat{H}_1$, has also been included to account for coherence losses due to interchannel effects.

For well separated and non-overlapping pump and probe pulses, the three transient absorption lines in Kr^+ corresponding to the transitions $[4p_{3/2}^m]^{-1} \rightarrow [3d_{5/2}^m]^{-1}$, $[4p_{1/2}^m]^{-1} \rightarrow [3d_{3/2}^m]^{-1}$, and $[4p_{3/2}^m]^{-1} \rightarrow [3d_{3/2}^m]^{-1}$ (see Fig. 3.20) contain all information about the tunnel-ionized Kr^+ ion with a hole in the $4p_j$ orbital manifold. As theoretically [190] and experimentally [186] shown, this information can be used to reconstruct the full ion density matrix (IDM). Establishing a direct mapping between the transient absorption spectrum and the instantaneous IDM requires that the ionized electron does not influence the ion during and after the probe step. This condition does not hold anymore when the pump step (i.e., tunnel ionization) is probed, since the ionized electron as well as the pump field itself influence the ion state. Therefore, it is not clear to which extent the instantaneous IDM can be probed during the ionization process.

Additionally, strong modification of the transient absorption spectrum has been observed during tunnel ionization (see Fig. 3.20) indicating that the krypton ion cannot be

[8] The notation of the ionic states is explained in Sec. 3.1.6.

treated as isolated and field-free. Both aspects arising with probing the tunnel ionization process are addressed in my manuscript [214] "Theory of Attosecond Transient Absorption Spectroscopy of Krypton for Overlapping Pump and Probe Pulses" presented in Chap. 5.5.

The comparison between the hole populations obtained from a calculated transient absorption spectrum and the corresponding instantaneous hole populations revealed that the obtained hole populations match quite well with the instantaneous ones. A delay in the extracted hole motion of up to 200 as was found (see Fig. 5 in Ref. [214]/Chap. 5.5).

Beside the question of population dynamics, a new phenomenon has been identified during the ionization process. The transition lines do not just rise in strength as the hole populations do. They also show strong deformations in their shape as shown in Fig. 3.20. Before trying to understand where these deformations come from it is important to understand the basic mechanism behind the transient absorption spectrum.

The reduction in transmitted photons can also be described in a semi-classical picture, where the electric field is not quantized and treated as a classical field. In classical electrodynamics, the Larmor formula describes the generation of radiation due to the acceleration of charged particles [21]. Quantum mechanically, the electron motion is captured in the dipole moment $\langle \hat{z} \rangle (t)$. The generated and the absorbed radiation of an ion is, therefore, determined by the dynamics of the ionic dipole moment $\langle \hat{z} \rangle_{\text{ion}} (t)$. A field-independent photoionization cross section $\sigma(\omega)$ (see Sec. 3.1.2) reads in terms of the ionic dipole moment

$$\sigma(\omega) = 4\pi \, \alpha \, \omega \, \text{Im} \left[\frac{\langle \hat{z} \rangle_{\text{ion}} (\omega)}{E(\omega)} \right], \tag{3.37}$$

where ω is the photon energy and $E(\omega)$ is the spectrum of the incident electric field.

In the case of absorption, the ionic dipole, $\langle \hat{z} \rangle_{\text{ion}} (t) \propto \sin(\omega_0 \, t)$, oscillates 180° out of phase with respect to $E(t)$ such that the spectral strength $E(\omega_0)$ gets reduced for the specific oscillation frequency ω_0. If the dipole oscillates in phase, the electric field gets enhanced leading to an emitting behavior. The energetically lowest absorption line $[4p^m_{3/2}]^{-1} \rightarrow [3d^m_{5/2}]^{-1}$ in Fig. 3.20 shows a purely absorbing (Lorentzian) behavior when pump and probe pulses do not overlap[9]. The widths of the transition lines are determined by the lifetime of the $3d^{-1}$ ionic states and the detector resolution.

When the phase shift ϕ in the oscillating ionic dipole $[\langle \hat{z} \rangle (t) \propto \sin(\omega_0 \, t + \phi)]$ is not a multiple of π, the transition line shapes are not Lorentzian anymore (see Fig. 3.21a for $\tau = 0$). Figure 3.21a shows cuts of the transient absorption spectrum of Fig. 3.20 for the pump-probe delays $\tau = 0, 2.4$ fs. At $\tau = 0$ fs, the NIR field peaks and all three transition lines are strongly deformed. The ionic phase shifts $\phi(\tau)$ are shown in Fig. 3.21b for the energetically smallest and largest transition lines. They are obtained from the TDCIS results by fitting Eq. (3.37) with $\langle \hat{z} \rangle_{\text{ion}} (t) = z_0 \sin(\omega \, t + \phi)$ for each pump-probe

[9] The other two absorption lines do not show purely absorbing behavior due to coherences between the ionic states $[4p^{\pm 1/2}_{1/2}]^{-1}$ and $[4p^{\pm 1/2}_{3/2}]^{-1}$ (see Sec. 3.1.6).

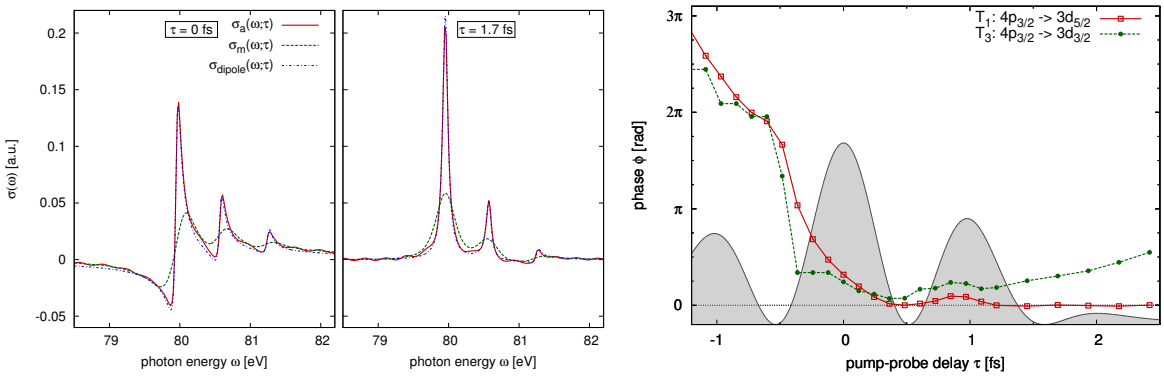

(a) Transient absorption spectrum (b) Ionic dipole phase $\phi(\tau)$

Figure 3.21: (a) The calculated atomic cross sections (red solid line), the measured cross sections (green dashed line), and the fit obtained from a simplified oscillating dipole model (yellow dotted line) are shown for the pump-probe delays $\tau = 0$ fs and $\tau = 2.4$ fs, respectively. (b) Ionic dipole phase $\phi(\tau)$ obtained from the fits for the transition lines $4p_{3/2}^{-1} \rightarrow 3d_{5/2}^{-1}$ (red solid line) and $4p_{3/2}^{-1} \rightarrow 3d_{3/2}^{-1}$ (green dashed line) are shown. The figures are taken from Ref. [214]. Copyright © 2012 American Physical Society (APS).

delay. The increasing phase shift in the $4p_{3/2}^{-1} \rightarrow 3d_{3/2}^{-1}$ transition for large τ is due to the coherent superposition of the ionic states $4p_{3/2}^{-1}$ and $4p_{1/2}^{-1}$ (see Sec. 3.1.6). There are three mechanisms that could contribute to ϕ:

- the quadratic Stark shift of the ionic energy levels due to the high electric field strength of the ionizing pulse,
- the residual Coulomb interaction between the ion and the electron,
- field-driven coupling between the freed electron and the parent ion via the neutral ground state Φ_0.

I found that the influence of the residual Coulomb interaction on ϕ is negligibly small. The ionic Stark shift is quite large for each ionic state. However, what matters are the differences in the energy shifts between the ionic states such that the transition energy gets modified. Even though the absolute energy shifts could be as large as 1 eV, the relative energy differences do not change by more than 100 meV, which leads to a maximum phase shift of $\approx \frac{\pi}{10}$. The phase shift shown in Fig. 3.21b is, however, much larger such that the only possible mechanism is the field-driven dressing of the neutral ground state. The large phase shifts disappear when the field-driven coupling to the neutral ground state is immediately switched off after the ion has been probed (see Fig. 9 in Chap. 5.5/Ref. [214]). Interestingly, the electric field cannot directly couple the ion with the ionized electron. Only via the neutral ground state (i.e., $\langle \Phi_0 | \hat{z} | \Phi_i^a \rangle$) is it possible to create a field-driven correlation interaction the ionic and electronic subsystems.

This study has shown that attosecond transient absorption spectroscopy is a versatile technique to investigate ultrafast electronic motion. It can be used to probe the electronic state of the ionic subsystem, and at the same time it is sensitive to interactions of the ionic subsystem with the environment.

3.5 Bibliography

[1] F. Krausz and M. Ivanov, Rev. Mod. Phys. **81**, 163 (2009).

[2] T. Brabec and F. Krausz, Rev. Mod. Phys. **72**, 545 (2000).

[3] T. Popmintchev, M.-C. Chen, D. Popmintchev, *et al.*, Science **336**, 1287 (2012).

[4] P. B. Corkum and F. Krausz, Nat. Phys. **3**, 381 (2007).

[5] W. Becker, X. Liu, P. J. Ho, and J. H. Eberly, Rev. Mod. Phys. **84**, 1011 (2012).

[6] S. Popruzhenko and D. Bauer, J. Mod. Opt. **55**, 2573 (2008).

[7] K. Burnett, V. C. Reed, and P. L. Knight, J. Phys. B **26**, 561 (1993).

[8] M. Y. Ivanov, M. Spanner, and O. Smirnova, J. Mod. Opt. **52**, 165 (2005).

[9] D. B. Milosević, G. G. Paulus, D. Bauer, and W. Becker, J. Phys. B **39**, R203 (2006).

[10] P. Agostini and L. F. DiMauro, Reports on Progress in Physics **67**, 813 (2004).

[11] A. Scrinzi, M. Y. Ivanov, R. Kienberger, and D. M. Villeneuve, J. Phys. B **39**, R1 (2006).

[12] T. Pfeifer, M. J. Abel, P. M. Nagel, *et al.*, Chem. Phys. Lett. **463**, 11 (2008).

[13] J. M. Dahlström, A. L'Huillier, and A. Maquet, J. Phys. B **45**, 183001 (2012).

[14] F. J. Wuilleumier and M. Meyer, J. Phys. B **39**, R425 (2006).

[15] J. Köhler, M. Wollenhaupt, T. Bayer, C. Sarpe, and T. Baumert, Opt. Express **19**, 11638 (2011).

[16] A. Rudenko, Y. H. Jiang, M. Kurka, *et al.*, J. Phys. B **43**, 194004 (2010).

[17] W. Ackermann, G. Asova, V. Ayvazyan, *et al.*, Nat. Photonics **1**, 336 (2007).

[18] M. Magrakvelidze, O. Herrwerth, Y. H. Jiang, *et al.*, Phys. Rev. A **86**, 013415 (2012).

[19] L. Keldysh, Sov. Phys. JETP **20**, 1307 (1965).

[20] T. Topcu and F. Robicheaux, Phys. Rev. A **86**, 053407 (2012).

[21] J. D. Jackson, *Classical Electrodynamics*, 3rd ed. (Wiley, New York, 1998).

[22] D. V. S. Michael E. Peskin, *An Introduction To Quantum Field Theory* (Westview Press, 1995).

[23] R. Santra, J. Phys. B **42**, 023001 (2009).

[24] M. H. Mittleman, *Introduction to the Theory of Laser-Atom Interactions*, 2nd ed. (Springer, New York, 1993).

[25] A. D. Bandrauk, F. Fillion-Gourdeau, and E. Lorin, arxiv:1302.2932 (2013).

[26] M. Göppert-Mayer, Ann. Phys. **401**, 273 (1931).

[27] W. C. Henneberger, Phys. Rev. Lett. **21**, 838 (1968).

[28] V. C. Reed and K. Burnett, Phys. Rev. A **42**, 3152 (1990).

[29] H. Hall, Rev. Mod. Phys. **8**, 358 (1936).

[30] U. Fano and J. W. Cooper, Rev. Mod. Phys. **40**, 441 (1968).

[31] A. F. Starace, in *Encyclopedia of Physics*, Vol. 31: Corpuscles and Radiation in Matter I, edited by W. Mehlhorn (Springer, Berlin, 1982) Chap. Theory of Atomic Photoionization, pp. 1–121.

[32] S. Chandrasekhar, Astrophys. J. **102**, 223 (1945).

[33] A. Stewart, Adv. At. Mol. Phys. **3**, 1 (1968).

[34] R. Crossley, Adv. At. Mol. Phys. **5**, 237 (1969).

[35] A. Szabo and N. S. Ostlund, *Modern Quantum Chemistry* (Dover Publication Inc., Mineola, NY, 1996).

[36] G. W. F. Drake, Phys. Scr. **1999**, 83 (1999).

[37] C. C. J. Roothaan, Rev. Mod. Phys. **23**, 69 (1951).

[38] A. Thompson, X-Ray Data Booklet, `http://xdb.lbl.gov`.

[39] J. J. Rehr and R. C. Albers, Rev. Mod. Phys. **72**, 621 (2000).

[40] G. Bunker and E. A. Stern, Phys. Rev. Lett. **52**, 1990 (1984).

[41] J. Als-Nielsen and D. McMorrow, *Elements of Modern X-ray Physics* (Wiley, Chichester, 2001).

[42] M. H. Carpenter, *Helium Atmosphere Chamber for Soft X-ray Spectroscopy of Biomolecules*, Master's thesis, University of California, Davis (2010).

[43] J. W. Cooper, Phys. Rev. **128**, 681 (1962).

[44] J. Samson and W. Stolte, J. Electron Spectrosc. **123**, 265 (2002).

[45] T. N. Chang and U. Fano, Phys. Rev. A **13**, 263 (1976).

[46] S.-K. Son, L. Young, and R. Santra, Phys. Rev. A **83**, 033402 (2011).

[47] J. C. Slater, Phys. Rev. **81**, 385 (1951).

[48] R. Latter, Phys. Rev. **99**, 510 (1955).

[49] J. L. Dehmer and D. Dill, Phys. Rev. Lett. **37**, 1049 (1976).

[50] D. Dill, A. F. Starace, and S. T. Manson, Phys. Rev. A **11**, 1596 (1975).

[51] U. Becker and D. A. Shirley, eds., *VUV and Soft X-Ray Photoionization*, Physics of atoms and molecules (Plenum Press, New York, 1996) p. 667.

[52] U. Fano and D. Dill, Phys. Rev. A **6**, 185 (1972).

[53] F. Heiser, O. Geßner, J. Viefhaus, K. Wieliczek, R. Hentges, and U. Becker, Phys. Rev. Lett. **79**, 2435 (1997).

[54] N. Böwering, T. Lischke, B. Schmidtke, N. Müller, T. Khalil, and U. Heinzmann, Phys. Rev. Lett. **86**, 1187 (2001).

[55] M. S. Schöffler, J. Titze, N. Petridis, *et al.*, Science **320**, 920 (2008).

[56] A. Damascelli, Z. Hussain, and Z.-X. Shen, Rev. Mod. Phys. **75**, 473 (2003).

[57] D. Lu, I. M. Vishik, M. Yi, Y. Chen, R. G. Moore, and Z.-X. Shen, Ann. Rev. Cond. Mat. Phys. **3**, 129 (2012).

[58] J. M. Blatt and L. C. Biedenharn, Rev. Mod. Phys. **24**, 258 (1952).

[59] M. Ilchen, *Coherence Effects in the Valence Photoionization of Small Molecules*, Ph.D. thesis, Fakultät II - Mathematik und Naturwissenschaften, Technischen Universität Berlin (2012).

[60] W. R. Johnson and K. T. Cheng, Phys. Rev. A **63**, 022504 (2001).

[61] L. Young, E. P. Kanter, B. Krässig, *et al.*, Nature **466**, 56 (2010).

[62] A. Saenz and P. Lambropoulos, J. Phys. B **32**, 5629 (1999).

[63] A. Sytcheva, S. Pabst, S.-K. Son, and R. Santra, Phys. Rev. A **85**, 023414 (2012).

[64] G. Doumy, C. Roedig, S.-K. Son, *et al.*, Phys. Rev. Lett. **106**, 083002 (2011).

[65] L. Landau and E. Lifschitz, *Quantum Mechanics: Non-Relativistic Theory* (Pergamon Press, New York, 1965).

[66] A. M. Perelomov, V. S. Popov, and M. V. Terent'ev, Sov. Phys. JETP **23**, 924 (1966).

[67] M. Ammosov, N. Delone, and V. Krainov, Sov. Phys. JETP **64**, 1191 (1986).

[68] X. M. Tong, Z. X. Zhao, and C. D. Lin, Phys. Rev. A **66**, 033402 (2002).

[69] P. B. Corkum, Phys. Today **64**, 36 (2011).

[70] S.-F. Zhao, C. Jin, A.-T. Le, T. F. Jiang, and C. D. Lin, Phys. Rev. A **80**, 051402 (2009).

[71] A. Scrinzi, M. Geissler, and T. Brabec, Phys. Rev. Lett. **83**, 706 (1999).

[72] C. Z. Bisgaard and L. B. Madsen, Amer. J. Phys. **72**, 249 (2004).

[73] R. N. Zare, *Angular Momentum* (Wiley, New York, 1988).

[74] S. Augst, D. Strickland, D. D. Meyerhofer, S. L. Chin, and J. H. Eberly, Phys. Rev. Lett. **63**, 2212 (1989).

[75] A. Becker and F. H. M. Faisal, J. Phys. B **38**, R1 (2005).

[76] P. Saliéres, B. Carré, L. Le Déroff, *et al.*, Science **292**, 902 (2001).

[77] F. H. M. Faisal, J. Phys. B **6**, L89 (1973).

[78] H. R. Reiss, Phys. Rev. A **22**, 1786 (1980).

[79] D. M. Wolkow (Volkov), Z. Phys. **94**, 250 (1935).

[80] C. C. Chirilă and M. Lein, Phys. Rev. A **73**, 023410 (2006).

[81] C. Figueira de Morisson Faria and B. B. Augstein, Phys. Rev. A **81**, 043409 (2010).

[82] N. B. Delone and V. P. Krainov, *Multiphoton Processes in Atoms* (Springer, Berlin, 2000).

[83] M. Bashkansky, P. H. Bucksbaum, and D. W. Schumacher, Phys. Rev. Lett. **60**, 2458 (1988).

[84] A. Rudenko, K. Zrost, T. Ergler, *et al.*, J. Phys. B **38**, L191 (2005).

[85] D. Bauer, D. B. Milošević, and W. Becker, Phys. Rev. A **72**, 023415 (2005).

[86] D. Bauer, D. B. Milośević, and W. Becker, J. Mod. Opt. **53**, 135 (2006).

[87] O. Smirnova, M. Spanner, and M. Ivanov, J. Phys. B **39**, S307 (2006).

[88] O. Smirnova, M. Spanner, and M. Ivanov, Phys. Rev. A **77**, 033407 (2008).

[89] Y. Huismans, A. RouzĂŠe, A. Gijsbertsen, *et al.*, Science **331**, 61 (2011).

[90] J. H. Shirley, Phys. Rev. **138**, B979 (1965).

[91] U. V. Riss and H. D. Meyer, J. Phys. B **26**, 4503 (1993).

[92] A. Gordon, R. Santra, and F. X. Kärtner, Phys. Rev. A **72**, 063411 (2005).

[93] X. Chu, Phys. Rev. A **82**, 023407 (2010).

[94] M. Abu-samha and L. B. Madsen, Phys. Rev. A **81**, 033416 (2010).

[95] N. Takemoto and A. Becker, Phys. Rev. Lett. **105**, 203004 (2010).

[96] M. Kohler, T. Pfeifer, K. Hatsagortsyan, and C. Keitel, *Advances in Atomic, Molecular, and Optical Physics*, Adv. At., Mol., Opt. Phys. **61**, 159 (2012).

[97] A. McPherson, G. Gibson, H. Jara, *et al.*, J. Opt. Soc. Am. B **4**, 595 (1987).

[98] M. Ferray, A. L'Huillier, X. F. Li, L. A. Lompre, G. Mainfray, and C. Manus, J. Phys. B **21**, L31 (1988).

[99] E. Goulielmakis, M. Schultze, M. Hofstetter, *et al.*, Science **320**, 1614 (2008).

[100] K. Zhao, Q. Zhang, M. Chini, Y. Wu, X. Wang, and Z. Chang, Opt. Lett. **37**, 3891 (2012).

[101] T. Popmintchev, M.-C. Chen, D. Popmintchev, *et al.*, in *CLEO:2011 - Laser Applications to Photonic Applications* (Optical Society of America, 2011) p. PDPC12.

[102] Y. Xiang, Y. Niu, Y. Qi, R. Li, and S. Gong, J. Mod. Opt. **57**, 385 (2010).

[103] P. B. Corkum, Phys. Rev. Lett. **71**, 1994 (1993).

[104] K. J. Schafer, B. Yang, L. F. DiMauro, and K. C. Kulander, Phys. Rev. Lett. **70**, 1599 (1993).

[105] T. Popmintchev, M.-C. Chen, P. Arpin, M. M. Murnane, and H. C. Kapteyn, Nat. Photonics **4**, 822 (2010).

[106] M. Lewenstein, P. Balcou, M. Y. Ivanov, A. L'Huillier, and P. B. Corkum, Phys. Rev. A **49**, 2117 (1994).

[107] C. D. Lin, A.-T. Le, Z. Chen, T. Morishita, and R. Lucchese, J. Phys. B **43**, 122001 (2010).

[108] S. Haessler, J. Caillat, and P. Saliéres, J. Phys. B **44**, 203001 (2011).

[109] B. Augstein and C. F. de Morisson Faria, J. Mod. Opt. **58**, 1173 (2011).

[110] B. B. Augstein and C. F. De Morisson Faria, Mod. Phys. Lett. B **26**, 1130002 (2012).

[111] A.-T. Le, R. R. Lucchese, S. Tonzani, T. Morishita, and C. D. Lin, Phys. Rev. A **80**, 013401 (2009).

[112] Y.-C. Han and L. B. Madsen, Phys. Rev. A **81**, 063430 (2010).

[113] M.-C. Chen, P. Arpin, T. Popmintchev, *et al.*, Phys. Rev. Lett. **105**, 173901 (2010).

[114] E. Seres, J. Seres, and C. Spielmann, Appl. Phys. Lett. **89**, 181919 (2006).

[115] R. López-Martens, K. Varjú, P. Johnsson, *et al.*, Phys. Rev. Lett. **94**, 033001 (2005).

[116] D. Strasser, T. Pfeifer, B. J. Hom, A. M. Müller, J. Plenge, and S. R. Leone, Phys. Rev. A **73**, 021805 (2006).

[117] T. Popmintchev, M.-C. Chen, A. Bahabad, *et al.*, PNAS (USA) **106**, 10516 (2009).

[118] A. Paul, E. Gibson, X. Zhang, *et al.*, IEEE J. Quantum Elect. **42**, 14 (2006).

[119] C. R. Gouy, C. R. Acad. Sci. Paris **110**, 1251 (1890).

[120] S. Feng and H. G. Winful, Opt. Lett. **26**, 485 (2001).

[121] C. Vozzi, M. Negro, F. Calegari, S. Stagira, K. Kovács, and V. Tosa, New J. Phys. **13**, 073003 (2011).

[122] A. Rundquist, C. G. Durfee, Z. Chang, C. Herne, S. Backus, M. M. Murnane, and H. C. Kapteyn, Science **280**, 1412 (1998).

[123] J. Tate, T. Auguste, H. G. Muller, P. Salières, P. Agostini, and L. F. DiMauro, Phys. Rev. Lett. **98**, 013901 (2007).

[124] K. Schiessl, K. L. Ishikawa, E. Persson, and J. Burgdörfer, Phys. Rev. Lett. **99**, 253903 (2007).

[125] M. V. Frolov, N. L. Manakov, and A. F. Starace, Phys. Rev. Lett. **100**, 173001 (2008).

[126] A. D. Shiner, C. Trallero-Herrero, N. Kajumba, *et al.*, Phys. Rev. Lett. **103**, 073902 (2009).

[127] P. Koval, F. Wilken, D. Bauer, and C. H. Keitel, Phys. Rev. Lett. **98**, 043904 (2007).

[128] W. Hong, Y. Li, P. Lu, P. Lan, Q. Zhang, and X. Wang, J. Opt. Soc. Am. B **25**, 1684 (2008).

[129] K. Ishikawa, Phys. Rev. Lett. **91**, 043002 (2003).

[130] A. Fleischer, Phys. Rev. A **78**, 053413 (2008).

[131] G.-T. Zhang, J. Wu, C.-L. Xia, and X.-S. Liu, Phys. Rev. A **80**, 055404 (2009).

[132] C. Buth, M. C. Kohler, J. Ullrich, and C. H. Keitel, Opt. Lett. **36**, 3530 (2011).

[133] C. Buth, F. He, J. Ullrich, C. H. Keitel, and K. Z. Hatsagortsyan, arXiv:1203.4127v1 (2012).

[134] A. Baltuska, T. Udem, M. Uiberacker, *et al.*, Nature **421**, 611 (2003).

[135] V. S. Yakovlev, M. Ivanov, and F. Krausz, Opt. Express **15**, 15351 (2007).

[136] A. Wirth, M. T. Hassan, I. Grguras, *et al.*, Science **334**, 195 (2011).

[137] P. M. Paul, E. S. Toma, P. Breger, *et al.*, Science **292**, 1689 (2001).

[138] Y. Mairesse, A. de Bohan, L. J. Frasinski, *et al.*, Science **302**, 1540 (2003).

[139] D. J. Kane and R. Trebino, Opt. Lett. **18**, 823 (1993).

[140] Y. Mairesse and F. Quéré, Phys. Rev. A **71**, 011401 (2005).

[141] G. Sansone, E. Benedetti, F. Calegari, *et al.*, Science **314**, 443 (2006).

[142] K. T. Kim, K. S. Kang, M. N. Park, T. Imran, G. Umesh, and C. H. Nam, arXiv:0707.4228v1 (2007).

[143] F. Quéré, Y. Mairesse, and J. Itatani, J. Mod. Opt. **52**, 339 (2005).

[144] I. Thomann, A. Bahabad, X. Liu, R. Trebino, M. M. Murnane, and H. C. Kapteyn, Opt. Express **17**, 4611 (2009).

[145] F. Ferrari, F. Calegari, M. Lucchini, C. Vozzi, S. Stagira, G. Sansone, and M. Nisoli, Nat. Photonics **4**, 875 (2010).

[146] B. K. McFarland, J. P. Farrell, P. H. Bucksbaum, and M. Gühr, Science **322**, 1232 (2008).

[147] J. Itatani, J. Levesque, D. Zeidler, *et al.*, Nature **432**, 867 (2004).

[148] C. Vozzi, M. Negro, F. Calegari, G. Sansone, M. Nisoli, S. De Silvestri, and S. Stagira, Nat. Phys. **7**, 822 (2011).

[149] L. S. Cederbaum, W. Domcke, J. Schirmer, and W. V. Niessen, *Advances in Chemical Physics*, Adv. Chem. Phys. **65**, 115 (2007).

[150] A. Kuleff, S. Lünnemann, and L. Cederbaum, J. Phys. Chem. A **114**, 8676 (2010).

[151] O. Smirnova, Y. Mairesse, S. Patchkovskii, N. Dudovich, D. Villeneuve, P. Corkum, and M. Y. Ivanov, Nature **460**, 972 (2009).

[152] B. E. Schmidt, A. D. Shiner, M. Giguére, *et al.*, J. Phys. B **45**, 074008 (2012).

[153] H. J. Wörner, H. Niikura, J. B. Bertrand, P. B. Corkum, and D. M. Villeneuve, Phys. Rev. Lett. **102**, 103901 (2009).

[154] A. D. Shiner, B. E. Schmidt, C. Trallero-Herrero, *et al.*, Nat. Phys. **7**, 464 (2011).

[155] J. Zhang and D.-S. Guo, Phys. Rev. Lett. **110**, 063002 (2013).

[156] J. P. Farrell, L. S. Spector, B. K. McFarland, P. H. Bucksbaum, M. Gühr, M. B. Gaarde, and K. J. Schafer, Phys. Rev. A **83**, 023420 (2011).

[157] J. Higuet, H. Ruf, N. Thiré, *et al.*, Phys. Rev. A **83**, 053401 (2011).

[158] S. Pabst, L. Greenman, D. A. Mazziotti, and R. Santra, Phys. Rev. A **85**, 023411 (2012).

[159] T. A. Carlson, M. O. Krause, F. A. Grimm, P. Keller, and J. W. Taylor, J. Chem. Phys. **77**, 5340 (1982).

[160] J. B. Bertrand, H. J. Wörner, P. Hockett, D. M. Villeneuve, and P. B. Corkum, Phys. Rev. Lett. **109**, 143001 (2012).

[161] M. C. H. Wong, A.-T. Le, A. F. Alharbi, *et al.*, Phys. Rev. Lett. **110**, 033006 (2013).

[162] J. Itatani, F. Quéré, G. L. Yudin, M. Y. Ivanov, F. Krausz, and P. B. Corkum, Phys. Rev. Lett. **88**, 173903 (2002).

[163] M. Drescher, M. Hentschel, R. Kienberger, *et al.*, Nature **419**, 803 (2002).

[164] J. C. Baggesen and L. B. Madsen, Phys. Rev. Lett. **104**, 043602 (2010).

[165] A. L. Cavalieri, N. Mueller, T. Uphues, *et al.*, Nature **449**, 1029 (2007).

[166] M. Uiberacker, T. Uphues, M. Schultze, *et al.*, Nature **446**, 627 (2007).

[167] U. Frühling, M. Wieland, M. Gensch, *et al.*, Nature Photonics **3**, 523 (2009).

[168] M. Schultze, M. Fiess, N. Karpowicz, *et al.*, Science **328**, 1658 (2010).

[169] M. Hofstetter, M. Schultze, M. Fieß, *et al.*, Opt. Express **19**, 1767 (2011).

[170] J. Gagnon, E. Goulielmakis, and V. Yakovlev, Appl. Phys. B **92**, 25 (2008).

[171] U. Frühling, J. Phys. B **44**, 243001 (2011).

[172] H. Aksela, S. Aksela, and H. Pulkkinen, Phys. Rev. A **30**, 2456 (1984).

[173] M. Jurvansuu, A. Kivimäki, and S. Aksela, Phys. Rev. A **64**, 012502 (2001).

[174] A. S. Kheifets and I. A. Ivanov, Phys. Rev. Lett. **105**, 233002 (2010).

[175] L. R. Moore, M. A. Lysaght, J. S. Parker, H. W. van der Hart, and K. T. Taylor, Phys. Rev. A **84**, 061404 (2011).

[176] K. Klünder, J. M. Dahlström, M. Gisselbrecht, *et al.*, Phys. Rev. Lett. **106**, 143002 (2011).

[177] S. Nagele, R. Pazourek, J. Feist, and J. Burgdörfer, Phys. Rev. A **85**, 033401 (2012).

[178] I. A. Ivanov and A. S. Kheifets, Phys. Rev. A **85**, 021401 (2012).

[179] M. Ivanov and O. Smirnova, Phys. Rev. Lett. **107**, 213605 (2011).

[180] S. Nagele, R. Pazourek, J. Feist, K. Doblhoff-Dier, C. Lemell, K. Tokési, and J. Burgdörfer, J. Phys. B **44**, 081001 (2011).

[181] D. Guenot, K. Klunder, C. L. Arnold, *et al.*, Phys. Rev. A **85**, 053424 (2012).

[182] E. H. Hauge and J. A. Støvneng, Rev. Mod. Phys. **61**, 917 (1989).

[183] R. Landauer and T. Martin, Rev. Mod. Phys. **66**, 217 (1994).

[184] P. Eckle, A. N. Pfeiffer, C. Cirelli, *et al.*, Science **322**, 1525 (2008).

[185] A. N. Pfeiffer, C. Cirelli, M. Smolarski, D. Dimitrovski, M. Abu-samha, L. B. Madsen, and U. Keller, Nat. Phys. **8**, 76 (2012).

[186] E. Goulielmakis, Z. Loh, A. Wirth, *et al.*, Nature **466**, 739 (2010).

[187] M. Dantus, M. J. Rosker, and A. H. Zewail, J. Chem. Phys. **87**, 2395 (1987).

[188] J. Aßmann, M. Kling, and B. Abel, Angew. Chem. Int. Edit. **42**, 2226 (2003).

[189] V. I. Klimov and D. W. McBranch, Phys. Rev. Lett. **80**, 4028 (1998).

[190] R. Santra, V. S. Yakovlev, T. Pfeifer, and Z.-H. Loh, Phys. Rev. A **83**, 033405 (2011).

[191] A. Wirth, R. Santra, and E. Goulielmakis, Chem. Phys. **414**, 149 (2012).

[192] J. C. Baggesen, E. Lindroth, and L. B. Madsen, Phys. Rev. A **85**, 013415 (2012).

[193] M. B. Gaarde, C. Buth, J. L. Tate, and K. J. Schafer, Phys. Rev. A **83**, 013419 (2011).

[194] M. Chini, B. Zhao, H. Wang, Y. Cheng, S. X. Hu, and Z. Chang, Phys. Rev. Lett. **109**, 073601 (2012).

[195] M. Tarana and C. H. Greene, Phys. Rev. A **85**, 013411 (2012).

[196] C. Ott, A. Kaldun, P. Raith, *et al.*, arXiv:1205.0519v1 (2012).

[197] S. Chen, M. J. Bell, A. R. Beck, *et al.*, Phys. Rev. A **86**, 063408 (2012).

[198] H. Wang, M. Chini, S. Chen, *et al.*, Phys. Rev. Lett. **105**, 143002 (2010).

[199] M. Holler, F. Schapper, L. Gallmann, and U. Keller, Phys. Rev. Lett. **106**, 123601 (2011).

[200] P. Lambropoulos, P. Maragakis, and J. Zhang, Phys. Rep. **305**, 203 (1998).

[201] E. K. U. Gross, E. Runge, and O. Heinonen, *Many Particle Theory* (Institute of Physics Publishing, 1992).

[202] R. J. Bartlett and J. F. Stanton, "Applications of post-hartree–fock methods: A tutorial," in *Rev. Comp. Chem.*, Vol. 5, edited by K. B. Lipkowitz and D. B. Boyd (John Wiley & Sons, Inc., Hoboken, NJ, USA, 2007) pp. 65–169.

[203] S.-K. Son and S.-I. Chu, Phys. Rev. A **77**, 063406 (2008).

[204] H. G. Muller, Phys. Rev. A **60**, 1341 (1999).

[205] Z. B. Walters and O. Smirnova, J. Phys. B **43**, 161002 (2010).

[206] S.-F. Zhao, C. Jin, A.-T. Le, T. F. Jiang, and C. D. Lin, Phys. Rev. A **81**, 033423 (2010).

[207] DALTON — a molecular electronic structure program, Release Dalton2011 (2011), see http://daltonprogram.org.

[208] R. G. Parr and W. Yang, *Density-Functional Theory of Atoms and Molecules* (Oxford University Press, New York, USA, 1989).

[209] S.-F. Zhao, C. Jin, A.-T. Le, and C. D. Lin, Phys. Rev. A **82**, 035402 (2010).

[210] R. Murray, M. Spanner, S. Patchkovskii, and M. Y. Ivanov, Phys. Rev. Lett. **106**, 173001 (2011).

[211] N. Rohringer, A. Gordon, and R. Santra, Phys. Rev. A **74**, 043420 (2006).

[212] N. Rohringer and R. Santra, Phys. Rev. A **79**, 053402 (2009).

[213] L. Greenman, P. J. Ho, S. Pabst, E. Kamarchik, D. A. Mazziotti, and R. Santra, Phys. Rev. A **82**, 023406 (2010).

[214] S. Pabst, A. Sytcheva, A. Moulet, A. Wirth, E. Goulielmakis, and R. Santra, Phys. Rev. A **86**, 063411 (2012).

[215] S. Pabst, L. Greenman, P. J. Ho, D. A. Mazziotti, and R. Santra, Phys. Rev. Lett. **106**, 053003 (2011).

[216] U. Fano, Rev. Mod. Phys. **29**, 74 (1957).

[217] K. Blum, *Density Matrix Theory and Applications*, 3rd ed. (Springer, Berlin, 2012).

[218] H.-P. Breuer and F. Petruccione, *The Theory of Open Quantum Systems* (Oxford University Press, 2002).

[219] J. Wang, S.-I. Chu, and C. Laughlin, Phys. Rev. A **50**, 3208 (1994).

[220] R. Santra and L. S. Cederbaum, Phys. Rep. **368**, 1 (2002).

[221] X. M. Tong and N. Toshima, Phys. Rev. A **81**, 063403 (2010).

[222] W. H. Press, B. P. Flannery, S. A. Teukolsky, and W. T. Vetterling, *Numerical Recipes in FORTRAN 77*, 2nd ed., Vol. 1 (Cambridge University Press, 1992).

[223] G. Engeln-Müllges and F. Uhlig, *Numerical Algorithms with Fortran* (Springer, Heidelberg, 1996).

[224] A. I. Kuleff, J. Breidbach, and L. S. Cederbaum, J. Chem. Phys. **123**, 044111 (2005).

[225] M. Nest, F. Remacle, and R. D. Levine, New J. Phys. **10**, 025019 (2008).

[226] J. Breidbach and L. S. Cederbaum, J. Chem. Phys. **118**, 3983 (2003).

[227] L. X. Chen, Annu. Rev. Phys. Chem. **56**, 221 (2005).

[228] D. Healion, Y. Zhang, J. D. Biggs, N. Govind, and S. Mukamel, J. Phys. Chem. Lett. **3**, 2326 (2012).

Part II

Publications

Chapter 4

Laser Alignment of Molecules

4.1 Computational Studies of X-ray Scattering From 3D-Aligned Asymmetric-Top Molecules

Stefan Pabst, Phay J. Ho, and Robin Santra

Published in Phys. Rev. A **81**, 043425 (2010)

Original publication: http://link.aps.org/doi/10.1103/PhysRevA.81.043425
Free preprint version: http://arxiv.org/abs/1003.5929

Statement of Contributions

All alignment calculations and the preparation of the manuscript have been done by myself. The phase-retrival section as well as the phase-retrieval code used for the analysis have been written by Phay J. Ho. He also generated the data of the structure reconstruction. The interpretation of the results were done together by Phay J. Ho, Robin Santra, and myself.

PHYSICAL REVIEW A **81**, 043425 (2010)

Computational studies of x-ray scattering from three-dimensionally-aligned asymmetric-top molecules

Stefan Pabst,[1,2] Phay J. Ho,[1] and Robin Santra[1,3,*]
[1]*Argonne National Laboratory, Argonne, Illinois 60439, USA*
[2]*Institut für Theoretische Physik, Universität Erlangen-Nuremberg, D-91058 Erlangen, Germany*
[3]*Department of Physics, University of Chicago, Chicago, Illinois 60637, USA*
(Received 3 February 2010; published 29 April 2010)

We theoretically and numerically analyze x-ray scattering from asymmetric-top molecules three-dimensionally aligned using elliptically polarized laser light. A rigid-rotor model is assumed. The principal axes of the polarizability tensor are assumed to coincide with the principal axes of the moment of inertia tensor. Several symmetries in the Hamiltonian are identified and exploited to enhance the efficiency of solving the time-dependent Schrödinger equation for each rotational state initially populated in a thermal ensemble. Using a phase-retrieval algorithm, the feasibility of structure reconstruction from a quasiadiabatically aligned sample is illustrated for the organic molecule naphthalene. The spatial resolution achievable strongly depends on the laser parameters, the initial rotational temperature, and the x-ray pulse duration. We demonstrate that for a laser peak intensity of 5 TW/cm^2, a laser pulse duration of 100 ps, a rotational temperature of 10 mK, and an x-ray pulse duration of 1 ps, the molecular structure may be probed at a resolution of 1 Å.

DOI: 10.1103/PhysRevA.81.043425 PACS number(s): 33.80.−b, 34.50.Rk, 61.05.cc, 42.30.Rx

I. INTRODUCTION

X-ray diffraction is a powerful method for investigating structures of molecules. X-ray crystallography has become the standard tool for identifying the structure of large molecules and proteins [1–3]. Recent developments in x-ray sources have opened new opportunities [4–13] for imaging membrane proteins and other macromolecules that cannot be crystallized [14]. One possibility is single-molecule imaging, where one molecule at a time is probed by an intense x-ray pulse [7–11], which subjects the molecule to severe damage [8,15]. A series of diffraction patterns has to be collected and classified according to the molecular orientation to get full structural information from randomly oriented molecules [9]. New iterative phase-retrieval algorithms for noncrystalline specimens have been developed to invert the diffraction data [9–12,16–18].

Alternative approaches with laser-aligned molecules have been proposed, where an ensemble of molecules, rather than a single molecule, is exposed to x-ray pulses [4,5]. In this approach the radiation dose for each molecule is strongly reduced and stays well below the critical value for damage [4]. Three-dimensional information on the single-molecule structure can be gained from a well-aligned ensemble by capturing many two-dimensional diffraction patterns. The ability to accumulate the signal over a large number of x-ray pulses reduces the radiation dose further. Notice that alignment, rather than orientation, of the molecules is expected to be sufficient for the reconstruction of the molecular structure [16,19]. Nevertheless, various methods have been proposed to orient molecules [20,21] by the linear Stark effect [22], the AC Stark effect [23], or two-color fields [24].

Much theoretical and experimental research has been done on laser-induced alignment [25–71]. With nonresonant laser frequencies, an induced dipole moment can be created that couples back to the laser electric field and forces the molecule to be aligned. Earlier work has focused on one-dimensional alignment of the most polarizable axis by using linearly polarized light [25–56]. The demonstration of three-dimensional alignment [57–63], which requires an asymmetric-top molecule and an elliptically polarized pulse (or two linearly polarized pulses) opens the door for probing the three-dimensional structure. The Coulomb explosion technique has been exploited to detect three-dimensional alignment [58,60], where rotational temperatures down to 1 K have been accomplished [72].

Depending on the duration of the laser pulse, τ_L, relative to the rotational period of the molecule, τ_{rot}, the alignment dynamics can be classified into three distinct regimes. In the limits of adiabatic ($\tau_L \gg \tau_{\mathrm{rot}}$) and impulsive ($\tau_L \ll \tau_{\mathrm{rot}}$) alignment, the dynamics can be described analytically [32,33]. Impulsive alignment reveals the quantum mechanical nature of this process by showing alignment revivals after the laser pulse is over [34–41]. In the adiabatic limit, the alignment dynamics follow the laser pulse shape [55]. No analytic solution exists in the intermediate regime ($\tau_L \approx \tau_{\mathrm{rot}}$), and the time propagation of the molecular ensemble in the presence of the laser pulse has to be performed numerically [33,61]. Especially the quantum mechanical description of three-dimensional alignment [57,59,63] has proved to be numerically expensive [61].

A general theory of x-ray diffraction from laser-aligned symmetric-top molecules was developed in Ref. [52]. Applications to adiabatically aligned molecules may be found in Refs. [52,53]. Reference [40] describes calculations on x-ray scattering from impulsively aligned molecules, exploiting the alignment revivals for probing field-free molecular structure. It has been shown that, for a symmetric-top molecule containing a single heavy scatterer, a holographic algorithm can successfully reconstruct the molecular structure from an x-ray scattering pattern [53].

In this article, we discuss x-ray scattering from an ensemble of rigid, asymmetric-top molecules aligned three-dimensionally by elliptically polarized light at finite rotational

*Corresponding author.

temperature. We point out the symmetries in the quantum mechanical theory of three-dimensionally aligned molecules that can be used to significantly reduce the numerical time propagation. We restrict our analysis to electronic and vibrational ground-state configurations and neglect deformations. Our approach allows us to investigate x-ray diffraction from molecules in all three alignment regimes (adiabatic, impulsive, and intermediate). In order to probe molecular structure of gas-phase molecules by x-ray scattering, the degree of alignment must be rather high for sufficient resolution. This favors the adiabatic alignment approach [43] with low-temperature molecules [25,55]. In Sec. II, we present the theory and inherent symmetries of the Hamiltonian underlying x-ray diffraction from laser-aligned molecules. Section III focuses on the numerical implementation and computational efficiency, and basic ideas are presented of the phase-retrieval algorithm that is used for structure reconstruction. In Sec. IV, the three-dimensional alignment dynamics and their impact on the reconstruction are demonstrated using the example of the organic molecule naphthalene. We conclude with a discussion of the feasibility and limitations of x-ray diffraction from laser-aligned gas-phase molecules. Atomic units [73] are employed throughout, unless otherwise noted.

II. THEORY

The Hamiltonian for x-ray diffraction from laser-aligned molecules is [52]

$$\hat{H}_{\rm tot} = \hat{H}_{\rm rot} + \hat{H}_{\rm XEM} + \hat{H}_{\rm L}(t) + \hat{H}_{\rm X}, \tag{1}$$

where $\hat{H}_{\rm rot}$ describes the field-free rotational motion of a molecule, $\hat{H}_{\rm XEM}$ is the Hamiltonian of the free quantized x-ray fields, and $\hat{H}_{\rm L}(t)$ and $\hat{H}_{\rm X}$ describe the interactions of a molecule with the laser and x-ray field, respectively. The electronic and vibrational states of the molecule are omitted, since we assume that the molecule remains in its electronic and vibrational ground state throughout our discussion. The x-ray field and its interaction with the molecule is described in a quantized manner. The laser field is formulated as a classical field. The eigenstates of the noninteracting system, i.e., $\hat{H}_0 = \hat{H}_{\rm rot} + \hat{H}_{\rm XEM}$, are

$$|J\tau M;\{n\}\rangle = |J\tau M\rangle \otimes |\{n\}\rangle\,, \tag{2}$$

with

$$\hat{H}_{\rm XEM}\,|\{n_i\}\rangle = E^X_{\{n_i\}}\,|\{n_i\}\rangle\,, \tag{3a}$$

$$\hat{H}_{\rm rot}\,|J\tau M\rangle = E^{\rm rot}_{J\tau}\,|J\tau M\rangle\,, \tag{3b}$$

where $|J\tau M\rangle$ are the rotational eigenstates of an asymmetric-top molecule [57,74] and $|\{n\}\rangle$ are the x-ray Fock states [52]. The density matrix of the whole system is

$$\hat{\rho}_{\rm tot} = \sum_{J\tau M}\sum_{\{n_1\},\{n_2\}} \rho^X_{\{n_1\},\{n_2\}}\, w_{J\tau}\, |\Psi_{J\tau M;\{n_1\}}(t)\rangle\langle\Psi_{J\tau M;\{n_2\}}(t)|, \tag{4}$$

where the gas-phase molecules [75,76] are described by a canonical ensemble [77–79], $w_{J\tau}$ is the statistical weight, and $\rho^X_{\{n_1\},\{n_2\}}$ denotes the initial distribution of all the occupied field modes [80,81].

With including both interactions, $\hat{H}_{\rm L}(t)$ and $\hat{H}_{\rm X}$, the states of Eq. (2) are no longer eigenstates of the system. However, each state $|\Psi_{J_0\tau_0M_0;\{n_0\}}(t)\rangle$ can be written as

$$\left|\Psi_{J_0\tau_0M_0;\{n_0\}}(t)\right\rangle = \sum_{J_1\tau_1M_1,\{n_1\}} [C(t)]^{J_1\tau_1M_1;\{n_1\}}_{J_0\tau_0M_0;\{n_0\}}\,|J_1\tau_1M_1;\{n_1\}\rangle\,, \tag{5}$$

where the expansion coefficients $[C(t)]^{J_1\tau_1M_1;\{n_1\}}_{J_0\tau_0M_0;\{n_0\}}$ statisfy the initial condition

$$[C(-\infty)]^{J_1\tau_1M_1;\{n_1\}}_{J_0\tau_0M_0;\{n_0\}} = \delta_{J_0J_1}\delta_{\tau_0\tau_1}\delta_{M_0M_1}\delta_{\{n_0\},\{n_1\}}. \tag{6}$$

The equation of motion for the expansion coefficients in the interaction picture (subscript I) reads

$$\begin{aligned} i\frac{d}{dt}&[C_I(t)]^{J_1\tau_1M_1;\{n_1\}}_{J_0\tau_0M_0;\{n_0\}} \\ &= \sum_{J_2\tau_2M_2,\{n_2\}} \langle J_1\tau_1M_1;\{n_1\}|\,\hat{H}_L(t)+\hat{H}_X\,|J_2\tau_2M_2;\{n_2\}\rangle \\ &\quad\times e^{i(E^{\rm rot}_{J_1\tau_1}-E^{\rm rot}_{J_2\tau_2}+E^X_{\{n_1\}}-E^X_{\{n_2\}})t}\,[C_I(t)]^{J_2\tau_2M_2;\{n_2\}}_{J_0\tau_0M_0;\{n_0\}}. \end{aligned} \tag{7}$$

In the following, we assume we found $[C_{L,I}(t)]^{J_1\tau_1M_1}_{J_0\tau_0M_0}$, the solution for the laser-only problem, i.e., $\hat{H}_{\rm rot}+\hat{H}_{\rm L}(t)$. Note that in the laser-only Hamiltonian no x-ray field is involved and we will drop the x-ray field indices in its solution.

The interaction between the laser-aligned molecules and the x-ray field is taken into account by first-order perturbation theory. The solution of Eq. (7) becomes

$$\begin{aligned} [C_I(t)]^{J_1\tau_1M_1;\{n_1\}}_{J_0\tau_0M_0;\{n_0\}} = -i \sum_{\substack{J_2\tau_2M_2,J_3\tau_3M_3\\ J_4\tau_4M_4}} &[C_{L,I}(t)]^{J_1\tau_1M_1}_{J_4\tau_4M_4}\int_{-\infty}^{t} dt'\, e^{i(E^{\rm rot}_{J_3\tau_3}-E^{\rm rot}_{J_2\tau_2}+E^X_{\{n_1\}}-E^X_{\{n_0\}})t'} \\ &\times \left[C^{-1}_{L,I}(t')\right]^{J_4\tau_4M_4}_{J_3\tau_3M_3}\langle J_3\tau_3M_3;\{n_1\}|\,\hat{H}_X\,|J_2\tau_2M_2;\{n_0\}\rangle\,[C_{L,I}(t')]^{J_2\tau_2M_2}_{J_0\tau_0M_0}. \end{aligned} \tag{8}$$

The expectation values of interest can be calculated by

$$\begin{aligned} \mathcal{O}(t) &= {\rm Tr}[\hat{O}\hat{\rho}_{\rm tot}(t)] \\ &= \sum_{\substack{J\tau M,J_1\tau_1M_1,J'\tau'M'\\ \{n\},\{n_1\},\{n'\},\{n''\}}} w_{J'\tau'}\,\rho^X_{\{n'\},\{n''\}}\,\langle J\tau M;\{n\}|\,\hat{O}\,|J_1\tau_1M_1;\{n_1\}\rangle\, e^{i(E^{\rm rot}_{J\tau}-E^{\rm rot}_{J_1\tau_1}+E^X_{\{n\}}-E^X_{\{n_1\}})t}[C_I(t)]^{J_1\tau_1M_1;\{n_1\}}_{J'\tau'M';\{n'\}}[C^*_I(t)]^{J\tau M;\{n\}}_{J'\tau'M';\{n''\}}, \end{aligned} \tag{9}$$

from which the alignment signals (cf. Sec. II D) and the x-ray scattering probability (cf. Sec. II E) can be derived. We followed here the strategy that is laid out in Ref. [52] for x-ray diffraction from symmetric-top molecules and adapt it to the asymmetric-top case. The structures of $\hat{H}_{XEM}$ and $\hat{H}_X$ are the same for symmetric-top and asymmetric-top molecules. The most dramatic changes for asymmetric-top molecules happen in the laser-only system. Therefore, we focus for the rest of our discussion just on the laser-only system.

In the following subsections the structure of the field-free Hamiltonian $\hat{H}_{\rm rot}$ and the laser–molecule interaction matrix $\hat{H}_L(t)$ will be investigated. For this purpose it is convenient to stay in the Schrödinger picture. In Sec. II C we return to the equation of motion of the laser-only system and point out the symmetries of its solutions $[C_{L,I}(t)]^{J'\tau'M'}_{J\tau M}$. The measure of three-dimensional alignment is described in Sec. II D. The theory section closes with exploiting the symmetries in the angular density distribution and the diffraction signal.

A. Free asymmetric-top rotor

Assuming that structural deformation of the molecule may be neglected, we treat the molecules as rigid rotors. The corresponding field-free Hamiltonian reads [74]

$$\begin{aligned}\hat{H}_{\rm rot} &= A\hat{J}_a^2 + B\hat{J}_b^2 + C\hat{J}_c^2 \\ &= \frac{A+B}{2}\hat{J}^2 + \frac{2C-A-B}{2}\hat{J}_0^2 + \frac{A-B}{2}\left[\hat{J}_{+1}^2 + \hat{J}_{-1}^2\right],\end{aligned} \tag{10}$$

where A,B,C are the rotational constants associated with the principal axes of inertia; $\hat{J}_a,\hat{J}_b,\hat{J}_c$ are the Cartesian components of the angular-momentum operator in the molecular frame; and $\hat{J}_{\pm1},\hat{J}_0$ are the spherical basis components. For symmetric-top ($A = B \neq C$) and asymmetric-top ($A \neq B \neq C, A \neq C$) rotors, the angular momentum J and its projection on the space-fixed z axis, M, are conserved. The angular-momentum projection on the molecular c axis, K, is conserved only for symmetric-top molecules. A new quantum number τ, replacing K, must be introduced for asymmetric-top rotors diagonalizing the field-free Hamiltonian [cf. Eq. (3b)]. Note the rotational energies $E^{\rm rot}_{J\tau}$ are independent of the quantum number M. Hence, each energy level $E^{\rm rot}_{J\tau}$ is $(2J+1)$-fold degenerate. It is possible to express the asymmetric-top eigenstates $|J\tau M\rangle$ as a superposition of the analytically known symmetric-top eigenstates $|JKM\rangle$ [57],

$$|J\tau M\rangle = \sum_K a^{[J]}_{K\tau}\,|JKM\rangle\,, \tag{11}$$

$$\langle\phi,\theta,\chi|JKM\rangle = \sqrt{\frac{2J+1}{8\pi^2}}\,D^{*[J]}_{M,K}(\phi,\theta,\chi), \tag{12}$$

where the coefficients $a^{[J]}_{K\tau}$ are real and ϕ,θ,χ are the three Euler angles connecting the space-fixed laser frame (L) with the principal axes of inertia in the molecular reference frame (M). $D^{*[J]}_{M,K}(\phi,\theta,\chi)$ is the complex conjugate of the Wigner D matrix with angular momentum J. Unfortunately, it is not possible to find a general relation between the τ and K classification [82].

There are two symmetries incorporated between the symmetric-top (K) and asymmetric-top (τ) classification. The first symmetry decouples states with even K from states with odd K, since $\hat{H}_{\rm rot}$ is a linear combination of $\hat{J}^2_{\pm1}$ and $\hat{J}^2_0$ [Eq. (10)]. The state class with even K is labeled E, the one with odd K is labeled O. Asymmetric eigenstates inherit this separation and are superpositions of just even or odd K states. The invariance of $\hat{H}_{\rm rot}$ under the substitutions $M \to -M$ and $K \to -K$ leads to the second symmetry, the Wang symmetry [74,77], where asymmetric-top eigenstates decompose in symmetric and antisymmetric linear combinations,

$$|J\tau M\rangle = \sum_{K\geqslant 0} a^{[J]}_{K\tau}[|JKM\rangle + (-1)^\tau|J(-K)M\rangle], \tag{13}$$

where $(-1)^\tau$ denotes the parity of τ,

$$(-1)^\tau = \begin{cases} +1, & \tau \text{ symmetric in } K, \\ -1, & \tau \text{ antisymmetric in } K. \end{cases} \tag{14}$$

Thus, overall there are four separate state classes, which are summarized in Table I.

TABLE I. Rotational classes of asymmetric-top rotors.

E^+ :	$\lvert J\tau M\rangle = \sum_{K\geqslant 0,K\text{even}} a^{[J]}_{K\tau}[\lvert JKM\rangle + \lvert J(-K)M\rangle]$
E^- :	$\lvert J\tau M\rangle = \sum_{K\geqslant 0,K\text{even}} a^{[J]}_{K\tau}[\lvert JKM\rangle - \lvert J(-K)M\rangle]$
O^+ :	$\lvert J\tau M\rangle = \sum_{K\geqslant 0,K\text{odd}} a^{[J]}_{K\tau}[\lvert JKM\rangle + \lvert J(-K)M\rangle]$
O^- :	$\lvert J\tau M\rangle = \sum_{K\geqslant 0,K\text{odd}} a^{[J]}_{K\tau}[\lvert JKM\rangle - \lvert J(-K)M\rangle]$

With knowing the energy levels of $\hat{H}_{\rm rot}$, it is possible to calculate the laser-only density matrix

$$\hat{\rho}^{\rm mol}(t) = \sum_{J\tau M} w_{J\tau}\,|\Psi_{J\tau M}(t)\rangle\,\langle\Psi_{J\tau M}(t)|\,, \tag{15}$$

with the statistical weights,

$$w_{J\tau} = g_{J\tau}\frac{e^{-E^{\rm rot}_{J\tau}/kT}}{Z(T)}, \tag{16}$$

where $Z(T)$ is the partition function at temperature T and k is the Boltzmann constant. Every state is additionally weighted by the nuclear spin statistical weight $g_{J\tau}$, which represents the number of allowed nuclear spin states for a given rotational state and can be derived from symmetry arguments that have to obey spin statistics [83]. The computation of $g_{J\tau}$ for asymmetric-top molecules and in particular for naphthalene is discussed in Appendix A.

B. Laser-molecule interaction

Three-dimensional alignment may be achieved by using an intense, nonresonant, elliptically polarized laser field,

$$\boldsymbol{E}(t) = \sqrt{8\pi\alpha I(t)}[\epsilon_x\cos(\omega t)\boldsymbol{e}_x + \epsilon_z\sin(\omega t)\boldsymbol{e}_z], \tag{17}$$

where $I(t)$ is the intensity of the laser field, α is the fine structure constant, ω is the laser frequency, and $\boldsymbol{e}_z,\boldsymbol{e}_x$ are the unit vectors of the major and minor polarization directions. The parameters ϵ_x and ϵ_z satisfy $\epsilon_x^2 + \epsilon_z^2 = 1$ and $0 \leqslant \epsilon_x < \epsilon_z$.

The laser-molecule interaction reads [59]

$$\hat{H}_L(t) = -\frac{1}{2}\sum_{i,j\in\{x,y,z\}} \alpha_{ij}^{\mathrm{pol}} U_{ij}(t)$$

$$= -\frac{1}{2}\sum_{J=0}^{2}\sum_{M=-J}^{J} (-1)^{J+M} [\alpha^{\mathrm{pol}}]_M^{[J]_L} U_{-M}^{[J]_L}(t), \quad (18)$$

where α^{pol} is the dipole-polarizability tensor and $U(t) = \boldsymbol{E}(t)\otimes\boldsymbol{E}(t)$ is the electric-field tensor. On the right-hand side of Eq. (18), the interaction is written first as a Cartesian tensor product and then as a spherical tensor product. Only spherical tensor components with $J = 0,2$ are nonzero and contribute to the tensor product, since both tensors are symmetric. (All components with $J = 1$ are zero for symmetric tensors.) The $J = 0$ component shifts all rotational energy levels by a state-independent amount and may therefore be dropped.

The laser period, $2\pi/\omega$, is typically several orders of magnitude smaller than the rotational time scale, $\tau_{\mathrm{rot}} \approx 1/(A+B)$. Cycle averaging leads to a diagonal U_{ij}, and only three spherical components remain nonzero,

$$[U(t)]_0^{[2]_L} = \frac{4\pi\alpha}{\sqrt{6}}\left(2-3\epsilon_x^2\right) I(t), \quad (19a)$$

$$[U(t)]_{\pm2}^{[2]_L}(t) = 2\pi\alpha\epsilon_x^2 I(t). \quad (19b)$$

Hence, only the terms involving $[\alpha^{\mathrm{pol}}]_0^{[2]_L}$ and $[\alpha^{\mathrm{pol}}]_{\pm2}^{[2]_L}$ contribute to the laser-molecule interaction [Eq. (18)]. This holds for any molecule. However, the polarizability α^{pol} is a molecular property and is therefore most conveniently expressed in the molecular reference frame $[\alpha^{\mathrm{pol}}]_K^{[J]_M}$. Wigner D matrices provide the connection to the space-fixed components [59],

$$[\alpha^{\mathrm{pol}}]_M^{[J]_L} = \sum_K D_{M,K}^{*[J]}(\phi,\theta,\chi)[\alpha^{\mathrm{pol}}]_K^{[J]_M}. \quad (20)$$

When the principal axes of the polarizability tensor do not coincide with the principal axes of the moment-of-inertia tensor, the polarizability tensor is not diagonal in the molecular reference frame (cf. Sec. II A) and all $[\alpha^{\mathrm{pol}}]_K^{[J]_M}$ for $J = 0,2$ may be nonzero. We will restrict our discussion to the case where both frames coincide. The remaining tensor components are [59]

$$[\alpha^{\mathrm{pol}}]_0^{[2]_M} = \frac{2\alpha_{cc}^{\mathrm{pol}} - \alpha_{bb}^{\mathrm{pol}} - \alpha_{aa}^{\mathrm{pol}}}{\sqrt{6}}, \quad (21a)$$

$$[\alpha^{\mathrm{pol}}]_{\pm2}^{[2]_M} = \frac{\alpha_{aa}^{\mathrm{pol}} - \alpha_{bb}^{\mathrm{pol}}}{2}. \quad (21b)$$

Using Eqs. (19)–(21), the matrix elements of the laser-molecule interaction operator with respect to the symmetric-top eigenstates read

$$\langle JKM|\hat{H}_L(t)|J'K'M'\rangle = -\frac{1}{2}\sqrt{\frac{2J+1}{2J'+1}}\left([\alpha^{\mathrm{pol}}]_0^{[2]_M}\langle J,K;2,0|J',K'\rangle + [\alpha^{\mathrm{pol}}]_2^{[2]_M}[\langle J,K;2,2|J'K'\rangle + \langle J,K;2,-2|J',K'\rangle]\right)$$
$$\times\left([U(t)]_0^{[2]_L}\langle J,M;2,0|J',M'\rangle + [U(t)]_2^{[2]_L}[\langle J,M;2,-2|J',M'\rangle + \langle J,M;2,2|J',M'\rangle]\right), \quad (22)$$

where the matrix elements of the Wigner D matrices have been expressed in terms of Clebsch-Gordan coefficients [54,74].

Three-dimensional alignment of asymmetric-top molecules conserves neither K nor M. The asymmetric-top rotor breaks the χ symmetry (K conservation), and elliptically polarized light breaks the ϕ symmetry (M conservation). However, there are remaining symmetries in the laser interaction that can be employed,

$$\langle JKM|\hat{H}_L(t)|J'K'M'\rangle$$
$$= 0, \quad K'-K, M'-M \notin \{\pm2,0\}, \quad (23a)$$
$$= (-1)^{J-J'}\langle JK(-M)|\,\hat{H}_L(t)|J'K'(-M')\rangle, \quad (23b)$$
$$= (-1)^{J-J'}\langle J(-K)M|\hat{H}_L(t)\,|J'(-K')M'\rangle. \quad (23c)$$

This follows from properties of the Clebsch-Gordan coefficients [74]. As a result of Eq. (23a), states with even K (M) remain separate from states with odd K (M). The consequences of Eqs. (23b) and (23c) will be discussed in the following sections.

C. Equation of motion

In the laser-only system, the equation of motion [Eq. (7)] for the initially populated state $|JKM\rangle$ reduces to [59]

$$i\frac{d}{dt}[C_{L,I}(t)]_{JKM}^{J'\tau'M'} = \sum_{J_1\tau_1M_1} e^{i[E_{J',\tau'}^{\mathrm{rot}} - E_{J_1,\tau_1}^{\mathrm{rot}}]t}$$
$$\times\langle J'\tau'M'|\hat{H}_L(t)|J_1\tau_1M_1\rangle\,[C_{L,I}(t)]_{JKM}^{J_1\tau_1M_1}, \quad (24)$$

where the interaction matrix elements are expressed in the symmetric-top basis and the symmetries from Eqs. (23) can be used.

The symmetries of the rotational eigenstates $|J\tau M\rangle$ [cf. Eq. (13) and Table I] in combination with the symmetries of $\hat{H}_L(t)$ [cf. Eqs. (23)] pass on to $[C_{L,I}(t)]_{JKM}^{J'K'M'}$ such that

$$[C_{L,I}(t)]_{JKM}^{J'K'M'} = (-1)^{J-J'}[C_{L,I}(t)]_{JK(-M)}^{J'K'(-M')}, \quad (25a)$$
$$= (-1)^{J-J'}[C_{L,I}(t)]_{J(-K)M}^{J'(-K')M'}. \quad (25b)$$

The laser-molecule interaction preserves the separation of even or odd K and M states [cf. Eq. (23a)] but breaks the Wang

symmetry [cf. Eq. (13)]. The indices from the asymmetric-top basis transform to the symmetric-top basis according to

$$[C_{L,I}(t)]^{J'K'M'}_{JKM} = \sum_{\tau,\tau'} a^{[J']}_{\tau' K'} a^{[J]}_{\tau K} [C_{L,I}(t)]^{J'\tau'M'}_{J\tau M}. \quad (26)$$

The symmetric-top representation is especially favorable for the laser-molecules interaction; the field-free propagation is naturally expressed in the asymmetric-top basis.

D. Measure of alignment

The degree of three-dimensional alignment can be characterized in terms of the quantities $\cos^2\theta_{lm}$, where θ_{lm} is the angle between the space-fixed axis l and the body-fixed axis m. The following relations hold among the $\cos^2\theta_{lm}$ [63]:

$$\sum_l \cos^2\theta_{lm_0} = \sum_m \cos^2\theta_{l_0 m} = 1 \quad \forall\, m_0, l_0, \quad (27)$$

where five of the six relations are independent. These relations reduce the number of independent $\cos^2\theta_{lm}$ to 4. The matrix elements $\langle JKM|\cos^2\theta_{lm}|J'K'M'\rangle$ of one set of independent $\cos^2\theta_{lm}$ ($l \in \{x,z\}, m \in \{a,c\}$) are given in Appendix B. The symmetries of $\cos^2\theta_{lm}$ are the same as for $\hat{H}_L(t)$,

$$\begin{aligned}
&\langle JKM|\cos^2\theta_{lm}|J'K'M'\rangle \\
&\quad = 0, \quad K'-K, M'-M \notin \{\pm 2, 0\}, && (28a)\\
&\quad = (-1)^{J-J'}\langle JK(-M)|\cos^2\theta_{lm}|J'K'(-M')\rangle, && (28b)\\
&\quad = (-1)^{J-J'}\langle J(-K)M|\cos^2\theta_{lm}|J'(-K')M'\rangle. && (28c)
\end{aligned}$$

The restriction imposed on $K'-K$ by Eq. (28a) makes it attractive to store the matrix elements of $\cos^2\theta_{lm}$ in the symmetric-top basis; the same is true for $\hat{H}_L(t)$.

The ensemble-averaged expectation values at time t are

$$\langle\cos^2\theta_{lm}\rangle(t) = \sum_{J\tau M} w_{J\tau}\langle\cos^2\theta_{lm}\rangle_{J\tau M}(t), \quad (29a)$$

$$\begin{aligned}
\langle\cos^2\theta_{lm}\rangle_{J\tau M}(t) = &\sum_{J_1K_1M_1}\sum_{J_2K_2M_2}\langle J_1K_1M_1|\cos^2\theta_{lm}|J_2K_2M_2\rangle \\
&\times [C_L(t)]^{J_2K_2M_2}_{J\tau M}[C^*_L(t)]^{J_1K_1M_1}_{J\tau M} \quad (29b)
\end{aligned}$$

with

$$[C_L(t)]^{J'K'M'}_{J\tau M} = \sum_{\tau'} a^{[J']}_{\tau' K'} e^{-iE^{\rm rot}_{J',\tau'}t}[C_{L,I}(t)]^{J'\tau'M'}_{J\tau M}. \quad (30)$$

Making use of the symmetries in Eqs. (25) and (28), each $\langle\cos^2\theta_{lm}\rangle_{JKM}(t)$ fulfills the relations

$$\langle\cos^2\theta_{lm}\rangle_{J\tau M}(t) = \langle\cos^2\theta_{lm}\rangle_{J\tau(-M)}(t). \quad (31)$$

E. Angular probability distribution

For the calculation of the x-ray scattering probability $\frac{dP}{d\Omega}$ the solution for the full Hamiltonian [Eq. (1)] has to be known. The laser-only problem is solved as described in Sec. II C. The x-ray interaction is treated in first-order perturbation theory as indicated in Eq. (8). Furthermore, the following assumptions of the x-ray pulse are made: (1) The coherence time of the x-ray pulse is significantly larger as the rotational time scale of the molecules. (2) The bandwidth of the x-ray pulse is much larger than any rotational transition energy. (3) The angular spread of the x-ray pulse is considerably small. In Ref. [52], the detailed derivation of $\frac{dP}{d\Omega}$ is given with the final result

$$\frac{dP}{d\Omega} = \frac{d\sigma_{\rm th}}{d\Omega} S(\boldsymbol{Q}), \quad (32)$$

where $d\sigma_{\rm th}/d\Omega$ is the Thomson scattering cross section,

$$\begin{aligned}
S(\boldsymbol{Q}) = &\int_{-\infty}^{\infty} dt\; j_X(t) \iiint d\phi\, d\theta\, d\chi\, \sin\theta \\
&\times \rho(\phi,\theta,\chi;t)\,|F_{\rm mol}(\boldsymbol{Q},\phi,\theta,\chi)|^2 \quad (33)
\end{aligned}$$

is the diffraction signal, and $j_X(t)$ is the x-ray flux. The molecular information in the diffraction signal is contained in the molecular form factor,

$$F_{\rm mol}(\boldsymbol{Q},\phi,\theta,\chi) = \int d^3r_M\; \rho(\boldsymbol{r}_M)\, e^{-i\,\boldsymbol{Q}[\boldsymbol{R}(\phi,\theta,\chi)\boldsymbol{r}_M]} \quad (34)$$

which is a function of the molecular orientation, i.e., Euler angles, and the momentum transfer $\boldsymbol{Q}$ given in the space-fixed frame (L). The integration d^3r_M is done in the molecular rest frame (M) with $\rho(\boldsymbol{r}_M)$ being the electron density of the molecule. The rotation matrix $\boldsymbol{R}(\phi,\theta,\chi)$ transforms the vector $\boldsymbol{r}_M$ into the space-fixed frame. The angular probability distribution,

$$\rho(\phi,\theta,\chi;t) = \sum_{J\tau M} w_{J\tau}|\langle\phi,\theta,\chi|\Psi_{J\tau M}(t)\rangle|^2, \quad (35)$$

is linked to the Wigner D matrices $D^{[J]}_{M,K}(\phi,\theta,\chi)$ through Eqs. (11) and (12).

From the fact that the molecules are aligned rather than oriented, symmetries additional to the ones of $D^{[J]}_{M,K}(\phi,\theta,\chi)$ [84] enter into $\rho(\phi,\theta,\chi;t)$. These additional symmetries originate from Eqs. (25) and the separation of the rotational classes $E^{\pm}$ and $O^{\pm}$ throughout the alignment process (cf. Sec. II B). In terms of Euler angels, the symmetries of $\rho(\phi,\theta,\chi;t)$ are:

$$\begin{aligned}
&\rho(\phi,\theta,\chi;t) \\
&\quad = \rho(\phi+\pi,\theta,\chi;t) = \rho(-\phi,\pi-\theta,\chi+\pi;t), && (36a)\\
&\quad = \rho(\phi,\theta,\chi+\pi;t) = \rho(\phi+\pi,\pi-\theta,-\chi;t). && (36b)
\end{aligned}$$

The first two symmetries [Eq. (36a)] correspond to C_2 rotations about the space-fixed axes z and x, respectively. The last two symmetries [Eq. (36b)] correspond to C_2 rotations about the body-fixed axes c and a, respectively. In Eq. (34), these symmetries translate into a replacement of $\boldsymbol{R}(\phi,\theta,\chi)$ by $\boldsymbol{C}_{2,x/z}\boldsymbol{R}(\phi,\theta,\chi)$ and $\boldsymbol{R}(\phi,\theta,\chi)\boldsymbol{C}_{2,a/c}$, respectively. By letting the $\boldsymbol{C}_{2,x/z}$ rotations act on $\boldsymbol{Q}$ rather than on $\boldsymbol{r}_M$, the $S(\boldsymbol{Q})$ symmetries are found,

$$\begin{aligned}
S(Q_x,Q_y,Q_z) &= S(-Q_x,Q_y,Q_z), && (37a)\\
&= S(Q_x,-Q_y,Q_z), && (37b)\\
&= S(Q_x,Q_y,-Q_z). && (37c)
\end{aligned}$$

Additionally, the Friedel law [85], i.e., $F^*(\boldsymbol{Q}) = F(-\boldsymbol{Q}) \Rightarrow S(\boldsymbol{Q}) = S(-\boldsymbol{Q})$, has been used. The symmetries of Eq. (36b) can be used to reduce the integration range of the Euler angles in Eq. (33) but only the symmetries of Eq. (36a) survive the integration, which are expressed in Cartesian coordinates in Eqs. (37). Regardless of their internal structure, Eqs. (37) hold for all aligned molecules. Note that alignment does

not distinguish between parallel and antiparallel orientations. Thus, even for perfect alignment, i.e., $\phi = \theta = \chi = 0$, four distinct molecular orientations contribute incoherently to the diffraction signal $S(\boldsymbol{Q})$ [19].

III. NUMERICAL METHODS

Earlier work has addressed the problem of numerical efficiency in the computational treatment of three-dimensional alignment of asymmetric-top molecules [61]. In Sec. III A, we describe numerical techniques and symmetry arguments we have implemented to decrease the numerical effort. As far as we are aware, these specific points have not been discussed earlier in the literature. In Sec. III B, we explain the phase-retrieval method we employ to reconstruct molecular structures from x-ray scattering patterns.

A. Alignment dynamics

The density matrix of a canonical ensemble is a sum of density matrices $|J\tau M\rangle\, w_{J\tau}\, \langle J\tau M|$ [cf. Eq. (15)]. Analogously, all observables can be written as a sum of independent contributions, which may be calculated separately. This was shown for $\langle\cos^2\theta_{lm}\rangle$ [Eq. (29)] and $\rho(\phi,\theta,\chi;t)$ [Eq. (35)]. Each contribution has a well-defined behavior under the substitution $M \to -M$, which can be used to avoid the calculation of $|\Psi_{J\tau M}(t)\rangle$ for $M < 0$. The same is true for the quantum number K, but unfortunately K is not a good quantum number for asymmetric-top molecules, and the wave function $|\Psi_{J\tau M}(t)\rangle$ has to be known to calculate the expectation values. However, $|\Psi_{J\tau M}(t)\rangle$ can be written as a superposition of $|\Psi_{JKM}(t)\rangle$ [cf. Eq. (11)], and by using the same argument as for M, only $|\Psi_{JKM}(t)\rangle$ for $K \geqslant 0$ are necessary to build all $|\Psi_{J\tau M}(t)\rangle$ [cf. Eq. (13)]. This makes it attractive to propagate $|\Psi_{JKM}(t)\rangle$ rather than $|\Psi_{J\tau M}(t)\rangle$. Taking both symmetries together only the states $|\Psi_{JKM}(t)\rangle$ for $0 \leqslant K,M \leqslant J$ have to be propagated to understand the full system response, which can save up to a factor 4 in computational effort.

The decoupling between even and odd K/τ states and M states also enhances efficiency and does not get destroyed by the presence of the interaction $\hat{H}_L(t)$. Therefore, many $[C_L(t)]^{J'\tau'M'}_{JKM}$ remain zero throughout the alignment process. This holds for symmetric-top as good as for asymmetric-top rotors, since each $|J\tau M\rangle$ can be classified into the class $E^{\pm}$ or $O^{\pm}$ (cf. Sec. II A). The benefit is not just a speed-up by a factor 4; also the memory requirement to store $[C_L(t)]^{J'\tau'M'}_{JKM}$, the matrix $\hat{H}_L(t)$, and the matrices $\cos^2\theta_{lm}$ is reduced by a factor 4. Memory size can become an issue on PCs when high J states are not negligible.

A significant time factor in the calculation, besides the time propagation, is the computation of $\rho(\phi,\theta,\chi;t)$. By employing all symmetries described in Eq. (36), the range of Euler angles with nonredundant information is reduced by a factor of 16 compared to the entire domain of Euler angles.

Besides the physical symmetries that can be retrieved from the Hamiltonian, there are two numerical aspects that may improve the propagation speed. First, the numerical time propagation is commonly done by the fourth-order Runge-Kutta method, where it is important that the change in the wave function per propagation step is small and stays in the convergent region [86]. Yet too small step sizes quickly lead to numerical inefficiency. For our problem the change in $[C_L(t)]^{J'\tau'M'}_{JKM}$ is directly proportional to the product $I(t)dt$, where dt is the propagation time step. With decreasing $I(t)$, dt can be chosen larger without leaving the convergent region. Variable step sizes are, therefore, important and improve the propagation efficiency further. Numerical tests have shown that the optimized program runs faster by a factor between 3 and 4, where we assumed a Gaussian laser pulse centered at t_0 with a full width at half maximum of τ_L. Outside of the laser pulse, i.e., $t \notin [t_0 - 3\tau_L, t_0 + 3\tau_L]$, the molecules are treated as field-free, and the propagation is performed analytically.

The second improvement takes place at the equation of motion [Eq. (24)]. To solve the equation numerically, it has to be discretized in time. We chose the fourth-order Runge-Kutta method as our discretization method. Only the contribution of $\hat{H}_L(t)$ is approximated when the discretization in time in the equation of motion is made in the interaction picture. The time propagation of $\hat{H}_{\text{rot}}$ is analytically exact such that in the field-free case the numerically calculated solution matches the analytical result. To improve the efficiency in solving the equation of motion, we reduce the need for repeated calculating of $e^{i(E^{\text{rot}}_j - E^{\text{rot}}_i)t}$, which goes with N^2 for the propagation of all $[C_{L,I}(t)]^{J'\tau'M'}_{JKM}$, where N is the number of rotational states involved in the propagation. The evaluation of exponential functions does not occur when the equation of motion is discretized in the Schrödinger picture [27,28,57]. As a consequence, the propagation of the field-free part is now discretized, which has two major limitations: (1) the field-free propagation is not exact even in the field-free case, where the analytic solution is known, and (2) the propagation step size depends, in addition to the laser-molecule interaction strength, on the highest rotational energy $E^{\text{rot}}_{J\tau}$. In order to use the advantages of both pictures, we discretize the equation of motion in the interaction picture and transform it afterwards back into the Schrödinger picture by reformulating the propagation in terms of $[C_L(t)]^{J'\tau'M'}_{JKM}$. The final discretized equation of motion is:

$$[C_L(t+dt)]^j_i = e^{-2i\varphi_j}[C_L(t)]^j_i + dt\,\frac{e^{-2i\varphi_j}[D^{(1)}]^j_i + 2e^{-i\varphi_j}[D^{(2)}]^j_i + 2e^{-i\varphi_j}[D^{(3)}]^j_i + [D^{(4)}]^j_i}{6}, \tag{38}$$

$$[D^{(a)}]^j_i = -i\sum_k [H_L(t)]^j_k \big[\tilde{C}^{(a)}_L\big]^k_i, \quad a = 1,2,3,4, \tag{39}$$

where the indices i,j,k are shortcuts for the sets of asymmetric-top quantum numbers, $[H_L(t)]_i^j = \langle j|\hat{H}_L(t)|i\rangle$, $e^{-iE_j^{\rm rot}dt/2} = e^{-i\varphi_j}$, and intermediate solutions are

$$\left[\tilde{C}_L^{(1)}\right]_i^j = [C_L(t)]_i^j, \tag{40a}$$

$$\left[\tilde{C}_L^{(2)}\right]_i^j = e^{-i\varphi_j}\left[\tilde{C}_L^{(1)}\right]_i^j + \frac{dt}{2}e^{-i\varphi_j}[D^{(1)}]_i^j, \tag{40b}$$

$$\left[\tilde{C}_L^{(3)}\right]_i^j = e^{-i\varphi_j}\left[\tilde{C}_L^{(1)}\right]_i^j + \frac{dt}{2}[D^{(2)}]_i^j, \tag{40c}$$

$$\left[\tilde{C}_L^{(4)}\right]_i^j = e^{-2i\varphi_j}\left[\tilde{C}_L^{(1)}\right]_i^j + \frac{dt}{2}e^{-i\varphi_j}[D^{(3)}]_i^j. \tag{40d}$$

Since $e^{-i\varphi_j}$ depends only on dt and not on the time t itself, it needs to be evaluated only once at the beginning of the propagation. During the time propagation, the evaluation of the exponential function is not necessary as long as dt does not change. In our simulations, we gained a factor 2 to 5 depending on the simulation parameters, when we employed Eqs. (38)–(40). Note, in the field-free limit the time propagation in Eq. (38) is analytically exact.

Overall, the use of the symmetries and numerical techniques described allows us to simulate three-dimensional alignment of asymmetric-top molecules from the impulsive to the adiabatic regime up to two orders of magnitude faster. In the case of quasiadiabatic alignment of naphthalene at 1 K, the total computation time was 2457 h (41 days) with a PC (CPU: 3 GHz). The calculation of $S(\boldsymbol{Q})$ took approximately 8% of the total time (ϕ,θ,χ,t-grid points: $25\times30\times30\times11$). Without exploiting the symmetries for the Euler angles, this calculation would be almost 1.5 times longer than the time propagation itself. A detailed list of the physical parameters used for the computations is given in Sec. IV.

B. Phase-retrieval algorithm

For imperfectly aligned molecules, the diffraction pattern is an incoherent average of single-molecule diffraction patterns of different orientations. In the limit that a high degree of molecular alignment is attained, the obtained pattern can be approximated as a single-molecule coherent diffraction pattern. (This is true for naphthalene, since orientation and alignment are equivalent for this molecule.) One may thus retrieve structural information from the single-molecule electron density map, which is the Fourier transform of the single-molecule scattering form factor, $F(\boldsymbol{Q})$. Since the diffraction pattern provides only $|F(\boldsymbol{Q})|$, we need to obtain the associated phase before we can recover the molecular structure. There are iterative numerical algorithms that permit reconstructing the phase directly from the intensity data [17,18,87–101]. These algorithms require intensity data sampled at twice the Nyquist frequency. Successful structural reconstruction using these algorithms has been demonstrated with experimental data [7,12,102–110].

Here we use the hybrid-input-output (HIO) algorithm [89–91], which involves iterative Fourier transformation back and forth between the object and Fourier domains. A solution is found when the known constraints are satisfied in both domains. We begin by obtaining an initial estimate of the object electronic density via an inverse Fourier transformation of the form factor, $F(\boldsymbol{Q}) = |F(\boldsymbol{Q})|e^{i\phi_{\boldsymbol{Q}}}$, which is obtained by assigning a random phase, $\phi_{\boldsymbol{Q}}$, to the measured modulus, $|F(\boldsymbol{Q})|$. The random phase $\phi_{\boldsymbol{Q}}$ is chosen such that Friedel's law, $F^*(\boldsymbol{Q}) = F(-\boldsymbol{Q})$, is satisfied. With this estimate, we initiate an iterative four-step algorithm, in which the k-th iteration is given as follows:

(i) Fourier transform of the object electron density, $\rho_k(\mathbf{r})$, to obtain $F_k(\boldsymbol{Q})$.

(ii) A Fourier domain operation (FDO) is applied to $F_k(\boldsymbol{Q})$ to obtain $F'_k(\boldsymbol{Q})$ that satisfies the Fourier constraint. In our FDO, the modulus of $F'_k(\boldsymbol{Q})$ is set to be the measured modulus, $|F(\boldsymbol{Q})|$, and the phase of $F'_k(\boldsymbol{Q})$ is the phase of $F_k(\boldsymbol{Q})$.

(iii) Inverse Fourier transform of $F'_k(\boldsymbol{Q})$ to give $\rho'_k(\boldsymbol{r})$.

(iv) An object domain operation (ODO) is applied to $\rho'_k(\boldsymbol{r})$ to get a new estimate of the object electron density, $\rho_{k+1}(\boldsymbol{r})$, that satisfies the object constraint. Our ODO is given as

$$\rho_{k+1}(\boldsymbol{r}) = \begin{cases} \rho'_k(\boldsymbol{r}), & \text{for } \boldsymbol{r}\in\mathcal{S} \text{ and } \rho'_k(\boldsymbol{r}) \geqslant 0 \\ \rho_k(\boldsymbol{r}) - \beta\rho'_k(\boldsymbol{r}), & \text{otherwise,} \end{cases} \tag{41}$$

where β is chosen to be 0.9 [93,98,100] and $\mathcal{S}$ is a predefined support of the object.

In order to obtain a correctly reconstructed object, a support $\mathcal{S}$ of good quality is needed [91]. In our algorithm, the support $\mathcal{S}$ is changed dynamically throughout the HIO algorithm via the Shrink-wrap (SW) procedure [93]. The inverse Fourier transform of the scattering intensity, $|F(\boldsymbol{Q})|^2$, equals the autocorrelation function of $\rho(\mathbf{r})$. Treating the autocorrelation function as a distribution function, the initial $\mathcal{S}$ is chosen as a region centered at the mean of the autocorrelation function with a spatial extension of two standard deviations. This choice of $\mathcal{S}$ is fixed during the first 2000 iterations before applying the SW procedure periodically after every 200 iterations of the HIO algorithm to obtain a new $\mathcal{S}$. In the SW procedure, the modulus of the object, $|\rho_k(\boldsymbol{r})|$, is convolved with a Gaussian of width σ. The new $\mathcal{S}$ is then selected as the region for which the value of the convolved function is above a threshold of 20% of its maximum [93]. The initial width of the Gaussian is chosen to be 2.5 Å and is shrunk linearly to a minimum of 0.25 Å after 400 iterations of the SW procedure. Using the last updated $\mathcal{S}$, an additional 200 iterations of the HIO algorithm are performed.

Figure 1 illustrates the application of the phase-retrieval algorithm described to an x-ray scattering pattern calculated for perfectly aligned naphthalene molecules with one set of initial random phases. X-ray scattering patterns in this article are based on the assumption that the molecular electron density equals the sum over spherically averaged atomic electron densities [85]. Only the carbon atoms are visible in the reconstruction in Fig. 1(b), since x-ray scattering from carbon is much stronger than x-ray scattering from hydrogen.

Note that the real-space pixel size in each dimension is given by $\pi/Q_{\rm max}$, where $Q_{\rm max}$ is the maximum momentum transfer for which diffraction data are available. In the case of perfect alignment, the real-space resolution, $d_{\rm res}$, attained from the reconstruction is two times the real-space pixel size. (In Fig. 1, $d_{\rm res} = 0.25$ Å.) However, in the case of imperfect molecular alignment, $d_{\rm res}$ depends on $Q_{\rm max}$ and $Q_{\rm coh}$, where $Q_{\rm coh}$ is the range of useful diffraction data for which the assumption of coherent scattering holds and the effect of incoherent averaging

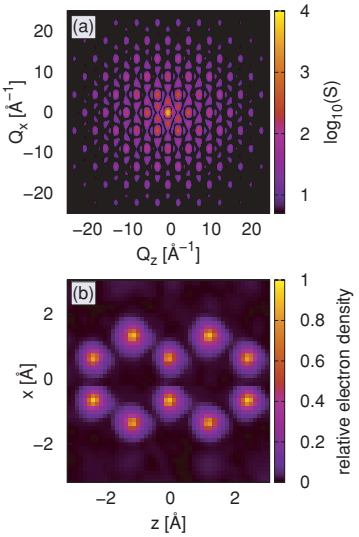

FIG. 1. (Color online) (a) The diffraction signal $S(Q_y = 0)$ for naphthalene perfectly aligned in the xz plane. The spatial resolution is 0.25 Å. $S(0) = 68^2$ is the number of electrons squared. (b) The reconstructed structure.

is small. In fact, we find that including diffraction data beyond Q_{coh} can diminish the quality of the reconstructed object.

IV. RESULTS

In this section, we present numerical results based on the theory and the numerical strategies summarized in Secs. II and III. We demonstrate quasiadiabatic, three-dimensional alignment of the organic molecule naphthalene ($C_{10}H_8$). The experimental parameters that we are using are based on previous work [56]. X-ray energies and fluxes that are used in our discussion are accessible at the Advanced Photon Source at Argonne National Laboratory.

After investigating the alignment dynamics, we focus on the diffraction signal and structure reconstruction. The rotational temperature and the x-ray pulse duration impact the effective alignment and limit the structural information stored in the x-ray scattering pattern. A phase-retrieval algorithm is used to reconstruct the structure. In this context, the degree of alignment and its impact on the spatial resolution are discussed.

A. Three-dimensional alignment

Naphthalene is a planar molecule. The molecular reference frame is chosen such that all atoms lie in the ac plane and the b axis is perpendicular to it. The choice of axes as well as the structure of naphthalene are shown in Fig. 2. The rotational constants of naphthalene are $A = 0.041$ cm^{-1}, $B = 0.029$ cm^{-1}, and $C = 0.104$ cm^{-1} [111].[1] The polarizability constants are $\alpha_{aa}^{\text{pol}} = 121.4a_0^3$, $\alpha_{bb}^{\text{pol}} = 63.2a_0^3$, and $\alpha_{cc}^{\text{pol}} = 163.9a_0^3$ [112]. The nuclear spin statistical weights $g_{J\tau}$ for naphthalene are given in Table II. (We assume that the carbon nuclei are ^{12}C isotopes, and the hydrogen nuclei are protons.) The derivation of $g_{J\tau}$ is outlined in Appendix A.

[1] In contrast to spectroscopic convention, the rotational constants A, B and C are not ordered according to magnitude. We reorder the rotational constants such that for perfect alignment the molecular frame (a,b,c) coincides with the space-fixed frame (x,y,z).

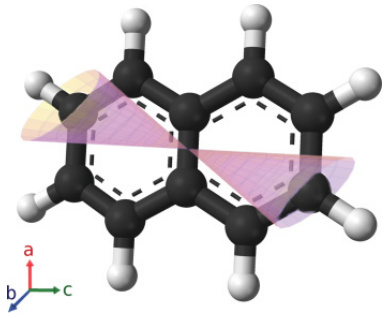

FIG. 2. (Color online) The structure of naphthalene ($C_{10}H_8$). All atoms lie in the ac plane of the body-fixed reference frame. The coordinate system is shown in the lower left corner. The cones symbolize the resolution limit of the carbon atoms due to imperfect alignment.

Three-dimensional alignment of naphthalene is obtained by employing elliptically polarized light. The z and x axes of the space-fixed frame are defined by the major and minor axes, respectively, of the ellipse that characterizes the elliptically polarized light. Following Ref. [63], we choose the ratio between the field components using

$$\frac{\epsilon_x^2}{\epsilon_z^2} = \frac{\alpha_{cc}^{\text{pol}} - \alpha_{aa}^{\text{pol}}}{\alpha_{cc}^{\text{pol}} - \alpha_{bb}^{\text{pol}}} = 0.422, \tag{42}$$

which maximizes the three-dimensional alignment of naphthalene. Perfect three-dimensional alignment with respect to the space-fixed frame is achieved when $\langle\cos^2\theta_{xa}\rangle = \langle\cos^2\theta_{yb}\rangle = \langle\cos^2\theta_{zc}\rangle = 1$. Random orientation corresponds to $\langle\cos^2\theta_{lm}\rangle = 1/3$ for all angles.

The typical distance between two neighboring carbon atoms in naphthalene is 1.4 Å. In order to resolve the atomic structure, the resolution must be smaller than this value. Imperfect alignment limits the resolution. To build a connection between the resolution and the alignment in terms of $\langle\cos^2\theta_{lm}\rangle$, it is helpful to view the angle θ_{lm} as an opening angle within which the residual motion of the atoms takes place (cf. Fig. 2). Hence, the length characterizing the smallest resolvable structure is

$$d_{\text{coh}} \approx 2R\sqrt{1 - \langle\cos^2\theta_{lm}\rangle}, \tag{43}$$

where R is the linear dimension of the molecule (measured from the center of mass of the molecule). The degree of

TABLE II. The nuclear spin statistical weights $g_{J\tau}$ of naphthalene classified by the rotational symmetry classes.

Rotation class	E^+	E^-	O^+	O^-
$g_{J\tau}$ (J even)	76	60	60	60
$g_{J\tau}$ (J odd)	60	76	60	60

alignment needed for a resolution of 1 Å for the outermost carbon atom ($R = 2.5$ Å) is $\langle\cos^2\theta_{lm}\rangle = 0.96$. For a given resolution, smaller opening angles θ_{lm} are required when the molecules become larger. In the adiabatic regime at sufficiently low temperature the maximum alignment for a linear rotor ($A = B, C = 0$) is given by $\langle\cos^2\theta_{zc}\rangle = 1 - \sqrt{4B/\gamma}, \gamma = \sqrt{96\pi}\alpha I[\alpha^{\rm pol}]_0^{[2]}$ [32,33]. The polarizability $[\alpha^{\rm pol}]_0^{[2]}$ is approximately proportional to R^3, and B scales approximately as R^{-5} [19,40]. The smallest resolvable dimension $d_{\rm coh}$ is thus proportional to $1/R$ and might be expected to decrease with increasing molecular size. Note, however, that the temperature required to suppress thermal effects ($kT/B \ll 1$) also decreases as a function of the molecular size. Additionally, in order to remain in the adiabatic regime, the laser pulse duration must increase with increasing molecular size. In practice this means the laser intensity will decrease. For large molecules it is more realistic to consider the high temperature limit ($kT/B \gg 1$), where the degree of alignment is a competitive interplay between rotational temperature and coupling strength γ; more precisely, $\langle\cos^2\theta_{zc}\rangle = 1 - \sqrt{\pi kT/\gamma}$ [25,33]. By using the same scaling arguments, we find $d_{\rm coh} \propto \sqrt[4]{kTR}$. The expected resolution is now reversed and increases with molecular size and rotational temperature. Consequently, larger molecules can be resolved less precisely.

In Fig. 3, the alignment dynamics of naphthalene at 10 mK and 1 K, respectively, are shown. We assumed a Gaussian laser pulse with a peak intensity of $I = 5$ TW/cm^2 and a pulse duration of $\tau_L = 100$ ps (FWHM). At a rotational temperature of $T = 10$ mK, almost all naphthalene molecules are in the rotational ground state. The rotational period of naphthalene at such a low temperature, $\tau_{\rm rot} \approx 1/(A + B) \approx 476$ ps, is of the order of $\tau_L = 100$ ps, suggesting that the alignment dynamics are quasiadiabatic [55]. This is consistent with the observation that the overall alignment follows the laser pulse shape and, in addition, clear nonadiabatic features (fast oscillations) are visible. One can make use of the nonadiabatic behavior by probing the molecules with an x-ray pulse of 1 ps duration, which is fast enough to resolve the nonadiabatic oscillations. For instance, at $t = 20.75$ ps the alignment is transiently enhanced in all three dimensions (cf. Fig. 3). At $T = 1$ K, the rotational period of naphthalene is small in comparison to τ_L, so the alignment dynamics are adiabatic and fast oscillations are significantly suppressed. As a consequence of the increased thermal motion, the maximum degree of alignment at $T = 1$ K is clearly reduced.

The diffraction signal $S(\boldsymbol{Q})$ [cf. Eq. (33)] collected over the x-ray pulse duration reflects a pulse-averaged, effective alignment

$$\langle\cos^2\theta_{lm}\rangle_{\rm eff} = \int dt\ \bar{j}_X(t)\langle\cos^2\theta_{lm}\rangle(t), \qquad (44)$$

where $\bar{j}_X(t)$ is the normalized x-ray flux. We assume a Gaussian temporal envelope for the x-ray pulse, with a full width at half maximum of τ_X. In Fig. 4, $\langle\cos^2\theta_{lm}\rangle_{\rm eff}$ is shown as a function of τ_X. We may conclude from Fig. 4 that the effective alignment of the body-fixed axes decreases rapidly when the x-ray pulse duration is longer than the laser pulse duration. An enhancement in the effective alignment is visible

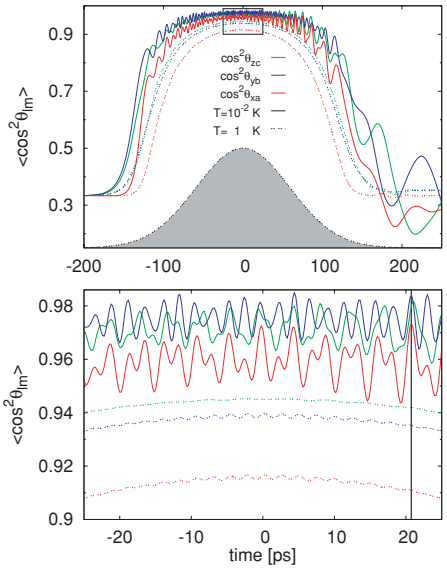

FIG. 3. (Color online) Alignment dynamics of three axes of naphthalene at rotational temperatures $T = 10$ mK (solid) and $T = 1$ K (dotted). The pump laser shown in gray has a peak intensity of $I = 5$ TW/cm^2, a width of $\tau_L = 100$ ps, and an ellipticity of $\epsilon_x^2/\epsilon_z^2 = 0.422$. The upper panel pictures the alignment dynamics on the time scale of the pulse duration. The lower panel is a close-up view of the region highlighted in the upper graph. At $t = 20.75$ ps, nonadiabatic oscillation enhances the alignment for all axes at $T = 10$ mK and is ideal for a 1-ps x-ray probe pulse.

for $\tau_X \approx 1$ ps at $T = 10$ mK, where nonadiabatic oscillations are not suppressed and can be resolved by the x-ray pulse.

When $\tau_X \lesssim \tau_L$, the influence of τ_X is rather weak and the degree of alignment is mainly affected by the rotational temperature, T. Figure 5 shows the effective alignment of the molecular axes as a function of T for $\tau_X = 1$ ps and $\tau_X = 100$ ps. Below 0.25 K, the best aligned axis is the body-fixed

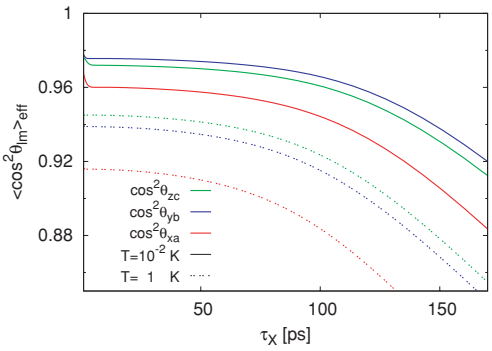

FIG. 4. (Color online) The effective alignment of the body-fixed axes is shown as a function of the x-ray pulse duration, τ_X, for $T = 10$ mK (solid) and $T = 1$ K (dotted). The pump laser has a peak intensity of $I = 5$ TW/cm^2, a width of $\tau_L = 100$ ps, and an ellipticity of $\epsilon_x^2/\epsilon_z^2 = 0.422$. The x-ray pulses are centered at $t = 0$ ps.

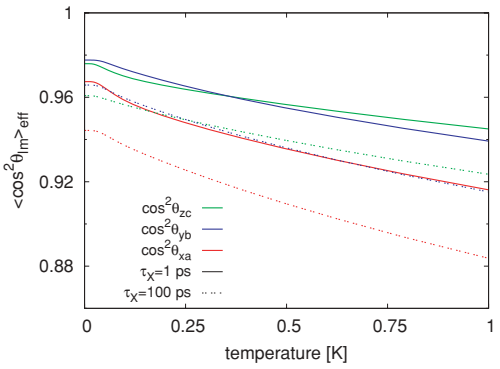

FIG. 5. (Color online) The effective alignment of the body-fixed axes is shown as a function of the rotational temperature for $\tau_X = 1$ ps (solid) and $\tau_X = 100$ ps (dotted). The pump laser has a peak intensity of $I = 5$ TW/cm^2, a width of $\tau_L = 100$ ps, and an ellipticity of $\epsilon_x^2/\epsilon_z^2 = 0.422$. The x-ray pulses are centered at $t = 0$ ps.

b axis in the space-fixed y direction for $\tau_X \leqslant 100$ ps, despite the fact that no laser field is applied in this direction. The strong alignment of the b axis translates to well-aligned naphthalene molecules in the polarization plane of the laser (xz plane). Within the plane, the body-fixed c axis is always more strongly aligned in the z direction than the a axis is aligned in the x direction. (Recall that $\alpha_{cc}^{\rm pol} > \alpha_{aa}^{\rm pol}$ and $\epsilon_z > \epsilon_x$.) For higher temperatures, the body-fixed c axis is the most strongly aligned axis, since the alignment of the b axis is affected by the more rapidly decreasing alignment of the a axis.

As may be seen in Fig. 4, the effective alignment $\langle\cos^2\theta\rangle_{\rm eff}$ of all molecular axes is at least 0.96 for 10 mK naphthalene molecules probed by x-ray pulses shorter than ~20 ps. Hence, the smallest resolvable dimension limited by residual pendular motion is $d_{\rm coh} = 1$ Å. Only the rotational ground state is initially occupied, and the minimum intensity required to accomplish 1 Å resolution is $I = 5$ TW/cm^2. Dissociation and ionization play only a minor role at this intensity but become important at higher intensities [113]. With an effective alignment of $\langle\cos^2\theta_{xa}\rangle_{\rm eff} = 0.88$ at 1 K and $\tau_X = 100$ ps, the smallest resolvable dimension $d_{\rm coh}$ is 1.73 Å, which is larger than the distance between neighboring carbon atoms.

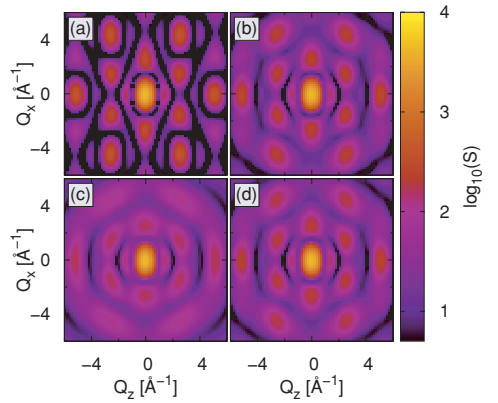

FIG. 6. (Color online) X-ray diffraction signal $S(Q_y = 0)$ of naphthalene. (a) Perfect alignment. (b) $T = 10$ mK, $\tau_X = 1$ ps, x-ray pulse centered at $t = 20.75$ ps (cf. Fig. 3). (c) $T = 1$ K, $\tau_x = 100$ ps, x-ray pulse centered at $t = 0$ ps. (d) $T = 10$ mK, $\tau_X = 100$ ps, x-ray pulse centered at $t = 0$ ps. For the alignment pulses in (b), (c), and (d), we assumed $I = 5$ TW/cm^2 and $\tau_L = 100$ ps.

B. X-ray diffraction patterns

In Fig. 6, diffraction patterns $S(\boldsymbol{Q})$ of three-dimensionally aligned naphthalene are shown for perfect alignment as well as for imperfect alignment at different temperatures and x-ray pulse widths. The laser parameters are the same as for Fig. 3. The laser polarization plane is assumed to be the xz plane so that the molecules are aligned as illustrated in Fig. 2. The diffraction patterns in Fig. 6 are two-dimensional planar slices through the three-dimensional $\boldsymbol{Q}$ space, taken at $Q_y = 0$. (Due to the curvature of the Ewald sphere [85], experimental scattering patterns do not correspond to exactly planar slices through $\boldsymbol{Q}$ space, but this is of no consequence here.) The signal strength falls rapidly for high Q. Therefore, to highlight the structure at high momentum transfers, the scattering intensities are shown on a logarithmic scale. The effective alignment in Fig. 6 decreases clockwise, from $\langle\cos^2\theta_{xa}\rangle_{\rm eff} = 1$ for perfect alignment to $\langle\cos^2\theta_{xa}\rangle_{\rm eff} = 0.88$ for naphthalene molecules at 1 K probed by a 100-ps x-ray pulse. By increasing the x-ray pulse width from 1 to 100 ps, the effective alignment at $T = 10$ mK decreases from $\langle\cos^2\theta_{xa}\rangle_{\rm eff} = 0.967$ to $\langle\cos^2\theta_{xa}\rangle_{\rm eff} = 0.944$ [cf. Fig. 6(b) and 6(d)] and is significantly smaller than the impact of temperature rise from 10 mK to 1 K [cf. Fig. 6(c) and 6(d)].

Although the basic features of the x-ray scattering pattern for perfectly aligned naphthalene [Fig. 6(a)] are preserved in the scattering patterns for laser-aligned naphthalene [Figs. 6(b), 6(c), and 6(d)], the contours are washed out and the contrast between maxima and minima is less pronounced with decreasing alignment. Incoherent averaging for laser-aligned naphthalene renders the diffraction patterns more cylindrically symmetric with respect to the y direction, which limits the accessible structural information particularly at high momentum transfer.

Side views of naphthalene in $\boldsymbol{Q}$ space are shown in Fig. 7, where Fig. 7(a) depicts the long side ($Q_x = 0$) and Fig. 7(b) the short side ($Q_z = 0$) of naphthalene. Both display strong similarities to multislit diffraction patterns, consistent with

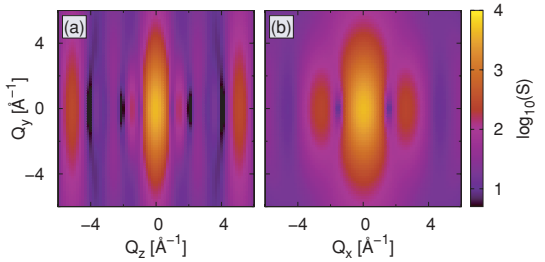

FIG. 7. (Color online) (a) Diffraction signal of naphthalene for $Q_x = 0$. (b) Diffraction signal of naphthalene for $Q_z = 0$. Other parameters are the same as for Fig. 6(b).

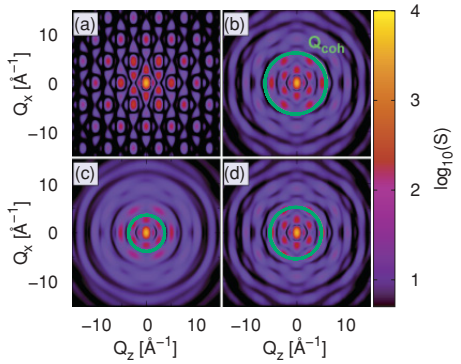

FIG. 8. (Color online) Same as for Fig. 6, except $Q_{max} = 8\pi$ Å^{-1}. The momentum transfer Q_{coh} (see the text) is highlighted by a solid green circle in (b)–(d).

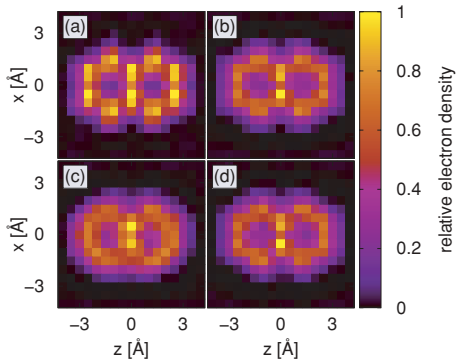

FIG. 9. (Color online) Structure of naphthalene, reconstructed from the diffraction signals shown in Fig. 6. The pixel size is 0.5 Å. (a) Perfect alignment. (b) $T = 10$ mK, $\tau_X = 1$ ps, x-ray pulse centered at $t = 20.75$ ps. (c) $T = 1$ K, $\tau_X = 100$ ps, x-ray pulse centered at $t = 0$ ps. (d) $T = 10$ mK, $\tau_X = 100$ ps, x-ray pulse centered at $t = 0$ ps.

the planar structure of naphthalene being well aligned in the xz plane.

The achievable real-space resolution depends on two aspects. On the one hand, the smallest resolvable dimension d_{coh} is a function of the degree of alignment [Eq. (43)]. On the other hand, the pixel size of the real-space structure reconstruction is determined by the maximum momentum transfer Q_{max} in the diffraction signal $S(\boldsymbol{Q})$. Here, $Q_{max} = 2\pi$ Å^{-1}, corresponding to a pixel size of 0.5 Å. The approximate range in momentum space within which the assumption of coherent scattering holds may be defined by $Q_{coh} = 2\pi/d_{coh}$. In Fig. 8, the diffraction signals of Fig. 6 are shown up to $Q_{max} = 8\pi$ Å^{-1}. The respective ranges defined by Q_{coh} are highlighted. It is not possible to increase the resolution of the real-space structure reconstruction by choosing Q_{max} much greater than Q_{coh}. In fact, numerical tests have indicated that data beyond Q_{coh} can lead to poor convergent structures.

For 12-keV x-ray photons, a real-space pixel size of 0.5 Å requires the detection of photons scattered up to 60° with respect to the x-ray propagation axis. The azimuthally averaged differential x-ray scattering cross section per naphthalene molecule for $Q = 2\pi$ Å^{-1} is $d\sigma/d\Omega_{avg} = 0.6$ barn. Since the largest distance between carbon atoms in naphthalene is ∼5 Å, the area of a pixel in momentum space must not exceed $4\pi^2/25$ Å^{-2}. At a scattering angle of 60°, this corresponds to a solid angle $d\Omega = 0.012$. For a molecular beam width of 1 mm and an x-ray focus area of 100 μm^2, it has been demonstrated that the number of molecules in the interaction volume can be as large as 10^7 [56]. Hence, requiring a minimum of five scattered photons per pixel [114], the estimated acquisition time for one diffraction pattern is around 70 s with an x-ray fluence of 10^{13} photons/(pulse/mm^2) and a repetition rate of 1 kHz.

C. Structure reconstruction

We applied the phase-retrieval algorithm described in Sec. III B to the naphthalene diffraction signals shown in Fig. 6. The maximum momentum transfer of 2π Å^{-1} in Fig. 6 corresponds to a pixel size of 0.5 Å, which is of the order of the structure we want to resolve in naphthalene. As a consequence, each pixel encodes a lot of structure information. Calculations have shown that the reconstruction routine becomes sensitive to the set of initial random phases. Therefore, we follow the spirit of Ref. [101] and average over reconstructions obtained for 100 different sets of initial phases to define a quality criterion, which we apply subsequently to all 100 reconstructions to select the most meaningful results and average over these selected reconstructions. Our quality criterion is defined as follows: (i) All pixels of the unfiltered averaged result that have at least 20% of the maximum electron density are selected to build a density core region. (ii) The quality criterion uses the density core region and selects only the reconstructions that have at least 50% of their total electron density within this density core region.

The filtered averages for the x-ray scattering patterns of Fig. 6 are displayed in Fig. 9. In our calculations, we employed a grid spacing in $\boldsymbol{Q}$ space of 0.16 Å^{-1}, corresponding to a maximum object size 8 times larger than the size of naphthalene.

Figure 9 illustrates that with better effective alignment in the diffraction pattern more structural information can be reconstructed. In the perfect alignment case (cf. Fig. 9a), the positions of the atoms can be resolved. A comparison with the perfect alignment reconstruction in Fig. 1(b), where the pixel size is 0.125 Å and no averaging over several initial random phases was performed, illustrates that the reconstruction of the carbon positions is more difficult when the pixel size is comparable with the size of the atoms. Incoherent averaging for imperfectly aligned molecules affects the effective resolution further, since the assumption of coherent scattering limits the usable diffraction signal to $Q \leqslant Q_{coh}$. As a consequence, Q_{max} should be of the order of Q_{coh} and, therefore, the pixel size in the reconstruction is limited by the degree of effective alignment.

All results displayed in Fig. 9 recover the two-ring structure of naphthalene, indicating an effective resolution below 2 Å. Especially the two carbon atoms connecting both carbon rings are distinctly visible. Figures 9(b) and 9(d) show the reconstruction for naphthalene at 10 mK with $\tau_X = 1$ps and

$\tau_X = 100$ ps, respectively. Both have a similar effective alignment and reconstruction. In both cases, the electron density peaks on the two-ring structure indicate the positions of all carbon atoms and are consistent with the theoretically expected effective resolutions, which are below the typical distance between neighboring carbon atoms (1.4 Å). The predicted effective resolution at 1 K ($d_{\mathrm{coh}} = 1.73$ Å) is sufficient to resolve the overall structure of naphthalene, which can be seen in Fig. 9(c). For the central region of naphthalene, the effective resolution improves and makes it possible to identify the two central carbon atoms at 1 K.

V. CONCLUSION

We have theoretically studied the theory of x-ray diffraction from asymmetric-top molecules that are three-dimensionally aligned by elliptically polarized light and have discussed a phase-retrieval method in order to reconstruct molecular structure from the x-ray scattering pattern. The interaction of the gas phase molecules with the laser and x-ray fields was studied in the density matrix formalism. We have assumed rigid rotor molecules. Symmetries in the time-dependent Hamiltonian and in its solutions as well as in the angular density distribution were exploited and used to improve numerical efficiency. In combination with further computational aspects, a significant enhancement in numerical efficiency has been achieved.

A feasibility study of x-ray diffraction from three-dimensionally laser-aligned molecules has been performed using the organic molecule naphthalene. We have linked the degree of alignment to an effective resolution and have studied the impact of x-ray pulse duration and temperature on the diffraction patterns. A phase-retrieval reconstruction was performed on diffraction patterns taken for different effective alignments. The enhancement of incoherent averaging due to imperfect alignment destroys structural information and hinders the recovery of detailed atomic configurations within the molecule. The reconstruction of naphthalene confirms our discussion that the degree of alignment is a good indicator for the achievable resolution in the reconstruction. To decode structures on an atomic length scale, high degree of alignment in all three molecular axes must be achieved. Molecules have to be cooled down to a few Kelvin or even sub-Kelvin temperatures so rotational motion is sufficiently reduced. Experiments have shown that it is feasible to cool molecules to 1 K [72,115,117]. To accomplish rotational temperatures well below 1 K is a great challenge and would open the opportunity to image large gas-phase molecules at atomic resolution. The problem of incoherent averaging over a finite range of different orientations has to be further addressed, especially in the case where molecular symmetries do not coincide with the symmetries of the diffraction pattern imposed by alignment.

With the ability to detect molecular structure, x-ray scattering from gas phase molecules can be used to study torsion effects and laser-induced deformations that are expected to occur during alignment in the presence of intense laser pulses [116]. By systematically varying the delay time between pump (laser) and probe (x-ray) pulse, it is possible to follow molecular motion on an ultrafast time scale. Of particular interest is the study of physical and chemical processes in the presence of intense laser fields, which simultaneously provide the required alignment for imaging of reactions with atomic resolution in space and time.

ACKNOWLEDGMENTS

We thank Cassandra Hunt for helpful comments on the manuscript. This work was supported by the Office of Basic Energy Sciences, US Department of Energy under Contract No. DE-AC02-06CH11357.

APPENDIX A: NUCLEAR SPIN STATISTICAL WEIGHTS

In the density matrix, statistical weights, $w_{J\tau} = g_{J\tau}\frac{\exp(-E^{\mathrm{rot}}_{J\tau}/kT)}{Z(T)}$, define the relative number of particles in an ensemble that are in a given quantum mechanical state for a well-defined temperature T. The nuclear spin statistical weights $g_{J\tau}$ are based on symmetry arguments and represent the number of the allowed nuclear spin states for a given rotational state $|J\tau M\rangle$.

The overall symmetry Γ_{tot} of the total molecular wave function is independent of rotational or nuclear spin states and determined by the spin statistic theorem [82]. However, Γ_{tot} is also a direct product of symmetries of the different quantum states [77],

$$\Gamma_{\mathrm{tot}} = \Gamma_r \otimes \Gamma_{\mathrm{ns}}, \tag{A1}$$

where Γ_r is the rotational state symmetry and Γ_{ns} is the nuclear spin state symmetry. Molecules are in their electronic and vibrational ground states and their contributions can be omitted in Eq. (A1).

The representation of symmetries depends on the symmetry group of the molecule. The molecular symmetry group of asymmetric-top molecules without an inversion center is D_{2h} or lower [118]. The rotational symmetry group of an asymmetric-top rotor is always V (isomorphic to D_{2h}) [119,120]. If there is no common symmetry class between Γ_r and Γ_{ns}, $g_{J\tau} = 1$. In other words, molecular symmetries come only into play when molecular rotations are identical to particle exchanges.

All symmetry representations are written as linear combinations of irreducible representations (irrep) of V in Table III. In addition, the character table for the nuclear spin and rotational

TABLE III. Character table and irreducible representations of overall, rotational, and nuclear spin states for naphthalene. The symmetry point group is V.

	Operations P of V				Irrep.	
	E	C_c	C_b	C_a	J even	J odd
Γ_{tot}	1	1	1	1	A	
E^+	1	1	$(-1)^J$	$(-1)^J$	A	B_c
E^-	1	1	$(-1)^{J+1}$	$(-1)^{J+1}$	B_c	A
O^-	1	−1	$(-1)^J$	$(-1)^{J+1}$	B_b	B_a
O^+	1	−1	$(-1)^{J+1}$	$(-1)^J$	B_a	B_b
Γ_{ns}	2^8	2^4	2^4	2^4	$76\,A + 60(B_a + B_b + B_c)$	

states are shown. The four molecular rotations and particle exchanges defining V are E, C_a, C_b, C_c.

The characters of the overall wave function χ_{tot} can be derived from the Pauli principle [83] and correspond to the overall sign changes induced by the molecular rotations. First, we assume all carbon atoms in naphthalene are ^{12}C with nuclear spin 0. By remembering only odd permutations of half-integer particles (fermions) change the sign of the overall wave function [77], we find all group operation leave the overall sign for naphthalene unchanged, since all Hydrogen permutations are even. Hence, $\chi_{\text{tot}}[P] = 1$, $\forall P \in V$ and $\Gamma_{\text{tot}} = A$.

The rotational symmetry classes, in which each rotational state can be classified (cf. Sec. II A), coincide with the irreps of V [74]. However, whether or not J is even or odd defines which irrep corresponds to which symmetry class (cf. Table III).

The sum of characters over all possible nuclear spin states $\chi_{\text{ns}}[P]$ for each operation P can be derived by the formula [83,119]

$$\chi_{\text{ns}}[P] = \prod_{G_P} (2S_{G_P} + 1)\, \text{sgn}(P_{G_P})^{2S_{G_P}}, \tag{A2}$$

where the atom group G_P is defined by the minimum number of identical atoms in the molecule such that after the atom permutation P each atom in G_P is replaced by an atom of G_P. $\text{sgn}(P_{G_P})$ is the sign of the permutation P within in the atom group G_P, which is $+1$ or -1 depending whether the permutation is even or odd in G_P. The smallest atom group consist of one atom, which does not change position under the operation P. S_{G_P} is the nuclear spin of the atoms in G_P.

Imposing Eq. (A1), nuclear spin and rotational symmetries are linked together. (For naphthalene: $\Gamma_{\text{tot}} = \Gamma_r \otimes \Gamma_{\text{ns}} = A$). The multiplication of symmetry representations is done by multiplying their characters. The nuclear spin statistical weights $g_{J\tau}$ are the number of irreps in Γ_{ns} such that the product with a given rotational class is Γ_{tot}. As an example: When $|J\tau M\rangle \in O^-$ and J is even, then $\Gamma_r \in B_b$ and only the product $B_b \otimes B_b = A$ [119] fulfills Eq. (A1). Since there are 60 B_b irreps in Γ_{ns}, the nuclear spin statistical weight is 60. For all rotational states of naphthalene, the nuclear spin statistical weights are

$$g_{J\tau} = \begin{cases} 76, & \Gamma_r \in A \\ 60, & \text{otherwise.} \end{cases} \tag{A3}$$

APPENDIX B: MATRIX ELEMENTS OF $\cos^2\theta_{lm}$

The squares of the matrix elements of the rotation matrix $R(\phi,\theta,\chi)$, i.e., $\cos^2\theta_{lm}$, give a complete picture of the three-dimensional alignment. Knowing four $\cos^2\theta_{lm}$ is sufficient to describe all, where at least two axes of each reference frame have to be involved in the four $\cos^2\theta_{lm}$. Our choice is $l \in \{x,z\}$, $m \in \{a,c\}$, since it is one of the least computationally expensive choices. The $\cos^2\theta_{lm}$ matrices are diagonal in M or K when $l = z$ or $m = c$, respectively. Only the matrix $\cos^2\theta_{xa}$ is nondiagonal in K and M. Each $\cos^2\theta_{lm}$ can be written in terms of $D^{[J]}_{MK}(\phi,\theta,\chi)$ [29], where the matrix elements of the Wigner D functions are given in Refs. [49,54,74]. The matrix elements of the four matrices that we have chosen are:

$$\langle JKM|\cos^2\theta_{zc}|J'K'M'\rangle = \frac{1}{3}\delta_{JJ'}\delta_{KK'}\delta_{MM'} + \frac{2}{3}\sqrt{\frac{2J+1}{2J'+1}}\langle J,M;2,0|J',M'\rangle\langle J,K;2,0|J',K'\rangle, \tag{B1a}$$

$$\langle JKM|\cos^2\theta_{xc}|J'K'M'\rangle = \frac{1}{3}\delta_{JJ'}\delta_{KK'}\delta_{MM'} - \sqrt{\frac{1}{6}}\sqrt{\frac{2J+1}{2J'+1}}\langle J,K;2,0|J',K'\rangle \times\left(\sqrt{\frac{2}{3}}\langle J,M;2,0|J',M'\rangle - [\langle J,M;2,2|J',M'\rangle + \langle J,M;2,-2|J',M'\rangle]\right), \tag{B1b}$$

$$\langle JKM|\cos^2\theta_{za}|J'K'M'\rangle = \frac{1}{3}\delta_{JJ'}\delta_{KK'}\delta_{MM'} - \sqrt{\frac{1}{6}}\sqrt{\frac{2J+1}{2J'+1}}\langle JM;20|J'M'\rangle \times\left(\sqrt{\frac{2}{3}}\langle J,K;2,0|J',K'\rangle - [\langle J,K;2,2|J',K'\rangle + \langle J,K;2,-2|J',K'\rangle]\right), \tag{B1c}$$

$$\langle JKM|\cos^2\theta_{xa}|J'K'M'\rangle = \frac{1}{3}\delta_{JJ'}\delta_{KK'}\delta_{MM'} + \frac{1}{4}\sqrt{\frac{2J+1}{2J'+1}} \times\left(\sqrt{\frac{2}{3}}\langle J,M;2,0|J',M'\rangle - [\langle J,M;2,2|J',M'\rangle + \langle J,M;2,-2|J',M'\rangle]\right) \times\left(\sqrt{\frac{2}{3}}\langle J,K;2,0|J',K'\rangle - [\langle J,K;2,2|J',K'\rangle + \langle J,K;2,-2|J',K'\rangle]\right). \tag{B1d}$$

[1] J. D. Watson and F. H. C. Crick, Nature **171**, 737 (1953).
[2] M. Chergui and A. H. Zewail, Chem. Phys. Chem. **10**, 28 (2009).
[3] J. Drenth, *Principles of Protein X-Ray Crystallography*, 3rd ed. (Springer, Berlin, 2006).
[4] J. C. H. Spence and R. B. Doak, Phys. Rev. Lett. **92**, 198102 (2004).
[5] U. Weierstall, R. B. Doak, J. C. H. Spence, D. Starodub, D. Shapiro, P. Kennedy, J. Warner, G. G. Hembree, P. Fromme, and H. N. Chapman, Exp. Fluids **44**, 675 (2008).
[6] R. Neutze, G. Huldt, J. Hajdu, and D. van der Spoel, Radiat. Phys. Chem. **71**, 905 (2004).
[7] D. Shapiro, P. Thibault, T. Beetz, V. Elser, M. Howells, C. Jacobsen, J. Kirz, E. Lima, H. Miao, A. M. Neiman, and D. Sayre, Proc. Natl. Acad. Sci. USA **102**, 15343 (2005).
[8] R. Neutze, R. Wouts, D. van der Spoel, E. Weckert, and J. Hajdu, Nature (London) **406**, 752 (2000).
[9] G. Huldt, A. Szoke, and J. Hajdu, J. Struct. Biol. **144**, 219 (2003).
[10] K. J. Gaffney and H. N. Chapman, Science **316**, 1444 (2007).
[11] J. W. Miao, H. N. Chapman, J. Kirz, D. Sayre, and K. O. Hodgson, Annu. Rev. Biophys. Biomol. Struct. **33**, 157 (2004).
[12] J. Miao, C. Charalambous, J. Kirz, and D. Sayre, Nature (London) **400**, 342 (1999).
[13] J. C. H. Spence, M. R. Howells, L. D. Marks, and J. Miao, Ultramicroscopy **90**, 1 (2001).
[14] D. Sayre, Structural Chemistry **13**, 81 (2002).
[15] M. R. Howells, T. Beetz, H. N. Chapman, C. Cui, J. M. Holton, C. J. Jacobsen, J. Kirz, E. Lima, S. Marchesini, H. Miao, D. Sayre, D. A. Shapiro, J. C. H. Spence, and D. Starodub, J. Electron Spectrosc. Relat. Phenom. **170**, 4 (2009).
[16] V. Elser and R. P. Milane, Acta Crystallogr. Sect. A **64**, 273 (2008).
[17] J. Miao, D. Sayre, and H. N. Chapman, J. Opt. Soc. Am. A **15**, 1662 (1998).
[18] V. Elser, J. Opt. Soc. Am. A **20**, 40 (2003).
[19] J. C. H. Spence, K. Schmidt, J. S. Wu, G. Hembree, U. Weierstall, B. Doak and P. Fromme, Acta Crystallogr. Sect. A **61**, 237 (2005).
[20] B. Friedrich and D. Herschbach, J. Chem. Phys. **111**, 6157 (1999).
[21] B. Friedrich and D. Herschbach, J. Phys. Chem. A **103**, 10280 (1999).
[22] H. Sakai, S. Minemoto, H. Nanjo, H. Tanji, and T. Suzuki, Phys. Rev. Lett. **90**, 083001 (2003).
[23] X. Chu, Phys. Rev. A **78**, 043408 (2008).
[24] S. De, I. Znakovskaya, D. Ray, F. Anis, N. G. Johnson, I. A. Bocharova, M. Magrakvelidze, B. D. Esry, C. L. Cocke, I. V. Litvinyuk, and M. F. Kling, Phys. Rev. Lett. **103**, 153002 (2009).
[25] V. Kumarappan, C. Z. Bisgaard, S. S. Viftrup, L. Holmegaard, and Henrik Stapelfeldt, J. Chem. Phys. **125**, 194309 (2006).
[26] H. Stapelfeldt and T. Seideman, Rev. Mod. Phys. **75**, 543 (2003).
[27] T. Seideman, J. Chem. Phys. **103**, 7887 (1995).
[28] T. Seideman, J. Chem. Phys. **111**, 4397 (1999).
[29] T. Seideman, Chem. Phys. Lett. **253**, 279 (1996).
[30] T. Seideman and E. Hamilton, Adv. At. Mol. Opt. Phys. **52**, 289 (2005).
[31] E. Péronne, M. D. Poulsen, C. Z. Bisgaard, H. Stapelfeldt, and T. Seideman, Phys. Rev. Lett. **91**, 043003 (2003).
[32] B. Friedrich and D. Herschbach, Phys. Rev. Lett. **74**, 4623 (1995).
[33] T. Seideman, J. Chem. Phys. **115**, 5965 (2001).
[34] M. D. Poulsen, E. Péronne, H. Stapelfeldt, C. Z. Bisgaard, S. S. Viftrup, E. Hamilton, and T. Seideman, J. Chem. Phys. **121**, 783 (2004).
[35] M. Renard, E. Hertz, S. Guérin, H. R. Jauslin, B. Lavorel, and O. Faucher, Phys. Rev. A **72**, 025401 (2005).
[36] M. Leibscher, I. Sh. Averbukh, and H. Rabitz, Phys. Rev. Lett. **90**, 213001 (2003).
[37] K. F. Lee, D. M. Villeneuve, P. B. Corkum, and E. A. Shapiro, Phys. Rev. Lett. **93**, 233601 (2004).
[38] G. Zeng, F. Zhong, C. Wu, H. Jiang, and Q. Gong, Laser Physics **19**, pp. 1691–1696.
[39] D. Daems, S. Guérin, E. Hertz, H. R. Jauslin, B. Lavorel, and O. Faucher, Phys. Rev. Lett. **95**, 063005 (2005).
[40] P. J. Ho, M. R. Miller, and R. Santra, J. Chem. Phys. **130**, 154310 (2009).
[41] T. Seideman, Phys. Rev. Lett. **83**, 4971 (1999).
[42] E. Péronne, M. D. Poulsen, H. Stapelfeldt, C. Z. Bisgaard, E. Hamilton, and T. Seideman, Phys. Rev. A **70**, 063410 (2004).
[43] M. D. Poulsen, T. Ejdrup, H. Stapelfeldt, E. Hamilton, and T. Seideman, Phys. Rev. A **73**, 033405 (2006).
[44] E. Hamilton, T. Seideman, T. Ejdrup, M. D. Poulsen, C. Z. Bisgaard, S. S. Viftrup, and H. Stapelfeldt, Phys. Rev. A **72**, 043402 (2005).
[45] C. Z. Bisgaard, S. S. Viftrup, and H. Stapelfeldt, Phys. Rev. A **73**, 053410 (2006).
[46] C. Z. Bisgaard, M. D. Poulsen, E. Péronne, S. S. Viftrup, and H. Stapelfeldt, Phys. Rev. Lett. **92**, 173004 (2004).
[47] S. Guérin, A. Rouzée, and E. Hertz, Phys. Rev. A **77**, 041404(R) (2008).
[48] A. Keller, C. M. Dion, and O. Atabek, Phys. Rev. A **61**, 023409 (2000).
[49] E. Gershnabel and I. Sh. Averbukh, Phys. Rev. A **78**, 063416 (2008).
[50] C. M. Dion, A. Keller, O. Atabek, and A. D. Bandrauk, Phys. Rev. A **59**, 1382 (1999).
[51] A. Rouzée, S. Guérin, V. Boudon, B. Lavorel, and O. Faucher, Phys. Rev. A **73**, 033418 (2006).
[52] P. J. Ho and R. Santra, Phys. Rev. A **78**, 053409 (2008).
[53] P. J. Ho, D. Starodub, D. K. Saldin, V. L. Shneerson, A. Ourmazd, and R. Santra, J. Chem. Phys. **131**, 131101 (2009).
[54] C. Buth and R. Santra, Phys. Rev. A **77**, 013413 (2008).
[55] C. Buth and R. Santra, J. Chem. Phys. **129**, 134312 (2008).
[56] E. R. Peterson, C. Buth, D. A. Arms, R. W. Dunford, E. P. Kanter, B. Krässig, E. C. Landahl, S. T. Pratt, R. Santra, S. H. Southworth, and L. Young, Appl. Phys. Lett. **92**, 094106 (2008).
[57] M. Artamonov and T. Seideman, J. Chem. Phys. **128**, 154313 (2008).
[58] J. J. Larsen, K. Hald, N. Bjerre, H. Stapelfeldt, and T. Seideman, Phys. Rev. Lett. **85**, 2470 (2000).
[59] J. G. Underwood, B. J. Sussman, and A. Stolow, Phys. Rev. Lett. **94**, 143002 (2005).

[60] K. F. Lee, D. M. Villeneuve, P. B. Corkum, A. Stolow, and J. G. Underwood, Phys. Rev. Lett. **97**, 173001 (2006).

[61] S. S. Viftrup, V. Kumarappan, L. Holmegaard, C. Z. Bisgaard, H. Stapelfeldt, M. Artamonov, E. Hamilton, and T. Seideman, Phys. Rev. A **79**, 023404 (2009).

[62] S. S. Viftrup, V. Kumarappan, S. Trippel, H. Stapelfeldt, E. Hamilton, and T. Seideman, Phys. Rev. Lett. **99**, 143602 (2007).

[63] A. Rouzée, S. Guérin, O. Faucher, and B. Lavorel, Phys. Rev. A **77**, 043412 (2008).

[64] W. Kim and P. M. Felker, J. Chem. Phys. **104**, 1147 (1996).

[65] H. Sakai, C. P. Safvan, J. J. Larsen, K. M. Hilligsøe, K. Hald, and H. Stapelfeldt, J. Chem. Phys. **110**, 10235 (1998).

[66] R. M. Dickson, D. J. Norris, and W. E. Moerner, Phys. Rev. Lett. **81**, 5322 (1998).

[67] A. Rouzée, V. Renard, S. Guérin, O. Faucher, and B. Lavorel, Phys. Rev. A **75**, 013419 (2007).

[68] L. Holmegaard, J. H. Nielsen, I. Nevo, H. Stapelfeldt, F. Filsinger, J. Küpper, and G. Meijer, Phys. Rev. Lett. **102**, 023001 (2009).

[69] S. M. Purcell and P. F. Barker, Phys. Rev. Lett. **103**, 153001 (2009).

[70] J. J. Larsen, I. Wendt-Larsen, and H. Stapelfeldt, Phys. Rev. Lett. **83**, 1123 (1999).

[71] J. J. Larsen, H. Sakai, C. P. Safvan, I. Wendth-Larsen, and H. Stapelfeldt, J. Chem. Phys. **111**, 7774 (1999).

[72] U. Even, J. Jortner, D. Noy, and N. Lavie, J. Chem. Phys. **112**, 8068 (2000).

[73] G. W. Drake, *Atomic, Molecular, & Optical Physics Handbook* (AIP, Melville, NY, 1996).

[74] R. N. Zare, *Angular Momentum* (Wiley, New York, 1988).

[75] N. Rohringer and R. Santra, Phys. Rev. A **76**, 033416 (2007).

[76] J. J. Sakurai, *Modern Quantum Mechanics* (Addison Wesley, Reading, MA, 1993).

[77] H. W. Kroto, *Molecular Rotation Spectra* (Wiley, London, 1975).

[78] L. E. Reichl, *A Modern Course in Statistical Physics*, 3rd ed. (Wiley-VCH, Weinheim, 2009).

[79] K. Blum, *Density Matrix Theory and Applications, Physics of Atoms and Molecules*, 2nd ed. (Springer, Berlin, 1996).

[80] R. Loudon, *The Quantum Theory of Light* (Oxford University Press, Oxford, 1983).

[81] L. Mandel and E. Wolf, *Optical Coherence and Quantum Optics* (Cambridge University Press, Cambridge, UK, 1995).

[82] L. D. Landau and L. M. Lifshitz, *Quantum Mechanics Non-Relativistic Theory, Volume 3*, 3rd ed. (Butterworth-Heinemann, Oxford, UK, 1981).

[83] W. Pauli, Phys. Rev. **58**, 716 (1940).

[84] D. A. Varshalovich, A. N. Moskalev, and V. K. Khersonskii (eds.), *Quantum Theory of Angular Momentum* (World Scientific, Singapore, 1988).

[85] J. Als-Nielsen and D. McMorrow, *Elements of Modern X-ray Physics* (Wiley, New York, 2001).

[86] G. Engeln-Müllges and F. Uhlig, *Numerical Algorithms with Fortran* (Springer-Verlag, Heidelberg, 1996).

[87] R. W. Gerchberg and W. 0. Saxton, Optik **35**, 237 (1972).

[88] W. O. Saxton, *Computer Techniques for Image Processing in Electron Microscopy* (Academic Press, New York, 1978).

[89] J. R. Fienup, Appl. Opt. **21**, 2758 (1982).

[90] J. R. Fienup, T. R. Crimmins, and W. Holsztynski, J. Opt. Soc. Am. **72**, 610 (1982).

[91] J. R. Fienup, J. Opt. Soc. Am. A **4**, 118 (1987).

[92] J. Miao and D. Sayre, Acta Crystallogr. Sect. A **56**, 596 (2000).

[93] S. Marchesini, H. He, H. N. Chapman, S. P. Hau-Riege, A. Noy, M. R. Howells, U. Weierstall, and J. C. H. Spence, Phys. Rev. B **68**, 140101(R) (2003).

[94] G. Oszlányic and A. Sütő, Acta Crystallogr. Sect. A **60**, 134 (2004).

[95] B. Carrozzini, G. L. Cascarano, L. De Caro, C. Giacovazzo, S. Marchesini, H. Chapman, H. He, M. Howells, J. S. Wu, U. Weierstall, and J. C. H. Spence, Acta Crystallogr. Sect. A **60**, 331 (2004).

[96] D. R. Luke, Inverse Probl. **21**, 37 (2005).

[97] J. S. Wu and J. C. H. Spence, Acta Crystallogr. Sect. A **61**, 194 (2005).

[98] H. N. Chapman, A. Barty, S. Marchesini, A. Noy, S. P. Hau-Riege, C. Cui, M. R. Howells, R. Rosen, H. He, J. C. H. Spence, U. Weierstall, T. Beetz, C. Jacobsen, and D. Shapiro, J. Opt. Soc. Am. A **23**, 1179 (2006).

[99] K. A. Nugent, J. Opt. Soc. Am. A **24**, 536 (2007).

[100] S. Marchesini, Rev. Sci. Instrum. **78**, 011301 (2007).

[101] J. Miao, T. Ishikawa, Q. Shen, and T. Earnest, Annu. Rev. Phys. Chem. **59**, 387 (2008).

[102] I. K. Robinson, I. A. Vartanyants, G. J. Williams, M. A. Pfeifer, and J. A. Pitney, Phys. Rev. Lett. **87**, 195505 (2001).

[103] U. Weierstall, Q. Chen, J. C. H. Spence, M. R. Howells, M. Isaacson, and R. R. Panepucci, Ultramicroscopy **90**, 171 (2002).

[104] J. C. H. Spence, U. Weierstall, and M. R. Howells, Philos. Trans. R. Soc. London **360**, 875 (2002).

[105] J. Miao, T. Ishikawa, B. Johnson, E. H. Anderson, B. Lai, and K. O. Hodgson, Phys. Rev. Lett. **89**, 088303 (2002).

[106] K. A. Nugent, A. G. Peele, H. N. Chapman, and A. P. Mancuso, Phys. Rev. Lett. **91**, 203902 (2003).

[107] J. Miao, K. O. Hodgson, T. Ishikawa, C. A. Larabell, M. A. LeGros, and Y. Nishino, Proc. Natl. Acad. Sci. USA **100**, 110 (2003).

[108] X. Xiao and Q. Shen, Phys. Rev. B **72**, 033103 (2005).

[109] H. M. Quiney, A. G. Peele, Z. Cai, D. Paterson, and K. A. Nugent, Nature Phys. **2**, 101 (2006).

[110] J. Miao, C.-C. Chen, C. Song, Y. Nishino, Y. Kohmura, T. Ishikawa, D. Ramunno-Johnson, T.-K. Lee, and S. H. Risbud, Phys. Rev. Lett. **97**, 215503 (2006).

[111] D.-L. Joo, R. Takahashi, J. O'Reilly, H. Katô, and M. Baba, J. Mol. Spectrosc. **215**, 155 (2002).

[112] S. T. Howard, I. A. Fallism, and D. J. Willock, Mol. Phys. **97**, 913 (1999).

[113] D. J. Smith, K. W. D. Ledingham, R. P. Singhal, H. S. Kilic, T. McCanny, A. J. Langley, P. F. Taday, and C. Kosmidis, Rapid Commun. Mass Spectrom. **12**, 813 (1998).

[114] Q. Shen, I. Bazarov and P. Thibault, J. Synchrotron Radiat. **11**, 432 (2004).

[115] F. Filsinger, J. Küpper, G. Meijer, L. Holmegaard, J. H. Nielsen, I. Nevo, J. L. Hansen, and H. Stapelfeldt, J. Chem. Phys. **131**, 064309 (2009).

[116] D. M. Villeneuve, S. A. Aseyev, P. Dietrich, M. Spanner, M. Y. Ivanov, and P. B. Corkum, Phys. Rev. Lett. **85**, 542 (2000).
[117] H. Stapelfeldt, Eur. Phys. J. D **26**, 15 (2003).
[118] G. Herzberg, *Molecular Spectra and Molecular Structure: II. Infrared and Raman Spectra of Polyatomic Molecules* (D. Van Nostrand Company, Toronto, 1968).
[119] P. R. Bunker and P. Jensen, *Molecular Symmetry and Spectroscopy*, 2nd ed. (National Research Council of Canada, Ottowa, 1998).
[120] G. Herzberg, *Molecular Spectra and Molecular Structure: III. Electronic Spectra and Electronic Structure of Polyatomic Molecules* (D. Van Nostrand Company, Toronto, 1966).

4.2 Alignment of Asymmetric-Top Molecules Using Multiple-Pulse Trains

Stefan Pabst and Robin Santra

Published in Phys. Rev. A **81**, 065401 (2010)

Original publication: http://link.aps.org/doi/10.1103/PhysRevA.81.065401
Free preprint version: http://arxiv.org/abs/1005.5157

Statement of Contributions

All calculations, the interpretation of the results, and the preparation of the manuscript have been done by myself.

PHYSICAL REVIEW A **81**, 065401 (2010)

Alignment of asymmetric-top molecules using multiple-pulse trains

Stefan Pabst[1,2] and Robin Santra[1,3,*]

[1]*Argonne National Laboratory, Argonne, Illinois 60439, USA*

[2]*Institut für Theoretische Physik, Universität Erlangen-Nürnberg, D-91058 Erlangen, Germany*

[3]*Department of Physics, University of Chicago, Chicago, Illinois 60637, USA*

(Received 14 April 2010; published 7 June 2010)

We theoretically analyze the effectiveness of multiple-pulse laser alignment methods for asymmetric-top molecules. As an example, we choose SO_2 and investigate the alignment dynamics induced by two different sequences, each consisting of four identical laser pulses. Each sequence differs only in the time delay between the pulses. Equally spaced pulses matching the alignment revival of the symmetrized SO_2 rotor model are exploited in the first sequence. The pulse separations in the second sequence are short compared to the rotation dynamics of the molecule and monotonically increase the degree of alignment until the maximum alignment is reached. We point out the significant differences between the alignment dynamics of SO_2 treated as an asymmetric-top and a symmetric-top rotor, respectively. We also explain why the fast sequence of laser pulses creates considerably stronger one-dimensional molecular alignment for asymmetric-top molecules. In addition, we show that multiple-pulse trains with elliptically polarized pulses do not enhance one-dimensional alignment or create three-dimensional alignment.

DOI: 10.1103/PhysRevA.81.065401 PACS number(s): 37.10.Vz, 42.50.Hz, 42.50.Md, 33.20.Sn

Molecular alignment techniques have become important for controlling processes like photoabsorption [1,2], multiphoton ionization [3–5], high harmonic generation (HHG) [6,7], and molecular imaging [8–10]. Alignment of molecules can be achieved with intense laser fields making use of the quadratic Stark effect [11]. In general it is true that more intense laser fields create higher degrees of alignment. However, intense laser fields trigger side effects, like multiphoton ionization and molecular defragmentation, that irreversibly damage molecules [12–14]. For alignment purposes, ionization is an unwanted effect that multiple-pulse alignment techniques try to prevent [15].

Laser alignment can be accomplished adiabatically or impulsively [11]. In the former case, the laser pulse duration is long compared to the rotational period of the molecule $\tau_{\rm rot}$; in the latter case it is short compared to $\tau_{\rm rot}$. For a given laser intensity, adiabatic alignment leads to a higher degree of alignment than does impulsive alignment; however, enhancing alignment through several consecutive, nonoverlapping laser pulses is only possible in the impulsive regime. Theoretical and experimental studies with up to three laser pulses, where pulse separations, pulse intensities, and pulse shapes were systematically varied, have been performed [16–18]. Recently, field-free alignment of N_2 was reported in an experiment with eight identical, Fourier transform limited, consecutive laser pulses [15]. All eight pulses were separated by the rotational period $\tau_{\rm rot} = 1/(2B)$ [15,19]. The degree of alignment achieved in Ref. [15] with eight pulses is much greater than the alignment induced by a single ionization-limited pulse.

Attempts to use a sequence of pulses to enhance alignment have so far been focused on linear or symmetric-top molecules, which possess well-defined alignment revivals separated by $\tau_{\rm rot}$. The irregular or incommensurable spacings of the rotational energy levels for asymmetric-top molecules prevent full rephasing of the rotational wave packet [20] and, therefore, the appearance of periodic alignment revivals. Experiments involving asymmetric-top molecules with one-dimensional, field-free alignment [20–24] and three-dimensional alignment using two linearly polarized laser pulses [25,26] have been reported.

Another source of rotational wave-packet dephasing is centrifugal distortion, which becomes relevant when rotational states with high angular momentum, needed to get high degrees of alignment, are populated. This effect is not limited to asymmetric-top molecules and affects linear and symmetric-top molecules as well [27].

In this work, we extend the idea of multiple-pulse alignment to rigid, asymmetric-top molecules, omitting the effect of additional dephasing through centrifugal distortion. Specifically, we theoretically investigate the feasibility of enhancing one-dimensional alignment. We consider two different pulse trains, each consisting of four identical laser pulses. The pulses are equally separated by the revival period in the first pulse train. This strategy follows Ref. [15]. In the second train, pulses are separated such that the molecule experiences an additional kick when it reaches the maximum alignment induced by the previous pulse, resulting in a monotonic increase in the degree of alignment [28]. Furthermore, we point out the consequences of approximating an asymmetric-top rotor as a symmetric-top rotor. We then investigate four-pulse trains using elliptically polarized laser pulses and ask the questions whether one-dimensional alignment is enhanced in comparison to the use of linearly polarized pulses and if it is possible to create field-free three-dimensional alignment.

We do not review our numerical propagation method, which is described in Ref. [10]. In the following, we choose to subject the molecule SO_2 to an electric laser field,

$$\vec{E}(t) = \sqrt{8\pi\, I(t)/c}[\epsilon_x\, \vec{e}_x \cos(\omega t) + \epsilon_z\, \vec{e}_z \sin(\omega t)], \qquad (1)$$

where c is the speed of light, $I(t)$ is the cycle-averaged laser intensity, and ϵ_x and ϵ_z are the minor and major field components with $\epsilon_x^2 \leqslant \epsilon_z^2$ and $\epsilon_x^2 + \epsilon_z^2 = 1$. We set $\epsilon_x = 0$ to describe linearly polarized light. The molecule SO_2 has the

*Corresponding author

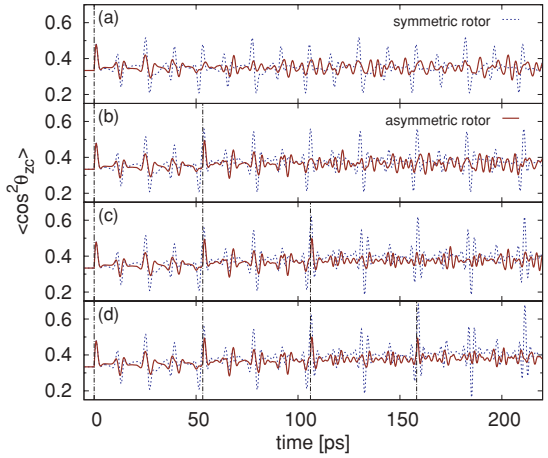

FIG. 1. (Color online) Alignment dynamics of SO_2 treated, respectively, as a symmetric-top rotor (dashed) and an asymmetric-top rotor (solid), at rotational temperature $T = 10$ K. From panels (a) to (d) the number of pulses successively increases from one to four. The linearly polarized laser pulses, which are indicated by vertical dashed lines, have a peak intensity of 20 TW/cm^2 and a pulse duration of 50 fs.

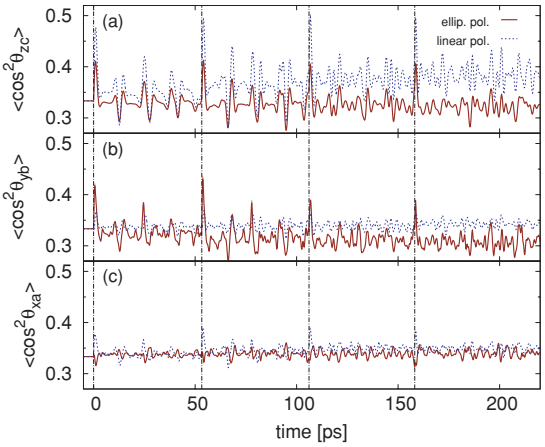

FIG. 2. (Color online) Alignment dynamics of SO_2 for linearly polarized (dashed) and elliptically polarized (solid) laser pulses with $\epsilon_z^2 = 0.5462$. The peak intensity associated with the z direction (20 TW/cm^2) is kept the same in both cases, as is the pulse duration of 50 fs. SO_2 is treated in both cases as an asymmetric-top rotor.

rotational constants $A = 0.3442\,\mathrm{cm}^{-1}$, $B = 0.2935\,\mathrm{cm}^{-1}$, and $C = 2.028\,\mathrm{cm}^{-1}$ [29–31] and polarizabilities $\alpha_{aa}^{\mathrm{pol}} = 20.80$ Å^3, $\alpha_{bb}^{\mathrm{pol}} = 18.66$ Å^3, and $\alpha_{cc}^{\mathrm{pol}} = 31.32$ Å^3 [32]. The nuclear spin statistical weights of SO_2 are 1 if $|J\tau M\rangle \in A, B_a$ and 0 if $|J\tau M\rangle \in B_c, B_b$, where $|J\tau M\rangle$ denotes a rotational eigenstate of an asymmetric-top rotor and B_a, B_b, B_c, and A are irreducible representations of D_2 (isomorphic to C_{2v}) [33].

Figure 1 presents the alignment dynamics of SO_2, treated as a symmetric-top rotor and an asymmetric-top rotor, respectively, for a sequence of up to four linearly polarized, consecutive Gaussian-shaped laser pulses spaced equally by $\tau_{\mathrm{rot}} = 1/(A + B)$. The laser intensity is 20 TW/cm^2 and the pulse duration (FWHM) is 50 fs. The chosen rotational temperature of 10 K is a realistic estimate that has been experimentally achieved for SO_2 [25]. The symmetric-top rotor is approximated by symmetrization of the a and b axes, that is, $A, B \to (A + B)/2$ and $\alpha_{aa}^{\mathrm{pol}}, \alpha_{bb}^{\mathrm{pol}} \to (\alpha_{aa}^{\mathrm{pol}} + \alpha_{bb}^{\mathrm{pol}})/2$.

In the symmetric-top model, the molecules show the expected revival dynamics in Fig. 1. By increasing the number of laser pulses [Figs. 1(a)–1(d)], the maximum alignment increases monotonically from $\langle\cos^2\theta_{zc}\rangle = 0.52$ (one pulse) to $\langle\cos^2\theta_{zc}\rangle = 0.68$ (four pulses). When SO_2 is treated exactly as an asymmetric-top rotor, no regularly repeating alignment motion can be identified. The dephasing, due to the incommensurable spacing between the rotational energy levels, increases with time and is the reason why the maximum alignment achieved after the fourth laser pulse is weaker than the alignment created directly after the third laser pulse [cf. Fig. 1(d)].

Another question we want to address is whether multiple elliptically polarized laser pulses can be used to create three-dimensional alignment in the same manner as linearly polarized laser pulses can be used to achieve one-dimensional alignment. Figure 2 shows a direct comparison of the alignment of SO_2 (treated as an asymmetric-top rotor) for four linearly ($\epsilon_x = 0$) and four elliptically polarized laser pulses ($\epsilon_z^2 = 0.5462$). The specific value of ϵ_z^2 for elliptically polarized light is chosen such that optimal three-dimensional alignment is obtained [34]. The laser intensity associated with the z direction is the same for both types of polarized laser pulses. The total intensity of the elliptically polarized laser pulses is adjusted accordingly.

The additional electric field in the perpendicular x direction decreases the $\langle\cos^2\theta_{zc}\rangle$ alignment [cf. Fig. 2(a)] and simultaneously increases the alignment of the body-fixed c axis in the x direction ($\langle\cos^2\theta_{xc}\rangle$). However, elliptically polarized laser pulses improve the alignment of the molecules in the elliptical polarization plane of the laser pulses (zx plane), which is given by $\langle\cos^2\theta_{yb}\rangle$ [see Fig. 2(b)]. The alignment dynamics of $\langle\cos^2\theta_{xa}\rangle$ are counterintuitive and show an antialignment effect rather than an alignment effect [cf. Fig. 2(c)]. By analyzing all $\langle\cos^2\theta_{lm}\rangle$, we find that each molecular axis is aligned or antialigned simultaneously in the x and z directions. From the relation $\sum_{m'}\langle\cos^2\theta_{lm'}\rangle = \sum_{l'}\langle\cos^2\theta_{l'm}\rangle = 1\,\forall\, l, m$, it follows that the alignment in the y direction is reversed from the alignment in the x and z directions. Since the molecular alignments $\langle\cos^2\theta_{zc}\rangle$ and $\langle\cos^2\theta_{xc}\rangle$ are strongly pronounced, the molecular a and b axes are antialigned in these two space-fixed directions and, hence, aligned in the y direction ($\langle\cos^2\theta_{ya}\rangle$ and $\langle\cos^2\theta_{yb}\rangle$). Only in the adiabatic limit would we see strong alignment in $\langle\cos^2\theta_{xa}\rangle, \langle\cos^2\theta_{yb}\rangle$, and $\langle\cos^2\theta_{zc}\rangle$.

Improving the degree of alignment of symmetric-top molecules by applying consecutive laser pulses at maximum alignment can be done either at the first alignment peak directly after the previous pulse or at later times at alignment revivals. In the case of asymmetric-top molecules, the accessibility of revivals is limited to the very first revivals (cf. Fig. 1) and the maximum achievable degree of alignment is reduced in comparison to the linear and symmetric-top rotor models. However, the dynamics immediately following the first laser

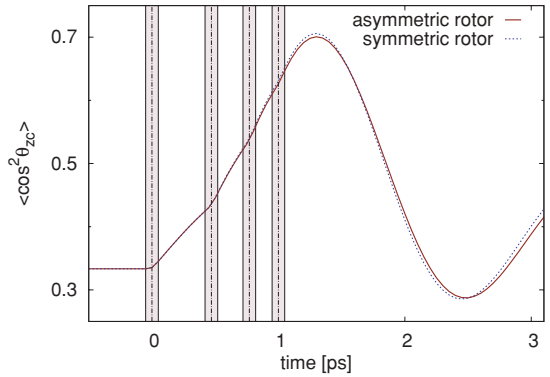

FIG. 3. (Color online) Alignment dynamics of SO_2 treated, respectively, as a symmetric-top rotor (dashed) and an asymmetric-top rotor (solid). The four laser pulses are linearly polarized with a peak intensity of 20 TW/cm^2. The shaded areas indicate the FWHM width of 50-fs pulses centered around the vertical, dashed lines.

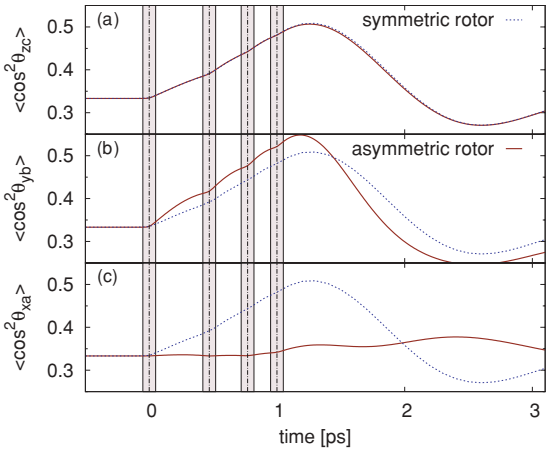

FIG. 4. (Color online) Alignment dynamics of SO_2 treated, respectively, as a symmetric-top rotor (dashed) and an asymmetric-top rotor (solid). The four laser pulses are elliptically polarized with $\epsilon_z^2 = 0.5462$, a peak intensity of 36.6 TW/cm^2 ($I_z = 20$ TW/cm^2), and a pulse duration of 50 fs.

pulse are almost identical for both rotor models, since the dephasing effects are still small. It is in this time frame that the very first alignment peak occurs. Therefore, applying subsequent laser pulses close to the very first laser pulse promises better alignment. In that way the alignment is increasing monotonically until it has reached its maximum degree of alignment. In Fig. 3 such a pulse sequence is presented. The alignment profiles for both rotor models are almost identical with a maximum alignment comparable with the revival kicking technique for symmetric-top rotors shown in Fig. 1(d). The alignment response, which is the time after a pulse until maximum alignment is reached, decreases with the number of pulses—and so does the spacing between neighboring laser pulses [28]. This limits the maximum number of laser pulses that may be employed to accomplish field-free alignment. However, the maximum degree of alignment for both rotor models differs by less than 1% in Fig. 3.

By exploiting the same method for elliptically polarized laser pulses, we find that the alignment dynamics for the symmetric-top and asymmetric-top rotor models are identical in terms of $\langle\cos^2\theta_{zc}\rangle$ [cf. Fig. 4(a)], as in the linearly polarized case (cf. Fig. 3). The alignment of the asymmetric-top rotor model in the polarization plane, which is characterized by $\langle\cos^2\theta_{yb}\rangle$, is enhanced compared to the symmetric-top rotor model [cf. Fig. 4(b)]. During all four laser pulses the alignment $\langle\cos^2\theta_{xa}\rangle$ stays almost isotropic and increases only slightly. However, $\langle\cos^2\theta_{xa}\rangle$ does not show any antialignment within the first few picoseconds [see Fig. 4(c)] like Fig. 2(c) shows for the revival-kicking pulse sequence. The lack of $\langle\cos^2\theta_{xa}\rangle$ alignment is not a problem of intensity; it is the result of the rich rotational dynamics of the asymmetric-top rotor SO_2. Only in the limit of adiabatic alignment does this motion cease and all three molecular axes become well aligned.

In conclusion, we studied multiple-pulse alignment of asymmetric-top molecules, using SO_2 as an example. We showed that approximating an asymmetric-top molecule as a symmetric-top rotor has significant consequences for the alignment dynamics; specifically, alignment revivals do not occur for asymmetric-top molecules. The dephasing of the rotational wave packet for asymmetric-top molecules limits the effectiveness of aligning the molecules by multiple pulses applied at alignment revivals. Enhanced alignment for asymmetric-top molecules can be better accomplished by a fast train of pulses. Here the time delays between consecutive pulses are small compared to the rotational time scale such that dephasing effects are minimized. Therefore, for this method the maximum degree of alignment is not affected by the more complex rotational dynamics of an asymmetric-top molecule. However, when elliptically polarized pulses are used, none of these approaches attains significant three-dimensional alignment or improves the one-dimensional alignment further. We conclude that a train of elliptically polarized laser pulses is not suitable for achieving field-free three-dimensional alignment.

We thank James P. Cryan, Christian Buth, and Ryan N. Coffee for inspiring discussions and Cassandra Hunt for comments on the manuscript. This work was supported by the Office of Basic Energy Sciences, US Department of Energy under Contract No. DE-AC02-06CH11357.

[1] C. Z. Bisgaard, O. J. Clarkin, G. Wu, A. M. D. Lee, O. Gessner, C. C. Hayden, and A. Stolow, Science **323**, 1464 (2009).

[2] E. R. Peterson, C. Buth, D. A. Arms, R. W. Dunford, E. P. Kanter, B. Krässig, E. C. Landahl, S. T. Pratt, R. Santra, S. H. Southworth, and L. Young, Appl. Phys. Lett. **92**, 094106 (2008).

[3] M. Plummer and J. F. McCann, J. Phys. B **30**, L401 (1997).

[4] I. V. Litvinyuk, K. F. Lee, P. W. Dooley, D. M. Rayner, D. M. Villeneuve, and P. B. Corkum, Phys. Rev. Lett. **90**, 233003 (2003).

[5] V. Kumarappan, L. Holmegaard, C. Martiny, C. B. Madsen, T. K. Kjeldsen, S. S. Viftrup, L. B. Madsen, and H. Stapelfeldt, Phys. Rev. Lett. **100**, 093006 (2008).

[6] D. G. Lappas and J. P. Marangos, J. Phys. B **33**, 4679 (2000).

[7] R. Velotta, N. Hay, M. B. Mason, M. Castillejo, and J. P. Marangos, Phys. Rev. Lett. **87**, 183901 (2001).

[8] J. Itatani, J. Levesque, D. Zeidler, Hiromichi Niikura, H. Ppin, J. C. Kieffer, P. B. Corkum, and D. M. Villeneuve, Nature (London) **432**, 867 (2004).

[9] J. C. H. Spence and R. B. Doak, Phys. Rev. Lett. **92**, 198102 (2004).

[10] S. Pabst, P. J. Ho, and R. Santra, Phys. Rev. A **81**, 043425 (2010).

[11] H. Stapelfeldt and T. Seideman, Rev. Mod. Phys. **75**, 543 (2003).

[12] B. J. Pearson, S. R. Nichols, and T. Weinacht, J. Chem. Phys. **127**, 131101 (2007).

[13] A. N. Markevitch, D. A. Romanov, S. M. Smith, H. B. Schlegel, M. Yu. Ivanov, and R. J. Levis, Phys. Rev. A **69**, 013401 (2004).

[14] M. Lezius, V. Blanchet, D. M. Rayner, D. M. Villeneuve, A. Stolow, and M. Yu. Ivanov, Phys. Rev. Lett. **86**, 51 (2001).

[15] J. P. Cryan, P. H. Bucksbaum, and R. N. Coffee, Phys. Rev. A **80**, 063412 (2009).

[16] M. Leibscher, I. Sh. Averbukh, and H. Rabitz, Phys. Rev. Lett. **90**, 213001 (2003).

[17] C. Z. Bisgaard, M. D. Poulsen, E. Péronne, S. S. Viftrup, and H. Stapelfeldt, Phys. Rev. Lett. **92**, 173004 (2004).

[18] S. Guérin, A. Rouzée, and E. Hertz, Phys. Rev. A **77**, 041404(R) (2008).

[19] C. Buth and R. Santra, J. Chem. Phys. **129**, 134312 (2008).

[20] A. Rouzée, S. Guérin, V. Boudon, B. Lavorel, and O. Faucher, Phys. Rev. A **73**, 033418 (2006).

[21] E. Péronne, M. D. Poulsen, C. Z. Bisgaard, H. Stapelfeldt, and T. Seideman, Phys. Rev. Lett. **91**, 043003 (2003).

[22] E. Péronne, M. D. Poulsen, H. Stapelfeldt, C. Z. Bisgaard, E. Hamilton, and T. Seideman, Phys. Rev. A **70**, 063410 (2004).

[23] M. D. Poulsen, E. Péronne, H. Stapelfeldt, C. Z. Bisgaard, S. S. Viftrup, E. Hamilton, and T. Seideman, J. Chem. Phys. **121**, 783 (2004).

[24] L. Holmegaard, S. S. Viftrup, V. Kumarappan, C. Z. Bisgaard, H. Stapelfeldt, E. Hamilton, and T. Seideman, Phys. Rev. A **75**, 051403(R) (2007).

[25] K. F. Lee, D. M. Villeneuve, P. B. Corkum, A. Stolow, and J. G. Underwood, Phys. Rev. Lett. **97**, 173001 (2006).

[26] J. G. Underwood, B. J. Sussman, and A. Stolow, Phys. Rev. Lett. **94**, 143002 (2005).

[27] D. W. Broege, R. N. Coffee, and P. H. Bucksbaum, Phys. Rev. A **78**, 035401 (2008).

[28] I. Sh. Averbukh and R. Arvieu, Phys. Rev. Lett. **87**, 163601 (2001).

[29] G. Herzberg, *Molecular Spectra and Molecular Structure: III. Electronic Spectra and Electronic Structure of Polyatomic Molecules* (D. Van Nostrand Company, Toronto, 1966).

[30] H. M. Frey, P. Beaud, T. Gerber, B. Mischler, P. P. Radi, and A. P. Tzannis, J. Raman Spectrosc. **31**, 71 (2000).

[31] In contrast to spectroscopic convention, the rotational constants A, B, and C are not ordered according to magnitude. We reorder the rotational constants such that for perfect alignment the molecular frame (a,b,c) coincides with the space-fixed frame (x,y,z).

[32] D. Xenides and G. Maroulis, Chem. Phys. Lett. **319**, 618 (2000).

[33] P. R. Bunker and P. Jensen, *Molecular Symmetry and Spectroscopy*, 2nd ed. (National Research Council of Canada, 1998).

[34] A. Rouzée, S. Guérin, O. Faucher, and B. Lavorel, Phys. Rev. A **77**, 043412 (2008).

Erratum: Alignment of Asymmetric-Top Molecules Using Multiple-Pulse Trains [Phys. Rev. A 81, 065401 (2010)]

Stefan Pabst and Robin Santra

Published in Phys. Rev. A **82**, 049901(E) (2010)

Original publication: http://link.aps.org/doi/10.1103/PhysRevA.82.049901

PHYSICAL REVIEW A **82**, 049901(E) (2010)

Erratum: Alignment of asymmetric-top molecules using multiple-pulse trains [Phys. Rev. A 81, 065401 (2010)]

Stefan Pabst* and Robin Santra†

(Received 30 September 2010; published 15 October 2010)

DOI: 10.1103/PhysRevA.82.049901 PACS number(s): 37.10.Vz, 42.50.Hz, 42.50.Md, 33.20.Sn, 99.10.Cd

In the left column of p. 2 of our original article, we used incorrect units for the polarizabilities. The polarizabilities should read $\alpha_{aa}^{\mathrm{pol}} = 20.80 a_0^3$, $\alpha_{bb}^{\mathrm{pol}} = 18.66 a_0^3$, and $\alpha_{cc}^{\mathrm{pol}} = 31.32 a_0^3$, where a_0 denotes the Bohr radius. We thank Varun Makhija and Vinod Kumarappan from Kansas State University for bringing this issue to our attention. All results shown in the article were calculated with the correct units.

*Present address: Center for Free-Electron Laser Science, DESY and University of Hamburg, Germany.
†Corresponding author; present address: Center for Free-Electron Laser Science, DESY and University of Hamburg, Germany.

Chapter 5

Ultrafast Ionization Dynamics in Noble Gas Atoms

5.1 Implementation of the Time-Dependent Configuration-Interaction Singles Method for Atomic Strong-Field Processes

Loren Greenman, Phay J. Ho, Stefan Pabst, Eugene Kamarchik, David A. Mazziotti, and Robin Santra

Published in Phys. Rev. A **82**, 023406 (2010)

Original publication: http://link.aps.org/doi/10.1103/PhysRevA.82.023406

Statement of Contributions

The derivation of the CAP correction of the ion density matrix has been done by myself. Phay J. Ho and I were involved in co-developing and debugging the TDCIS program of Loren Greenman.

PHYSICAL REVIEW A **82**, 023406 (2010)

Implementation of the time-dependent configuration-interaction singles method for atomic strong-field processes

Loren Greenman,[1] Phay J. Ho,[2] Stefan Pabst,[2,3,*] Eugene Kamarchik,[1] David A. Mazziotti,[1,†] and Robin Santra[2,4,‡]

[1]*Department of Chemistry and The James Franck Institute, The University of Chicago, Chicago, Illinois 60637, USA*

[2]*Argonne National Laboratory, Argonne, Illinois 60439, USA*

[3]*Institut für Theoretische Physik, Universität Erlangen-Nürnberg, D-91058 Erlangen,Germany*

[4]*Department of Physics, The University of Chicago, Chicago, Illinois 60637, USA*

(Received 8 June 2010; published 4 August 2010)

We present an implementation of the time-dependent configuration-interaction singles (TDCIS) method for treating atomic strong-field processes. In order to absorb the photoelectron wave packet when it reaches the end of the spatial grid, we add to the exact nonrelativistic many-electron Hamiltonian a radial complex absorbing potential (CAP). We determine the orbitals for the TDCIS calculation by diagonalizing the sum of the Fock operator and the CAP using a flexible pseudospectral grid for the radial degree of freedom and spherical harmonics for the angular degrees of freedom. The CAP is chosen such that the occupied orbitals in the Hartree-Fock ground state remain unaffected. Within TDCIS, the many-electron wave packet is expanded in terms of the Hartree-Fock ground state and its single excitations. The virtual orbitals satisfy nonstandard orthogonality relations, which must be taken into consideration in the calculation of the dipole and Coulomb matrix elements required for the TDCIS equations of motion. We employ a stable propagation scheme derived by second-order finite differencing of the TDCIS equations of motion in the interaction picture and subsequent transformation to the Schrödinger picture. Using the TDCIS wave packet, we calculate the expectation value of the dipole acceleration and the reduced density matrix of the residual ion. The technique implemented will allow one to study electronic channel-coupling effects in strong-field processes.

DOI: 10.1103/PhysRevA.82.023406 PACS number(s): 32.80.Rm, 31.15.A−, 02.70.−c

I. INTRODUCTION

With the invention of the technique of chirped pulse amplification (CPA), modern high-power laser systems can now easily produce high repetition-rate femtosecond laser pulses, leading to peak optical intensities greater than 10^{14} W/cm^2 or as high as 10^{20} W/cm^2 in the focal region. The availability of such intense radiation has opened up new and important venues of research in atomic, molecular, and optical (AMO) physics. High photon-flux radiation can drive atomic and molecular systems into nonlinear regimes and initiate nonperturbative single-atom and single-molecule intense-field phenomena, including multiphoton ionization [1–17], above-threshold ionization (ATI) [18–27], high-harmonic generation (HHG) [28–42], and nonsequential multielectron ionization [43–52].

Understanding these field-induced phenomena has tremendous technological implications. HHG, for example, has been used as a convenient tool for the production of coherent XUV and soft x-ray radiation [33–37] and attosecond pulses [53,54]. These novel light sources have enabled ultrafast molecular probing [55–72] and the study of AMO physics in the attosecond regime [53,54,73–77]. As a result, various theoretical methods have been developed to investigate strong-field AMO physics. Among these methods, solving the time-dependent Schrödinger equation provides the most accurate description. Unfortunately, this method is practically unfeasible for many-electron atoms and molecules beyond helium. Hence, many efforts have been devoted to one-electron formulations of the strong-field problems.

These one-electron formulations are guided by the first step in all the strong-field processes, in which an electron is pulled away from the parent ion by the laser field. Treating this electron as the only active electron has been shown to be sufficient for accurate prediction of single-ionization production [7,78–80], cutoff in the HHG spectrum [31,80], and ATI photoelectron spectra [79] in different atoms. In spite of its successes, this single-active-electron (SAE) approach has its limitations. First, it cannot account for multielectron effects in strong-field processes. For instance, Gordon *et al.* have shown that the accurate inclusion of multielectron effects is necessary to explain the scaling of the HHG radiation intensity with the atomic number [39]. Second, the SAE theory lacks the dynamical description of the residual ion by focusing only on the wave-packet dynamics of the excited electron. In particular, the theory offers only a single-channel description, in which the ion created is treated to be in a single ionic eigenstate.

Recent experimental efforts have now begun to require an accurate strong-field description of the residual ion. It was revealed from the ATI photo-electron spectrum that Xe^+ ions in both the $5p_{3/2}^{-1}$ ground-state and the $5p_{1/2}^{-1}$ excited manifolds were generated in an intense optical pulse [81,82]. Also, experiments at the Advanced Photon Source (APS) using resonant x-ray absorption techniques have unveiled the alignment dynamics of the residual Kr^+ ions created in a strong optical field [83,84]. Furthermore, complete quantum ion state populations, which are the diagonal entries of the ion density matrix in the ion eigenstates basis, were measured experimentally and confirmed theoretically [85,86].

*Present address: Center for Free-Electron Laser Science, DESY and University of Hamburg, Germany.

†damazz@uchicago.edu

‡Corresponding author: robin.santra@cfel.de; present address: Center for Free-Electron Laser Science, DESY and University of Hamburg, Germany.

An approximate one-electron approach that goes beyond the SAE treatment is time-dependent configuration interaction with single excitations (TDCIS). This is an *ab initio* electronic-structure technique, where the time-dependent wave function is restricted to spin-singlet conserving single-particle excitations from the ground-state determinant. Rohringer and coworkers have shown that TDCIS can be formulated as an effective one-electron theory with coupled channels [87]. This method includes the description of the electronic structure of many-electron atoms and molecules through the Fock operator and allows the determination of the ion density matrix, both the diagonal and off-diagonal elements. Knowledge of the off-diagonal matrix elements reveals the coherence properties associated with the electronic wave-packet dynamics of the residual ion [85,86,88,89]. Using a one-dimensional helium model in a strong laser field, it was shown that TDCIS is superior to the SAE approach [87]. There are other rigorous effective one-electron approaches, including the single-configuration and multi-configuration time-dependent Hartree-Fock methods [78,90–92] and time-dependent density-functional theory in the Kohn-Sham formulation [93,94]. These methods have known limitations and challenges [95–99]. Recently, Spanner and Patchkovskii used a set of coupled time-dependent single-particle Schrödinger equations derived from a multielectron wave-function ansatz to examine multielectron effects in strong-field one-electron ionization processes [100].

The purpose of this paper is to describe a full numerical implementation of the three-dimensional TDCIS method with an added radial complex absorbing potential (CAP). A set of complex orbitals for the TDCIS calculation is determined by diagonalizing the sum of the Fock operator and the CAP using a flexible pseudospectral grid for the radial degree of freedom and spherical harmonics for the angular degrees of freedom. We found that this complex-orbital formulation of TDCIS has computational advantages, because it allows stable propagation of the TDCIS wave packet. Atomic units are used throughout.

II. THEORETICAL BACKGROUND

In this section, we provide the theoretical background for a complex-orbital formulation of TDCIS. We start in Sec. II A with the general description of an atom in linearly polarized laser fields within the configuration-interaction singles (CIS) model. Then, an expression for calculating expectation values and the derivation of the reduced ion density are presented in Secs. II C and II D, respectively. In Sec. II E we discuss the Hartree-Fock equations for closed-shell atoms in the presence of a CAP.

A. TDCIS with a CAP

Within the CIS model, excitations beyond a particle-hole (1p-1h) excitation $|\Phi_i^a\rangle$ with respect to the ground state, which is in our case the Hartree-Fock (HF) ground state $|\Phi_0\rangle$, are not considered. Therefore, the wave packet is written in terms of $|\Phi_0\rangle$ and $|\Phi_i^a\rangle$,

$$|\Psi(t)\rangle = \alpha_0(t)|\Phi_0\rangle + \sum_{i,a} \alpha_i^a(t)\big|\Phi_i^a\big\rangle, \tag{1}$$

$$|\Phi_i^a\rangle = \frac{1}{\sqrt{2}}\{\hat{c}_{a+}^\dagger \hat{c}_{i+} + \hat{c}_{a-}^\dagger \hat{c}_{i-}\}|\Phi_0\rangle, \tag{2}$$

where i,j,k,l symbolize occupied orbitals, a,b,c,d symbolize virtual orbitals, and p,q,r,s stand for occupied or virtual orbitals. The operators $\hat{c}_{p\sigma}^\dagger$ and $\hat{c}_{p\sigma}$ create and annihilate electrons, respectively, in the spin orbital $|\varphi_{p\sigma}\rangle$, which is an eigenstate of the modified Fock operator

$$\hat{F}_{\mathrm{CAP}}|\varphi_{p\sigma}\rangle = \varepsilon_p|\varphi_{p\sigma}\rangle, \tag{3a}$$

$$\hat{F}_{\mathrm{CAP}} = \hat{F} - i\eta\hat{W}, \tag{3b}$$

where $\hat{F}$ is the Fock operator and $-i\eta\hat{W}$ is the CAP.

The full Hamiltonian of our system is

$$\hat{H}(t) = \hat{F}_{\mathrm{CAP}} + \hat{V}_C - \hat{V}_{\mathrm{HF}} - E_{\mathrm{HF}} - \mathcal{E}(t)\hat{z}, \tag{4}$$

where $\hat{V}_C$ is the electron-electron Coulomb interaction, $\hat{V}_{\mathrm{HF}}$ is the Hartree-Fock mean-field potential, E_{HF} is the Hartree-Fock ground-state energy, $\hat{z}$ is the dipole operator, and $\mathcal{E}(t)$ is the electric field component of the strong-field laser pulse.

By projecting the time-dependent Schrödinger equation onto the states $|\Phi_0\rangle$ and $|\Phi_i^a\rangle$, the equations of motion of the expansion coefficients $\alpha_0(t)$ and $\alpha_i^a(t)$ are obtained as

$$i\dot{\alpha}_0(t) = -\sqrt{2}\mathcal{E}(t)\sum_{i,a}\alpha_i^a(t)z_{(i,a)}, \tag{5a}$$

$$\begin{aligned} i\dot{\alpha}_i^a(t) &= (\varepsilon_a - \varepsilon_i)\alpha_i^a(t) + \sum_{i',a'}\alpha_{i'}^{a'}(t)(2v_{(a,i',i,a')} - v_{(a,i',a',i)}) \\ &\quad - \mathcal{E}(t)\left\{\sqrt{2}\alpha_0(t)z_{(a,i)} + \sum_{a'}\alpha_i^{a'}(t)z_{(a,a')}\right. \\ &\quad \left. - \sum_{i'}\alpha_{i'}^a(t)z_{(i',i)}\right\}. \end{aligned} \tag{5b}$$

The projection is done with respect to the symmetric inner product discussed in Sec. II C. The matrix elements in Eqs. (5) are defined via this symmetric inner product [101]:

$$z_{(p,q)} = (\varphi_p|\hat{z}|\varphi_q), \tag{6a}$$

$$v_{(p,q,r,s)} = (\varphi_p\varphi_q|1/\hat{r}_{12}|\varphi_r\varphi_s). \tag{6b}$$

We include parentheses in the subscripts of these matrix elements in order to differentiate them from

$$z_{p,q} = \langle\varphi_p|\hat{z}|\varphi_q\rangle, \tag{7a}$$

$$v_{p,q,r,s} = \langle\varphi_p\varphi_q|1/\hat{r}_{12}|\varphi_r\varphi_s\rangle, \tag{7b}$$

which are defined by the standard Hermitian inner product. Explicit expressions for the matrix elements in Eqs. (5) may be found in the Appendix.

B. Complex absorbing potential

When the wave packet reaches the end of the numerical grid, artificial reflections arise. These lead to unphysical results, but can be suppressed by applying a complex absorbing potential (CAP) [102–107] near the end of the grid. As a result, the CAP only affects virtual orbitals. Occupied orbitals are localized near the origin and, therefore, are not influenced by the CAP. Additionally, the CAP does not mix occupied with virtual orbitals. The CAP strength η has to be chosen carefully to avoid reflections either off the grid wall or off the CAP [105,107]. The explicit form of our CAP is

$$W(r) = h(r - r_{\mathrm{abs}})(r - r_{\mathrm{abs}})^2, \tag{8}$$

where $h(x)$ is the Heaviside step function, and r is the distance from the origin. This CAP is zero until a radius r_{abs}, after which it is a quadratically growing potential.

C. Expectation values

Since $\hat{F}_{\text{CAP}}$ is not Hermitian, the orthogonality relations for its eigenstates are not given in terms of the ordinary Hermitian inner product. If $|\varphi_p\rangle \equiv |\varphi_p)$ is a right eigenvector of $\hat{F}_{\text{CAP}}$, then $\langle\varphi_p|$ is generally not a left eigenvector. There is, nevertheless, a one-to-one mapping between right and left eigenvectors. The left eigenvector corresponding to $|\varphi_p\rangle$ is denoted $(\varphi_p|$. The corresponding orthogonality relations read

$$(\varphi_p|\varphi_q) = (\varphi_p|\varphi_q\rangle = \delta_{p,q}. \tag{9}$$

From the orthogonality relations of the orbitals follow the orthogonality relations of the 1p-1h excitations,

$$\left(\Phi_i^a\middle|\Phi_j^b\right) = \left(\Phi_i^a\middle|\Phi_j^b\right\rangle = \delta_{a,b}\delta_{i,j}. \tag{10}$$

Since the $|\Phi_i^a\rangle$ are not orthogonal with respect to the Hermitian inner product, we define an overlap integral between 1p-1h excitations as

$$\left\langle\Phi_i^a\middle|\Phi_j^b\right\rangle = \left\langle\Phi_i^a\middle|\Phi_j^b\right) = \delta_{i,j}\langle\varphi_a|\varphi_b\rangle = \delta_{i,j}o_{a,b}. \tag{11}$$

Since the complex absorbing potential does not affect the occupied orbitals φ_i, the orthogonality relation between different φ_i survives in the Hermitian inner product in Eq. (11).

The expectation value of an operator $\hat{A}$ is defined via the Hermitian inner product. By expanding $\langle\Psi(t)|\hat{A}|\Psi(t)\rangle$ using Eq. (1), we obtain

$$\begin{aligned}\langle A\rangle = {} & |\alpha_0|^2 2\sum_j A_{j,j} + \sum_{i,a} 2\sqrt{2}\,\mathrm{Re}\left(\alpha_0^*\alpha_i^a A_{i,a}\right) \\ & + \sum_{i,a,a'} \mathrm{Re}\left(\alpha_i^{a*}\alpha_i^{a'} A_{a,a'}\right) - \sum_{i,i',a,a'} \mathrm{Re}\left(\alpha_i^{a*}\alpha_{i'}^{a'} A_{i',i} o_{a,a'}\right) \\ & + \sum_{i,a,a'} \mathrm{Re}\left(\alpha_i^{a*}\alpha_i^{a'} o_{a,a'} 2\sum_j A_{j,j}\right).\end{aligned} \tag{12}$$

In order to compute the dipole acceleration, which is required for describing high-harmonic generation, it is possible to calculate the expectation value of the dipole moment and then calculate its second time derivative [96]. Alternatively, the expectation value of the dipole acceleration can be calculated directly. To this end, we employ the dipole acceleration operator obtained using the exact atomic Hamiltonian [39,108]. In the atomic case, assuming that the laser field is linearly polarized along the z axis, this operator is given by

$$\hat{a} = \frac{Z\cos\theta}{\hat{r}^2}, \tag{13}$$

where Z is the nuclear charge. Since atomic eigenstates are parity eigenstates, it follows that $a_{i,i} = 0$. This simplifies the evaluation of Eq. (12) when $\hat{A} = \hat{a}$.

D. Reduced ion density matrix

In order to construct the reduced ion density matrix (IDM) from the state $|\Psi(t)\rangle$, the trace over the unobserved photoelectron of the total density matrix $\hat{\tilde{\rho}}(t)$ has to be performed [109]:

$$\hat{\tilde{\rho}}^{\text{IDM}}(t) = \mathrm{Tr}_a[\hat{\tilde{\rho}}(t)], \tag{14a}$$

$$\hat{\tilde{\rho}} = |\Psi(t)\rangle\langle\Psi(t)|, \tag{14b}$$

where Tr_a stands for the trace over all virtual orbitals a [cf. Eq. (16a)] and $\hat{\tilde{\rho}}^{\text{IDM}}(t)$ symbolizes the ion density matrix. Since the virtual orbitals do not obey the Hermitian orthogonality relations [see Eqs. (10) and (11)], we have to be careful to define the trace in Eq. (14a). The explicit form of the density matrix can be derived from the norm $||\Psi(t)||^2$,

$$\begin{aligned}\langle\Psi(t)|\Psi(t)\rangle &= \sum_I \langle\Psi(t)|\Phi_I\rangle(\Phi_I|\Psi(t)\rangle \\ &= \sum_I (\Phi_I|\Psi(t)\rangle\langle\Psi(t)|\Phi_I) = \mathrm{Tr}[\hat{\tilde{\rho}}(t)],\end{aligned} \tag{15}$$

where Tr stands for the trace over the entire configuration space I, i.e., all 1p-1h excitations Φ_i^a and the HF ground state Φ_0. Based on this, natural definitions of the traces over only occupied and only virtual orbitals in the 1p-1h-configuration space, which are symbolized by Tr_i and Tr_a, respectively, are

$$\{\mathrm{Tr}_a[\hat{\tilde{\rho}}(t)]\}_{i,j} = \sum_a \left(\Phi_i^a|\Psi(t)\rangle\langle\Psi(t)|\Phi_j^a\right), \tag{16a}$$

$$\{\mathrm{Tr}_i[\hat{\tilde{\rho}}(t)]\}_{a,b} = \sum_i \left(\Phi_i^a|\Psi(t)\rangle\langle\Psi(t)|\Phi_i^b\right). \tag{16b}$$

Hence, the matrix elements of $\hat{\tilde{\rho}}^{\text{IDM}}(t)$ have the form

$$\tilde{\rho}_{i,j}^{\text{IDM}}(t) = \sum_a \left(\Phi_i^a|\Psi(t)\rangle\langle\Psi(t)|\Phi_j^a\right) = \sum_{a,b} \alpha_i^a(t)\left[\alpha_j^b(t)\right]^* o_{b,a}, \tag{17}$$

where we have used the explicit form of the wave function [cf. Eq. (1)]. To analyze the impact of the CAP on the dynamics of $\hat{\tilde{\rho}}(t)$ and $\hat{\tilde{\rho}}^{\text{IDM}}(t)$, it is convenient to go into the interaction picture (labeled I)

$$|\Psi_I(t)\rangle = e^{i\hat{F}t}|\Psi(t)\rangle, \tag{18a}$$

$$\hat{A}_I = e^{i\hat{F}t}\hat{A}e^{-i\hat{F}t}, \tag{18b}$$

where $\hat{A}$ stands for any operator in the Schrödinger picture. The time evolution of $|\Psi_I(t)\rangle$ is given by

$$i\frac{\partial}{\partial t}|\Psi_I(t)\rangle = (\hat{V}_{C,I} - \hat{V}_{\text{HF},I} - E_{\text{HF}} - \mathcal{E}(t)\hat{z}_I - i\eta\hat{W}_I)|\Psi_I(t)\rangle. \tag{19}$$

Because of the CAP, the norm $||\Psi_I(t)||^2$ is not conserved. That affects the time evolution of the trace of the IDM

$$\begin{aligned}\frac{\partial}{\partial t}\mathrm{Tr}_i\left[\hat{\tilde{\rho}}_I^{\text{IDM}}(t)\right] + \frac{\partial}{\partial t}|\alpha_0(t)|^2 &= \frac{\partial}{\partial t}\langle\Psi_I(t)|\Psi_I(t)\rangle \\ &= -2\eta\,\mathrm{Tr}[\hat{W}_I\hat{\tilde{\rho}}_I(t)],\end{aligned} \tag{20}$$

where $\hat{\tilde{\rho}}_I(t) = |\Psi_I(t)\rangle\langle\Psi_I(t)|$. Since the probability that there is no hole ($|\alpha_0(t)|^2$) and the probability that there is a hole ($\mathrm{Tr}_i[\hat{\tilde{\rho}}_I^{\text{IDM}}(t)]$) should add up to one, we must correct $\hat{\tilde{\rho}}_I^{\text{IDM}}(t)$ for the loss of norm.

In order to understand how to construct a corrected IDM, $\hat{\rho}_I^{\mathrm{IDM}}(t)$, that does not lose norm over time and describes the full interaction dynamics of the electrons, we have to analyze the equations of motion (von Neumann equations) of $\hat{\tilde{\rho}}_I(t)$ and $\hat{\tilde{\rho}}_I^{\mathrm{IDM}}(t)$

$$\frac{\partial}{\partial t}\hat{\tilde{\rho}}_I(t) = -i[\hat{V}_{C,I} - \hat{V}_{\mathrm{HF},I} - \mathcal{E}(t)\hat{z}_I, \hat{\tilde{\rho}}_I(t)] - \eta\{\hat{\tilde{\rho}}_I(t), \hat{W}_I\}, \tag{21a}$$

$$\frac{\partial}{\partial t}\hat{\tilde{\rho}}_I^{\mathrm{IDM}}(t) = -i\mathrm{Tr}_a\big[[\hat{V}_{C,I} - \hat{V}_{\mathrm{HF},I} - \mathcal{E}(t)\hat{z}_I, \hat{\tilde{\rho}}_I(t)]\big] - 2\eta\mathrm{Tr}_a[\hat{W}_I\hat{\tilde{\rho}}_I(t)], \tag{21b}$$

where $\{\cdot,\cdot\}$ stands for the anticommutator. Equation (21a) can be derived by taking the time derivative of Eq. (14b) and using Eq. (19). In addition, we use the fact that

$$\mathrm{Tr}[\hat{W}_I\hat{\tilde{\rho}}_I(t)] = \mathrm{Tr}[\hat{\tilde{\rho}}_I(t)\hat{W}_I], \tag{22a}$$

$$\mathrm{Tr}[\hat{W}_I] = \mathrm{Tr}_a[\hat{W}_I]. \tag{22b}$$

Remember that $\hat{W}$ acts only on virtual orbitals. The first terms on the right-hand side of Eqs. (21) describe the dynamics of the system (imaginary prefactor), and the second terms are responsible for the norm decay of the density matrix (real prefactor).

In the case of no residual Coulomb interaction ($\hat{V}_{C,I} - \hat{V}_{\mathrm{HF},I} = 0$) and no electric field [$\mathcal{E}(t) = 0$], the correct density matrix has to be constant in time. The density matrix $\hat{\tilde{\rho}}_I(t)$ does not fulfill this requirement due to the CAP. Hence, the equation of motion in Eq. (21a) has to be corrected such that no term violates the norm conservation. The corresponding von Neumann equations of the corrected density matrix and the corrected IDM are

$$\frac{\partial}{\partial t}\hat{\rho}_I(t) = \frac{\partial}{\partial t}\hat{\tilde{\rho}}_I(t) + \eta\{\hat{\tilde{\rho}}_I(t), \hat{W}_I\} = -i[\hat{V}_{C,I} - \hat{V}_{\mathrm{HF},I} - \mathcal{E}(t)\hat{z}_I, \hat{\tilde{\rho}}_I(t)], \tag{23a}$$

$$\frac{\partial}{\partial t}\hat{\rho}_I^{\mathrm{IDM}}(t) = \frac{\partial}{\partial t}\hat{\tilde{\rho}}_I^{\mathrm{IDM}}(t) + 2\eta\mathrm{Tr}_a[\hat{W}_I\hat{\tilde{\rho}}_I(t)] = -i\mathrm{Tr}_a\big[[\hat{V}_{C,I} - \hat{V}_{\mathrm{HF},I} - \mathcal{E}(t)\hat{z}_I, \hat{\tilde{\rho}}_I(t)]\big]. \tag{23b}$$

The corrected density matrices, as defined in Eqs. (23), experience no damping. The norm of $\hat{\rho}_I(t)$ is conserved, which can be seen by taking the trace of Eq. (23a). By just taking the trace over all 1p-1h excitations, Eq. (23a) reduces to

$$\frac{\partial}{\partial t}\big(\mathrm{Tr}_i\big[\hat{\rho}_I^{\mathrm{IDM}}(t)\big]\big) = -i\mathrm{Tr}_i\mathrm{Tr}_a\big[[\hat{V}_{C,I} - \hat{V}_{\mathrm{HF},I} - \mathcal{E}(t)\hat{z}_I, \hat{\tilde{\rho}}_I(t)]\big], = -i\langle\Phi_0|[\mathcal{E}(t)\hat{z}_I, \hat{\tilde{\rho}}^I(t)]|\Phi_0\rangle = -\frac{\partial}{\partial t}|\alpha_0(t)|^2. \tag{24}$$

In the second step in Eq. (24), we used

$$\big(\Phi_i^a\big|\hat{V}_{C,I} - \hat{V}_{\mathrm{HF},I}\big|\Phi_0\big) = \big(\Phi_i^a\big|\hat{z}_I\big|\Phi_i^a\big) = (\Phi_0|\hat{z}_I|\Phi_0) = 0, \quad \forall a,i. \tag{25}$$

Hence, we can conclude that after the pulse $\mathcal{E}(t) = 0$, where $\frac{\partial}{\partial t}|\alpha_0(t)|^2 = 0$, the trace of $\hat{\rho}_I^{\mathrm{IDM}}(t)$ is constant in time. In addition, $\hat{\rho}_I(t)$ fulfills the requirement [see Eq. (24)] that the probability of leaving the atom in its ground state ($|\alpha_0(t)|^2$) and the probability to create 1p-1h excitations ($\mathrm{Tr}_i[\hat{\rho}_I^{\mathrm{IDM}}(t)]$) add up to one at all times.

Since $\hat{\tilde{\rho}}^{\mathrm{IDM}}(t)$ can be calculated quite efficiently from the solutions of Eqs. (5a) and (5b), it is sufficient to calculate the correction matrix

$$\delta\hat{\rho}_I^{\mathrm{IDM}}(t) = \hat{\rho}_I^{\mathrm{IDM}}(t) - \hat{\tilde{\rho}}_I^{\mathrm{IDM}}(t). \tag{26}$$

The equation of motion of $\delta\hat{\rho}_I^{\mathrm{IDM}}(t)$ can be derived from Eqs. (23b) and (26),

$$\frac{\partial}{\partial t}\delta\hat{\rho}_I^{\mathrm{IDM}}(t) = 2\eta\mathrm{Tr}_a[\hat{W}_I\hat{\tilde{\rho}}_I(t)] = -i\mathrm{Tr}_a\big[[-i\eta\hat{W}_I, \delta\hat{\rho}_I(t)]\big] + 2\eta\mathrm{Tr}_a[\hat{W}_I\hat{\tilde{\rho}}_I(t)], \tag{27}$$

where we used Eqs. (22) to insert a commutator that includes the CAP. In the Schrödinger picture, Eq. (27) transforms into

$$\frac{\partial}{\partial t}\delta\rho_{i,j}^{\mathrm{IDM}}(t) = i(\varepsilon_i - \varepsilon_j)\delta\rho_{i,j}^{\mathrm{IDM}}(t) + 2\eta\sum_{a,b} w_{b,a}\alpha_i^a(t)\big[\alpha_j^b(t)\big]^*. \tag{28}$$

Here, it was exploited that $\sum_c o_{b,c}w_{(c,a)} = \langle\varphi_b|\hat{W}|\varphi_a\rangle = w_{b,a}$. The solution to Eq. (28) is

$$\delta\rho_{i,j}^{\mathrm{IDM}}(t) = 2\eta\, e^{i(\varepsilon_i-\varepsilon_j)t}\int_{-\infty}^{t} dt' \sum_{a,b} w_{b,a}\,\alpha_i^a(t') \times \big[\alpha_j^b(t')\big]^* e^{-i(\varepsilon_i-\varepsilon_j)t'}, \tag{29}$$

and hence, we have found an expression for the corrected IDM,

$$\rho_{i,j}^{\mathrm{IDM}}(t) = \tilde{\rho}_{i,j}^{\mathrm{IDM}}(t) + 2\eta\, e^{i(\varepsilon_i-\varepsilon_j)t}\int_{-\infty}^{t} dt' \times \sum_{a,b} w_{b,a}\,\alpha_i^a(t')\big[\alpha_j^b(t')\big]^* e^{-i(\varepsilon_i-\varepsilon_j)t'}. \tag{30}$$

Equation (30) is identical to the definition of the IDM in Ref. [89], where the states $|\Phi_i^a\rangle$ are eigenstates of $\hat{F}$ rather than $\hat{F}_{\mathrm{CAP}}$ and fulfill different orthogonality relations. Therefore, it was not obvious that both sets of basis states lead to a formally identical expression. In contrast to Ref. [89], the exact Coulomb interaction is considered in the current treatment. As a consequence of the Coulomb interaction between the excited electron and the ion, the IDM in the interaction picture is not necessarily constant after the laser pulse is over. However, since within the one-hole configuration space, the one-hole channel states are eigenstates of the exact, laser-free Hamiltonian, the IDM in the interaction picture becomes constant if the excited electron is unbound and drifts away from the ion.

E. Atomic Hartree-Fock equations

The theory formulated in Secs. II A–II D holds for any electronic system where the Born-Oppenheimer approximation can be made. In the following, we focus our discussion on closed-shell atoms, where the total orbital and spin angular

momenta of the ground state are 0. The Fock operator for a closed-shell atom is given by [110]

$$\hat{F} = -\frac{1}{2}\nabla^2 - \frac{Z}{r} + \sum_i (2J_i - K_i), \tag{31}$$

which consists of a kinetic part $(-\nabla^2/2)$, a Coulomb potential due to the nucleus $(-Z/r)$, and direct $(2J_i)$ and exchange (K_i) Coulomb interactions between the electrons. The CAP used in this work (see Sec. II B) preserves the spherical symmetry of the atomic-structure problem, so that the one-electron eigenfunctions of $\hat{F}_{\rm CAP} = \hat{F} - i\eta\hat{W}$ may be written as a product of a (generally complex) radial function $u_{n,l}$ and a spherical harmonic $Y_{l,m}(\theta,\phi)$,

$$\langle r,\theta,\phi|\varphi_p\rangle = \langle r,\theta,\phi|\varphi_p\rangle = \varphi_p(r,\theta,\phi) = \frac{u_{n,l}(r)}{r} Y_{l,m}(\theta,\phi). \tag{32}$$

The $u_{n,l}$ satisfy the radial self-consistent-field equations,

$$\begin{aligned} &-\frac{1}{2}\frac{d^2u_{n,l}(r)}{dr^2} + \left\{\frac{l(l+1)}{2r^2} - \frac{Z}{r} - i\eta W(r)\right\} u_{n,l}(r) \\ &\quad + \sum_{n_o,l_o}(4l_o+2)v^{(0)}(n_o,l_o;n_o,l_o;r)u_{n,l}(r) \\ &\quad - \sum_{n_o,l_o}\sum_{L=|l-l_o|}^{l+l_o} C(l,L,l_o;0,0,0)^2 v^{(L)}(n_o,l_o;n,l;r)u_{n_o,l_o}(r) \\ &= \varepsilon_{n,l}u_{n,l}(r), \end{aligned} \tag{33}$$

where

$$v^{(L)}(n,l;n',l';r_1) = \int_0^\infty dr_2 \frac{r_<^L}{r_>^{L+1}} u_{n,l}(r_2)u_{n',l'}(r_2), \tag{34}$$

$$r_< = \min\{r_1,r_2\},\ \ r_> = \max\{r_1,r_2\}, \tag{35}$$

and $C(l_1,l_2,l_3;m_1,m_2,m_3)$ is a Clebsch-Gordan coefficient [111]. The summation over n_o,l_o in Eq. (33) extends over all subshells occupied in the Hartree-Fock ground state. In our calculations, the $u_{n,l}(r)$ are subject to the boundary conditions $u_{n,l}(0) = 0$ and $u_{n,l}(r_{\rm max}) = 0$. Here, $r_{\rm max}$ stands for the end point of the numerical grid employed (see Sec. III).

The Hartree-Fock mean-field potential, $\sum_i(2J_i - K_i)$, depends only on the occupied orbitals. However, all orbitals—occupied and virtual—are influenced by the mean-field potential. On the other hand, since the CAP we have introduced in Sec. II B starts far away from the origin such that occupied orbitals are not affected, the Hartree-Fock mean field does not depend on the CAP. Therefore, the occupied orbitals φ_i are eigenstates of both $\hat{F}$ and $\hat{F}_{\rm CAP}$, and may be calculated by solving the self-consistent-field problem, Eq. (33), assuming $\eta = 0$. After determining the φ_i, and thus fixing the Hartree-Fock mean field, a single diagonalization of $\hat{F}_{\rm CAP}$ for nonzero η gives the virtual orbitals φ_a.

The dual wave function of $|\varphi_p\rangle$ is $(\varphi_p|$ rather than $\langle\varphi_p|$, as discussed in Sec. II C. The matrix representation of Eq. (33) in a real basis gives rise to a complex symmetric eigenvalue problem [106] (see Sec. III B). From this and from Eq. (32), it follows that the spatial representation of $(\varphi_p|$ is given by

$$(\varphi_p|r,\theta,\phi\rangle = Y^*_{l_p,m_p}(\theta,\phi)\frac{u_{n_p,l_p}(r)}{r}. \tag{36}$$

The corresponding orthogonality relations were given in Sec. II C.

III. NUMERICAL IMPLEMENTATION

In this section, we present our numerical method to implement the three-dimensional TDCIS. In Sec. III A, our choice of the pseudospectral grid for the radial degree of freedom is discussed. Then, the atomic Hartree-Fock equations on the numerical grid are shown in Sec. III B. In Secs. III D and III E we describe propagation schemes based on two different ways of partitioning the Hamiltonian in Eq. (4).

A. Pseudospectral grid

Due to the nature of the strong-field problem, a grid is required with sufficient density near the atomic nucleus to describe the electronic structure of the atom, as well as far from the nucleus to describe the wave packet of the ejected electron. We have chosen a Gauss-Lobatto grid [112–115], which uses as its grid points the roots of the first derivative of the Nth-order Legendre polynomial (P'_N) as well as the selected end points of the grid ($r = 0$ and $r = r_{\rm max}$). We map these roots, which lie on the interval $x \in [-1,1]$, onto the radial space of the atom [113] using

$$r(x) = L\frac{1+x}{1-x+\zeta}. \tag{37}$$

L and ζ are parameters which control the extent of the grid and the density of the mapped points near the origin, respectively.

As described in Ref. [113], a wave function $\phi(x)$ may be approximated using a finite basis set of orthogonal polynomials. Using Legendre polynomials $P_l(x)$,

$$\phi(x) \approx \phi_N(x) = \sum_{l=0}^{N} a_l P_l(x), \tag{38}$$

which may also be written in terms of cardinal functions $g_k(x)$,

$$\phi_N(x) = \sum_{k=0}^{N} g_k(x)\phi_N(x_k). \tag{39}$$

Analytical functions of the wave function $\phi(x)$ can now be written in terms of analytical functions of the cardinal functions. For the Gauss-Lobatto grid points, the second derivative of $g_k(x)$, which is needed to calculate the radial kinetic energy, is (for grid points not at the edge of the grid, which we will not need)

$$g''_k(x_{k'}) = d^{(2)}_{k,k'}\frac{P_N(x_{k'})}{P_N(x_k)}, \tag{40}$$

where

$$\begin{aligned} d^{(2)}_{k,k} &= -\frac{N(N+1)}{3(1-x_k^2)}, \\ d^{(2)}_{k,k'} &= -\frac{2}{(x_k - x_{k'})^2}. \end{aligned} \tag{41}$$

B. Atomic Hartree-Fock equations in the Gauss-Lobatto grid

After employing the mapping of Eq. (37), the Hartree-Fock equations [Eq. (31)] read

$$\begin{aligned}
&-\frac{1}{2}\left(-\frac{r''(x)}{r'(x)^3}\frac{d}{dx}+\frac{1}{r'(x)^2}\frac{d^2}{dx^2}\right)u_{n,l}(x)\\
&\quad+\left\{\frac{l(l+1)}{2r(x)^2}-\frac{Z}{r(x)}-i\eta W(r(x))\right\}u_{n,l}(x)\\
&\quad+\sum_{n_o,l_o}(4l_o+2)v^{(0)}(n_o,l_o;n_o,l_o;r(x))u_{n,l}(x)\\
&\quad-\sum_{n_o,l_o}\sum_{L=|l-l_o|}^{l+l_o}C(lLl_o;000)^2v^{(L)}(n_o,l_o;n,l;r(x))u_{n_o,l_o}(x)\\
&=\varepsilon_{n,l}u_{n,l}(x). \qquad (42)
\end{aligned}$$

In order to symmetrize the Laplacian, the function $A(x)$ is introduced such that

$$A_{n,l}(x)=\sqrt{r'(x)}u_{n,l}(x). \qquad (43)$$

After expanding $A(x)$ with Eq. (39), substituting the relation $g_k(x_{k'})=\delta_{k,k'}$ and $A^k_{n,l}=A_{n,l}(x_k)/P_N(x_k)$ and using Eqs. (40) and (41), we obtain

$$\begin{aligned}
&\sum_k\left\{-\frac{1}{2}\frac{1}{r'(x_{k'})}d^{(2)}_{k,k'}\frac{1}{r'(x_{k'})}A^k_{n,l}\right\}\\
&\quad+\left\{\frac{l(l+1)}{2r(x_{k'})^2}-\frac{Z}{r(x_{k'})}-i\eta W(r(x_{k'}))\right\}A^{k'}_{n,l}\\
&\quad+\sum_{n_o,l_o}(4l_o+2)v^{(0)}(n_o,l_o;n_o,l_o;r(x_{k'}))A^{k'}_{n,l}\\
&\quad-\sum_{n_o,l_o}\sum_{L=|l-l_o|}^{l+l_o}C(lLl_o;000)^2v^{(L)}(n_o,l_o;n,l;r(x_{k'}))A^{k'}_{n_o,l_o}\\
&=\varepsilon_{n,l}A^{k'}_{n,l}. \qquad (44)
\end{aligned}$$

The integrals of Eq. (34) can now be written using the quadrature

$$v^{(L)}(n,l;n',l';r(x_{k'}))=\sum_k\frac{r(k,k')^L_<}{r(k,k')^{L+1}_>}A^k_{n,l}A^k_{n',l'}\frac{2}{N(N+1)}, \qquad (45)$$

where

$$\begin{aligned}
r(k,k')_< &= \min\{r(x_k),r(x_{k'})\},\\
r(k,k')_> &= \max\{r(x_k),r(x_{k'})\}. \qquad (46)
\end{aligned}$$

Substituting this integral into Eq. (44), the atomic Hartree-Fock equations can be written as

$$\begin{aligned}
&\sum_k\left\{-\frac{1}{2}\frac{1}{r'(x_{k'})}d^{(2)}_{k,k'}\frac{1}{r'(x_{k'})}A^k_{n,l}\right\}\\
&\quad+\left\{\frac{l(l+1)}{2r(x_{k'})^2}-\frac{Z}{r(x_{k'})}-i\eta W(r(x_{k'}))\right\}A^{k'}_{n,l}\\
&\quad+\sum_{k,n_o,l_o}\frac{2}{N(N+1)}(4l_o+2)|A^k_{n_o,l_o}|^2\frac{1}{r(k,k')_>}A^{k'}_{n,l}\\
&\quad-\sum_{k,n_o,l_o}\sum_{L=|l-l_o|}^{l+l_o}\frac{2}{N(N+1)}C(lLl_o;000)^2\\
&\quad\times\frac{r(k,k')^L_<}{r(k,k')^{L+1}_>}A^{k'}_{n_o,l_o}A^k_{n_o,l_o}A^k_{n,l}=\varepsilon_{n,l}A^{k'}_{n,l}, \qquad (47)
\end{aligned}$$

which is a complex symmetric eigenvalue problem.

C. Approximation for large angular-momentum Coulomb matrix elements

In the context of TDCIS, two types of Coulomb matrix elements of the form $v_{(a,i',i,a')}$ and $v_{(a,i',a',i)}$ are of interest. In the case that excited orbitals with large angular momenta are important, a substantial number of Coulomb matrix elements need to be computed. This computational task can be the bottleneck in solving the TDCIS equations.

To make this task manageable, we employ the approximations

$$\begin{aligned}
v_{(a,i',i,a')}&=0,\\
v_{(a,i',a',i)}&=\delta_{i,i'}\left(\varphi_a\left|\frac{1}{r}\right|\varphi_{a'}\right), \qquad (48)
\end{aligned}$$

if either l_a or $l_{a'}$ is larger than a threshold value L_{coul}. These approximations are valid for an excited electron that is far away from the residual ion. We choose the value of L_{coul} such that numerical convergence is reached.

D. Numerical propagation scheme

In order to propagate the ground-state coefficient α_0, we directly apply the second-order finite-differencing scheme [116] to Eq. (5a):

$$\alpha_0(t+dt)=\alpha_0(t-dt)+2idt\sqrt{2}\mathcal{E}(t)\sum_i\sum_a\alpha^a_i(t)z_{(i,a)}. \qquad (49)$$

To propagate the coefficients $\alpha^a_i(t)$, we temporarily transform to the interaction picture,

$$\alpha^a_i(t)=e^{-i(\varepsilon_a-\varepsilon_i)t}\tilde{\alpha}^a_i(t). \qquad (50)$$

The propagation equation for $\tilde{\alpha}^a_i$ becomes

$$\dot{\tilde{\alpha}}^a_i(t)=-ie^{i(\varepsilon_a-\varepsilon_i)t}f^a_i(t), \qquad (51)$$

where

$$\begin{aligned}
f^a_i(t)\equiv&\sum_{i'}\sum_{a'}\alpha^{a'}_{i'}(t)(2v_{(a,i',i,a')}-v_{(a,i',a',i)})\\
&-\mathcal{E}(t)\left\{\sqrt{2}\alpha_0(t)z_{(a,i)}+\sum_{a'}\alpha^{a'}_i(t)z_{(a,a')}\right.\\
&\left.-\sum_{i'}\alpha^a_{i'}(t)z_{(i',i)}\right\}. \qquad (52)
\end{aligned}$$

Now we apply the second-order differencing scheme to Eq. (51),

$$\tilde{\alpha}^a_i(t+dt)=\tilde{\alpha}^a_i(t-dt)-2idte^{i(\varepsilon_a-\varepsilon_i)t}f^a_i(t), \qquad (53)$$

and then convert back to the Schrödinger picture,

$$\begin{aligned}\alpha_i^a(t+dt) &= e^{-i(\varepsilon_a-\varepsilon_i)(t+dt)}\tilde{\alpha}_i^a(t+dt)\\ &= e^{-i(\varepsilon_a-\varepsilon_i)(t+dt)}\tilde{\alpha}_i^a(t-dt) - 2idte^{-i(\varepsilon_a-\varepsilon_i)dt}f_i^a(t)\\ &= e^{-2i(\varepsilon_a-\varepsilon_i)dt}\alpha_i^a(t-dt) - 2idte^{-i(\varepsilon_a-\varepsilon_i)dt}f_i^a(t).\end{aligned} \tag{54}$$

Equations (49) and (54) are the equations used to propagate the coefficients.

E. Complex-orbital versus real-orbital formulation of TDCIS

As shown in the previous section, the complex-orbital formulation of TDCIS is rather compact, because the CAP is chosen such that the occupied orbitals in the Hartree-Fock ground state remain unaffected. However, this complex-orbital formulation has the disadvantage that the usual physical interpretation of the virtual orbitals is lost. It is therefore natural to ask whether it is more advantageous to use a real-orbital formulation of TDCIS. Real radial wave functions $u_{n,l}(r)$ are obtained by diagonalizing $\hat{F}$ rather than $\hat{F}_{\mathrm{CAP}}$. The full Hamiltonian, Eq. (4), is left unmodified. Using the real-orbital formulation, all integrals and orbital energies are real. However, there is a CAP-dependent term in the equations of motion for the wave-packet expansion coefficients [which is absent in the complex-orbital formulation of Eq. (5)]. In the following, we show that even though the real-orbital and complex-orbital formulations are equivalent, the implementation of the complex-orbital formulation is numerically more stable.

For simplicity, we performed the numerical comparison using hydrogen exposed to a laser electric field with a peak amplitude of 0.1 a.u. and an angular frequency of 0.057 a.u. In this case, the $\sqrt{2}$ factors, the Coulomb matrix elements, and the dipole matrix elements $z_{i,i'}$ in Eq. (5) disappear since there is only one electron. In these tests, 800 radial grid points, $r_{\max} = 130$ (Sec. II E), $r_{\mathrm{abs}} = 90$ (Sec. II B), $\zeta = 0.4$ (Sec. III A), and $dt = 0.004$ (Sec. III D) are employed. In order to accurately reflect the strong-field physics, it is important to note that the choice of CAP strength, which is characterized by η, is also important apart from these parameters. With $\eta = 10^{-3}$, our calculation performed with the complex orbitals reproduces the hydrogen result obtained by Gordon and Kärtner [117]. This is not the case if a smaller value of η is chosen. Figure 1 shows that the expectation value of the dipole acceleration obtained with $\eta = 10^{-5}$ is noisier than that for $\eta = 10^{-3}$. This is because the CAP with η less than 10^{-3} is too weak to absorb completely the photoelectron wave packet reaching the end of the spatial grid, leading to reflections from the grid wall.

To compare the results obtained with the complex orbitals, we repeated the calculations using the real orbitals. We found that, depending on the value of η, the numerical propagation using the real-orbital formulation may not be stable. Figure 2 shows that the expectation values of the dipole acceleration obtained with the complex and real orbitals, respectively, agree with each other when $\eta = 10^{-5}$. In this case, the two formulations are numerically equivalent. However, for $\eta = 10^{-3}$, which is required for an accurate description of the dipole acceleration, the numerical propagation of the wave packet using the real orbitals diverges. The divergence persists even after reducing dt by a factor of 10.

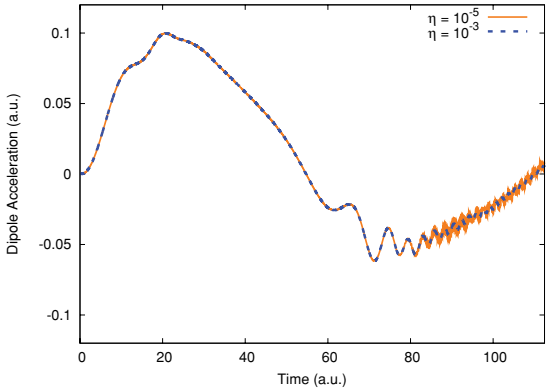

FIG. 1. (Color online) Effect of the CAP strength η on the expectation value of the dipole acceleration calculated with the complex-orbital formulation of TDCIS.

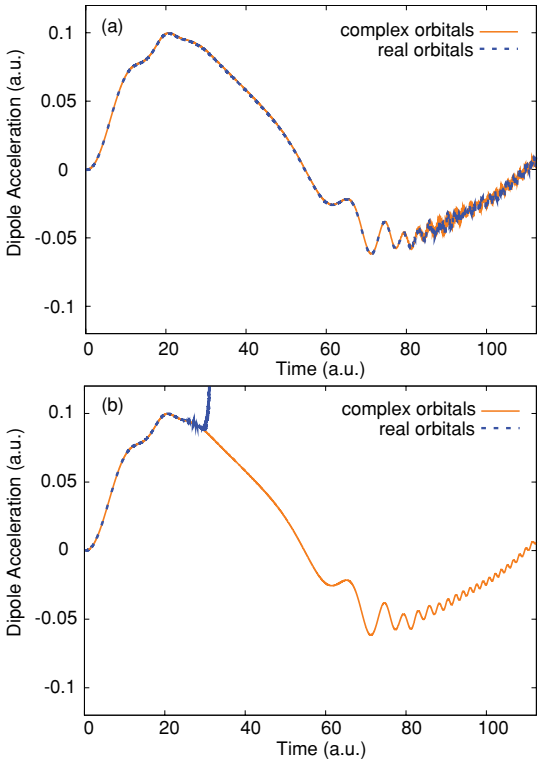

FIG. 2. (Color online) The expectation value of the dipole acceleration calculated with both the real-orbital (dashed line) and complex-orbital (solid line) formulations of TDCIS using (a) $\eta = 10^{-5}$ and (b) $\eta = 10^{-3}$.

IV. RESULTS AND DISCUSSION

To demonstrate applications of our implementation of TDCIS, we performed calculations on argon. First, we carried out a convergence study with the $3p_0$ orbital active and all other orbitals frozen. The laser field chosen was $\mathcal{E}(t) = \mathcal{E}_0 \sin(\omega t)$, with an $\mathcal{E}_0$ of 0.125 a.u. and an ω of 0.057 a.u. Classically, an electron that can recollide with its parent ion will travel $\sim \mathcal{E}_0/\omega^2 = 38.5$ a.u. before recollision. Therefore, to fully eliminate any CAP-induced perturbation of recolliding trajectories, we have put our absorbing potential at $r_{\text{abs}} = 90$ a.u., and our grid wall at $r_{\text{max}} = 120$ a.u., with a ζ [Eq. (37)] of 0.5. In general, the ζ parameter was chosen as $60/r_{\text{max}}$.

The convergence of a number of different parameters is illustrated in Fig. 3. Figures 3(a) and 3(b) show the convergence with the CAP strength. Low η's produced successively greater oscillations due to reflections off the grid wall, while the large η values did not have such obvious effects. However, close examination of large η values such as the one shown in Fig. 3(b) showed that reflections from the CAP did affect the dipole acceleration by shifting the oscillations out toward times around 113 a.u. An η of 5.0×10^{-3} produced the least amount of reflections off of either the grid wall or the absorbing potential. It should be noted that this η is in the region where the real-orbital formulation is numerically unstable. At a grid size of 500 grid points, the dependence of the dipole acceleration on the maximum angular-momentum value allowed for the dipole (L_{max}) and Coulomb (L_{coul}) integrals was determined [Fig. 3(c)]. An L_{max} of 60 was determined to be necessary for convergence of the dipole acceleration, while for the Coulomb integrals an L_{coul} of 4 was sufficient. For the angular-momentum quantum numbers between 5 and 60, the Coulomb interaction was approximated as a $\frac{1}{r}$ interaction (Sec. III C). Additionally, orbitals with Hartree-Fock energies higher than 50 a.u. (real part of the orbital energies) were determined to be unnecessary and were not included in the propagation calculations. Finally, the convergence of the size of the grid was found. Small grids led to extra oscillations in the dipole acceleration, as well as unphysical behaviors in the norms and density matrix elements. The argon system converged at a grid size of 750 grid points, although 1000 grid points were used for the following calculations.

Figure 4 shows the difference in the calculated dipole acceleration for the single-channel TDCIS method and the single-channel Hartree-Slater method [39], which approximates the exchange correlation using a local function. The added effects of using the exact nonlocal exchange potential can be seen in the figure. At the peak of the dipole acceleration, the TDCIS method peaks slightly sooner than the Hartree-Slater method. The oscillation after the peak is shorter for the TDCIS method. Finally, there are a greater number of smaller oscillations after the trough of the TDCIS dipole acceleration than for the Hartree-Slater method.

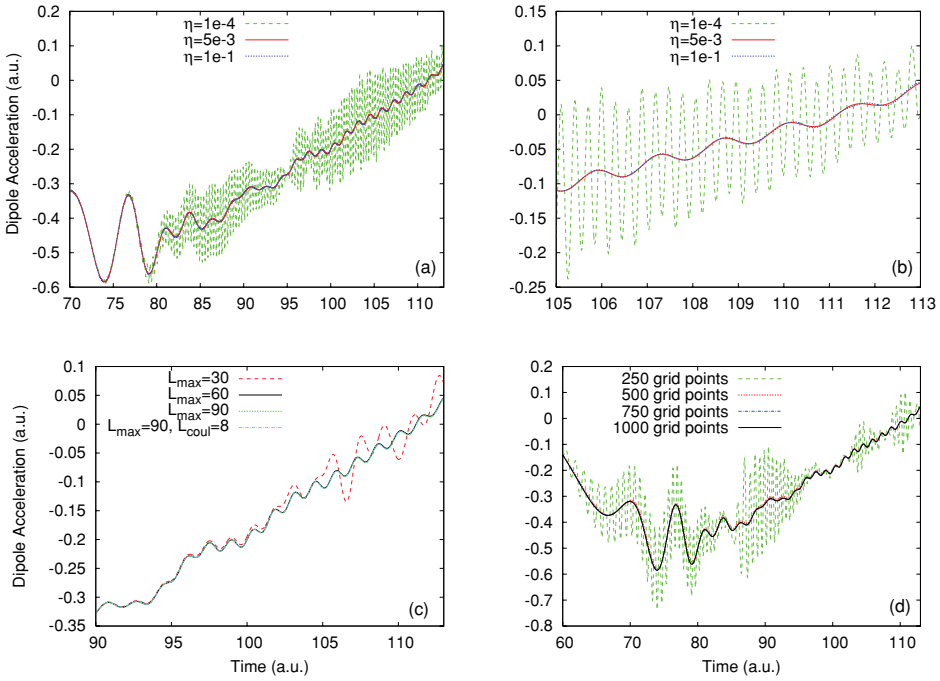

FIG. 3. (Color online) The convergence of the dipole acceleration of argon with the $3p_0$ orbital active. (a), (b) Convergence with the CAP strength. (c) Convergence with maximum angular momentum for the dipole (L_{max}) and Coulomb (L_{coul}) integrals. (d) Convergence with the size of the pseudospectral grid. Convergence is reached at a CAP strength of 5×10^{-3}, an L_{max} of 60, an L_{coul} of 4, and a grid size of 750.

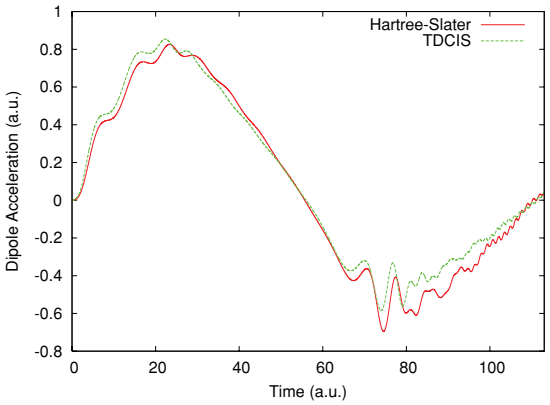

FIG. 4. (Color online) A comparison of the dipole acceleration of the single-channel TDCIS and Hartree-Slater methods. The nonlocal exchange effects are evident.

The multichannel capacity of the TDCIS framework was tested by performing calculations of the ion density matrix elements for argon with only the $3p_0$ orbital active as well as with all $3p$ orbitals active (see Fig. 5). For the case in which only the $3p_0$ orbital is active, the population of the orbital increases in two steps corresponding to the two half-cycles of the driving potential. There are minor oscillations especially in the second half-cycle. When all $3p$ orbitals are active, the population of the $3p_0$ orbital follows a similar pattern but is smaller than the single-channel case. The oscillations of the $3p_0$ population are slightly smaller as well for the three-channel case. Importantly, the combined populations of the $3p_1$ and $3p_{-1}$ orbitals are more than 10% of the $3p_0$ population. This result conflicts with the models that ignore channel coupling and assume that these populations are sufficiently small.

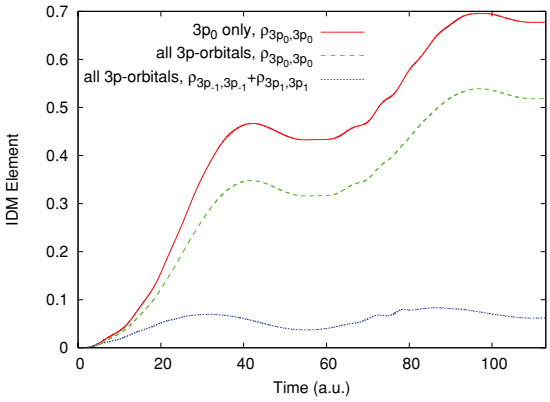

FIG. 5. (Color online) The ion density matrix elements are compared for the single-channel case and the three-channel case. The $3p_1$ element plus the $3p_{-1}$ element comprises more than 10% of the $3p_0$ element in the three-channel case.

V. CONCLUSION

We have developed a time-dependent configuration-interaction singles formalism with a complex absorbing potential in order to describe strong-field atomic processes in the nonperturbative regime. Previous theoretical approaches have relied on a single active electron approach, while with TDCIS, multichannel processes can be investigated. Two-electron reduced density matrix (2-RDM) methods [118–122] may provide a framework in the future for examining laser-field interactions with the inclusion of explicit electron correlation and additional multireference states. The flexible pseudospectral grid allows us to calculate orbitals with sufficient density in each region of the space in order to describe weakly bound and ionized electrons as well as strongly bound atomic electrons. We have also shown that applying the CAP in the Hartree-Fock step is more numerically stable than applying it in the propagation step. This leads to a non-Hermitian modified Fock operator, as well as complex orbitals which are orthogonal with respect to a symmetric inner product. Using these complex orbitals, a reduced ion density matrix was formulated in order to determine the populations and coherences of the one-hole states. The dipole acceleration of argon was calculated as well, which requires overlap integrals between the complex orbitals.

The TDCIS dipole acceleration for argon with its $3p_0$ orbital active was converged on the pseudospectral grid and then compared with the dipole acceleration calculated using the Hartree-Slater method. Local potential approximations are used in many theoretical treatments of strong-field processes. We determined that using the nonlocal exchange of the TDCIS method significantly affects the dipole acceleration. We then used the ion density matrix to compare the populations of the $3p$ orbitals of argon in single-channel and multichannel calculations. In the single-channel calculations, only the $3p_0$ orbital was allowed to be active. When all $3p$ orbitals were open for excitation, the population of the $3p_0$ orbital decreased as expected, although the time evolution was similar in shape. However, the combined $3p_1$ and $3p_{-1}$ populations were determined to be greater than 10% of the $3p_0$ population. This is a significant occupation, and it shows that methods which assume a single channel do not take into account possibly important effects. The TDCIS method provides a multichannel approach for nonperturbative strong-field processes which can be used to study effects that previous theoretical methods did not take into account.

ACKNOWLEDGMENTS

We thank Nina Rohringer for helpful discussions. This work was supported by the Office of Basic Energy Sciences, US Department of Energy under Contract No. DE-AC02-06CH11357. L.G. would like to thank Martha Ann and Joseph A. Chenicek and their family for financial support.

APPENDIX: CALCULATING INTEGRALS

Using the orbitals represented on a quadrature grid, we compute one- and two-body matrix elements, which are needed to solve the TDCIS equation of motion. For a general

one-electron operator $\hat{f}$, its matrix element defined by the symmetric inner product is given by

$$f_{(p,q)} = \int dr d\theta d\phi \sin\theta Y^*_{l_p,m_p}(\theta,\phi) u_{n_p,l_p}(r) f(r,\theta,\phi) \times Y_{l_q,m_q}(\theta,\phi) u_{n_q,l_q}(r). \quad \text{(A1)}$$

We perform the quadrature, such that

$$f_{(p,q)} = \frac{2}{N(N+1)} \int d\theta d\phi \ \sin\theta \sum_k A^k_{n_p,l_p} Y^*_{l_p,m_p}(\theta,\phi) \times f(r_k,\theta,\phi) A^k_{n_q,l_q} Y_{l_q,m_q}(\theta,\phi). \quad \text{(A2)}$$

To obtain $f_{p,q}$, which is defined by the conjugated inner product, we replace $A^k_{n_p,l_p}$ in Eq. (A2) with its complex conjugate.

Using Eq. (A2), all one-electron integrals can be constructed. For the overlap integrals, the angular part becomes a δ function, and we are left with

$$o_{p,q} = \delta_{l_p,l_q}\delta_{m_p,m_q} \sum_k \frac{2}{N(N+1)} \left(A^k_{n_p,l_p}\right)^* A^k_{n_q,l_q}. \quad \text{(A3)}$$

For the nonconjugated dipole integrals ($\hat{z} = r\cos\theta$), we need for the propagation, using the relation $Y_{1,0} = \frac{4}{3\pi}\cos\theta$ and the fact that the integral of three spherical harmonics can be written using Clebsch-Gordan coefficients [111],

$$z_{(p,q)} = \sqrt{\frac{2l_q+1}{2l_p+1}} C(l_q,1,l_p;0,0,0) C(l_q,1,l_p;m_q,0,m_p) \times \sum_k \frac{2}{N(N+1)} A^k_{n_p,l_p} A^k_{n_q,l_q} r(x_k). \quad \text{(A4)}$$

We also need the conjugated dipole acceleration integrals ($\hat{a} = Z\cos\theta/r^2$),

$$a_{p,q} = \sqrt{\frac{2l_q+1}{2l_p+1}} C(l_q,1,l_p;0,0,0) C(l_q,1,l_p;m_q,0,m_p) \times \sum_k \frac{2}{N(N+1)} \left(A^k_{n_p,l_p}\right)^* A^k_{n_q,l_q} \frac{Z}{r(x_k)^2}. \quad \text{(A5)}$$

The nonconjugated two-electron Coulomb integrals are also required for the propagation, and they are constructed using a two-index quadrature. The expansion

$$\frac{1}{r_{12}} = \sum_{L=0}^{\infty} \frac{4\pi}{2L+1} \frac{r^L_<}{r^{L+1}_>} \sum_{M=-L}^{L} Y^*_{L,M}(\theta_1,\phi_1) Y_{L,M}(\theta_2,\phi_2) \quad \text{(A6)}$$

is used. Thus, the angular part of the Coulomb integrals reduce to Clebsch-Gordan coefficients, and the radial part becomes

$$v_{(p,q,s,t)} \Rightarrow \sum_{k,k'} A^k_{n_p,l_p} A^{k'}_{n_q,l_q} A^k_{n_s,l_s} A^{k'}_{n_t,l_t} \frac{r(k,k')^L_<}{r(k,k')^{L+1}_>}. \quad \text{(A7)}$$

[1] L. V. Keldysh, Zh. Eksp. Teor. Fiz. **47**, 1945 (1964) [Sov. Phys. JETP **20**, 1307 (1965)].
[2] A. M. Perelomov, V. S. Popov, and M. V. Terentev, Zh. Eksp. Teor. Fiz. **50**, 1393 (1965) [Sov. Phys. JETP **23**, 924 (1966)].
[3] F. H. M. Faisal, J. Phys. B **6**, L89 (1973).
[4] L. A. Lompre, G. Mainfray, C. Manus, S. Repoux, and J. Thebault, Phys. Rev. Lett. **36**, 949 (1976).
[5] H. R. Reiss, Phys. Rev. A **22**, 1786 (1980).
[6] P. Lambropoulos, Phys. Rev. Lett. **55**, 2141 (1985).
[7] M. V. Ammosov, N. B. Delone, and V. P. Krainov, Zh. Eksp. Teor. Fiz. **91**, 2008 (1986) [Sov. Phys. JETP **64**, 1191 (1986)].
[8] F. Yergeau, S. L. Chin, and P. Lavigne, J. Phys. B **20**, 723 (1987).
[9] S. Augst, D. Strickland, D. D. Meyerhofer, S. L. Chin, and J. H. Eberly, Phys. Rev. Lett. **63**, 2212 (1989).
[10] T. E. Glover, J. K. Crane, M. D. Perry, R. W. Lee, and R. W. Falcone, Phys. Rev. Lett. **75**, 445 (1995).
[11] G. N. Gibson, M. Li, C. Guo, and J. Neira, Phys. Rev. Lett. **79**, 2022 (1997).
[12] J. Muth-Böhm, A. Becker, and F. H. M. Faisal, Phys. Rev. Lett. **85**, 2280 (2000).
[13] R. Taïeb, V. Véniard, and A. Maquet, Phys. Rev. Lett. **87**, 053002 (2001).
[14] R. Moshammer *et al.*, Phys. Rev. Lett. **91**, 113002 (2003).
[15] E. Gubbini, U. Eichmann, M. Kalashnikov, and W. Sandner, Phys. Rev. Lett. **94**, 053602 (2005).
[16] O. Smirnova, M. Spanner, and M. Ivanov, Phys. Rev. A **77**, 033407 (2008).
[17] P. Eckle, A. N. Pfeiffer, C. Cirelli, A. Staudte, R. Dörner, H. G. Muller, M. Büttiker, and U. Keller, Science **322**, 1525 (2008).
[18] P. Agostini, F. Fabre, G. Mainfray, G. Petite, and N. K. Rahman, Phys. Rev. Lett. **42**, 1127 (1979).
[19] R. R. Freeman, P. H. Bucksbaum, H. Milchberg, S. Darack, D. Schumacher, and M. E. Geusic, Phys. Rev. Lett. **59**, 1092 (1987).
[20] P. B. Corkum, N. H. Burnett, and F. Brunel, Phys. Rev. Lett. **62**, 1259 (1989).
[21] E. Mevel, P. Breger, R. Trainham, G. Petite, P. Agostini, J. P. Chambaret, A. Migus, and A. Antonetti, J. Phys. B **25**, L401 (1992).
[22] E. Mevel, P. Breger, R. Trainham, G. Petite, P. Agostini, A. Migus, J. P. Chambaret, and A. Antonetti, Phys. Rev. Lett. **70**, 406 (1993).
[23] U. Mohideen, M. H. Sher, H. W. K. Tom, G. D. Aumiller, O. R. Wood, R. R. Freeman, J. Boker, and P. H. Bucksbaum, Phys. Rev. Lett. **71**, 509 (1993).
[24] G. G. Paulus, F. Zacher, H. Walther, A. Lohr, W. Becker, and M. Kleber, Phys. Rev. Lett. **80**, 484 (1998).
[25] T. Morishita, A.-T. Le, Z. Chen, and C. D. Lin, Phys. Rev. Lett. **100**, 013903 (2008).
[26] M. Okunishi, T. Morishita, G. Prümper, K. Shimada, C. D. Lin, S. Watanabe, and K. Ueda, Phys. Rev. Lett. **100**, 143001 (2008).
[27] M. Busuladžić, A. Gazibegović-Busuladžić, D. B. Milošević, and W. Becker, Phys. Rev. Lett. **100**, 203003 (2008).

[28] A. McPherson, G. Gibson, H. Jara, U. Johann, T. S. Luk, I. A. McIntyre, K. Boyer, and C. K. Rhodes, J. Opt. Soc. Am. B **4**, 595 (1987).

[29] M. Ferray, A. L'Huillier, X. F. Li, L. A. Lompre, G. Mainfray, and C. Manus, J. Phys. B **21**, L31 (1988).

[30] A. L'Huillier, K. J. Schafer, and K. C. Kulander, Phys. Rev. Lett. **66**, 2200 (1991).

[31] P. B. Corkum, Phys. Rev. Lett. **71**, 1994 (1993).

[32] M. Lewenstein, Ph. Balcou, M. Yu. Ivanov, A. L'Huillier, and P. B. Corkum, Phys. Rev. A **49**, 2117 (1994).

[33] Ch. Spielmann, N. H. Burnett, S. Santania, R. Koppitsch, M. Schnürer, C. Kan, M. Lenzner, P. Wobrauschek, and F. Krausz, Science **278**, 661 (1997).

[34] Z. Chang, A. Rundquist, H. Wang, M. M. Murnane, and H. C. Kapteyn, Phys. Rev. Lett. **79**, 2967 (1997).

[35] E. A. Gibson *et al.*, Science **302**, 95 (2003).

[36] E. A. Gibson, A. Paul, N. Wagner, R. Tobey, S. Backus, I. P. Christov, M. M. Murnane, and H. C. Kapteyn, Phys. Rev. Lett. **92**, 033001 (2004).

[37] J. Seres *et al.*, Nature **433**, 596 (2005).

[38] A. Gordon and F. X. Kärtner, Phys. Rev. Lett. **95**, 223901 (2005).

[39] A. Gordon, F. X. Kärtner, N. Rohringer, and R. Santra, Phys. Rev. Lett. **96**, 223902 (2006).

[40] J. Levesque, D. Zeidler, J. P. Marangos, P. B. Corkum, and D. M. Villeneuve, Phys. Rev. Lett. **98**, 183903 (2007).

[41] M. Spanner and P. Brumer, Phys. Rev. A **78**, 033840 (2008).

[42] G. Jordan and A. Scrinzi, New J. Phys. **10**, 025035 (2008).

[43] B. Walker, B. Sheehy, L. F. DiMauro, P. Agostini, K. J. Schafer, and K. C. Kulander, Phys. Rev. Lett. **73**, 1227 (1994).

[44] Th. Weber *et al.*, Nature **405**, 658 (2000).

[45] R. Moshammer *et al.*, Phys. Rev. Lett. **84**, 447 (2000).

[46] A. Becker and F. H. M. Faisal, Phys. Rev. Lett. **84**, 3546 (2000).

[47] R. Kopold, W. Becker, H. Rottke, and W. Sandner, Phys. Rev. Lett. **85**, 3781 (2000).

[48] A. S. Alnaser *et al.*, Phys. Rev. Lett. **93**, 183202 (2004).

[49] P. J. Ho, R. Panfili, S. L. Haan, and J. H. Eberly, Phys. Rev. Lett. **94**, 093002 (2005).

[50] S. Gräfe and M. Yu. Ivanov, Phys. Rev. Lett. **99**, 163603 (2007).

[51] P. Koval, F. Wilken, D. Bauer, and C. H. Keitel, Phys. Rev. Lett. **98**, 043904 (2007).

[52] A. Rudenko, V. L. B. de Jesus, Th. Ergler, K. Zrost, B. Feuerstein, C. D. Schröter, R. Moshammer, and J. Ullrich, Phys. Rev. Lett. **99**, 263003 (2007).

[53] M. Hentschel *et al.*, Nature **414**, 509 (2001).

[54] P. Agostini and L. F. DiMauro, Rep. Prog. Phys. **67**, 813 (2004).

[55] R. Velotta, N. Hay, M. B. Mason, M. Castillejo, and J. P. Marangos, Phys. Rev. Lett. **87**, 183901 (2001).

[56] H. Niikura, F. Légaré, R. Hasbani, A. D. Bandrauk, M. Yu. Ivanov, D. M. Villeneuve, and P. B. Corkum, Nature **417**, 917 (2002).

[57] J. Itatani, J. Levesque, D. Zeidler, H. Niikura, H. Pépin, J. C. Kieffer, P. B. Corkum, and D. M. Villeneuve, Nature **432**, 867 (2004).

[58] J. Itatani, D. Zeidler, J. Levesque, M. Spanner, D. M. Villeneuve, and P. B. Corkum, Phys. Rev. Lett. **94**, 123902 (2005).

[59] Th. Ergler, A. Rudenko, B. Feuerstein, K. Zrost, C. D. Schröter, R. Moshammer, and J. Ullrich, Phys. Rev. Lett. **95**, 093001 (2005).

[60] R. Santra and A. Gordon, Phys. Rev. Lett. **96**, 073906 (2006).

[61] S. Patchkovskii, Z. Zhao, T. Brabec, and D. M. Villeneuve, Phys. Rev. Lett. **97**, 123003 (2006).

[62] B. D. Esry, A. M. Sayler, P. Q. Wang, K. D. Carnes, and I. Ben Itzhak, Phys. Rev. Lett. **97**, 013003 (2006).

[63] N. L. Wagner, A. Wüest, I. P. Christov, T. Popmintchev, X. Zhou, M. M. Murnane, and H. C. Kapteyn, Proc. Nat. Acad. Sci. USA **103**, 13279 (2006).

[64] S. Baker, J. S. Robinson, C. A. Haworth, H. Teng, R. A. Smith, C. C. Chirila, M. Lein, J. W. G. Tisch, and J. P. Marangos, Science **312**, 424 (2006).

[65] M. Lein, J. Phys. B **40**, R135 (2007).

[66] O. Smirnova, A. S. Mouritzen, S. Patchkovskii, and M. Yu. Ivanov, J. Phys. B **40**, F197 (2007).

[67] Z. Zhao, J. Yuan, and T. Brabec, Phys. Rev. A **76**, 031404 (2007).

[68] S. Patchkovskii, Z. Zhao, T. Brabec, and D. M. Villeneuve, J. Chem. Phys. **126**, 114306 (2007).

[69] B. Feuerstein, Th. Ergler, A. Rudenko, K. Zrost, C. D. Schröter, R. Moshammer, J. Ullrich, T. Niederhausen, and U. Thumm, Phys. Rev. Lett. **99**, 153002 (2007).

[70] E. V. van der Zwan, C. C. Chirila, and M. Lein, Phys. Rev. A **78**, 033410 (2008).

[71] Z. B. Walters, S. Tonzani, and C. H. Greene, J. Phys. Chem. A **112**, 9439 (2008).

[72] W. Li, X. Zhou, R. Lock, S. Patchkovskii, A. Stolow, H. C. Kapteyn, and M. M. Murnane, Science **322**, 1207 (2008).

[73] M. Drescher *et al.*, Nature **419**, 803 (2002).

[74] F. Lindner *et al.*, Phys. Rev. Lett. **95**, 040401 (2005).

[75] G. L. Yudin, A. D. Bandrauk, and P. B. Corkum, Phys. Rev. Lett. **96**, 063002 (2006).

[76] T. Pfeifer, M. J. Abel, P. M. Nagel, A. Jullien, Z.-H. Loh, M. J. Bell, D. M. Neumark, and S. R. Leone, Chem. Phys. Lett. **463**, 11 (2008).

[77] A. D. Bandrauk, S. Chelkowski, S. Kawai, and H. Lu, Phys. Rev. Lett. **101**, 153901 (2008).

[78] K. C. Kulander, Phys. Rev. A **36**, 2726 (1987).

[79] J. L. Krause, K. J. Schafer, and K. C. Kulander, Phys. Rev. Lett. **68**, 3535 (1992).

[80] K. J. Schafer, B. Yang, L. F. DiMauro, and K. C. Kulander, Phys. Rev. Lett. **70**, 1599 (1993).

[81] H. Rottke, J. Ludwig, and W. Sandner, J. Phys. B **29**, 1479 (1996).

[82] P. Kaminski, R. Wiehle, V. Renard, A. Kazmierczak, B. Lavorel, O. Faucher, and B. Witzel, Phys. Rev. A **70**, 053413 (2004).

[83] L. Young *et al.*, Phys. Rev. Lett. **97**, 083601 (2006).

[84] C. Höhr *et al.*, Phys. Rev. A **75**, 011403(R) (2007).

[85] Z.-H. Loh, M. Khalil, R. E. Correa, R. Santra, C. Buth, and S. R. Leone, Phys. Rev. Lett. **98**, 143601 (2007).

[86] S. H. Southworth *et al.*, Phys. Rev. A **76**, 043421 (2007).

[87] N. Rohringer, A. Gordon, and R. Santra, Phys. Rev. A **74**, 043420 (2006).

[88] R. Santra, R. W. Dunford, and L. Young, Phys. Rev. A **74**, 043403 (2006).

[89] N. Rohringer and R. Santra, Phys. Rev. A **79**, 053402 (2009).

[90] M. Lein, N. Hay, R. Velotta, J. P. Marangos, and P. L. Knight, Phys. Rev. Lett. **88**, 183903 (2002).

[91] J. Zanghellini, M. Kitzler, T. Brabec, and A. Scrinzi, J. Phys. B **37**, 763 (2004).

[92] M. Nest, T. Klamroth, and P. Saalfrank, J. Chem. Phys. **122**, 124102 (2005).
[93] X.-M. Tong and Shih I Chu, Phys. Rev. A **57**, 452 (1998).
[94] Xi Chu and Shih I Chu, Phys. Rev. A **63**, 023411 (2001).
[95] M. S. Pindzola, D. C. Griffin, and C. Bottcher, Phys. Rev. Lett. **66**, 2305 (1991).
[96] K. C. Kulander, K. J. Schafer, and J. L. Krause, in *Atoms in Intense Radiation Fields*, edited by M. Gavrila (Academic, New York, 1992).
[97] N. E. Dahlen and R. van Leeuwen, Phys. Rev. A **64**, 023405 (2001).
[98] V. Véniard, R. Taïeb, and A. Maquet, Laser Phys. **13**, 465 (2003).
[99] N. Rohringer, S. Peter, and J. Burgdörfer, Phys. Rev. A **74**, 042512 (2006).
[100] M. Spanner and S. Patchkovskii, Phys. Rev. A **80**, 063411 (2009).
[101] N. Moiseyev, Phys. Rep. **302**, 212 (1998).
[102] A. Goldberg and B. W. Shore, J. Phys. B **11**, 3339 (1978).
[103] C. Leforestier and R. E. Wyatt, J. Chem. Phys. **78**, 2334 (1983).
[104] G. Jolicard and E. J. Austin, Chem. Phys. Lett. **121**, 106 (1985).
[105] U. V. Riss and H.-D. Meyer, J. Phys. B **26**, 4503 (1993).
[106] R. Santra and L. S. Cederbaum, Phys. Rep. **368**, 1 (2002).
[107] J. G. Muga, J. P. Palao, B. Navarro, and I. L. Egusquiza, Phys. Rep. **395**, 357 (2004).
[108] H. A. Bethe and E. E. Salpeter, *Quantum Mechanics of One- and Two-Electron Atoms* (Dover, Mineola, New York, 2008).
[109] K. Blum, *Density Matrix Theory and Applications* (Plenum, New York, 1996).
[110] W. R. Johnson, *Atomic Structure Theory* (Springer, Berlin, 2007).
[111] M. E. Rose, *Elementary Theory of Angular Momentum* (Dover, New York, 1995).
[112] J. P. Boyd, *Chebyshev and Fourier Spectral Methods*, 2nd ed. (Dover, New York, 2001).
[113] J. Wang, Shih I Chu, and C. Laughlin, Phys. Rev. A **50**, 3208 (1994).
[114] G. H. Yao and Shih I Chu, Chem. Phys. Lett. **204**, 381 (1993).
[115] V. Szalay, J. Chem. Phys. **99**, 1978 (1993).
[116] C. Leforestier *et al.*, J. Comput. Phys. **94**, 59 (1991).
[117] A. Gordon and F. X. Kärtner, Opt. Express **13**, 2941 (2005).
[118] *Two-Electron Reduced-Density-Matrix Mechanics*, edited by D. A. Mazziotti, Advances in Chemical Physics Vol. 134 (Wiley, New York, 2007).
[119] D. A. Mazziotti, Phys. Rev. Lett. **97**, 143002 (2006).
[120] D. A. Mazziotti, Phys. Rev. A **76**, 052502 (2007).
[121] G. Gidofalvi and D. A. Mazziotti, Phys. Rev. A **80**, 022507 (2009).
[122] B. Schäfer-Bung and M. Nest, Phys. Rev. A **78**, 012512 (2008).

5.2 Decoherence in Attosecond Photoionization

Stefan Pabst, Loren Greenman, Phay J. Ho, David A. Mazziotti, and Robin Santra

Published in Phys. Rev. Lett. **106**, 053003 (2011)

Original publication: http://link.aps.org/doi/10.1103/PhysRevLett.106.053003
Free preprint version: http://arxiv.org/abs/1101.2314

Statement of Contributions

All calculations, the interpretation, and the preparation of the manuscript have been done by myself.

PRL 106, 053003 (2011) PHYSICAL REVIEW LETTERS week ending 4 FEBRUARY 2011

Decoherence in Attosecond Photoionization

Stefan Pabst,[1,2] Loren Greenman,[3] Phay J. Ho,[4] David A. Mazziotti,[3] and Robin Santra[1,2,*]

[1]*Center for Free-Electron Laser Science, DESY, Notkestrasse 85, 22607 Hamburg, Germany*
[2]*Department of Physics, University of Hamburg, Jungiusstrasse 9, 20355 Hamburg, Germany*
[3]*Department of Chemistry and The James Franck Institute, The University of Chicago, Chicago, Illinois 60637, USA*
[4]*Argonne National Laboratory, Argonne, Illinois 60439, USA*

(Received 15 October 2010; published 2 February 2011)

The creation of superpositions of hole states via single-photon ionization using attosecond extreme-ultraviolet pulses is studied with the time-dependent configuration-interaction singles (TDCIS) method. Specifically, the degree of coherence between hole states in atomic xenon is investigated. We find that interchannel coupling not only affects the hole populations, but it also enhances the entanglement between the photoelectron and the remaining ion, thereby reducing the coherence within the ion. As a consequence, even if the spectral bandwidth of the ionizing pulse exceeds the energy splittings among the hole states involved, perfectly coherent hole wave packets cannot be formed. For sufficiently large spectral bandwidth, the coherence can only be increased by increasing the mean photon energy.

DOI: 10.1103/PhysRevLett.106.053003 PACS numbers: 32.80.Aa, 03.65.Yz, 42.65.Re

The typical time scale of electronic motion in atoms, molecules, and condensed matter systems ranges from a few attoseconds (1 as $= 10^{-18}$ s) to tens of femtoseconds (1 fs $= 10^{-15}$ s) [1–3]. In the last decade the remarkable progress in high harmonic generation [4–8] made it possible to generate attosecond pulses as short as 80 as [9]. Attosecond pulses have opened the door to real-time observations of the most fundamental processes on the atomic scale [1,10]. For instance, the generation of attosecond pulses was utilized to determine spatial structures of molecular orbitals [11]; an interferometric technique using attosecond pulses was used to characterize attosecond electron wave packets [12]; and attosecond pulse trains [13] and isolated attosecond pulses [14], in combination with an intense few-cycle infrared pulse, enabled the control of electron localization in molecules. Attosecond technology demonstrated the ability to follow, on a sub-femtosecond time scale, processes such as photoionization [15], Auger decay [16], and valence electron motion driven by relativistic spin-orbit coupling [17]. Furthermore, the availability of attosecond pulses fueled a broad interest in exploring charge transfer dynamics following photoexcitation or photoionization [14].

In this Letter, we analyze the creation of hole states via single-photon ionization using a single extreme-ultraviolet attosecond pulse. We investigate the impact of the freed photoelectron on the remaining ion and demonstrate that the interaction between the photoelectron and the ion cannot be neglected for currently available state-of-the-art attosecond pulses. In particular, the interchannel coupling of the initially coherently excited hole states greatly enhances the entanglement between the photoelectron and the ionic states. Interchannel coupling is mediated by the photoelectron and mixes different ionization channels, i.e., hole configurations, with each other. Consequently, the degree of coherence among the ionic states is strongly reduced, making it impossible to describe the subsequent charge transfer in the ion with a pure quantum mechanical state. Experiments on photosynthetic systems [18–21] have revealed a correlation between highly efficient energy transport and coherent dynamics in molecules (nuclear and electronic dynamics in this case). Similarly, high degrees of coherence in nonstationary hole states may be necessary for efficient charge transport within molecules.

In the last decade, much work has been done in the realm of hole migration [22–24]. It was shown that electronic motion can be triggered solely by electron correlation [22]. Charge transfers mediated by electronic correlations typically take place in a few femtoseconds and are thus faster than electronic dynamics initiated by nuclear motion [25,26]. Recent experiments [27,28] have demonstrated that electronically excited ionic states can modify site-selective reactivity within tens of femtoseconds, making hole migration processes a promising tool to control chemical reactions. Up to now, theoretical calculations [22,24] investigating hole migration phenomena have neglected the interaction between the parent ion and the photoelectron and assumed a perfectly coherent hole wave packet. As long as the photoelectron departs sufficiently rapidly from the parent ion, this assumption is appropriate [29]. However, for attosecond pulses with large spectral bandwidths, the enhanced production of slow photoelectrons will affect (mainly via interchannel coupling) both the final hole populations and the coherence among these hole states. Furthermore, recent results in high harmonic spectroscopy suggest that interchannel coupling may be the missing link to understanding hole dynamics occurring in high harmonic generation processes before the ejected electron recombines with the parent ion [30].

PRL 106, 053003 (2011) PHYSICAL REVIEW LETTERS week ending 4 FEBRUARY 2011

We investigate the creation of hole states via attosecond photoionization using the implementation of the time-dependent configuration-interaction singles (TDCIS) approach described in Ref. [31] (see also [32,33]). TDCIS allows us to study ionization dynamics beyond the single-channel approximation and to understand systematically the relevance of interchannel coupling in the hole creation process. The TDCIS wave function for the entire system is

$$|\Psi(t)\rangle = \alpha_0(t)|\Phi_0\rangle + \sum_{a,i}\alpha_i^a(t)|\Phi_i^a\rangle, \tag{1}$$

where $|\Phi_0\rangle$ is the Hartree-Fock ground state and $|\Phi_i^a\rangle = \hat{c}_a^\dagger \hat{c}_i|\Phi_0\rangle$ is a one-particle-one-hole excitation ($\hat{c}_a^\dagger$ and $\hat{c}_i$ are creation and annihilation operators for an electron in orbitals a and i, respectively). The corresponding coefficients $\alpha_0(t)$ and $\alpha_i^a(t)$, respectively, are functions of time and describe the dynamics of the system. Throughout, indices i, j, are used for occupied orbitals in $|\Phi_0\rangle$; indices a, b, stand for unoccupied orbitals. We focus our discussion on the case where single-photon ionization is the dominant effect and higher order processes can be neglected. Our model system is atomic xenon. The corresponding Hamiltonian (neglecting spin-orbit coupling) is

$$\hat{H}(t) = \hat{H}_0 + \hat{H}_1 + E(t)\hat{z}, \tag{2a}$$

where $E(t)$ is the electric field, $\hat{z}$ the dipole operator, and $\hat{H}_0$ is the mean-field Fock operator, which is diagonal with respect to the basis used in Eq. (1). The residual Coulomb interaction,

$$\hat{H}_1 = \hat{V}_c - \hat{V}_{\mathrm{MF}}, \tag{2b}$$

is defined such that $\hat{H}_0 + \hat{H}_1$ gives the exact nonrelativistic Hamiltonian for the electronic system in the absence of external fields ($\hat{V}_c$ is the electron-electron interaction). We study the impact of different approximations for $\hat{H}_1$ on the hole state as follows. The Coulomb-free model, the simplest approximation, removes the residual Coulomb interaction ($\hat{H}_1 = 0$) between the excited electron and the parent ion. In this approximation, the excited electron always sees a neutral atom via the $\hat{V}_{\mathrm{MF}}$ potential [34]. A more realistic approximation is the intrachannel model including direct and exchange contributions of the Coulomb interaction only within a given channel. In this second model, the excited electron can only interact with the occupied orbital from which it originates. Interactions between different occupied orbitals are neglected, i.e., we set $\langle\Phi_i^a|\hat{H}_1|\Phi_j^b\rangle = 0$ for $i \neq j$. The third and final model describes the Coulomb interaction exactly within the TDCIS framework. We refer to this as the full model. Note that the exact nonrelativistic Hamiltonian $\hat{H}_0 + \hat{H}_1$ is diagonal with respect to the ionic one-hole states $|\Phi_i\rangle = \hat{c}_i|\Phi_0\rangle$. In the full model, the photoelectron can couple the hole states, as $\hat{H}_1$ in the particle-hole space is not diagonal with respect to the hole index (i.e., $\langle\Phi_i^a|\hat{H}_1|\Phi_j^b\rangle$ generally differs from zero). This type of photoelectron-mediated interaction is called interchannel coupling [35]. As a consequence, in the full model the hole index is not a good quantum number, whereas in the Coulomb-free and intrachannel models, excited eigenstates of $\hat{H}_0 + \hat{H}_1$ are characterized by a well-defined hole index. To describe the hole states of the remaining ion, we employ the ion density matrix [31]

$$\hat{\rho}_{i,j}^{\mathrm{IDM}}(t) = \mathrm{Tr}_a[|\Psi(t)\rangle\langle\Psi(t)|]_{i,j} = \sum_a \langle\Phi_i^a|\Psi(t)\rangle\langle\Psi(t)|\Phi_j^a\rangle, \tag{3}$$

where Tr_a stands for the trace over the photoelectron. The properties of the ion density matrix can be measured using attosecond transient absorption spectroscopy [17]. A description of the cationic eigenstates in terms of one-hole configurations is a physically meaningful approximation for noble-gas atoms such as xenon [36].

In Fig. 1 the hole populations $\rho_{5s,5s}^{\mathrm{IDM}}(t)$ and $\rho_{4d_0,4d_0}^{\mathrm{IDM}}(t)$ of the xenon $5s$ and $4d_0$ orbitals, respectively, are shown for all three interaction models ($4d_0$ stands for the $4d$ orbital with $m = 0$). The ionizing, Gaussian-shaped attosecond pulse is linearly polarized and has a peak field strength of 25 GV/m, a pulse duration of $\tau = 20$ as, and a (mean) photon energy of $\omega_0 = 136$ eV. The hole dynamics of the Coulomb-free and intrachannel models are alike. In both cases, the populations are constant after the pulse, since the hole index is a good quantum number within these models. The extension to the exact Coulomb interaction changes the situation. Interchannel coupling causes the hole populations to remain nonstationary as long as the photoelectron remains close to the ion. As the distance between the photoelectron and the ion increases, the interchannel coupling weakens and the populations $\rho_{i,i}^{\mathrm{IDM}}(t)$ become

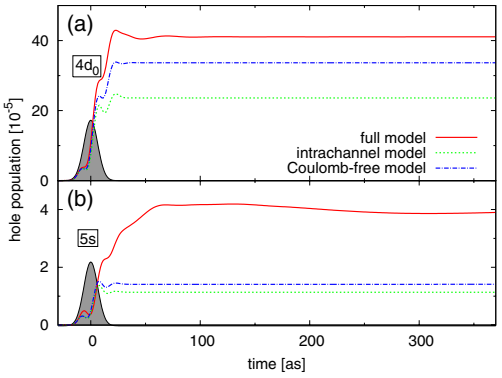

FIG. 1 (color online). The $4d_0$ [panel (a)] and $5s$ [panel (b)] hole populations of xenon as a function of time are shown for three different residual Coulomb interaction approximations: (1) the full model (red solid line), (2) the intrachannel model (green dotted line), and (3) the Coulomb-free model (blue dash-dotted line). The attosecond pulse has a peak field strength of 25 GV/m, a pulse duration of 20 as, a (mean) photon energy of 136 eV, and is centered at $t = 0$ as.

PRL 106, 053003 (2011) PHYSICAL REVIEW LETTERS week ending 4 FEBRUARY 2011

stationary (see Fig. 1). We confine our discussion to the first hundreds of attoseconds after the pulse, allowing us to neglect decay processes, which start to take place after a few femtoseconds.

As we will see in the following, interchannel coupling not only affects the hole populations but also the coherence between the created hole states. The degree of coherence between $|\Phi_i\rangle$ and $|\Phi_j\rangle$ is given by

$$g_{i,j}(t) = \frac{|\rho^{\mathrm{IDM}}_{i,j}(t)|}{\sqrt{\rho^{\mathrm{IDM}}_{i,i}(t)\rho^{\mathrm{IDM}}_{j,j}(t)}}. \quad (4)$$

Totally incoherent statistical mixtures result in $g_{i,j}(t) = 0$. The fact that the density matrix is positive semidefinite implies the Cauchy-Schwarz relations $|\rho^{\mathrm{IDM}}_{i,j}(t)|^2 \leq \rho^{\mathrm{IDM}}_{i,i}(t)\rho^{\mathrm{IDM}}_{j,j}(t)$, which bound the maximum achievable (perfect) coherence [$g_{i,j}(t) = 1$]. To investigate the effect of interchannel coupling on the coherence between the orbitals $4d_0$ and $5s$ in xenon, we restrict the definition of the $4d_0$ hole population to the events where the photoelectron has angular momentum $l = 1$. The other possible angular momentum for the $4d_0$ photoelectron, $l = 3$, does not contribute to the coherence, since the photoelectron from $5s$ can only have $l = 1$. For a similar reason, it is impossible to create a coherent superposition of $5p$ and $5s$ (or $4d$) hole states via one-photon absorption in the electric dipole approximation.

Figure 2 illustrates the time evolution of the coherence between $4d_0$ and $5s$ in xenon for different pulse durations and fixed photon energy ($\omega_0 = 136$ eV). Here, we use the full interaction model. Directly after the ionizing pulse is over, the initial degree of coherence (at $t \approx 0$ as) rises with decreasing pulse duration, i.e., increasing spectral bandwidth, and converges to a value close to unity. (The difference of the ionization potentials, $\varepsilon_{5s} - \varepsilon_{4d_0}$, is ≈ 50 eV.) At $t \approx 0$ as, the photoelectron is still in immediate contact with the parent ion. Therefore, the coherence properties of the system of interest—the parent ion—are affected by its interaction with the bath represented by the photoelectron. The system-bath interaction leads to a reduction in the coherence of the system [37], which can be seen by the rapid drops in all curves in Fig. 2 within tens of attoseconds after the pulse. With time, as the photoelectron departs from the ion, the Coulomb ("system-bath") interaction becomes less important and the coherence converges to a stationary value. The maximum for this stationary value is obtained with a 25 as pulse ($g_{4d_0,5s} \approx 0.6$). For pulses shorter than 25 as, oscillations in $g_{4d_0,5s}$ occur that persist for hundreds of attoseconds, and the final degree of coherence reached falls below 0.6. The spin-orbit dynamics associated with the fine structure within the $4d$ shell is slow in comparison to the time scale of the decoherence between $4d_0$ and $5s$, and is, therefore, not considered here.

We see in Fig. 3 that when holding the pulse duration fixed ($\tau = 20$ as), the degree of coherence rises with increasing ω_0. The magnitude of the oscillations decreases as

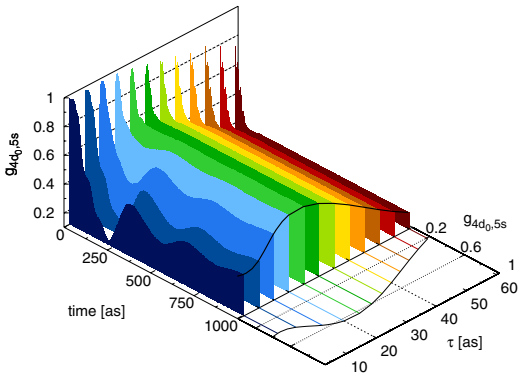

FIG. 2 (color online). The time evolution of the coherence between the $4d_0$ and $5s$ hole states in xenon is shown for the full Coulomb interaction model. The photon energy is 136 eV and the pulse duration varies from 5–60 as.

the final coherence (at $t \approx 1$ fs) increases. This trend indicates fewer system-bath interactions occur with higher photoelectron energies, keeping the degree of coherence among the hole states high.

In Fig. 4 we compare the impact of the different Coulomb approximations on the final coherence. The drops in coherence that occur for the full model for short pulses [Fig. 4(a)] and low photon energies [Fig. 4(b)] cannot be seen in the Coulomb-free and intrachannel models—which both neglect interchannel coupling. Hence, the decay of coherence is solely driven by the interchannel coupling due to the slow photoelectron. As a comparison to the Coulomb-free model shows, intrachannel coupling affects the coherence in an insignificant way. In the limit of long pulse durations (small spectral bandwidths), the coherence vanishes for all models, since photoelectrons from the $4d_0$

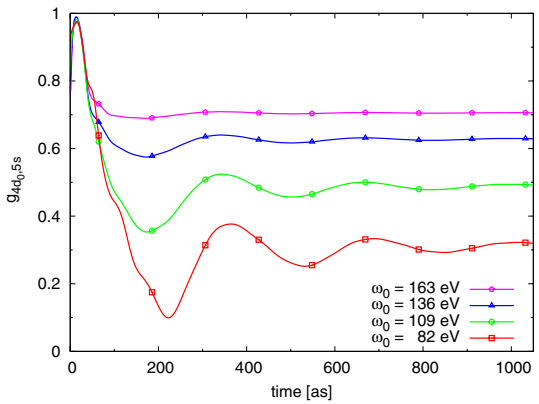

FIG. 3 (color online). The time evolution of the coherence between the $4d_0$ and $5s$ hole states, calculated with the full Coulomb interaction model, is shown for different photon energies. The pulse duration is in all cases 20 as.

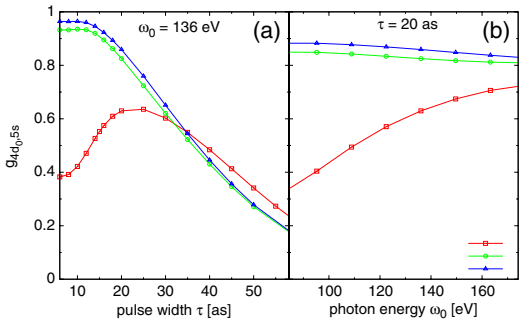

FIG. 4 (color online). The dependence of the coherence between the $4d_0$ and $5s$ hole states as function of the pulse duration (a) and as function of the photon energy (b) are shown for all three interaction approximations.

and $5s$ become energetically distinguishable and cannot contribute to a coherent statistical mixture of hole states. The slight drop in the coherence for the Coulomb-free and intrachannel models with increasing ω_0 [Fig. 4(b)] is related to the reduced factorizability of the numerator of Eq. (4). In contrast, the trend in the full model for increasing ω_0 is dominated by the gain in coherence due to higher photoelectron energy resulting in less system-bath interaction.

In conclusion, we demonstrated that the coherence of the ionic states produced via attosecond photoionization is not solely determined by the bandwidth of the ionizing pulse, but greatly depends on the kinetic energy of the photoelectron, which can be controlled by the (mean) photon energy. Interchannel coupling leads to an enhanced entanglement between the photoelectron and the parent ion resulting in a reduced coherence in the ionic states. This reduction can be mitigated with higher photon energies, thereby sacrificing high photon cross sections and the possibility of controlling independently the relative populations of the various hole states in the statistical mixture.

Our results have far-reaching consequences beyond the atomic case. Molecules will be even more strongly affected by interchannel coupling due to the reduced symmetry and smaller energy splittings between the cation many-electron eigenstates. Interchannel coupling is also likely to be significant for innervalence hole configurations in molecules, which show strong mixing to configurations outside the TDCIS model space. The present study suggests that interchannel coupling accompanying the hole creation process will affect attosecond experiments investigating charge transfer processes in photoionized systems. The control of decoherence requires widely tunable attosecond sources, thus offering a new opportunity for x-ray free-electron lasers [38].

P. J. H. was supported by the Office of Basic Energy Sciences, U.S. Department of Energy under Contract No. DE-AC02-06CH11357. L. G. thanks Martha Ann and Joseph A. Chenicek and their family for financial support. D. A. M. gratefully acknowledges the NSF, the Henry-Camille Dreyfus Foundation, the David-Lucile Packard Foundation, and the Microsoft Corporation for their support.

*robin.santra@cfel.de

[1] F. Krausz and M. Ivanov, Rev. Mod. Phys. **81**, 163 (2009).
[2] A. H. Zewail, J. Phys. Chem. A **104**, 5660 (2000).
[3] A. L. Cavalieri *et al.*, Nature (London) **449**, 1029 (2007).
[4] G. Doumy *et al.*, Phys. Rev. Lett. **102**, 093002 (2009).
[5] N. Dudovich *et al.*, Nature Phys. **2**, 781 (2006).
[6] R. López-Martens *et al.*, Phys. Rev. Lett. **94**, 033001 (2005).
[7] E. A. Gibson *et al.*, Phys. Rev. Lett. **92**, 033001 (2004).
[8] K. J. Schafer *et al.*, Phys. Rev. Lett. **70**, 1599 (1993).
[9] E. Goulielmakis *et al.*, Science **320**, 1614 (2008).
[10] T. Pfeifer *et al.*, Chem. Phys. Lett. **463**, 11 (2008).
[11] S. Haessler *et al.*, Nature Phys. **6**, 200 (2010).
[12] J. Mauritsson *et al.*, Phys. Rev. Lett. **105**, 053001 (2010).
[13] K. P. Singh *et al.*, Phys. Rev. Lett. **104**, 023001 (2010).
[14] G. Sansone *et al.*, Nature (London) **465**, 763 (2010).
[15] E. Skantzakis *et al.*, Phys. Rev. Lett. **105**, 043902 (2010).
[16] M. Drescher *et al.*, Nature (London) **419**, 803 (2002).
[17] E. Goulielmakis *et al.*, Nature (London) **466**, 739 (2010).
[18] H. Lee, Y.-C. Cheng, and G. R. Fleming, Science **316**, 1462 (2007).
[19] M. Sarovar *et al.*, Nature Phys. **6**, 462 (2010).
[20] E. Collini *et al.*, Nature (London) **463**, 644 (2010).
[21] E. Harel, A. F. Fidler, and G. S. Engel, Proc. Natl. Acad. Sci. U.S.A. **107**, 16444 (2010).
[22] J. Breidbach and L. S. Cederbaum, J. Chem. Phys. **118**, 3983 (2003).
[23] M. Nest, F. Remacle, and R. D. Levine, New J. Phys. **10**, 025019 (2008).
[24] A. Kuleff, S. Lünnemann, and L. Cederbaum, J. Phys. Chem. A **114**, 8676 (2010).
[25] D. Kröner *et al.*, Appl. Phys. A **88**, 535 (2007).
[26] B. H. Muskatel, F. Remacle, and R. D. Levine, Phys. Scr. **80**, 048101 (2009).
[27] R. Weinkauf *et al.*, J. Phys. Chem. A **101**, 7702 (1997).
[28] E. W. Schlag *et al.*, Angew. Chem., Int. Ed. **46**, 3196 (2007).
[29] L. Cederbaum *et al.*, Adv. Chem. Phys. **65**, 115 (1986).
[30] Y. Mairesse *et al.*, Phys. Rev. Lett. **104**, 213601 (2010).
[31] L. Greenman *et al.*, Phys. Rev. A **82**, 023406 (2010).
[32] H. B. Schlegel, S. M. Smith, and X. Li, J. Chem. Phys. **126**, 244110 (2007).
[33] S. Klinkusch, P. Saalfrank, and T. Klamroth, J. Chem. Phys. **131**, 114304 (2009).
[34] A. Szabo and N. S. Ostlund, *Modern Quantum Chemistry* (Dover, Mineola, NY, 1996).
[35] A. F. Starace, Appl. Opt. **19**, 4051 (1980).
[36] C. Buth, R. Santra, and L. S. Cederbaum, J. Chem. Phys. **119**, 7763 (2003).
[37] H.-P. Breuer and F. Petruccione, *The Theory of Open Quantum Systems* (Oxford University Press, New York, 2002).
[38] A. A. Zholents and W. M. Fawley, Phys. Rev. Lett. **92**, 224801 (2004).

5.3 Synthesized Light Transients

A. Wirth, M. Th. Hassan, I. Grguraš, J. Gagnon, A. Moulet, T. T. Luu, S. Pabst, R. Santra, Z. A. Alahmed, A. M. Azzeer, V. S. Yakovlev, V. Pervak, F. Krausz, and E. Goulielmakis

Published in Science **334**, 195 (2011)

Original publication: http://www.sciencemag.org/content/334/6053/195

Statement of Contributions

I performed theoretical calculations based on our TDCIS approach, which is described in the SOM. Adrian Wirth, Eleftherios Goulielmakis, Robin Santra, and I discussed the interpretation of the experimental observations in light of the TDCIS results.

RESEARCH ARTICLE

Synthesized Light Transients

A. Wirth,[1] M. Th. Hassan,[1,2] I. Grguraš,[1] J. Gagnon,[1] A. Moulet,[1] T. T. Luu,[1] S. Pabst,[3,4] R. Santra,[3,4] Z. A. Alahmed,[2] A. M. Azzeer,[2] V. S. Yakovlev,[1,5] V. Pervak,[5] F. Krausz,[1,5] E. Goulielmakis[1]*

Manipulation of electron dynamics calls for electromagnetic forces that can be confined to and controlled over sub-femtosecond time intervals. Tailored transients of light fields can provide these forces. We report on the generation of subcycle field transients spanning the infrared, visible, and ultraviolet frequency regimes with a 1.5-octave three-channel optical field synthesizer and their attosecond sampling. To demonstrate applicability, we field-ionized krypton atoms within a single wave crest and launched a valence-shell electron wavepacket with a well-defined initial phase. Half-cycle field excitation and attosecond probing revealed fine details of atomic-scale electron motion, such as the instantaneous rate of tunneling, the initial charge distribution of a valence-shell wavepacket, the attosecond dynamic shift (instantaneous ac Stark shift) of its energy levels, and its few-femtosecond coherent oscillations.

The generation and measurement (briefly, synthesis) of electric field transients permitted the characterization of electric circuits with sub-picosecond temporal resolution (*1*) and constitutes a base technology for advancing high-speed electronics and electron-based information technologies. Electronic processes on the atomic scale typically evolve on a few-femtosecond to sub-femtosecond time scale. Time-domain access to these dynamics requires the extension of electric field control to optical frequencies.

As a first step to this end, measurement (*2*, *3*) and control (*4*–*9*) of the phase of field oscillations relative to their envelope [carrier-envelope phase (CEP)] yielded reproducible few-cycle light waveforms (*10*). Attosecond metrology (*11*) was further advanced by the reproducible generation and measurement of isolated attosecond pulses

[1]Max-Planck-Institut für Quantenoptik (MPQ), Hans-Kopfermann-Strasse 1, D-85748 Garching, Germany. [2]Department of Physics and Astronomy, King Saud University, Riyadh 11451, Kingdom of Saudi Arabia. [3]Center for Free-Electron Laser Science, Deutsches Elektronen Synchrotron, Notkestrasse 85, 22607 Hamburg, Germany. [4]Department of Physics, University of Hamburg, Jungiusstrasse 9, 20355 Hamburg, Germany. [5]Department für Physik, Ludwig-Maximilians-Universität (LMU), Am Coulombwall 1, D-85748 Garching, Germany.

*To whom correspondence should be addressed. E-mail: elgo@mpq.mpg.de

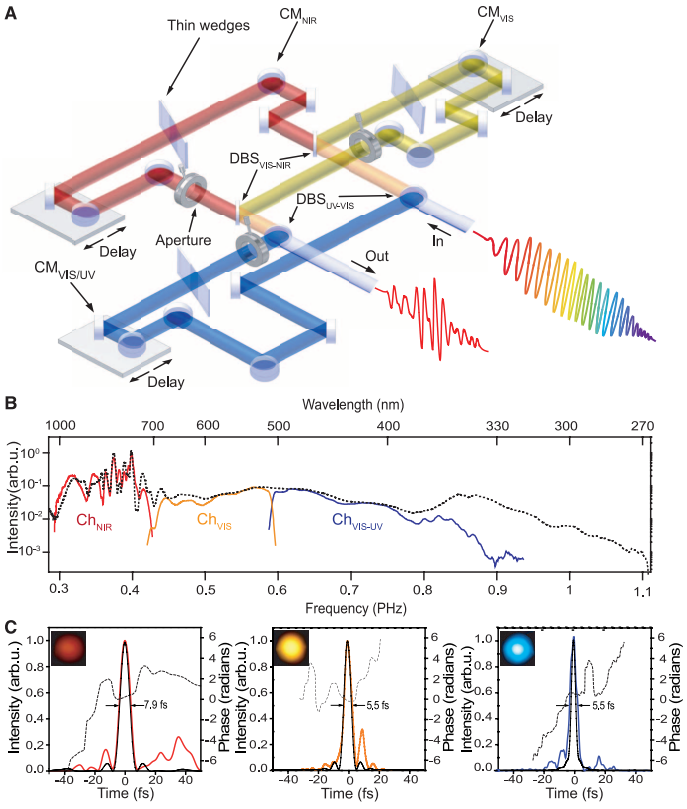

Fig. 1. Apparatus for infrared-visible-ultraviolet field synthesis. (**A**) Schematic representation of a prototypical three-channel light field synthesizer. (**B**) Spectrum of the coherent radiation at the exit of the hollow-core fiber (dashed line). Spectra exiting the individual channels (not to scale) are shown in red for Ch_{NIR} (700 to 1100 nm), yellow for Ch_{VIS} (500 to 700 nm), and blue for $Ch_{VIS\text{-}UV}$ (350 to 500 nm). (**C**) Temporal intensity (solid lines) and phase profiles (dashed curves) of the respective pulses. The thin black lines depict the intensity profiles of the corresponding bandwidth-limited pulses, with durations of $\tau_{Ch(NIR)}$ = 6.8 fs, $\tau_{Ch(VIS)}$ = 5 fs, and $\tau_{Ch(VIS\text{-}UV)}$ = 4.5 fs. Insets show photos of the respective beam profiles taken at the exit of the apparatus.

RESEARCH ARTICLE

(*12*–*14*). Control (*15*) and real-time observation (*16*–*21*) of electronic processes would greatly benefit from sub-femtosecond sculpting and confinement of strong light fields. We are able to demonstrate this capability along with some of its consequences.

Tailoring light fields on the electronic time scale requires the coherent superposition and manipulation of frequencies over more than an octave in the visible and flanking spectral ranges. So far, this demand could only be met through the technique of molecular modulation (*22*–*27*). This approach recently allowed the subcycle shaping of optical fields via the superposition of quasi-monochromatic waves in the infrared-visible range (*28*). Although these periodic waveforms are highly relevant to advancing modern electronics, time-domain access to electronic phenomena calls for the temporal confinement of the sculpted waveform to a single cycle or just a few oscillation cycles. We refer to such super-octave optical waveforms as light transients. Recent experiments have paved the way toward the synthesis of light transients (*29*–*33*), but they have not yet achieved the goal of subcycle field shaping and measurement.

Here, we report on the shaping, confinement, and attosecond sampling of the fields of intense light transients within their carrier wave cycle (~2.4 fs) over the frequency band of 0.3 to 0.9 PHz. A variety of on-demand waveforms with controlled subcycle field evolution, yielding sub-femtosecond rise times or subcycle confinement of instantaneous intensity, demonstrate the power of PHz field synthesis. As an application of enhanced atomic-scale electron control, we field-ionized atoms within a single wave crest and triggered valence electron motion on a sub-femtosecond scale. By providing a sub-femtosecond optical field trigger and a robust attosecond probe, subcycle light transients establish sub-femtosecond pump-probe spectroscopy.

1.5-octave optical field synthesizer. We produced coherent supercontinua by propagating ~0.8 mJ, ~25-fs pulses carried at a wavelength of λ_0 ~ 780 nm in a hollow-core fiber filled with neon gas. Spectral broadening was enhanced with respect to previous experiments (*34*) by raising the gas pressure to ~3.5 bar, resulting in a nearly uniform (to within 20 dB) energy distribution over a bandwidth of >0.6 PHz (330 to 1100 nm) (Fig. 1B). Manipulation of individual spectral components requires their spatial separation and subsequent recombination. The conventional approach, based on prisms and liquid crystal modulators (*31*), is hardly scalable for super-octave–spanning operation; therefore, we instead implemented chirped multilayer mirror technology, proposed in (*34*), which offers scalability to several octaves in the visible and nearby spectral regions. Our prototypical three-channel device (Fig. 1A) subdivides the aforementioned ~0.6-PHz spectral range into three bands of nearly equal width—Ch_{NIR}, 700 to 1100 nm; Ch_{VIS}, 500 to 700 nm; and $Ch_{VIS\text{-}UV}$, 350 to 500 nm—with the help of dichroic beamsplitters $DBS_{VIS\text{-}NIR}$ and $DBS_{UV\text{-}VIS}$ (fig. S1). Dispersive chirped mirrors $CM_{VIS/UV}$, CM_{VIS}, and CM_{NIR} compensate for the chirp carried by the pulse as well as that introduced by the thin fused silica wedge pairs incorporated in each channel and the beamsplitters near the edges of the spectral bands. As a result, the pulses in the individual channels are compressed close to their bandwidth-limited durations (Fig. 1C).

The chirp, the CEP, and the delay of the pulses formed in Ch_{NIR}, Ch_{VIS}, and $Ch_{VIS\text{-}UV}$ can be precisely controlled by wedges and nanometer-precision delay stages, respectively. The adjustment of the beam size in each channel—via an iris—allows control of the pulse's energy [supporting online material (SOM) text, section 1]. These control knobs offer both subcycle shaping of the generated fields and compression close to their bandwidth limit. Owing to the high efficiency of the chirped multilayer optics used (fig. S2), the device transmits some ~83% of the incident continuum beam (Fig. 1B, dotted line), resulting in a pulse energy of ~0.3 mJ/pulse at the exit of the apparatus (Ch_{NIR} ~ 250 μJ, Ch_{VIS} ~ 35 μJ, and $Ch_{VIS\text{-}UV}$ ~ 15 μJ). The setup is assembled on a monolithic aluminum base plate, with active thermal and interferometric path-length stabilization (fig. S3).

By analogy with femtosecond electro-optic sampling of THz transients (*1*), we can use attosecond streaking (*12*, *35*) for sampling the electric field of PHz transients. To this end, the PHz transients exiting our three-channel synthesizer were gently focused (to a peak intensity of ~10^{14} W/cm^2) into a neon gas jet, where they generated broadband extreme ultraviolet (XUV) radiation (*14*) emitted in a near-diffraction-limited beam collinear with the driving radiation (SOM text, section 2). Bandpass filtering (width of ~13 eV centered at ~85 eV) near the cut-off energy (~90 eV), implemented with multilayer

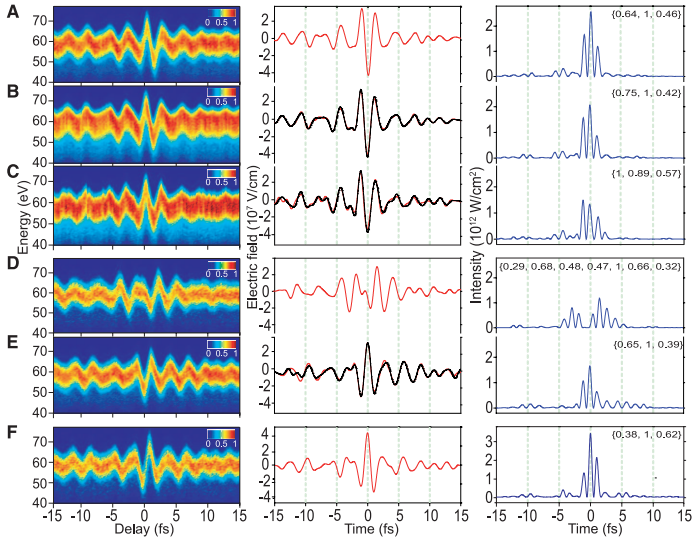

Fig. 2. Synthesis of petahertz light field transients. (**A** to **F**) Attosecond streaking spectrograms composed of photoelectron spectra normalized to their integral (left) and the respective retrieved electric fields (middle) and instantaneous intensity (right). Relative intensities for the most intense field crests—normalized to the maximum—are given in brackets. From (A) to (C), the delay of $Ch_{VIS\text{-}UV}$ is varied in steps of 200 as (~π/4). Dashed black lines in (B) and (C) show the field transients calculated from the reference waveform of (A). (D) Relative delays and CEPs of the individual channels are adjusted so as to create twin transients with a field minimum in between them. (E) Ch_{NIR} is delayed by 1.45 fs (~π), resulting in a high-frequency leading transient followed by a low-frequency tail. The dashed line in (E) shows the field transients calculated from the reference waveform of (D). Transients in (A) to (C), (E), and (F) carry less than one cycle within the FWHM of their temporal intensity profile. (F) τ_{FWHM} ~ 2.1 fs, incorporating only ~0.88 field cycles at the carrier wavelength of λ_0 ~ 710 nm.

optics and thin metal foils, isolated a single attosecond pulse (*12*, *14*). Both pulses were then focused into a second neon gas jet placed near the entrance of a time-of-flight electron spectrometer (TOF) for measuring the XUV-induced, laser-field–streaked photoelectron spectra versus delay (an attosecond streaking spectrogram) (*35*).

Attosecond streaking spectrograms of subcycle waveforms synthesized from near-bandwidth–limited fields exiting Ch_{NIR}, Ch_{VIS}, and $Ch_{VIS\text{-}UV}$ are shown in Fig. 2, left. The spectrograms are composed of a series of laser-field–streaked XUV photoelectron spectra recorded as a function of delay between the XUV pulse and the subcycle field. A delay step of 0.2 fs was used, which safely allows sampling up to the highest frequency components (~0.9 PHz) in the waveform. Remarkably, each spectrogram reveals an isolated <200-as XUV pulse. This is a direct consequence of the substantial subcycle variation of field amplitude (Fig. 2, right), which provides an efficient temporal gate—via ionization confinement and/or energy filtering—for isolating a single attosecond burst in the XUV radiation emitted by the ionizing atoms. The feasibility of generating a robust isolated attosecond probe for a wide range of waveforms not only is required for the sampling of the transients but is most important also for the interrogation of processes triggered and/or controlled by the optical field transients.

Any of the retrieved electric field waveforms (Fig. 2, middle) permits full characterization of the properties of the apparatus and subsequently on-demand synthesis of prescribed fields. To this end, we used the waveform in Fig. 2A as a reference and retrieved the values of the control parameters of the system such as the field amplitudes, phase delays, and the CEPs of the three channels through the numerical band-pass filtering of the measured output waveform within the spectral ranges defined by Ch_{NIR}, Ch_{VIS}, and $Ch_{VIS\text{-}UV}$. The field transients shown in Fig. 2, B and C, were then synthesized by delaying $Ch_{VIS\text{-}UV}$ in steps of $\pi/4$ (~200 as) with respect to the reference waveform. A more complex, nonsinusoidal transient, which is generated by delaying Ch_{NIR} so that the fields from the three channels cancel each other at the center of the waveform, is shown in Fig. 2D. The transient shown in Fig. 2E is generated via delay of Ch_{NIR} by $\sim\pi$ with respect to the waveform shown in Fig. 2D, resulting in a single intense field crest pointing in the opposite direction to the peak field in Fig. 2A. The full red and the dashed black lines in Fig. 2, middle, depict, respectively, waveforms measured or calculated from the constituent Ch_{NIR}, Ch_{VIS}, and $Ch_{VIS\text{-}UV}$ fields retrieved from the reference waveform (Fig. 2A), with control parameters changed by known amounts with respect to those of the reference waveform. The agreement between prediction and measurement demonstrates controlled sub-femtosecond shaping, complete characterization, and reproducibility (synthesis) of petahertz field transients.

The instantaneous intensity shown in Fig. 2, right, reveals substantial variations of the strength of consecutive wave crests upon these transformations. The reference waveform (Fig. 2A) exhibits half cycles with relative intensities of (0.64, 1, 0.46) underpinning the subcycle character of the transient. Delaying $Ch_{VIS\text{-}UV}$ gradually transforms the field into the highly asymmetric transient of Fig. 2C, with the temporal extension left almost unchanged. This transient carries its most intense field crest right at its leading edge, followed by half cycles of decreasing intensity (1, 0.89, 0.57), resulting in a sub-femtosecond rise time of its instantaneous intensity. On the other hand, a transient with its two most intense field crests separated by ~4.5 fs and a half-cycle virtually annihilated in between is revealed in Fig. 2D. The transient with the largest degree of temporal energy confinement is shown in Fig. 2F, with field crest intensities of (0.38, 1, 0.62) and with ~35% of its energy carried in a single wave crest.

Field ionization and its real-time sampling. We used transients with a central field crest ~1.7 times more intense than the adjacent half cycles (Fig. 3B) to ionize Kr atoms enclosed in a quasi-static gas cell (length $l \approx 0.74$ mm) at a density of $\approx 5.6 \times 10^{18}$ cm^{-3}. The gas cell was positioned at the laser focus, replacing the neon gas jet previously used for recording the streaking spectrograms shown in Fig. 3A (the experimental setup is shown in fig. S4). This procedure reveals the absolute timing of any process initiated or affected by the field transients with attosecond precision (SOM text, section 8).

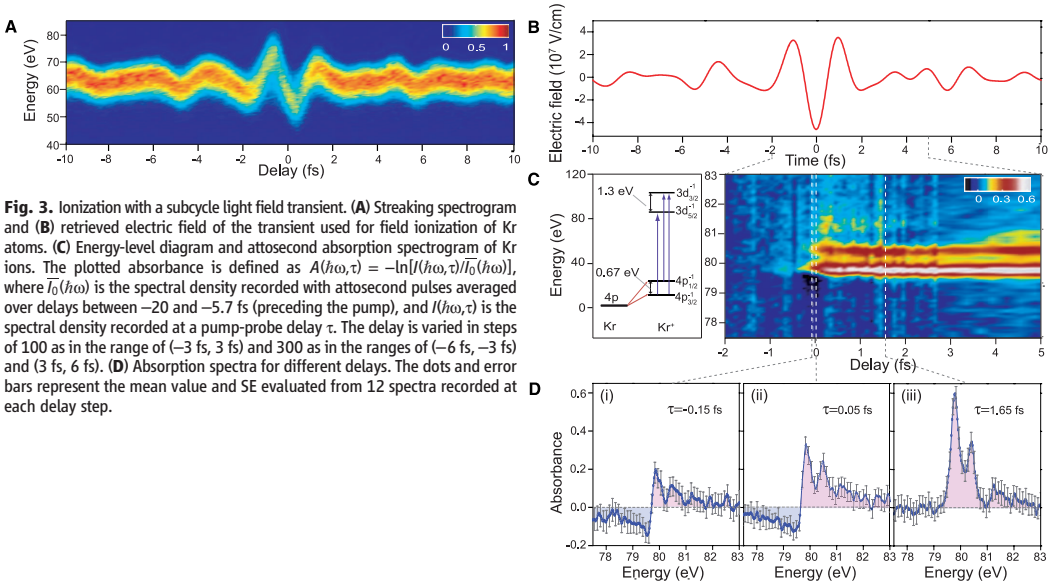

Fig. 3. Ionization with a subcycle light field transient. (**A**) Streaking spectrogram and (**B**) retrieved electric field of the transient used for field ionization of Kr atoms. (**C**) Energy-level diagram and attosecond absorption spectrogram of Kr ions. The plotted absorbance is defined as $A(\hbar\omega,\tau) = -\ln[I(\hbar\omega,\tau)/\overline{I_0}(\hbar\omega)]$, where $\overline{I_0}(\hbar\omega)$ is the spectral density recorded with attosecond pulses averaged over delays between −20 and −5.7 fs (preceding the pump), and $I(\hbar\omega,\tau)$ is the spectral density recorded at a pump-probe delay τ. The delay is varied in steps of 100 as in the range of (−3 fs, 3 fs) and 300 as in the ranges of (−6 fs, −3 fs) and (3 fs, 6 fs). (**D**) Absorption spectra for different delays. The dots and error bars represent the mean value and SE evaluated from 12 spectra recorded at each delay step.

RESEARCH ARTICLE

We increased the intensity with an iris to ≈4.8 × 10^{14} W/cm^2 and ionized ~16% of Kr atoms in the gas cell. We then probed strong-field ionization with a time-delayed attosecond pulse by measuring transient absorption spectra (*19*). Krypton ions created in their $4p^{-1}_{j=3/2}$ ground-state manifold and in the $4p^{-1}_{j=1/2}$ excited-state manifold, comprising four ($m_{j=3/2}$ = –3/2, –1/2, 1/2, 3/2) and two ($m_{j=1/2}$ = –1/2, 1/2) states, respectively, are promoted to the $3d^{-1}$ core-hole excited states by absorption of XUV photons from the attosecond pulse (Fig. 3C, left) (*36*). The resulting spectra transmitted through the gas cell were recorded as a function of the delay between the attosecond probe (pulse duration of ~200 as, centered at ~85 eV) and the ionizing field transient (pump), yielding the absorption spectrogram shown in Fig. 3C, right. The relevant transitions, $4p^{-1}_{3/2} \rightarrow 3d^{-1}_{5/2}$, $4p^{-1}_{1/2} \rightarrow 3d^{-1}_{3/2}$, and $4p^{-1}_{3/2} \rightarrow 3d^{-1}_{3/2}$, are indicated with arrows in the Fig. 3C level diagram. The absorption lines recorded at the leading edge of the ionizing field transient (Fig. 3D, i and ii, for example) have a characteristic profile revealing negative absorbance at photon energies below the resonances and positive absorbance above them (*37*). These transient line shapes gradually evolve to quasi-steady-state profiles toward the trailing edge of the ionizing field (Fig. 3D, iii).

State-selective sub-femtosecond tracing of field ionization. In order to relate the attosecond transient absorption spectra with ion population dynamics, we have performed numerical simulations by treating the generated Kr ions within a simplified, three-level model using the density matrix formalism (SOM text, section 3). The simulations reproduce well the experimental data (fig. S5) and demonstrate—in agreement with previous studies (*38*, *39*)—that the distortions of the transient absorption spectra are due to the synthesized pump field acting on the XUV-initiated, time-dependent ionic polarization response. Moreover, our simulations (based on an adiabatic tunnel-ionization calculation) suggest that—under the conditions of our experiments—the emerging absorption lines coincide with the population dynamics of the relevant ionic states, permitting retrieval of their transient evolution from the peak absorbances with good (~10%) accuracy (fig. S9). Figure 4A shows the sub-femtosecond evolution of the effective transient population in the ground state manifold $4p^{-1}_{j=3/2}$ (black dots), defined as $\rho^{\mathrm{eff}}_{3/2,3/2}(t) = \rho^{(\pm1/2)}_{3/2,3/2}(t) + a\rho^{(\pm3/2)}_{3/2,3/2}(t)$, where a = 2/3 reflects the higher transition cross-section for the ($m_j = \pm1/2$) transitions between $4p^{-1}_{j=3/2}$ and $3d^{-1}_{5/2}$ states; the $4p^{-1}_{j=1/2}$ manifold population $\rho^{(\pm1/2)}_{1/2,1/2}(t)$ is represented by black diamonds. These populations are retrieved from the $4p^{-1}_{3/2} \rightarrow 3d^{-1}_{5/2}$ and $4p^{-1}_{1/2} \rightarrow 3d^{-1}_{3/2}$ absorbances versus pump-probe delay, respectively. Because attosecond streaking is performed in the same apparatus, this evolution can be directly timed and contrasted with the evolution of the ionizing field $[|E_L(t)|^2$, shown by the dashed line].

The buildup of the retrieved ionic populations exhibits steps that are in synchrony with the field crests of the transient. This becomes even more evident from the population rates obtained by taking the time-derivative of the ionic populations in Fig. 4A. The ionization rate, which is estimated as $\frac{d}{dt}\rho^{\mathrm{eff}}_{3/2,3/2}(t)$ and shown in Fig. 4B (dots and red line), exhibits three main features at the crests of the ionizing field. The main ionization burst is responsible for approximately 80% of the ion population and has a full width at half maximum (FWHM) of <0.7 fs, indicating a sub-femtosecond confinement of field ionization. It is this confinement to a single field crest that allows quantitative evaluation of the time-dependent rate of optical field ionization and state-selective population dynamics. For the populations depicted, we evaluate a peak production rate for $\rho^{\mathrm{eff}}_{3/2,3/2}(t)$ of Γ_{peak} = (0.12 ± 0.01) fs^{-1} and for $\rho^{(\pm1/2)}_{1/2,1/2}(t)$ of Γ_{peak} = (0.059 ± 0.009) fs^{-1}, which is in excellent agreement with results obtained by numerically integrating the Schrödinger equation of a single-active electron model in three dimensions (SOM text, section 6), yielding $\Gamma_{\mathrm{peak}}(\rho^{\mathrm{eff}}_{3/2,3/2}) = 0.13$ fs^{-1} and $\Gamma_{\mathrm{peak}}(\rho^{(\pm1/2)}_{1/2,1/2}) = 0.059$ fs^{-1}, which also well reproduces details of the temporal evolution

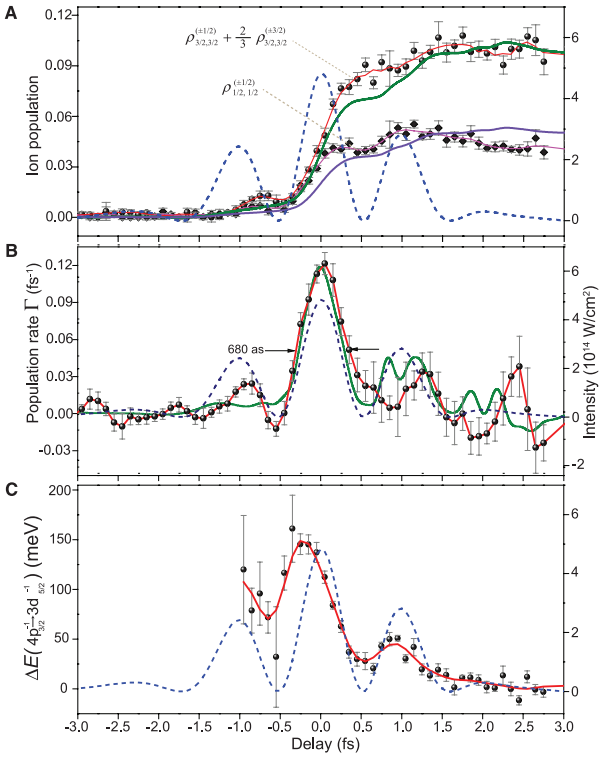

Fig. 4. Attosecond ionization and Stark effect dynamics in Kr^+. (**A**) Population dynamics in the ground-state $4p^{-1}_{j=3/2}$ manifold (dots), $\rho^{\mathrm{eff}}_{3/2,3/2}(t)$, and in the excited-state $4p^{-1}_{j=1/2}$ manifold (diamonds), $\rho^{(\pm1/2)}_{1/2,1/2}(t)$, retrieved from the absorption spectrogram of Fig. 3C and contrasted with the instantaneous intensity (dashed line) as well as with the prediction of numerical simulations convolved with the XUV probe pulse duration (green and purple lines). (**B**) Ionization (population) rate $d\rho^{\mathrm{eff}}_{3/2,3/2}(t)/dt$ evaluated from the data in (A) (dots and red line) in comparison with the theoretical prediction (green line). (**C**) Shift of the central energy of the $4p^{-1}_{3/2} \rightarrow 3d^{-1}_{5/2}$ transition evaluated by fitting a Lorentzian profile to the attosecond transient absorption spectra shown in Fig. 3C. Red curves in (A) to (C) and magenta curve in (A) are guides to the eye obtained by three adjacent point fast Fourier transform–smoothing.

of the ionic populations (Fig. 4A, green and purple lines, and B, green line).

Observation of the instantaneous optical Stark shift. The shift ΔE of quantum energy levels of atoms, molecules, or solids induced by an optical field $E_L(t)$—the ac Stark shift (*40*)—plays a central role in fundamental dynamical processes. So far, only cycle-averaged Stark effects have been accessible to experiments (*41*). If the laser frequency ω_L is much smaller than atomic resonance frequencies, the Stark shift of a nondegenerate atomic level is expected to instantly follow variations of the laser field: $\Delta E(t) = -1/2\mu E_L^2(t)$, where $\mu = \mu(\omega_L)$ is the atomic polarizability (*42*). When an XUV pulse creates a coherent superposition of two states with a difference in their respective polarizabilities $\Delta\mu(\omega_L)$, the induced polarization oscillations experience a phase shift, which is approximately given by

$$\Delta\varphi_{\text{dipole}}(t) \approx -\frac{\Delta\mu}{2\hbar}\int_{t_0}^{t} E_L^2(t')dt' \qquad (1)$$

where t_0 denotes the moment of arrival of the attosecond XUV pulse (with $\tau_{XUV} \ll 2\pi/\omega_L$). The instantaneous Stark shift detunes the energy at which the atom most efficiently absorbs photons from the XUV probe pulse—in our case, by the $3d \rightarrow 4p$ transition in Kr^+ ions—and modulates the frequency of the respective coherent dipole emission. Because the decay of the emission lasts several field cycles ($\tau = \tau_{3d} \sim 7.5$ fs), the Stark effect does not merely shift but also reshapes the transient absorption lines shown in Fig. 3D, i and ii. Thanks to the nearly instantaneous triggering of the polarization oscillations and their subsequent rapid decay, signatures of the instantaneous ac Stark shift come to light in our transient absorption spectra (Fig. 4C), which is in agreement with our simulations (figs. S8 and S9).

Valence wavepacket with well-defined quantum phase. Attosecond probing of few-cycle–driven field ionization of Kr atoms has revealed the emergence of a valence electron wavepacket in the 4*p* subshell of the Kr^+ ensemble—as a consequence of liberation of electrons from the $4p_{j=3/2}$ as well as the $4p_{j=1/2}$ manifolds—separated in energy by spin-orbit coupling in the Kr atoms (*19*). By repeating this attosecond absorption spectroscopic experiment with our subcycle transient shown in Fig. 3B, and supplementing it with attosecond streaking, we can now launch a valence wavepacket within a sub-femtosecond interval and with sub-femtosecond absolute timing accuracy.

From the recorded absorption spectrogram (Fig. 5A), we retrieve (SOM text, section 4) the fractional populations of the six ionic states, in the form of the diagonal matrix elements $\rho_{j,j'=j}^{(m_j)}$ of the reduced density matrix—$\rho_{3/2,3/2}^{(3/2)} + \rho_{3/2,3/2}^{(-3/2)} = 0.315 \pm 0.024$, $\rho_{3/2,3/2}^{(1/2)} + \rho_{3/2,3/2}^{(-1/2)} = 0.400 \pm 0.024$, $\rho_{1/2,1/2}^{(1/2)} + \rho_{1/2,1/2}^{(-1/2)} = 0.285 \pm 0.004$—and a degree of coherence of $g = 0.85 \pm 0.06$, which exceeds that measured in the previous experiment (*19*) by ~1.4 times and is unparalleled for long-lived (>1 fs) coherences in the valence shell. Our simulations [based on a state-of-the-art three-dimensional time-dependent configuration-interaction singles approach (*43*) that includes correlation dynamics between the field-generated hole and the photoelectron and has been extended to include spin-orbit interaction (*44*)] well predict the measured coherence as well as fractional populations in the $4p_{j=1/2}^{-1}$ and $4p_{j=3/2}^{-1}$ manifolds (SOM text, section 7).

The nearly perfect coherence is, once again, a direct consequence of the sub-femtosecond width of the ionization gate. This confinement, along with sub-femtosecond absolute timing information from streaking, has far-reaching consequences. The former allows launching of the wavepacket with a well-defined initial phase, whereas the latter permits reliable determination of this initial quantum phase. The retrieved phase $\phi(t)$ [equation 2 in (*19*)] of the quantum superposition is shown in Fig. 5, B and C, along with representative snapshots of the generated ensemble-averaged hole density distributions, as evaluated from our data in Fig. 5A. Linear extrapolation of $\phi(t)$ to "time zero," the birth of the hole at the peak of the ionizing field transient (Fig. 5B, blue line), yields $\phi(t_0) = (0.99 \pm 0.04)\pi$, which is in very good agreement with the prediction of our configuration-interaction–based simulations: $\phi(t_0) = 1.06\pi$. This initial quantum phase implies an elongated initial hole-density distribution aligned with the ionizing field vector, which is commensurate with our intuitive expectation.

Outlook. Subcycle engineering of optical field transients opens new prospects for steering the atomic-scale motion of electrons (*15*) with the electric force of light and for driving complex valence-shell dynamics in molecules (*45*). As a simple manifestation of enhanced control over valence shell dynamics, they allow sub-femtosecond temporal confinement of ionization and precise associated triggering of a wealth of subsequent electronic phenomena. They also provide an isolated attosecond photon probe for interrogating the unfolding electronic and—in molecules—nuclear motions by means of attosecond absorption and/or photoelectron spectroscopy, as well as an isolated electron probe for tracing these dynamics via electron diffraction (*46*) or high-harmonic interferometry (*47*). This constitutes a substantial extension of the repertoire of attosecond science, which was previously restricted to either triggering or probing electronic processes within a sub-femtosecond time window. The feasibility

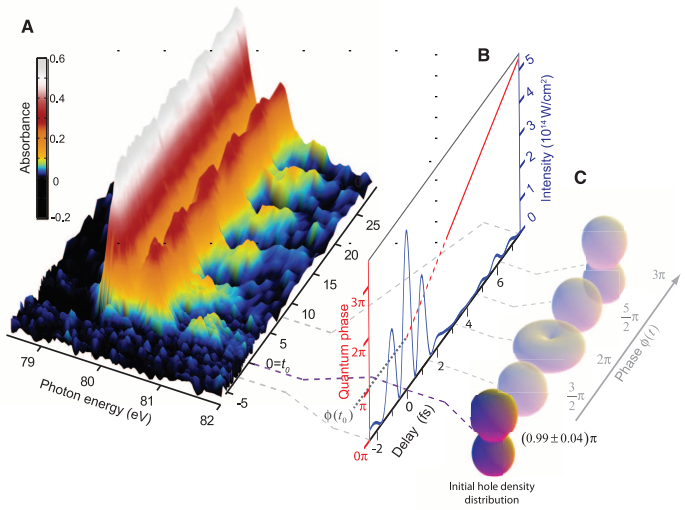

Fig. 5. Initial quantum phase and density distribution of a valence electron wavepacket. **(A)** Attosecond XUV transient absorption spectrogram of Kr atoms field-ionized by a subcycle field transient shown by the blue line in **(B)**. Linear extrapolation of the retrieved quantum phase $\phi(t)$ [shown by the red line in (B)] to time zero as determined through attosecond streaking, allows access to the initial quantum phase $\phi(t_0) = (0.99 \pm 0.04)\pi$ of the valence electron wavepacket. **(C)** Ensemble-averaged initial hole density distribution in the valence shell at the instant of ionization and its subsequent evolution, as evaluated from (A).

of sub-femtosecond pump-probe interrogation of strong-field phenomena opens exciting research prospects. Real-time insight into multiple ionization in multi- to single-cycle laser fields, or into strong-field–induced electron correlations in atoms, molecules, or solids (*48*, *49*), are but a few examples.

References and Notes

1. J. F. Whitaker *et al.*, *Microelectron. Eng.* **12**, 369 (1990).
2. L. Xu *et al.*, *Opt. Lett.* **21**, 2008 (1996).
3. T. Brabec, F. Krausz, *Rev. Mod. Phys.* **72**, 545 (2000).
4. J. Reichert *et al.*, *Opt. Commun.* **172**, 59 (1999).
5. D. J. Jones *et al.*, *Science* **288**, 635 (2000).
6. S. A. Diddams *et al.*, *Phys. Rev. Lett.* **84**, 5102 (2000).
7. A. Apolonski *et al.*, *Phys. Rev. Lett.* **85**, 740 (2000).
8. T. Udem, R. Holzwarth, T. W. Hänsch, *Nature* **416**, 233 (2002).
9. S. T. Cundiff, J. Ye, *Rev. Mod. Phys.* **75**, 325 (2003).
10. A. Baltuška *et al.*, *Nature* **421**, 611 (2003).
11. M. Hentschel *et al.*, *Nature* **414**, 509 (2001).
12. R. Kienberger *et al.*, *Nature* **427**, 817 (2004).
13. G. Sansone *et al.*, *Science* **314**, 443 (2006).
14. E. Goulielmakis *et al.*, *Science* **320**, 1614 (2008).
15. M. F. Kling *et al.*, *Science* **312**, 246 (2006).
16. G. Sansone *et al.*, *Nature* **465**, 763 (2010).
17. M. Schultze *et al.*, *Science* **328**, 1658 (2010).
18. J. Mauritsson *et al.*, *Phys. Rev. Lett.* **105**, 053001 2010).
19. E. Goulielmakis *et al.*, *Nature* **466**, 739 (2010).
20. S. Zherebtsov *et al.*, *Nat. Phys.*, published online 24 April 2011 (10.1038/nphys1983).
21. P. Eckle *et al.*, *Science* **322**, 1525 (2008).
22. S. E. Harris, A. V. Sokolov, *Phys. Rev. Lett.* **81**, 2894 (1998).
23. A. V. Sokolov, D. R. Walker, D. D. Yavuz, G. Y. Yin, S. E. Harris, *Phys. Rev. Lett.* **85**, 562 (2000).
24. J. Q. Liang, M. Katsuragawa, F. L. Kien, K. Hakuta, *Phys. Rev. Lett.* **85**, 2474 (2000).
25. A. V. Sokolov, D. R. Walker, D. D. Yavuz, G. Y. Yin, S. E. Harris, *Phys. Rev. Lett.* **87**, 033402 (2001).
26. T. Suzuki, M. Hirai, M. Katsuragawa, *Phys. Rev. Lett.* **101**, 243602 (2008).
27. Z.-M. Hsieh *et al.*, *Phys. Rev. Lett.* **102**, 213902 (2009).
28. H.-S. Chan *et al.*, *Science* **331**, 1165 (2011).
29. R. K. Shelton *et al.*, *Science* **293**, 1286 (2001).
30. M. Yamashita, K. Yamane, R. Morita, *IEEE J. Sel. Top. Quantum Electron.* **12**, 213 (2006).
31. S. Rausch, T. Binhammer, A. Harth, F. X. Kärtner, U. Morgner, *Opt. Express* **16**, 17410 (2008).
32. G. Krauss *et al.*, *Nat. Photonics* **4**, 33 (2010).
33. K. Okamura, T. Kobayashi, *Opt. Lett.* **36**, 226 (2011).
34. E. Goulielmakis *et al.*, *Science* **317**, 769 (2007).
35. E. Goulielmakis *et al.*, *Science* **305**, 1267 (2004).
36. This indicates that relative to the ground state configuration, a hole (or electron vacancy) is created in the nl_j^{-1} nl subshell, where j denotes the total angular momentum and m_j its projection on the z axis, the latter being aligned with the laser polarization.
37. B. R. Mollow, *Phys. Rev. A* **5**, 1522 (1972).
38. T. Unold, K. Mueller, C. Lienau, T. Elsaesser, A. D. Wieck, *Phys. Rev. Lett.* **92**, 157401 (2004).
39. C. H. B. Cruz, J. P. Gordon, P. C. Becker, R. L. Fork, C. V. Shank, *Int. J. Quant. Elec.* **24**, 261 (1988).
40. S. H. Autler, C. H. Townes, *Phys. Rev.* **100**, 703 (1955).
41. B. J. Sussman, *Am. J. Phys.* **79**, 477 (2011).
42. N. B. Delone, V. P. Krainov, *Phys. Uspekhi* **169**, 753 (1999).
43. L. Greenman *et al.*, *Phys. Rev. A* **82**, 023406 (2010).
44. S. Pabst, L. Greenman, P. J. Ho, D. A. Mazziotti, R. Santra, *Phys. Rev. Lett.* **106**, 053003 (2011).
45. F. Remacle, M. Nest, R. D. Levine, *Phys. Rev. Lett.* **99**, 183902 (2007).
46. M. Meckel *et al.*, *Science* **320**, 1478 (2008).
47. O. Smirnova *et al.*, *Nature* **460**, 972 (2009).
48. M. Gertsvolf, M. Spanner, D. M. Rayner, P. B. Corkum, *J. Phys. B* **43**, 131002 (2010).
49. M. Durach, A. Rusina, M. F. Kling, M. I. Stockman, *Phys. Rev. Lett.* **105**, 086803 (2010).

Acknowledgments: We acknowledge the development of dedicated attosecond soft x-ray optics by M. Hofstetter and U. Kleineberg (LMU, MPQ). This work was supported by the Max Planck Society, the European Research Council grant (Attoelectronics-258501), the Deutsche Forschungsgemeinschaft Cluster of Excellence: Munich Centre for Advanced Photonics (www.munich-photonics.de), the King Saud University–MPQ collaboration, and the European Research Training Network ATTOFEL.

Supporting Online Material

www.sciencemag.org/cgi/content/full/science.1210268/DC1
SOM Text
Figs. S1 to S10
References (*50*–*59*)

24 June 2011; accepted 30 August 2011
Published online 1 September 2011;
10.1126/science.1210268

REPORTS

Observation of Correlated Particle-Hole Pairs and String Order in Low-Dimensional Mott Insulators

M. Endres,[1]* M. Cheneau,[1] T. Fukuhara,[1] C. Weitenberg,[1] P. Schauß,[1] C. Gross,[1] L. Mazza,[1] M. C. Bañuls,[1] L. Pollet,[2] I. Bloch,[1,3] S. Kuhr[1,4]

Quantum phases of matter are characterized by the underlying correlations of the many-body system. Although this is typically captured by a local order parameter, it has been shown that a broad class of many-body systems possesses a hidden nonlocal order. In the case of bosonic Mott insulators, the ground state properties are governed by quantum fluctuations in the form of correlated particle-hole pairs that lead to the emergence of a nonlocal string order in one dimension. By using high-resolution imaging of low-dimensional quantum gases in an optical lattice, we directly detect these pairs with single-site and single-particle sensitivity and observe string order in the one-dimensional case.

The realization of strongly correlated quantum many-body systems using ultracold atoms has enabled the direct observation and control of fundamental quantum effects (*1*–*3*). A prominent example is the transition from a superfluid (SF) to a Mott insulator (MI), occurring when interactions between bosonic particles on a lattice dominate over their kinetic energy (*4*–*8*). At zero temperature and in the limit where the ratio of kinetic energy over interaction energy vanishes, particle fluctuations are completely suppressed and the lattice sites are occupied by an integer number of particles. However, at a finite tunnel coupling but still in the Mott insulating regime, quantum fluctuations create correlated particle-hole pairs on top of this fixed-density background, which can be understood as virtual excitations. These particle-hole pairs fundamentally determine the properties of the MI, such as its residual phase coherence (*9*), and lie at the heart of superexchange-mediated spin interactions that form the basis of quantum magnetism in multicomponent quantum gas mixtures (*10*–*12*).

In a one-dimensional system, the appearance of correlated particle-hole pairs at the transition point from a SF to a MI is intimately connected to the emergence of a hidden string-order parameter $\mathcal{O}_P$ (*13*, *14*):

$$\mathcal{O}_P^2 = \lim_{l\to\infty} \mathcal{O}_P^2(l) = \lim_{l\to\infty} \left\langle \prod_{k\le j\le k+l} e^{i\pi\delta\hat{n}_j} \right\rangle \quad (1)$$

Here, $\delta\hat{n}_j = \hat{n}_j - \overline{n}$ denotes the deviation in occupation of the jth lattice site from the average background density, and k is an arbitrary position along the chain. In the simplest case of a MI with unity filling ($\overline{n} = 1$), relevant to our experiments, each factor in the product of operators in Eq. 1 yields −1 instead of +1 when a single-particle fluctuation from the unit back-

[1]Max-Planck-Institut für Quantenoptik, 85748 Garching, Germany. [2]Theoretische Physik, Eidgenössische Technische Hochschule (ETH) Zurich, 8093 Zurich, Switzerland. [3]Ludwig-Maximilians-Universität, 80799 Munich, Germany. [4]University of Strathclyde, Scottish Universities Physics Alliance, Glasgow G4 0NG, UK.

*To whom correspondence should be addressed. E-mail: manuel.endres@mpq.mpg.de

Supplemental Materials

A. Wirth, M. Th. Hassan, I. Grguraš, J. Gagnon, A. Moulet, T. T. Luu, S. Pabst, R. Santra, Z. A. Alahmed, A. M. Azzeer, V. S. Yakovlev, V. Pervak, F. Krausz, and E. Goulielmakis

Published in Science **334**, 195 (2011)

Original publication: http://www.sciencemag.org/content/334/6053/195

www.sciencemag.org/cgi/content/full/science.1210268/DC1

Supporting Online Material for

Synthesized Light Transients

A. Wirth, M. Th. Hassan, I. Grguraš, J. Gagnon, A. Moulet, T.T. Luu, S. Pabst, R. Santra, Z. A. Alahmed, A. M. Azzeer, V. S. Yakovlev, V. Pervak, F. Krausz, E. Goulielmakis*

*To whom correspondence should be addressed. E-mail: elgo@mpq.mpg.de

Published 8 September 2011 on *Science* Express
DOI: 10.1126/science.1210268

This PDF file includes:

1. Optical properties of the light field synthesizer

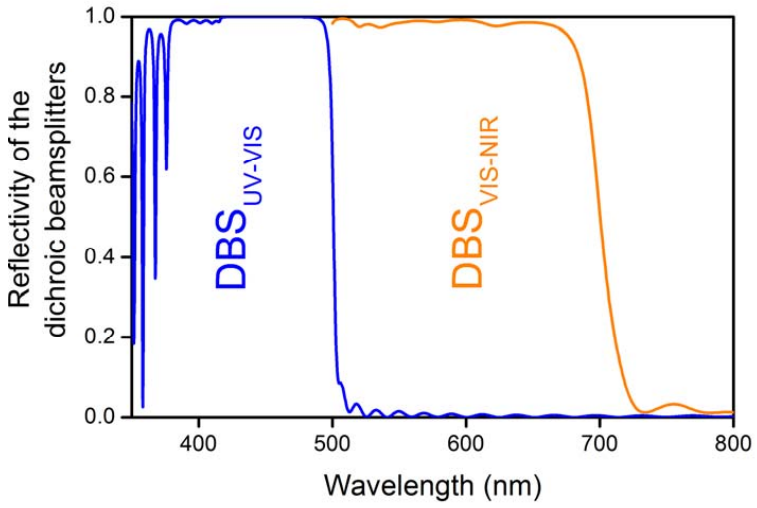

Fig. S1
Simulated reflectivity of the dichroic beamsplitters (DBS).

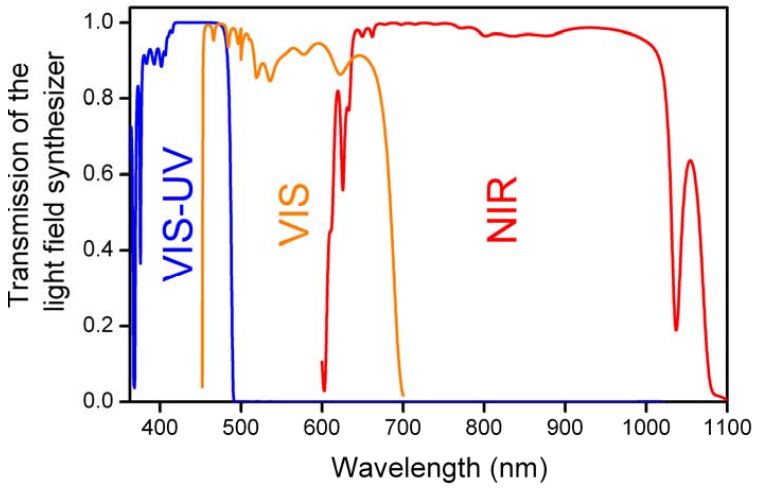

Fig. S2
Simulated total transmission of the individual channels of the optical field synthesizer. Blue (orange) line includes the reflectivity of two $DBS_{UV\text{-}VIS}$ ($DBS_{VIS\text{-}NIR}$) and six chirped mirrors (*50*) $CM_{VIS/UV}$ (CM_{VIS}), whereas the red curve shows the calculated transmission based on six CM_{NIR}.

Fig. S3
Photograph of the field synthesizer in operation. Beams have been visualized by nitrogen vapor.

Intensity control with adjustable apertures

To control the relative intensities between pulses in different channels of the light field synthesizer, apertures with controllable diameters were installed into the beam path of each channel.

Despite the fact that for the experiments presented in the main text this kind of control has not been utilized, we can conveniently tune the intensity in the focus of each channel by a factor of ~10. Due to this type of intensity control, spatial chirps may set in when pulses of various channels have slightly different beam diameter. However, these effects are not very critical for our experiments thanks to the extreme nonlinearity of the processes involved or studied.
For example, XUV pulse generation (or high harmonic generation in general) is confined to within a tiny fraction of the focused synthesized transient where the intensity is the highest and where all fields of the channels necessarily overlap. Moreover, at the probing stage of the light field or in a strong field experiment as reported here, the XUV attosecond pulse is focused onto a spot size that is more than 3 times smaller than that of the synthesized field, guaranteeing that the probed system is exposed to a spatially uniform field formed along the propagation axis, thereby rendering the measurement insensitive to a spatial chirp introduced by the variable apertures.

2. Attosecond Streaking and Transient Absorption experimental setup

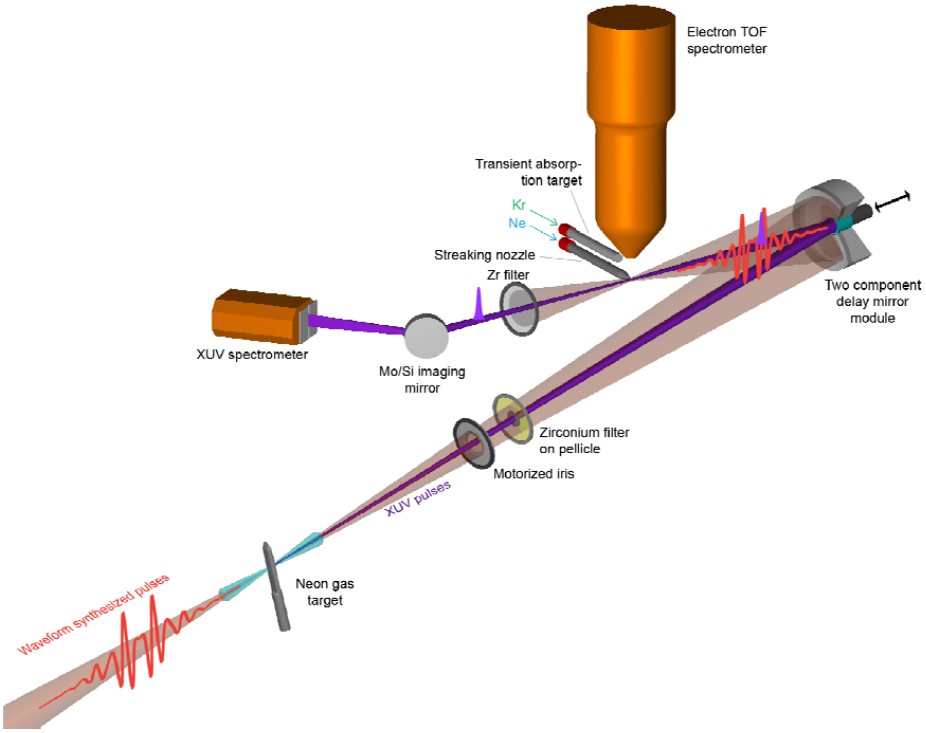

Fig. S4
Schematic diagram of the experimental setup for the characterization and application of synthesized light transients.

Light transients, synthesized by the apparatus shown in Fig. S3, are focused into a quasistatic gas cell filled with Ne (target), to generate XUV radiation by means of high order harmonic generation. The emerging, highly collimated XUV pulses are transmitted through a disk-like Zirconium (Zr) foil (150 nm) which is mounted on a thin pellicle (15 μm), while the residual visible pulses, which are also making their way through the Ne cell, are transmitted around the margins of the Zr disk to create an annular beam (see Fig. S4). A module comprised of a concave, multilayer coated inner mirror and an aluminum-coated concave annular sector (outer mirror) (*34*), is used to focus XUV and light transients respectively into a second gas jet or quasi static cell for either streaking or transient absorption experiments.
The inner mirror is mounted on a piezoelectric stage that allows the introduction of a delay between the light field transient and the XUV attosecond pulse along the propagation axis with nanometric precision.

A controllable iris is used to adjust the energy transported by the beam of the light transients from few microjoules (streaking) to several tens of microjoules (Transient absorption).
For streaking measurements a time of flight spectrometer is used to record electron spectra generated by photoionization of Ne atoms (*35*), while for transient absorption studies, spectra of the transmitted through the cell attosecond pulse are recorded by a high-resolution XUV spectrometer installed downstream the gas cell.

3. Modeling the absorption of XUV pulses in Kr^+ in the presence of a strong NIR-field.

Femtosecond transient absorption dynamics, probed by a weak probe pulse in the presence of a pump pulse which affects the polarization response of the absorbing medium, have been at the center of various studies (*38*,*51*).
To explore these effects in the XUV, we model Kr^+ ions as a simplified three-level system depicted in Fig. S5. The first two states, hereafter referred to as $|1\rangle$ and $|2\rangle$, represent the ground $4p_{3/2}^{-1}$ and the excited $3d_{5/2}^{-1}$ states of the ion, respectively, i.e. the states associated with the $4p_{3/2}^{-1} \rightarrow 3d_{5/2}^{-1}$ transition.
To introduce the polarizability of state $|1\rangle$ of the Kr^+ ion, a third state $|3\rangle$ is included in the present considerations. The energy spacing between the states $|1\rangle$ and $|3\rangle$ is set to 13.5 eV and the corresponding transition matrix element to $\mu = 1.87 \cdot 10^{-29}$ C·m. Both values are calculated via the COWAN atomic structure code (*52*) and they describe the coupling between the $4p_{3/2}^{-1}$ and the $4s_{1/2}^{-1}$ ($4s4p^6$ electron configuration). The unperturbed transition energy $\hbar\omega_{12}$ equals 79.95 eV, i.e. that of the $4p_{3/2}^{-1} \rightarrow 3d_{5/2}^{-1}$ absorption resonance. E_L, E_{XUV}, ω_L and ω_{XUV} denote the electric fields and the central frequencies of the light transient and that of the attosecond XUV pulse, respectively, while τ stands for their relative delay. The decay rate of state $|2\rangle$ is assumed to be $\Gamma_A \approx 1/7.5\,\text{fs}^{-1}$, which corresponds to an Auger decay time of the 3d hole of 7.5 fs (*53*). Strong-field ionization (SFI) in the Bloch model is introduced via an electric field dependent feeding rate $\Gamma_{SFI}(t)$ of the ground state, which is indicated schematically in Fig. S5. The ionization rate has been calculated from a fit of static field extracted values (*54*).

In all simulations, the field of the transient is the one evaluated by the streaking measurements (see Fig. 3B of the main publication) with the peak intensity adjusted to $\sim 4.8 \cdot 10^{14}$ W/cm^2. Similarly, the duration of the XUV pulse is set to 200 as and is spectrally centered at 80 eV.

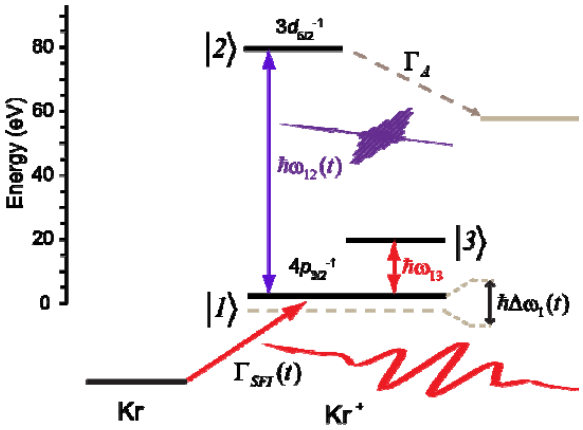

Fig. S5
Schematic diagram of the three-level system for modeling resonant XUV absorption of Kr^+.

Due to the presence of the additional state $|3\rangle$, the ground state $|1\rangle$ is more susceptible to the light transient, which translates into a significant periodic variation of its energy (ac Stark effect), thereby rendering the probed transition frequency ω_{12} time dependent:

$\omega_{12}(t) = \omega_{12} - \Delta\omega_1(t)$, where $\Delta\omega_1(t) = \sqrt{(\omega_{13} - \omega_L)^2 + 4\Omega_{13,L}(t)^2} + (\omega_L - \omega_{13})$ and

$\Omega_{13,L}(t) = \frac{\mu_{13} E_L(t)}{\hbar}$ denotes the instantaneous Rabi frequency between the states $|1\rangle$ and $|3\rangle$.

To calculate the absorption cross-section $\sigma(\omega,\tau)$ of the $|1\rangle \rightarrow |2\rangle$ transition, we numerically integrate the von Neumann equation:

$$i\hbar \frac{d\rho}{dt} = [H_0, \rho] - [\mu.E_{IR}(t), \rho] - [\mu.E_{XUV}(t-\tau), \rho] + i\hbar \left.\frac{d\rho}{dt}\right|_{SFI} + i\hbar \left.\frac{d\rho}{dt}\right|_{Relax}$$

with the unperturbed Hamiltonian H_0, the dipole operator μ in the dipole approximation and the density matrix ρ:

$$H_0 = \hbar \begin{pmatrix} \omega_{13} & 0 & 0 \\ 0 & \omega_{12} & 0 \\ 0 & 0 & 0 \end{pmatrix}; \qquad \mu = \begin{pmatrix} 0 & 0 & \mu_{31} \\ 0 & 0 & \mu_{21} \\ \mu_{13} & \mu_{12} & 0 \end{pmatrix}; \qquad \rho = \begin{pmatrix} \rho_{33} & \rho_{32} & \rho_{31} \\ \rho_{23} & \rho_{22} & \rho_{21} \\ \rho_{13} & \rho_{12} & \rho_{11} \end{pmatrix}.$$

The term $\left.\frac{d\rho}{dt}\right|_{SFI}$ phenomenologically describes the population rate of the ionic ground state $|1\rangle$ via strong-field ionization of the neutral atom. The decay rate Γ_A of the exited state as well as the spontaneous emission from level $|3\rangle$—which is assumed to be

infinitely long compared to characteristic scales of this experiment—is considered in the term $\left.\frac{d\rho}{dt}\right|_{Relax}$.

The radiating dipole is obtained through the equation of motion of the matrix elements as:

$$d(t,\tau) = Tr(\mu\rho(t)) = 2\,\mathrm{Re}\left(\mu_{12}\rho_{12}(t,\tau) + \mu_{13}\rho_{13}(t,\tau)\right) .$$

Hence, the absorption cross-section can be written as $\sigma(\omega,\tau) = \frac{\omega}{c\varepsilon_0}\,\mathrm{Im}\left[\frac{d(\omega,\tau)}{E_{XUV}(\omega)}\right]$.

Results 1: Distortion of the resonant XUV absorption line

Using our model, we explore the effects of spectral distortion of the $4p_{3/2}^{-1} \rightarrow 3d_{5/2}^{-1}$ absorption resonance due to the pump-induced perturbations to the generated ions by our light field transients.

Fig. S6 shows simulated transient dynamics encoded in the spectra corresponding to the $4p_{3/2}^{-1} \rightarrow 3d_{5/2}^{-1}$ transition for delays chosen to match those as in Fig. 3Di)-iii) of the main text.

The calculated absorption cross-sections are convolved with a Gaussian function (~300 meV FWHM) to account for the finite spectrometer resolution. The good reproduction of essential features, i.e. the negative absorbance at lower energies as well as positive absorbance at higher energies with respect to the main resonance, and the dynamic evolution of the absorption line as a function of the delay, validate the approach of modeling krypton ions with a simplified three-level system and confirm that the Stark effect is the key phenomenon behind the observed time-dependent spectral features.

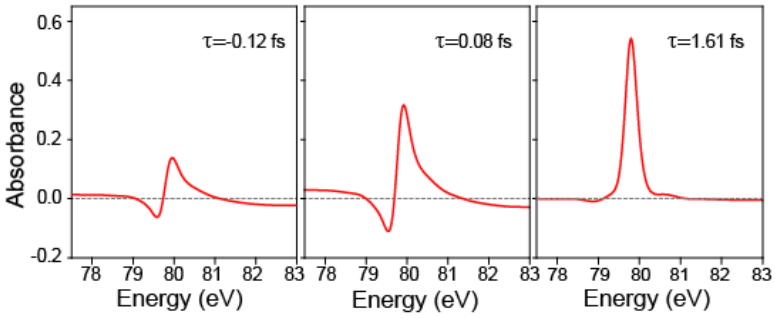

Fig. S6

Simulated absorbance spectra for the $4p_{3/2}^{-1} \rightarrow 3d_{5/2}^{-1}$ transition at three different delay instances, showing a good agreement with the corresponding experimental observation presented in Figs. 3D i)-iii). The finite spectrometer resolution is taken into account.

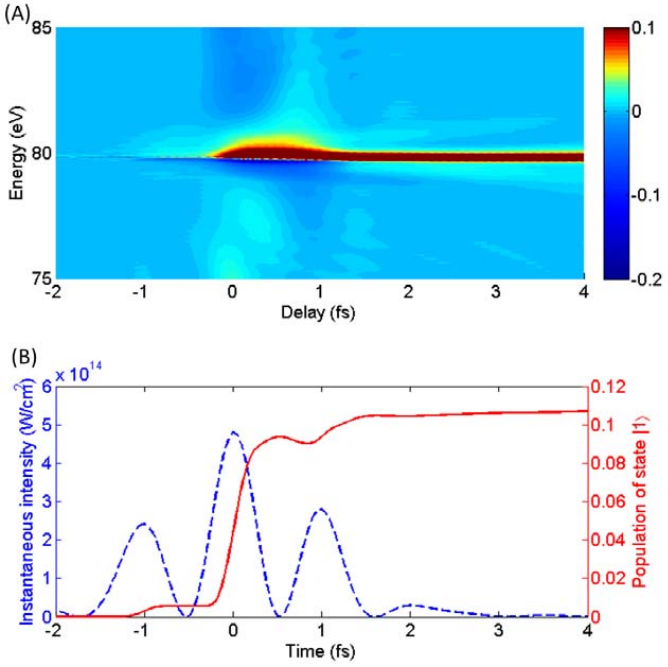

Fig. S7
Simulated transient absorbance spectra for an electric field dependent ionization rate $\Gamma_{SFI}(t)$ (**A**) and the underlying time dependent population of the ground state $|1\rangle$ (solid line) as well as the instantaneous intensity (dashed line) of the NIR laser pulse (**B**).

The false-color plot of Fig. S7A shows the calculated absorbance as a function of the pump-probe delay, while panel B depicts how the NIR field populates state $|1\rangle$ as a function of the delay, including the instantaneous intensity of the light transient.

In order to study how the lifetime of state $|2\rangle$ influences the distortion of the absorption in the presence of the NIR light field transient, the three-level system has been solved numerically for several lifetimes τ_A. Fig. S8 displays a series of absorbance spectrograms as a function of the pump-probe delay for a constant population $\left(\left.\frac{d\rho}{dt}\right|_{SFI}=0\right)$, where the lifetime τ_A was varied from 0.1 fs (panel A) to $\tau_{3d}=7.5$ fs (panel E), the latter being the theoretical Auger lifetime of the Kr^+ $3d^{-1}$ states (panel E).
For lifetimes significantly shorter than the half-period of the strong field, the emitting dipole undergoes (from (A) to (C)) a linear phase shift which is manifested by the characteristic modulation of its central energy at the double frequency of the pump field and corresponds to the (ac) Stark shift of state $|1\rangle$.

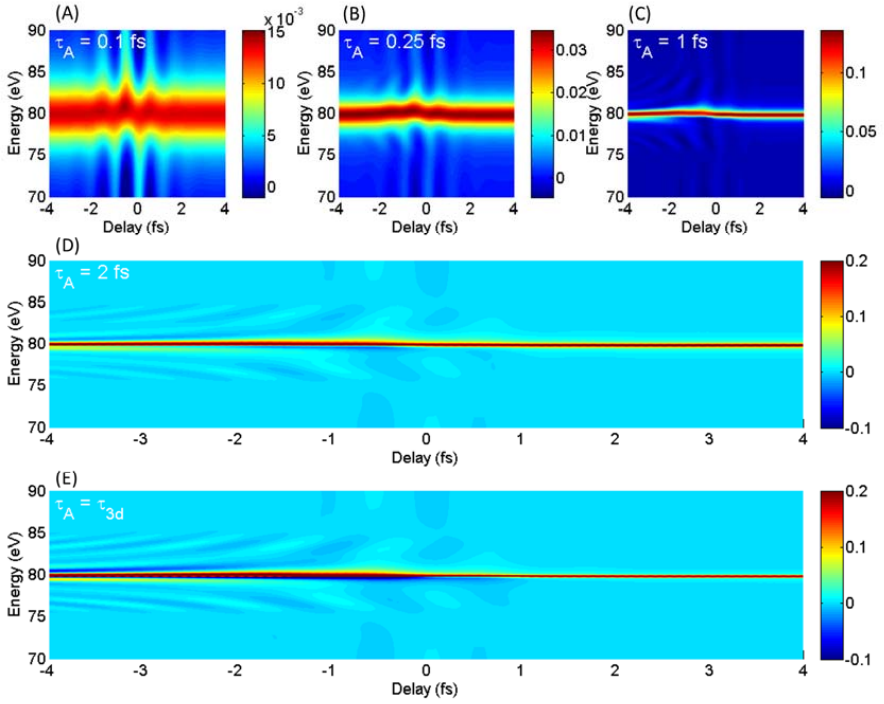

Fig. S8

The absorbance related to the $|1\rangle \rightarrow |2\rangle$ transition of Kr^+ ions computed as a function of the pump-probe delay for various settings of the lifetime τ_A of the excited state, as indicated in the upper left corner of each panel (assuming a static population). Graph **(E)** displays the simulated result for a lifetime equal to the $3d^{-1}$ hole decay time of Kr^+.

For significantly longer lifetimes ((D) and (E)), the phase introduced to the emitting dipole encompasses the action of several field cycles and results in a line distortion rather than a pure shift of its central energy. Due to the steep leading edge of the XUV polarization—induced by our attosecond pulse—some signatures of the instantaneous Stark effect are expected to survive despite the effects introduced by the integration over the few fs long lifetime. This is demonstrated in Fig. S9, where the central energy of the resonance in the data shown in Fig. S8E has been evaluated by fitting a Lorentzian profile.

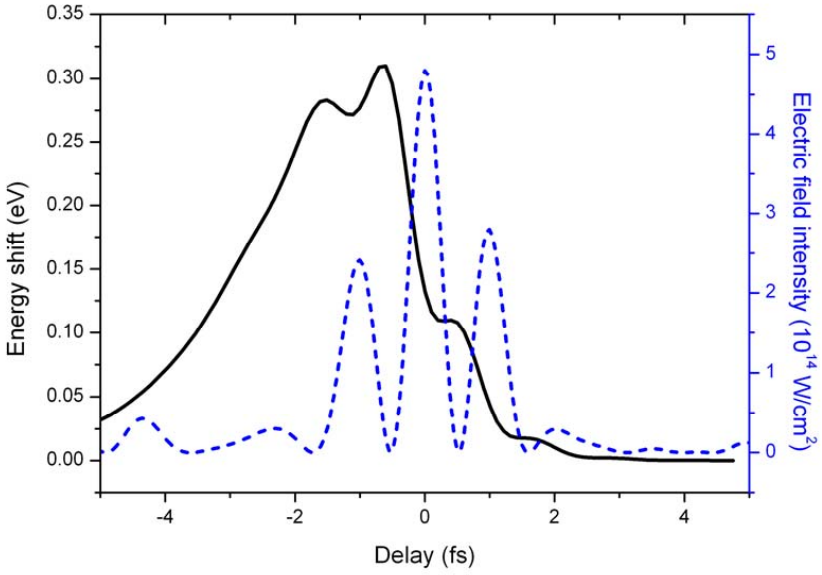

Fig. S9
Energy shift of the transition energy $\hbar\omega_{12}$ of the simulated absorption spectrogram as displayed in Fig. S8E (solid line) being analyzed by evaluating the central displacement of a fitted Lorentzian lineshape as a function of the delay τ. The blue dashed line shows the instantaneous intensity of the pump field.

Results 2: Strong-field ionization dynamics in the presence of pump polarization

Next, within our model, we attempt to accurately retrieve the population dynamics of the generated ions from an absorption spectrogram sampled under the conditions of our experiments.

Fig. S10 compares the ground state population of state $|1\rangle$, $\rho_{11}(t)$ (red curve), with that obtained by analyzing the simulated absorption spectra using the procedure described in section S4 of the SOM, which tracks the peak of the absorption line. The blue and green curves represent the retrieved populations based on our simulations with a 50 as and a 200 as XUV pulse, respectively. Note that the populations shown in Fig. S9 are based on an adiabatic tunnel-ionization model and therefore do not display the oscillatory behavior known from nonadiabatic calculations. The small "dip" in $\rho_{11}(t)$ at t=0.8 fs is due to the coupling between states $|1\rangle$ and $|3\rangle$. For the shorter XUV pulse (blue line), the ground-state population, estimated by tracking the peak of the absorption line, is significantly closer to $\rho_{11}(t)$. Since our experimental XUV probe pulse duration amounts to ~200 as, the present approach suggests that the technique of tracking the peak of the absorption

offers a possibility to recover the underlying population dynamics with an accuracy better than 10 %.

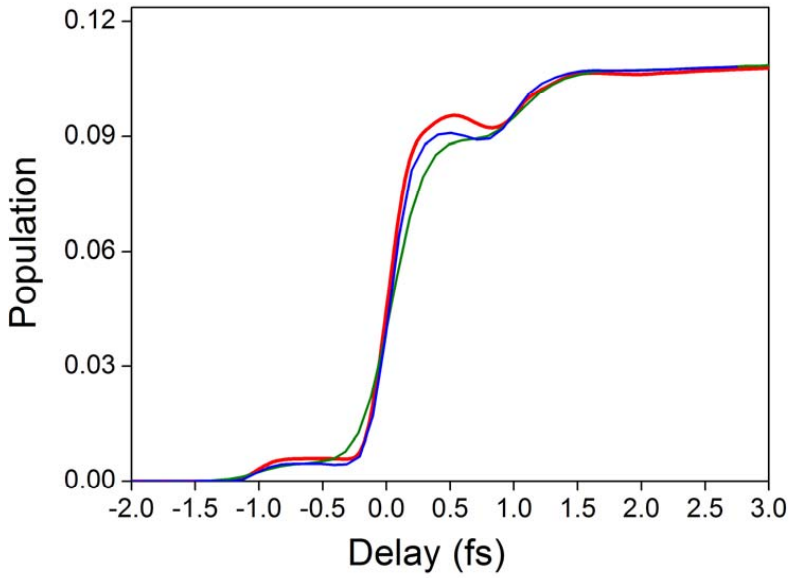

Fig. S10

Ground state population $\rho_{11}(t)$ derived by our model (red) and populations reconstructed by tracking the peak of the absorption line fitted with a Lorenzian profile. Blue (green) curve displays the retrieved population dynamics for an XUV probe pulse duration of 50 as (200 as).

4. Reconstruction of electron motion and determination of fractional ionization

Preparation of data prior to fitting

The absorbance spectrogram shown in Fig. 5A (in the main publication) was obtained by averaging over 12 consecutive scans, all taken under the same experimental conditions. All XUV spectra of the combined spectrogram were normalized in the spectral range from 83.0 - 86.7 eV (i.e. the high energy side next to the Kr^+ absorption lines) to reduce noise originating from flux variations of the XUV probe pulse. For calculating the absorbance $A(\omega,\tau)$, the mean spectral density in the time interval prior to ionization (-20.25 to -6.25 fs) has been used as a reference spectrum.

Fitting procedure

To reconstruct the Kr^+ quantum state distribution, the coherence of the spin-orbit wavepacket motion as well as the quantum phase, a fit of the experimental data shown in Fig. 5A is performed using the model equation

$$A(\omega,\tau) = -\ln\left[\exp\left[-n_0\sigma(\omega,\tau)L\right] * G(\omega)\right] + A_0 \qquad \text{(S1)}$$

applied to the spectrogram. Here, $\sigma(\omega,\tau)$ is an analytical description of the cross-section of the three absorption lines of Kr^+ based on eq. (35) in (*55*) where the reported reduced transition matrix elements are employed. Furthermore, τ indicates the time of probing, $n_0 = 5.75\cdot10^{18}\,\mathrm{cm}^{-3}$ the initial number density of neutral atoms, $L = 0.74$ mm the length of the target cell and $G(\omega)$ an area-normalized Gaussian convolution function with Δ being the FWHM value characterizing the finite spectrometer resolution and A_0 a constant offset. The coherence term in $\sigma(\omega,\tau)$ is described by $\rho^{(1/2)}_{3/2,1/2}(\tau) = \left|\rho^{(1/2)}_{3/2,1/2}\right|\exp\left(i\,\phi(\tau)\right) = \left|\rho^{(1/2)}_{3/2,1/2}\right|\exp\left(i\Delta E_{SO}\tau + i\delta\right)$, where ΔE_{SO} is the spin-orbit wavepacket splitting and δ is a phase offset which depends on the choice of the time origin $\tau = 0$ (atomic units $\hbar = e = m_e = a_0 = 1$ are used throughout this section). We chose $\tau = 0$ such that it coincides with the maximum of the instantaneous intensity of the synthesized light field transient. Hence, for a sufficiently short pump pulse, the quantity δ equals the initial quantum phase.

We fit the data set by employing the Levenberg-Marquardt optimization algorithm in the range 78.5 – 82 eV and for the delays 2.75 to 29.75 fs, avoiding the fit in the presence of the strong single-cycle initiation pulse since the model function (eq. (S1)) is not valid for describing XUV absorption under strong field influence. The fit parameters were the populations ($\rho^{(1/2)}_{1/2,1/2}$, $\rho^{(1/2)}_{3/2,3/2}$, $\rho^{(3/2)}_{3/2,3/2}$), the terms describing the coherence $\left(\left|\rho^{(1/2)}_{3/2,1/2}\right|, \Delta E_{SO}, \delta\right)$, the three central energies of the XUV transitions ($E_{3d_{5/2}} - E_{4p_{3/2}}$, $E_{3d_{3/2}} - E_{4p_{3/2}}$, $E_{3d_{3/2}} - E_{4p_{1/2}}$), as well as the spectrometer resolution Δ and the constant offset A_0 .

The sum of populations permits evaluation of the fractional ionization. The populations provided in the main publication are scaled to 100% fractional ionization.

Error analysis

Error bars of the fit quantities, reported in the main document, represent the standard error of fit results obtained by applying the described fitting approach to six consecutive pairs of the 12 delay scans. Besides the standard error, we have also calculated the standard deviations of the distributions, which on average yield values ~1.9 times larger than the standard error.

5. Retrieval of population during strong-field perturbation

Similar to the approach of fitting the absorption spectrogram after the NIR pump pulse, the formation of the population in the presence of the pump pulse has been addressed by fitting the transient absorption spectrogram using the model

$A_P(\omega,\tau) = -\ln\left[\exp\left[-c(\omega,\tau)\right] * G(\omega)\right] + A_0(\tau)$,

where $G(\omega)$ and $A_0(\tau)$ are introduced above, and $c(\omega,\tau)$ describes the absorption lines by three Lorentzian lineshape functions:

$$c(\omega,\tau) \propto \frac{1}{2\pi}\sum_{i=1}^{3} n_i(\tau)\frac{\Gamma}{\left(\omega-\omega_i(\tau)\right)^2+\left(\Gamma/2\right)^2} .$$

Here, the $n_i(\tau)$ denote the effective population and $\omega_i(\tau)$ represents the central frequency of the ith absorption line.

For the experimental parameters, this approach has been proven to allow the retrieval of the population to within an accuracy of ~10 % (see section S3).

The fit was carried out for the delay range of -20.25 to 29.75 fs and within the spectral window extending from 77.9 to 83 eV, where the results obtained in the range 2.75 to 29.75 fs served to scale the effective populations according to the determined population by utilizing eq. (S1).

All error bars in the main document depict standard errors (see section S3, *Error analysis*).

6. Numerical 3D-TDSE propagation

Theoretical modeling of strong-field ionization of the 4*p* sub-shell was done by numerically propagating the three-dimensional time-dependent Schrödinger equation (3D-TDSE) for a single active electron in the length gauge on a grid, using a standard technique (*56*). Assuming a spherically symmetric potential *V*(*r*), and the experimental laser field *F*(*t*) as shown in Fig. 3B polarized along the *z*-axis, the 3D-TDSE reads (in atomic units (a.u.): $\hbar = e = m_e = a_0 = 1$),

$$-\frac{1}{2}\Delta\psi(\vec{r},t) + \left(V(|\vec{r}|) + F(t)z\right)\psi(\vec{r},t) = i\frac{\partial}{\partial t}\psi(\vec{r},t) \qquad \text{(S2)}$$

where Δ is the Laplace operator, and $\psi(\vec{r},t)$ is the electron's wave function in coordinate space. Expanding the wave function in partial waves*,

$$\psi(\vec{r},t) = \sum_{l=0}^{L}\frac{w_l(r,t)}{r}\sum_{m=-1}^{1} Y_l^m(\theta,\varphi), \qquad \text{(S3)}$$

* The azimuthal quantum number *m* assumes only three values since the initial state is an orbital of the 4*p* sub-shell and the laser field preserves *m* due to the dipole selection rules, as evidenced by eq. (S6) and (S7).

allows us to write eq. (S2) as a set of coupled 1D radial Schrödinger equations with respect to the reduced radial wave functions $w_l(r,t)$:

$$\left(-\frac{1}{2}\frac{\partial^2}{\partial r^2}+B(r)\right)\vec{w}(r,t)+A(r,t)\vec{w}(r,t)=i\frac{\partial}{\partial t}\vec{w}(r,t), \tag{S4}$$

$$\vec{w}(r,t)=\begin{bmatrix} w_1(r,t) \\ w_2(r,t) \\ \vdots \\ w_L(r,t) \end{bmatrix}, \tag{S5}$$

$$B_{l,l'}(r)=\delta_{l,l'}\left(\frac{l(l+1)}{2r^2}+(2l+1)\begin{pmatrix} l & 0 & l \\ 0 & 0 & 0 \end{pmatrix}\begin{pmatrix} l & 0 & l \\ m & 0 & -m \end{pmatrix}V(r)\right), \tag{S6}$$

$$A_{l,l'}(r,t)=\delta_{l\pm1,l'}\sqrt{(2l+1)(2l'+1)}\begin{pmatrix} l' & 0 & l \\ 0 & 0 & 0 \end{pmatrix}\begin{pmatrix} l' & 0 & l \\ m & 0 & -m \end{pmatrix}rF(t), \tag{S7}$$

where the tabulated quantities in eq. (S6) and (S7) are Wigner-3*j* symbols—they arise naturally here by angularly integrating products of three spherical harmonics—and $\delta_{l,l'}$ is the Kronecker symbol; $V(r)$ is a pseudopotential that reproduces the ionization energy of neutral Kr. Time-propagation of eq. (S4) was achieved using the following symmetric splitting scheme:

$$\vec{w}(r,t+\delta t)=U(t,t+\delta t)\vec{w}(r,t); \tag{S8}$$

$$\begin{aligned} U(t,t+\delta t)=&\left[1+i\frac{\delta t}{2}\left(-\frac{1}{2}\frac{\partial^2}{\partial r^2}+B(r)\right)\right]^{-1}\left[1+i\frac{\delta t}{2}A(r,t+\delta t/2)\right]^{-1} \\ &\times\left[1-i\frac{\delta t}{2}A(r,t+\delta t/2)\right]\left[1-i\frac{\delta t}{2}\left(-\frac{1}{2}\frac{\partial^2}{\partial r^2}+B(r)\right)\right]. \end{aligned} \tag{S9}$$

Numerical convergence is more difficult to achieve in the length gauge than in the velocity gauge due to (i) a larger number of partial waves components required to represent the wave function in the laser field and (ii) because the phases of the wave function's components at large radial distances change rapidly, requiring a finer time step to accurately propagate these. Nevertheless, we achieved numerical convergence using an angular momentum grid up to L=100, and time and radial grid steps of 0.007 a.u. and 0.03 a.u., respectively, with a radial grid extending to 1000 a.u.. We also included a radial absorbing potential starting at r=750 a.u. to delete any unphysical reflections from the wave functions at confines of the finite simulation box.

The amount of ionization at some time t due to the strong infrared field can be defined as (*57*)

$$P(t)=1-\sum_n\left|\langle\phi_n|\psi(t)\rangle\right|^2, \tag{S10}$$

where the sum ranges over all bound states $\langle\phi_n|$ of the atom. However, calculations based on the atomic structure code (COWAN) (*52*) suggest that, excited neutrals would absorb XUV photons at approximately the same energy as Kr^+ ions. To account for this fact, we

limit the range of the summation in eq. (S10) to a sufficient number of bound states to ensure numerical convergence. In this way, Kr atoms excited to their Rydberg electronic states are considered as ions.

Now, since the numerical propagation of the 3D-TDSE was performed in the decoupled spin-orbit basis $\left|(ls)m_l m_s\right\rangle = \left|(1\text{½})m_l m_s\right\rangle := \left|m_l m_s\right\rangle$, while the measured absorption lines resolve populations in the coupled spin-orbit basis $\left|(ls)JM\right\rangle = \left|(1\text{½})JM\right\rangle := \left|JM\right\rangle$—$J(J+1)$ being the eigenvalue of $J^2 = \left(\vec{L}+\vec{S}\right)^2$—we evaluate $P(t)$ as

$$P(t) = 1 - \sum_{n,l,m_l,m_s} \left| \left\langle m_l m_s \middle| JM \right\rangle \int_0^\infty dr \phi_{nl}(r) w_l(r,t) \right|^2 ,$$

where $\left\langle m_l m_s \middle| JM \right\rangle$ is a Clebsch-Gordan coefficient and $\phi_{nl}(r)$ is the reduced radial wave function of a bound state with principal quantum number n and orbital quantum number l, obtained by solving the time-independent radial Schrödinger equation

$$-\frac{1}{2}\frac{\partial^2}{\partial r^2}\phi_{nl}(r) + \left(\frac{l(l+1)}{2r^2} + V(r)\right)\phi_{nl}(r) = \varepsilon_n \phi_{nl}(r).$$

7. TDCIS simulations and predictions for the valence electron dynamics of Kr^+

We model the strong-field ionized ensemble of krypton ions by utilizing our pioneering 3D time-dependent configuration-interaction singles (TDCIS) approach (*43*), which systematically captures correlations in photoionization processes.
Within the TDCIS approach, the Coulomb interaction between the NIR-generated hole state and the NIR-generated photoelectron is treated exactly. This interaction leads subsequently to correlation and to an entangled state between the parent ion and the photoelectron (*58*).

In this work, we extended our TDCIS approach (*43*) to account for spin-orbit interaction and spin-orbit driven valence electron wavepacket motion (*44*). To be able to simulate the strong-field ionization processes, a large range of the continuum spectrum must be covered with the need to cover angular momentum states up to L=60. To account for the multi-electron dynamics that can originate from several orbitals, we consider 18 spin orbitals ranging from $3d_{3/2}$ to $4p_{3/2}$. The total number of electronic configurations lies above 250 000, which is computationally a very challenging task.

The results of our simulations for the condition of the experiment yield the populations: $\rho^{(3/2)}_{3/2,3/2} + \rho^{(-3/2)}_{3/2,3/2} = 0.06$, $\rho^{(1/2)}_{3/2,3/2} + \rho^{(-1/2)}_{3/2,3/2} = 0.74$, $\rho^{(1/2)}_{1/2,1/2} + \rho^{(-1/2)}_{1/2,1/2} = 0.20$ (scaled to 100% fractional ionization) and a degree of coherence of $g = 0.72$, which are in good agreement with the experimental observations. Propagation effects of the EUV pulse in the medium can lead to modifications in the observed spectrum resulting in an apparent

ion density matrix that differs from the actual ion density matrix. In particular, the off-diagonal elements and, hence, the apparent hole coherence are affected by propagation effects. Based on previous theoretical work (*54*), we find that the apparent degree of coherence can be overestimated by up to 14 %. Applying this result to our theoretical prediction, we would expect an apparent degree of coherence of 0.82, which is in remarkable agreement with $g = 0.85 \pm 0.06$ retrieved from the experiment. The only open question that remains, is the discrepancy between the relative populations of the $m_j = \pm 3/2$ and $m_j = \pm 1/2$ states in the $j = 3/2$ manifold. This might indicate the need to include correlation effects that cannot be described by the TDCIS approach.

8. Delay correction between streaking and transient absorption spectrograms

Strong-field ionization, as studied in our attosecond transient absorption experiments, requires field intensities on the order of 10^{14} W/cm^2 and beyond. In contrast, streaking measurements of the light waveforms require intensities on the order of 10^{12} W/cm^2. In our experiments, the intensity of the laser beam is varied by adjusting its size with an adjustable aperture placed before the focusing mirror. The >10-fold increase of the illuminated area of the mirror between a streaking and a transient absorption (TA) measurement can be responsible for spatiotemporal effects, particularly a delay between the weak (streaking) and the strong (TA) pulse, which must be corrected before comparing the streaking and transient absorption measurements with respect to one and the same delay axis.

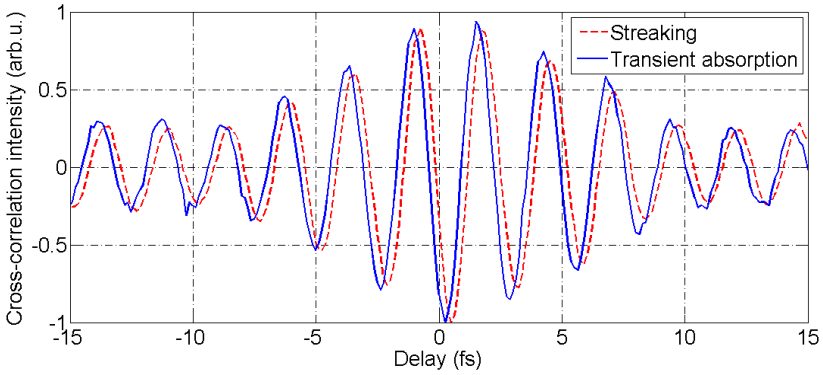

Fig. S11
Variation of the focal point intensity in a cross-correlation measurement obtained under streaking (red dashed curve) and transient absorption (blue solid line) intensity settings. An evaluation of the delay yields (280 ± 50) as.

This effect has been investigated by removing the metallic filter of the pellicle used in the experiments and recording the linear cross-correlation trace between the central part of the NIR beam, and the portion reflected off the outer mirror for two different radii of

illumination, corresponding to those of the streaking and TA measurements accordingly. Fig. S11 shows the variation of the intensity at the focal point of the beams imaged on a CCD camera (averaged over 5×5 pixels covering the central part of the beam) as a function of the delay between inner and outer mirror.

The delay between the two traces is evaluated by a linear fit of the spectral phases of both signals and amounts to (280 ± 50) as. This apparent delay, which is taken into account for the synchronous display of fields, can be attributed to simple geometrical effects introduced by spherical aberrations. The geometrical delay, evaluated at the focal plane, in the time of arrival between two pulses traveling along off-axis rays at a distance r from the mirror axis and on-axis pulses, for a spherical mirror of radius R (*59*), is given by

$$\Delta T(r) = \frac{3}{4}\frac{R}{c}\left(\frac{r}{R}\right)^4 .$$

For a pulse reflected by an annular portion of a spherical mirror situated between radii r_1 and r_2, the introduced delay (assuming a constant spatial intensity distribution) can be expressed as:

$$\Delta T_{r_1}^{r_2} = \frac{\frac{3}{4}\frac{R}{c}\int_0^{2\pi}\int_{r_1}^{r_2}\left(\frac{r}{R}\right)^4 r\, dr\, d\theta}{\int_0^{2\pi}\int_{r_1}^{r_2} r\, dr\, d\theta}$$

$$\Rightarrow \Delta T_{r_1}^{r_2} = \frac{1}{4}\frac{R}{c}\frac{1}{R^4}\frac{\left(r_2^6 - r_1^6\right)}{\left(r_2^2 - r_1^2\right)}.$$

For a mirror with $R = 250$ mm, an inner mirror radius $r_1 \approx 1.5$ mm and a streaking (TA) beam radius of $r_2 \approx 2.5$ mm ($r_2 \approx 8.1$ mm), the latter expression yields an effective delay between the streaking and transient absorption spectrograms of 240 as, which is in excellent agreement with the delay evaluated from the data shown in Fig. S11.

References and Notes

1. J. F. Whitaker *et al*., External electro-optic integrated circuit probing. *Microelectron. Eng.* **12**, 369 (1990). doi:10.1016/0167-9317(90)90050-4

2. L. Xu *et al*., Route to phase control of ultrashort light pulses. *Opt. Lett.* **21**, 2008 (1996). doi:10.1364/OL.21.002008 Medline

3. T. Brabec, F. Krausz, Intense few-cycle laser fields: Frontiers of nonlinear optics. *Rev. Mod. Phys.* **72**, 545 (2000). doi:10.1103/RevModPhys.72.545

4. J. Reichert *et al*., Measuring the frequency of light with mode-locked lasers. *Opt. Commun.* **172**, 59 (1999). doi:10.1016/S0030-4018(99)00491-5

5. D. J. Jones *et al*., Carrier-envelope phase control of femtosecond mode-locked lasers and direct optical frequency synthesis. *Science* **288**, 635 (2000). doi:10.1126/science.288.5466.635 Medline

6. S. A. Diddams *et al*., Direct link between microwave and optical frequencies with a 300 THz femtosecond laser comb. *Phys. Rev. Lett.* **84**, 5102 (2000). doi:10.1103/PhysRevLett.84.5102 Medline

7. A. Apolonski *et al*., Controlling the phase evolution of few-cycle light pulses. *Phys. Rev. Lett.* **85**, 740 (2000). doi:10.1103/PhysRevLett.85.740 Medline

8. T. Udem, R. Holzwarth, T. W. Hänsch, Optical frequency metrology. *Nature* **416**, 233 (2002). doi:10.1038/416233a Medline

9. S. T. Cundiff, J. Ye, Colloquium: Femtosecond optical frequency combs. *Rev. Mod. Phys.* **75**, 325 (2003). doi:10.1103/RevModPhys.75.325

10. A. Baltuška *et al*., Attosecond control of electronic processes by intense light fields. *Nature* **421**, 611 (2003). doi:10.1038/nature01414 Medline

11. M. Hentschel *et al*., Attosecond metrology. *Nature* **414**, 509 (2001). doi:10.1038/35107000 Medline

12. R. Kienberger *et al*., Atomic transient recorder. *Nature* **427**, 817 (2004). doi:10.1038/nature02277 Medline

13. G. Sansone *et al*., Isolated single-cycle attosecond pulses. *Science* **314**, 443 (2006). doi:10.1126/science.1132838 Medline

14. E. Goulielmakis *et al*., Single-cycle nonlinear optics. *Science* **320**, 1614 (2008). doi:10.1126/science.1157846 Medline

15. M. F. Kling *et al*., Control of electron localization in molecular dissociation. *Science* **312**, 246 (2006). doi:10.1126/science.1126259 Medline

16. G. Sansone *et al*., Electron localization following attosecond molecular photoionization. *Nature* **465**, 763 (2010). doi:10.1038/nature09084 Medline

17. M. Schultze *et al*., Delay in photoemission. *Science* **328**, 1658 (2010). doi:10.1126/science.1189401 Medline

18. J. Mauritsson *et al*., Attosecond electron spectroscopy using a novel interferometric pump-probe technique. *Phys. Rev. Lett.* **105**, 053001 (2010). doi:10.1103/PhysRevLett.105.053001 Medline

19. E. Goulielmakis *et al*., Real-time observation of valence electron motion. *Nature* **466**, 739 (2010). doi:10.1038/nature09212 Medline

20. S. Zherebtsov *et al*., *Nat. Phys.* (2011). 10.1038/nphys1983

21. P. Eckle *et al*., Attosecond ionization and tunneling delay time measurements in helium. *Science* **322**, 1525 (2008). doi:10.1126/science.1163439 Medline

22. S. E. Harris, A. V. Sokolov, Subfemtosecond Pulse Generation by Molecular Modulation. *Phys. Rev. Lett.* **81**, 2894 (1998). doi:10.1103/PhysRevLett.81.2894

23. A. V. Sokolov, D. R. Walker, D. D. Yavuz, G. Y. Yin, S. E. Harris, Raman generation by phased and antiphased molecular states. *Phys. Rev. Lett.* **85**, 562 (2000). doi:10.1103/PhysRevLett.85.562 Medline

24. J. Q. Liang, M. Katsuragawa, F. L. Kien, K. Hakuta, Sideband generation using strongly driven raman coherence in solid hydrogen. *Phys. Rev. Lett.* **85**, 2474 (2000). doi:10.1103/PhysRevLett.85.2474 Medline

25. A. V. Sokolov, D. R. Walker, D. D. Yavuz, G. Y. Yin, S. E. Harris, Femtosecond light source for phase-controlled multiphoton ionization. *Phys. Rev. Lett.* **87**, 033402 (2001). doi:10.1103/PhysRevLett.87.033402 Medline

26. T. Suzuki, M. Hirai, M. Katsuragawa, Octave-spanning Raman comb with carrier envelope offset control. *Phys. Rev. Lett.* **101**, 243602 (2008). doi:10.1103/PhysRevLett.101.243602 Medline

27. Z.-M. Hsieh *et al*., Controlling the carrier-envelope phase of Raman-generated periodic waveforms. *Phys. Rev. Lett.* **102**, 213902 (2009). doi:10.1103/PhysRevLett.102.213902 Medline

28. H.-S. Chan *et al*., Synthesis and measurement of ultrafast waveforms from five discrete optical harmonics. *Science* **331**, 1165 (2011). doi:10.1126/science.1198397 Medline

29. R. K. Shelton *et al*., Phase-coherent optical pulse synthesis from separate femtosecond lasers. *Science* **293**, 1286 (2001). doi:10.1126/science.1061754 Medline

30. M. Yamashita, K. Yamane, R. Morita, Quasi-automatic phase-control technique for chirp compensation of pulses with over-one-octave bandwidth-generation of few- to mono-cycle optical pulses. *IEEE J. Sel. Top. Quantum Electron.* **12**, 213 (2006). doi:10.1109/JSTQE.2006.871961

31. S. Rausch, T. Binhammer, A. Harth, F. X. Kärtner, U. Morgner, Few-cycle femtosecond field synthesizer. *Opt. Express* **16**, 17410 (2008). doi:10.1364/OE.16.017410 Medline

32. G. Krauss *et al*., Synthesis of a single cycle of light with compact erbium-doped fibre technology. *Nat. Photonics* **4**, 33 (2010). doi:10.1038/nphoton.2009.258

33. K. Okamura, T. Kobayashi, Octave-spanning carrier-envelope phase stabilized visible pulse with sub-3-fs pulse duration. *Opt. Lett.* **36**, 226 (2011). doi:10.1364/OL.36.000226 Medline

34. E. Goulielmakis *et al*., Attosecond control and measurement: lightwave electronics. *Science* **317**, 769 (2007). doi:10.1126/science.1142855 Medline

35. E. Goulielmakis *et al*., Direct measurement of light waves. *Science* **305**, 1267 (2004). doi:10.1126/science.1100866 Medline

36. indicates that relative to the ground state configuration a hole (or electron vacancy) is created in the $nl_j^{-1}\,nl$ sub-shell, where j denotes the total angular momentum and m_j its projection on the z axis, the latter being aligned with the laser polarization.

37. B. R. Mollow, Absorption and Emission Line-Shape Functions for Driven Atoms. *Phys. Rev. A* **5**, 1522 (1972). doi:10.1103/PhysRevA.5.1522

38. T. Unold, K. Mueller, C. Lienau, T. Elsaesser, A. D. Wieck, Optical Stark effect in a quantum dot: ultrafast control of single exciton polarizations. *Phys. Rev. Lett.* **92**, 157401 (2004). doi:10.1103/PhysRevLett.92.157401 Medline

39. C. H. B. Cruz, J. P. Gordon, P. C. Becker, R. L. Fork, C. V. Shank, *Int. J. Quant. Elec.* **24**, 261 (1988). doi:10.1109/3.122

40. S. H. Autler, C. H. Townes, Stark Effect in Rapidly Varying Fields. *Phys. Rev.* **100**, 703 (1955). doi:10.1103/PhysRev.100.703

41. B. J. Sussman, Five ways to the nonresonant dynamic Stark effect. *Am. J. Phys.* **79**, 477 (2011). doi:10.1119/1.3553018

42. N. B. Delone, V. P. Krainov, AC Stark shift of atomic energy levels. *Phys. Uspekhi* **169**, 753 (1999). doi:10.3367/UFNr.0169.199907c.0753

43. L. Greenman *et al*., Implementation of the time-dependent configuration-interaction singles method for atomic strong-field processes. *Phys. Rev. A* **82**, 023406 (2010). doi:10.1103/PhysRevA.82.023406

44. S. Pabst, L. Greenman, P. J. Ho, D. A. Mazziotti, R. Santra, Decoherence in attosecond photoionization. *Phys. Rev. Lett.* **106**, 053003 (2011). doi:10.1103/PhysRevLett.106.053003 Medline

45. F. Remacle, M. Nest, R. D. Levine, Laser steered ultrafast quantum dynamics of electrons in LiH. *Phys. Rev. Lett.* **99**, 183902 (2007). doi:10.1103/PhysRevLett.99.183902 Medline

46. M. Meckel *et al*., Laser-induced electron tunneling and diffraction. *Science* **320**, 1478 (2008). doi:10.1126/science.1157980 Medline

47. O. Smirnova *et al*., High harmonic interferometry of multi-electron dynamics in molecules. *Nature* **460**, 972 (2009). doi:10.1038/nature08253 Medline

48. M. Gertsvolf, M. Spanner, D. M. Rayner, P. B. Corkum, Demonstration of attosecond ionization dynamics inside transparent solids. *J. Phys. B* **43**, 131002 (2010). doi:10.1088/0953-4075/43/13/131002

49. M. Durach, A. Rusina, M. F. Kling, M. I. Stockman, Metallization of nanofilms in strong adiabatic electric fields. *Phys. Rev. Lett.* **105**, 086803 (2010). doi:10.1103/PhysRevLett.105.086803 Medline

50. V. Pervak, Recent development and new ideas in the field of dispersive multilayer optics. *Appl. Opt.* **50**, (Issue 9), C55 (2011). doi:10.1364/AO.50.000C55 Medline

51. K. Misawa, K. Minoshima, T. Kobayashi, Femtosecond inverse Raman spectrum of molecular J-aggregates. *J. Raman Spec.* **26**, 553 (1995). doi:10.1002/jrs.1250260710

52. R. D. Cowan, The theory of atomic structure and spectra, University of California Press, Ltd. (1981).

53. M. Jurvansuu, A. Kivimäki, S. Aksela, Inherent lifetime widths of Ar 2p^-1, Kr 3d^-1, Xe 3d^-1, and Xe 4d^-1 states. *Phys. Rev. A* **64**, 012502 (2001). doi:10.1103/PhysRevA.64.012502

54. R. Santra, R. Dunford, L. Young, Spin-orbit effect on strong-field ionization of krypton. *Phys. Rev. A* **74**, 043403 (2006). doi:10.1103/PhysRevA.74.043403

55. R. Santra, V. Yakovlev, T. Pfeifer, Z.-H. Loh, Theory of attosecond transient absorption spectroscopy of strong-field-generated ions. *Phys. Rev. A* **83**, 033405 (2011). doi:10.1103/PhysRevA.83.033405

56. H. G. Muller, *Laser Phys.* **9**, 138 (1999).

57. O. Smirnova, M. Spanner, M. Ivanov, Coulomb and polarization effects in sub-cycle dynamics of strong-field ionization. *J. Phys. At. Mol. Opt. Phys.* **39**, S307 (2006). doi:10.1088/0953-4075/39/13/S05

58. N. Rohringer, R. Santra, Multichannel coherence in strong-field ionization. *Phys. Rev. A* **79**, 053402 (2009). doi:10.1103/PhysRevA.79.053402

59. J.-C. Diels, W. Rudolph, Ultrashort Laser Pulse Phenomenon: Fundamentals, techniques and applications on a femtosecond time scale, Academic Press, Boston, (1996).

Acknowledgments: We acknowledge the development of dedicated attosecond soft X-ray optics by Michael Hofstetter and Ulf Kleineberg (LMU, MPQ). Supported by the Max Planck Society, the ERC grant (Attoelectronics-258501), the DFG Cluster of Excellence: Munich Centre for Advanced Photonics (www.munich-photonics.de), the King Saud University–Max-Planck-Institut für Quantenoptik collaboration and the European Research Training Network ATTOFEL.

5.4 Impact of Multichannel and Multipole Effects on the Cooper Minimum in the High-Order-Harmonic Spectrum of Argon

Stefan Pabst, Loren Greenman, David A. Mazziotti, and Robin Santra

Published in Phys. Rev. A **85**, 023411 (2012)

Original publication: http://link.aps.org/doi/10.1103/PhysRevA.85.023411
Free preprint version: http://arxiv.org/abs/1202.4855

Statement of Contributions

All calculations, all interpretations, and the generation of the manuscript have been done by myself.

PHYSICAL REVIEW A **85**, 023411 (2012)

Impact of multichannel and multipole effects on the Cooper minimum in the high-order-harmonic spectrum of argon

Stefan Pabst,[1,2] Loren Greenman,[3,*] David A. Mazziotti,[3] and Robin Santra[1,2,†]
[1]*Center for Free-Electron Laser Science, DESY, Notkestrasse 85, D-22607 Hamburg, Germany*
[2]*Department of Physics,University of Hamburg, Jungiusstrasse 9, D-20355 Hamburg, Germany*
[3]*Department of Chemistry and The James Franck Institute, The University of Chicago, Chicago, Illinois 60637, USA*
(Received 19 October 2011; published 21 February 2012)

We investigate the relevance of multiple-orbital and multipole effects during high-harmonic generation (HHG). The time-dependent configuration interaction singles (TDCIS) approach is used to study the impact of the detailed description of the residual electron-ion interaction on the HHG spectrum. We find that the shape and position of the Cooper minimum in the HHG spectrum of argon changes significantly whether or not interchannel interactions are taken into account. The HHG yield can be underestimated by up to 2 orders of magnitude in the energy region of 30–50 eV. We show that the argument of low ionization probability is not sufficient to justify ignoring multiple-orbital contributions. Additionally, we find the HHG yield is sensitive to the nonspherical multipole character of the electron-ion interaction.

DOI: 10.1103/PhysRevA.85.023411 PACS number(s): 32.80.Rm, 42.65.Re, 31.15.A−

I. INTRODUCTION

High-harmonic generation (HHG) is the key physical process underlying the generation of single attosecond pulses [1–3] and attosecond pulse trains [4–6], which are at the heart of attosecond science [7,8]. In recent years, the rapid progress in HHG has led to applications ranging from atomic systems [9–11] over molecular systems [12,13] to solid-state systems [14]. HHG has opened a new door to probe structural information [12,15] as well as electronic and nuclear dynamics [16–19] on fundamental time scales.

The mechanism behind HHG is well captured in the three-step model [20], where in the first step the electron is tunnel-ionized by a strong-field laser pulse, in the second step the electron is accelerated in the oscillating laser field, and finally in the last step the electron recollides with the parent ion and converts its excess energy into radiation energy in the extreme ultraviolet range [21,22]. The maximum photon energy is given by the cutoff law, $1.32I_p + 3.17U_p$, where I_p is the ionization potential of the system and U_p is the ponderomotive potential created by the intense laser field [20]. As a result, the heavier noble-gas atoms have lower cutoff energies than the lighter ones, whereas the HHG yield does increase with the atomic number [23,24]. Previous works have shown that the recombination step can be directly related to photoionization [25,26], enabling the retrieval of the electronic structure of the system [12,25,27,28]. A strong focus has been, in particular, on molecular systems [29–32].

The two most common theoretical approaches for describing HHG are the semiclassical strong-field approximation (SFA) [20], which has been extended to include Coulomb-interaction corrections [25,33–35], and the single-active-electron (SAE) approximation [36–39], where the electron-ion interaction for many-electron systems is described by a model potential [37]. The SAE approach is computationally more demanding than the SFA approach, and, therefore, has been limited to atoms and systems like H_2^+. In the literature [25], the SAE approximation has often been referred to as solving the time-dependent Schrödinger equation (TDSE). The SAE approach has some limitations. For example, it ignores contributions from multiple orbitals. Intensive studies have been performed to understand the impact of multiple-orbital contributions in molecular systems, which are essential to understand the HHG spectrum and subsequently to extract electronic-structure information [40,41]. Recently, it has been shown that even in atomic systems it is crucial to consider multiple-orbital effects [42].

In this paper, we investigate the importance of multiple-orbital (multichannel) contributions and multipole effects in the residual electron-ion interaction on the Cooper minimum in the HHG spectrum of argon [37,43,44]. Both aspects are commonly ignored in SFA and SAE calculations. Multichannel interactions [45] go beyond the independent-particle picture and cannot be captured in the language of SFA and SAE, whereas multipole effects could, in principle, arise even in a single-channel model such as SAE. However, in atomic SAE calculations, it is common to model the electron-ion interaction by a spherically symmetric potential [37]. The interaction of the liberated electron with the hole state (channel), from which it originates, is called intrachannel interaction and leads for large electron-ion distances to the $1/r$ behavior of the Coulomb potential. If the liberated electron is influenced by other orbitals the interaction is called interchannel coupling [45]. The importance of interchannel coupling for HHG has been shown for xenon, where a clear signature of the giant dipole resonance of the 4*d* subshell [45] known from photoionization studies has been directly observed in the HHG spectrum of xenon [42]. The theoretical model we are utilizing to capture these aspects is based on a time-dependent configuration-interaction singles (TDCIS) approach [46,47]. We have demonstrated in previous works that this TDCIS approach is ideal to study systematically multichannel effects in situations involving ionization [48,49].

The paper is organized as follows. In Sec. II, we give an overview of our theoretical method, which we use to

*Present address: Department of Chemistry, Berkeley Center for Quantum Information and Computation, University of California, Berkeley, CA 94720, USA.
†robin.santra@cfel.de

systematically study the influence of various approximations of the residual electron-ion interaction on the HHG spectrum. In Sec. III, we explain the system parameters used in our calculations. The results are discussed in detail in Sec. IV. Atomic units [50] are employed throughout, unless otherwise noted.

II. THEORETICAL METHODS

The time-dependent Schrödinger equation of an N-electron system exposed to a linearly polarized external electric field is given by

$$i\frac{\partial}{\partial t}|\Psi(t)\rangle = \hat{H}(t)|\Psi(t)\rangle, \tag{1a}$$

$$\hat{H}(t) = \hat{H}_0 + \hat{H}_1 - E(t)\hat{z}, \tag{1b}$$

where $|\Psi(t)\rangle$ is the full N-electron wave function and $\hat{H}(t)$ is the exact N-body Hamiltonian, which can be partitioned into three main parts: (1) $\hat{H}_0 = \hat{F} - i\eta\hat{W}$ is the sum of the time-independent Fock operator $\hat{F}$ and a complex absorbing potential (CAP), where $\langle\mathbf{x}|\,\hat{W}\,|\mathbf{x}'\rangle = [r - r_{\mathrm{CAP}}]^2\,\Theta(r - r_{\mathrm{CAP}})\,\delta(\mathbf{x} - \mathbf{x}')$ and $\Theta(r)$ is the Heaviside step function; (2) the electron-electron interactions that cannot be described by the mean-field potential in $\hat{H}_0$ are captured by $\hat{H}_1$ ($= \hat{V}_C - \hat{V}_{\mathrm{HF}} - E_{\mathrm{HF}}$; for a detailed description of these quantities, see Ref. [47]); (3) the term $E(t)\,\hat{z}$ is the laser-matter interaction in the electric dipole approximation. The CAP serves a purely numerical purpose. It prevents artificial reflections of the ionized photoelectron from the radial grid boundary and is located far away from the atom. This is controlled by the parameter r_{CAP}.

Solving numerically the full N-electron system is currently out of reach without making any approximations to the Hamiltonian or the wave function. In strong-field processes such as HHG, Eq. (1a) is commonly reduced to an effective one-electron system, where only one electron of the outermost valence shell is allowed to respond to the electric field and all other electrons are frozen or completely neglected. Here, we take an alternative way, by describing the full N-electron wave function and making no approximations to the Hamiltonian. Specifically, we use the configuration-interaction language, where we assume the field-free ground state is well captured by the Hartree-Fock ground state $|\Phi_0\rangle$. We consider only singly excited 1-particle-1-hole configurations ($1p1h$ configurations) $|\Phi_i^a\rangle$. The corresponding TDCIS N-electron wave function reads

$$|\Psi(t)\rangle = \alpha_0(t)|\Phi_0\rangle + \sum_{i,a}\alpha_i^a(t)|\Phi_i^a\rangle, \tag{2a}$$

$$|\Phi_i^a\rangle = \frac{1}{\sqrt{2}}(\hat{c}_{a,\uparrow}^\dagger\hat{c}_{i,\uparrow} + \hat{c}_{a,\downarrow}^\dagger\hat{c}_{i,\downarrow})|\Phi_0\rangle, \tag{2b}$$

where i,j, and a,b refer to occupied orbitals and unoccupied (virtual) orbitals, respectively, in the Hartree-Fock ground state $|\Phi_0\rangle$. The operators $\hat{c}_{a,\sigma}^\dagger$ and $\hat{c}_{a,\sigma}$ create and annihilate, respectively, an electron in the orbital a with spin σ. By restricting our wave function to $1p1h$ configurations, the interaction captured by $\hat{H}_1$ is the residual electron-ion interaction. The equations of motion for the expansion coefficients $\alpha_0(t)$ and $\alpha_i^a(t)$ read

$$i\dot{\alpha}_0(t) = -E(t)\sum_{i,a}(\Phi_0|\hat{z}|\Phi_i^a)\alpha_i^a(t), \tag{3a}$$

$$i\dot{\alpha}_i^a(t) = (\epsilon_a - \epsilon_i)\alpha_i^a(t) + \sum_{b,j}(\Phi_i^a|\hat{H}_1|\Phi_j^b)\alpha_j^b(t) - E(t)\Big((\Phi_i^a|\hat{z}|\Phi_0)\alpha_0(t) + \sum_{b,j}(\Phi_i^a|\hat{z}|\Phi_j^b)\alpha_j^b(t)\Big), \tag{3b}$$

where ϵ_p are the orbital energies of the orbitals $|\varphi_p\rangle$, which are eigenstates of the time-independent Fock operator (i.e., $\hat{H}_0|\varphi_p\rangle = \epsilon_p|\varphi_p\rangle$). The expression ($|$ stands for a dual vector with respect to the symmetric inner product [i.e., $(\varphi_p|\varphi_q) = \delta_{p,q}$], which differs from the Hermitian inner product. A detailed description of our implementation of the TDCIS method can be found in Ref. [47].

The exact treatment of the residual electron-ion interaction is numerically very demanding. In order to be able to treat the full electron-ion interaction, we are exploiting as much symmetry as possible. We have already used one symmetry with Eq. (2b) [i.e., the total spin of the system ($S = 0$) is conserved]. The second symmetry we are exploiting arises from the restriction to linearly polarized pulses and benefits us in two ways. Firstly, the orbital-angular-momentum projection m_a of the excited electron and the orbital-angular-momentum projection m_i of the hole state must be the same for each $|\Phi_i^a\rangle$. Secondly, the coefficients $\alpha_i^a(t)$ are the same whether an electron with orbital-angular-momentum projection m or $-m$ is excited. As a result, only the gerade parity configurations $|\Phi_i^a\rangle_g$ need to be considered because ungerade parity configurations $|\Phi_i^a\rangle_u$ will not be populated due this symmetry. The gerade and ungerade parity configurations are defined as

$$|\Phi_i^a\rangle_{g/u} := \frac{1}{\sqrt{2}}\big(|\Phi_{+i}^{+a}\rangle \pm |\Phi_{-i}^{-a}\rangle\big), \tag{4}$$

where the orbital indices $\pm a$ and $\pm i$ stand for triplets of quantum numbers $(n,l,\pm m)$ with n being the radial quantum number, l being the orbital angular momentum, and $\pm m$ being the orbital-angular-momentum projection. The configuration $|\Phi_i^a\rangle$ with $m_i = m_a = 0$ is a special case and has gerade parity. Since, as already mentioned, for linearly polarized light $|\Phi_i^a\rangle_u$ will not be populated and only $|\Phi_i^a\rangle_g$ needs to be considered, we drop the index g such that $|\Phi_i^a\rangle$ refers to gerade parity configurations from now on. The matrix elements for the gerade parity configurations as they appear in Eq. (3) are given by

$$(\Phi_i^a|\hat{z}|\Phi_j^b) = z_{(+a,+b)}\delta_{i,j} - z_{(+j,+i)}\delta_{a,b}, \tag{5a}$$

$$(\Phi_0|\hat{z}|\Phi_i^a) = z_{(+i,+a)}\begin{cases}\sqrt{2}, & m_a = m_i = 0\\ 2, & m_a = m_i \neq 0\\ 0, & m_a \neq m_i,\end{cases} \tag{5b}$$

$$\begin{aligned}&\left(\Phi_i^a|\hat{H}_1|\Phi_j^b\right)\\&= (4v_{(+a,+j;+i,+b)} - v_{(+a,+j;+b,+i)} - v_{(+a,-j;-b;+i)})\\&\times\begin{cases}1, & m_i \neq 0 \neq m_j,\\ \frac{1}{2}, & m_i = 0 = m_j,\\ \sqrt{2}^{-1}, & \text{otherwise,}\end{cases}\end{aligned} \tag{5c}$$

where we made use of the symmetries $z_{(+a,+i)} = z_{(-a,-i)}, v_{+a,+j;+b,+i} = v_{-a,-j;-b,-i}$ and $v_{+a,+j;+i,+b} = v_{-a,-j;-i,-b} = v_{+a,-j;+i,-b}$. In the last equation the relations $m_a = m_i$ and $m_b = m_j$ are used, which holds only in the case of linearly polarized light. The round parentheses in the indices of the matrix elements indicate the symmetric inner product mentioned above [47].

In the following, we study in detail three scenarios for $\hat{H}_1$: (1) no approximation is made and the residual Coulomb interaction is treated exactly within the CIS configuration space, (2) only intrachannel interactions $[(\Phi_i^a|\hat{H}_1|\Phi_j^b) = 0$ if $i \neq j]$ are considered, (3) a symmetrized version of the intrachannel interaction is used such that the angular momentum of the excited electron cannot be changed, thus simulating a spherically symmetric ion potential. When only intrachannel interactions are allowed, different orbitals will behave almost independently. Only via the ground-state depopulation can they indirectly influence each other. The symmetrization in model (3) is done by averaging over all hole states within each (n,l) subshell such that the excited electron sees only a spherically symmetric ion. The symmetrized matrix elements read

$$v^{\text{symm}}_{(a,i;b,i)} := \frac{1}{2l_i+1}\sum_{m_i} v_{(a,i;b,i)}, \tag{6a}$$

$$v^{\text{symm}}_{(a,i;i,b)} := \frac{1}{2l_i+1}\sum_{m_i} v_{(a,i;i,b)}, \tag{6b}$$

where in Eq. (6b) we additionally set $m_a = m_i = m_b$ before we perform the sum. This step can be justified, since we are using linearly polarized light and our model can only have 1-particle-1-hole configurations with $m_a = m_i$. In both cases, one finds that the symmetrized matrix elements are proportional to δ_{l_a,l_b} and δ_{m_a,m_b}.

The HHG spectrum, which is calculated via the expectation value of the electric dipole moment $\langle z\rangle(t)$, reads [51,52]

$$S(\omega) = \frac{1}{20}\frac{1}{3\pi c^3}\left|\int_{-\infty}^{\infty} dt\left[\frac{d^2}{dt^2}\langle z\rangle(t)\right]e^{-i\omega t}\right|^2. \tag{7}$$

Next to the HHG spectrum, we will focus our discussion also on the hole populations $\rho_i(t)$ generated during the HHG process. These populations are calculated with the help of the ion density matrix, which is described in detail in Ref. [47]. The ground-state population is given by $\rho_0(t) = |\alpha_0(t)|^2$.

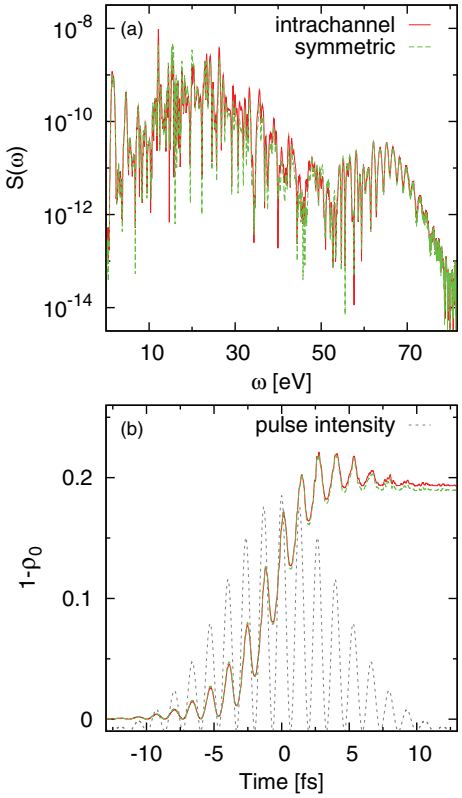

FIG. 1. (Color online) The HHG spectra (a) and the depopulations of the ground state (b) of argon are compared for the intrachannel approximation (red solid line) and for the symmetrized intrachannel approximation (green dashed line). In both cases only $3p_0$ (single-channel) is active. The intensity profile of the pulse is shown in (b). The pulse parameters are as follows: $E_{\max} = 0.085$, $\omega = 0.057$ ($\approx$800 nm), and $\tau = 413$ ($\approx$10 fs).

III. NUMERICAL DISCUSSION

All presented results were calculated with the XCID package,[1] which makes explicit use of the symmetries discussed in Sec. II. All argon calculations presented in Sec. IV were done for a laser pulse with a peak field strength of $E_{\max} = 0.085$, a carrier frequency $\omega = 0.057$ ($\approx$800 nm), and a full width at half maximum (FWHM) pulse duration of $\tau = 413$ ($\approx$10 fs). The classical turning radius of the electron for such a pulse is $r_{\text{HHG}} = E_{\max}/\omega^2 \approx 26$. As described in Ref. [47], we use a nonuniform grid with the mapping function,

$$r(x) = r_{\max}\frac{\zeta}{2}\frac{1+x}{1-x+\zeta}, \quad x \in [-1,1]. \tag{8}$$

[1] S. Pabst, L. Greenman, and R. Santra, XCID program package for multichannel ionization dynamics, DESY, Hamburg, Germany, 2011, Rev. 481, with contributions from P. J. Ho.

All calculations were done with a radial grid radius $r_{\max} = 120$, 480 radial grid points, and mapping parameter $\zeta = 1.0$. The CAP starts at a radius $r_{\mathrm{CAP}} = 100$ and has a strength $\eta = 0.01$. The maximum angular momentum employed was $l_{\max} = 80$. Furthermore, we find that for excited electrons with an orbital angular momentum $l > 6$ the multipole terms with $L_c > 0$ are negligibly small and the dominant $\hat{H}_1$ contribution comes from the monopole term. It is, therefore, a good approximation to consider only the monopole term of $\hat{H}_1$ when any orbital angular momentum of the involved orbitals is larger than 6 [for details see Ref. [47]].

IV. RESULTS

We begin our discussion with the single-channel model by allowing only the $3p_0$ orbital to be active. In Fig. 1, we compare the HHG spectra and the depopulations of the ground state of argon for a spherically symmetric electron-ion interaction (labeled symmetric) with the exact electron-ion interaction (labeled intrachannel). Note, interchannel contributions do not exist in a single-channel model. The spherically symmetric $\hat{H}_1$ has no tensorial multipole moments besides a monopole term, since the angular momentum of the electron cannot be changed. In the intrachannel and interchannel models all multipole contributions are included in $\hat{H}_1$. The depopulations [shown in Fig. 1(b)] show only small deviations during and after the pulse. The final depopulation probabilities are almost identical. Similarly, the HHG spectra [see Fig. 1(a)] show only small differences in the energy region of 30–50 eV, where also the photoionization cross sections (not shown) differ by up to 30% from each other. The Cooper minimum in the HHG spectra can be reproduced and lies between 40 and 50 eV. The low curvature of the shape of the Cooper minimum prevents a more precise localization of the minimum.

Due to the costly treatment of the residual electron-ion interaction it is common to reduce an HHG calculation to a one-electron calculation, where the electron moves in a local, spherically symmetric model potential, which describes the correct behavior for short and long distances of the electron-ion interaction and reproduces the ionization potential. This is the SAE approach, which is in spirit very close to our single-channel model with a spherically symmetric $\hat{H}_1$ (green dashed line in Fig. 1). However, there exists one major difference to typical SAE calculations. In the SAE approach one only describes one electron, which can move freely everywhere on the pseudopotential surface, and does not fulfill the Pauli principle, meaning there is no mechanism in this approach that can prevent the electron to move into orbitals that are already occupied by the $N - 1$ frozen electrons. Enforcing the Pauli principle is critical for the one-electron reduced density matrix to be N-representable, that is, to represent a realistic N-electron system [53,54]. In our theory, we describe always the entire N-electron wave function and due to the anticommutator relation of the creation and annihilation operators in Eq. (2b) the Pauli principle is ensured at all times. Recent works for molecular systems have pointed out the importance of the Pauli principle particularly for tomographic purposes [55,56].

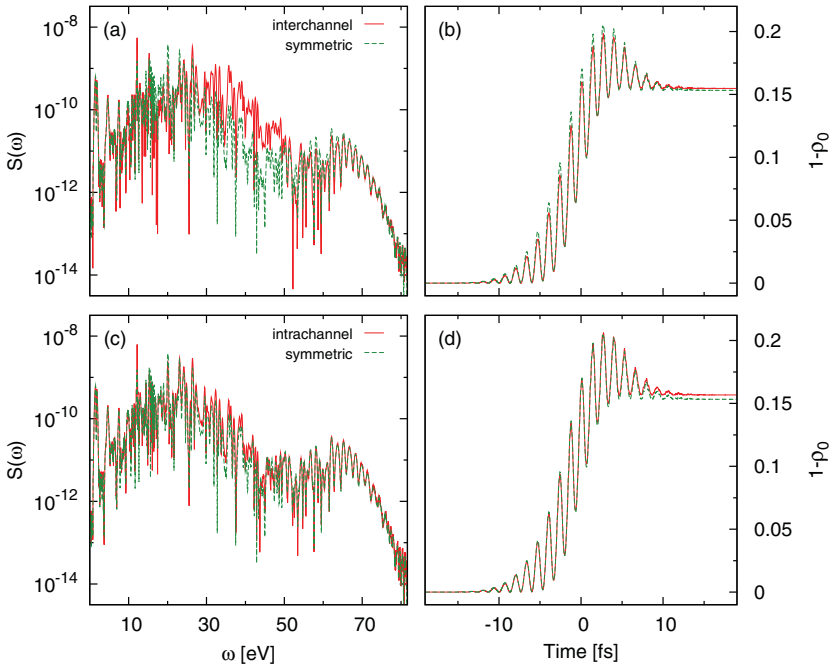

FIG. 2. (Color online) The HHG spectra (a) and (c) and the depopulations of the ground state (b) and (d) of argon are shown for $3s$ and all $3p$ orbitals active. In (a) and (b) the interchannel and in (c) and (d) the intrachannel approximation is compared with the symmetrized intrachannel approximation. The pulse parameters are the same as in Fig. 1.

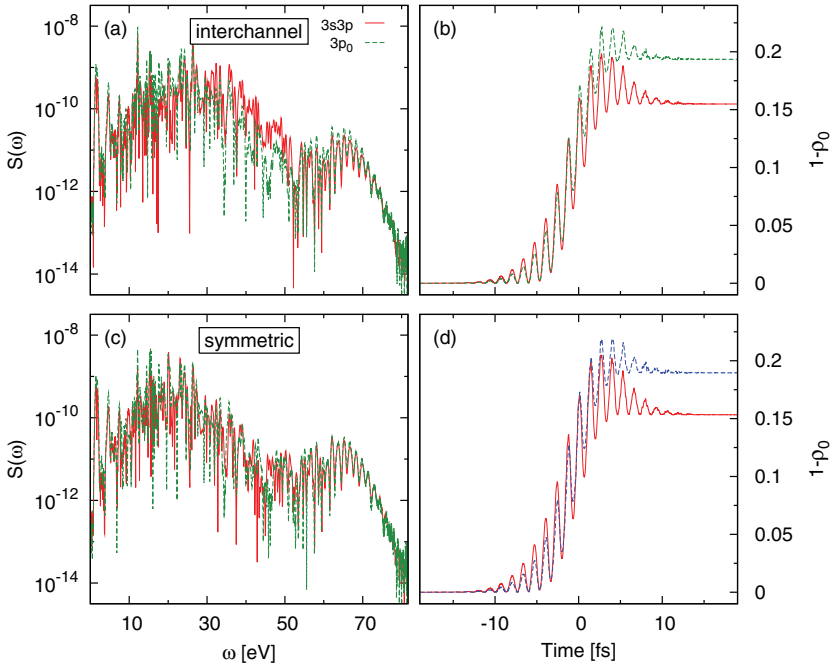

FIG. 3. (Color online) The HHG spectra [(a) and (c)] and the depopulations of the ground state [(b) and (d)] of argon are shown. The single-channel (only $3p_0$ active) calculation is compared with the multichannel calculation ($3s$ and all $3p$ active). No approximation [(a) and (b)] and the symmetrized intrachannel approximation [(c) and (d)] are made to the electron-ion interaction. The pulse parameters are the same as in Fig. 1.

Now we consider the impact of the approximation of the residual electron-ion interaction in the multichannel scenario, where we allow also $3p_{\pm1}$ electrons and the $3s$ electrons to get ionized. All differences seen in Figs. 2, 3, and 4 originate solely from physics within the $3p$ manifold. The impact of the $3s$ orbital is rather small on the HHG spectra as well as on the depopulation of the ground state. That is not a surprise due to the high $3s$ ionization potential, which is around 18 eV higher than the ionization potential of the $3p$ orbitals. The hole population of $3s$ (not shown) is over 100 times smaller than the hole populations in the $3p$ shell.

In Fig. 2 the HHG spectra and depopulations are shown for different approximations of $\hat{H}_1$. The simplification to a spherically symmetric potential [see Figs. 2(a) and 2(b)] underestimates the HHG spectrum by up to two orders of magnitude in the energy region of 30–50 eV. In addition, the shape of the Cooper minimum has now drastically changed. The position of the Cooper minimum is much more clearly defined in the interchannel case and lies slightly above 50 eV as found in recent experiments [37,43,44]. For the symmetrized intrachannel approximation, the Cooper minimum lies between 40 and 50 eV, similar to the single-channel results. The depopulation dynamics is not affected by the approximation of the electron-ion interaction. In Figs. 2(c) and 2(d) the results of the intrachannel calculation are compared with the results obtained from the symmetrized intrachannel approximation. The relative differences between these two models never exceed a factor larger than 2 and are confined to the energy region of 30–50 eV. The origin of these differences is the lack of multipole effects in the symmetrized intrachannel model. In comparison to the interchannel results, the multipole effects are much smaller than the interchannel effects seen in Fig. 2(a).

The photon energy range of 30–50 eV corresponds to a recollision electron energy range of 15–35 eV and a de Broglie wavelength of 2–3 Å. It seems that electrons with these wavelengths are most sensitive to the exact residual ion-electron interaction and, therefore, simplifications of the interaction become most evident in the corresponding photon energy regime. In the same energy region the photoionization cross section is most sensitive to the approximation made to the electron-ion interaction [45]. Our calculations (not shown) confirm that the differences in the cross sections between the intrachannel and symmetrized intrachannel model are quite small, whereas the differences to the interchannel model are up to one order of magnitude larger (and can reach values up to 20 Mb). The fact that the photoionization cross sections and the HHG spectra behave similarly (for different approximations to the electron-ion interaction) supports the picture that HHG has a close connection to photoionization. In the limit that the electron de Broglie wavelength is much longer or shorter than the characteristic length scale of the residual electron-ion interaction, the results do not depend on the detailed structure of electron-ion interaction. This may explain why the HHG

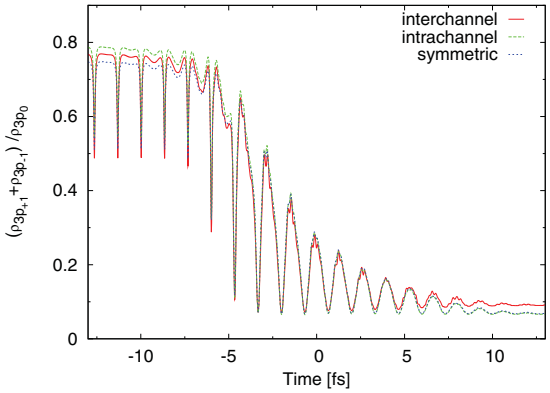

FIG. 4. (Color online) The ratio of the hole populations $\rho_{3p_1} + \rho_{3p_{-1}}$ and ρ_{3p_0} is shown for different approximations to the electron-ion interaction. The pulse parameters are the same as in Fig. 1.

spectrum does not alter significantly for photon energies smaller than 20 eV and photon energies close to the cutoff region.

We have seen that approximations to the electron-ion interaction can cause differences in the HHG yield, particularly, when multiple orbitals are considered. Not all electron-ion approximations make the HHG spectrum sensitive to whether a single orbital or multiple orbitals are active. In Fig. 3 we compare the HHG spectrum and the depopulation of the ground state for a single-channel (only $3p_0$ active) and for a multichannel (all $3p$ and $3s$ are active) calculations. Figures 3(a) and 3(b) are calculated with the exact $\hat{H}_1$ term including interchannel and multipole effects in the residual electron-ion interaction. The HHG signal strength for the single-channel calculation is strongly reduced in the spectral range of 30–50 eV, whereas the signal is slightly enhanced in the cutoff region. When the symmetrized intrachannel approximation is made [see Figs. 3(c) and 3(d)], the HHG spectra are almost identical whether single-channel or multichannel calculations are performed. This stands in contrast to the interchannel results, where the interchannel coupling causes strong differences in the HHG yield. The depopulation is overestimated by $\approx$25% regardless of the approximation made to the electron-ion interaction.

We have seen the strong differences in the HHG spectra and in the depopulations depending on whether only $3p_0$ or all $3p$ electrons are active (the contributions from $3s$ are negligible small). Does that also mean the ionization probabilities of $3p_{\pm1}$ are comparable with $3p_0$? The ratio $(\rho_{3p_1} + \rho_{3p_{-1}})/\rho_{3p_0}$ is shown in Fig. 4 for the different models. Note that for linearly polarized light $\rho_{3p_{+1}} = \rho_{3p_{-1}}$. Before the pulse, all ratios are close to 0.8 and drop to $\approx$0.1 after the pulse. Both intrachannel models lead even to the same final ratio. The small ratios after the pulse show that, at least ultimately, mainly the $3p_0$ orbital gets ionized, which is at the heart of the SAE approximation. The oscillations in the ratios during the pulse are in phase with the oscillations in the electric field. They are a direct consequence of the projection of the wave function onto the field-free states in the presence of the laser field. In contrast to the HHG spectra (see Fig. 2), the effects of the intrachannel or symmetric approximation on the population dynamics are quite small.

V. CONCLUSION

We have described the HHG process with a many-body approach, namely TDCIS, where we describe the entire N-electron wave function. This allows us to fulfill the Pauli principle at all times. Our results show that multichannel effects in the residual electron-ion interaction, which is a combination of the bare nuclear potential and the electron-electron interaction for many-electron systems, have a significant influence on the HHG spectrum. They cannot generally be neglected for atoms and specifically not for molecules as recent experiments have shown [40,41]. We have demonstrated that orbitals, despite their relatively low ionization probability by the end of the pulse, can lead to surprisingly large modifications of up to 2 orders of magnitude in the HHG spectrum (especially in the energy region of 30–50 eV). While we confirm that after the end of the pulse, the populations of the $3p_{\pm1}$ orbitals are relatively small, their contributions during the pulse are not small and have indirectly through interchannel coupling a significant impact on the HHG yield.

We saw that neglecting interchannel interactions leads to large changes in the HHG yield. Multipole effects influence the spectra but not as dramatically as interchannel effects do. All deviations in the HHG yield are in the 30–50 eV energy region, which corresponds to a de Broglie wavelength of the recolliding electron between 2–3 Å. This coincides with the characteristic length scale on which the electron-ion interaction goes over into a pure long-range $1/r$ potential. In contrast to the large disagreement in the HHG spectra between the single-channel and multichannel calculations including interchannel interactions we found that by using the symmetric interaction the HHG spectra look quite the same whether or not a single or multiple channels participate in the HHG process. This comparison directly shows that the population of an orbital does not map directly to its importance in the HHG mechanism.

All these observations demonstrate that many-body effects enter in the HHG spectrum and need to be understood in order to successfully use them for tomographic imaging [12]. The time-dependent configuration-interaction approach provides a clear pathway how these and higher-order effects can be taken into account. Recent works [57] have suggested that multielectron excitations are not a dominant factor. All essential multielectron effects can be captured by single-electron excitations including interchannel interactions. This makes the TDCIS approach perfectly suited for studying many-body effects in HHG.

ACKNOWLEDGMENTS

This work has been supported by the Deutsche Forschungsgemeinschaft (DFG) under Grant No. SFB 925/A5. We thank Sang-Kil Son for helpful discussions.

[1] M. Hentschel, R. Kienberger, C. Spielmann, G. A. Reider, N. Milosevic, T. Brabec, P. Corkum, U. Heinzmann, M. Drescher, and F. Krausz, Nature (London) **414**, 509 (2001).

[2] G. Sansone, F. Kelkensberg, J. F. Perez-Torres, F. Morales, M. F. Kling, W. Siu, O. Ghafur, P. Johnsson, M. Swoboda, E. Benedetti, F. Ferrari, F. Lepine, J. L. Sanz-Vicario, S. Zherebtsov, I. Znakovskaya, A. L'Huillier, M. Yu. Ivanov, M. Nisoli, F. Martin, and M. J. J. Vrakking, Nature (London) **465**, 763 (2010).

[3] T. Sekikawa, A. Kosuge, T. Kanai, and S. Watanabe, Nature (London) **432**, 605 (2004).

[4] N. A. Papadogiannis, B. Witzel, C. Kalpouzos, and D. Charalambidis, Phys. Rev. Lett. **83**, 4289 (1999).

[5] P. M. Paul, E. S. Toma, P. Breger, G. Mullot, F. Aug, P. Balcou, H. G. Muller, and P. Agostini, Science **292**, 1689 (2001).

[6] K. P. Singh, F. He, P. Ranitovic, W. Cao, S. De, D. Ray, S. Chen, U. Thumm, A. Becker, M. M. Murnane, H. C. Kapteyn, I. V. Litvinyuk, and C. L.Cocke, Phys. Rev. Lett. **104**, 023001 (2010).

[7] F. Krausz and M. Ivanov, Rev. Mod. Phys. **81**, 163 (2009).

[8] P. H. Bucksbaum, Science **317**, 766 (2007).

[9] E. A. Gibson, A. Paul, N. Wagner, R. Tobey, S. Backus, I. P. Christov, M. M. Murnane, and H. C. Kapteyn, Phys. Rev. Lett. **92**, 033001 (2004).

[10] M. Uiberacker, T. Uphues, M. Schultze, A. J. Verhoef, V. Yakovlev, M. F. Kling, J. Rauschenberger, N. M. Kabachnik, H. Schroder, M. Lezius, K. L. Kompa, H.-G. Muller, M. J. J. Vrakking, S. Hendel, U. Kleineberg, U. Heinzmann, M. Drescher, and F. Krausz, Nature (London) **446**, 627 (2007).

[11] A. L. Lytle, X. Zhang, J. Peatross, M. M. Murnane, H. C. Kapteyn, and O. Cohen, Phys. Rev. Lett. **98**, 123904 (2007).

[12] J. Itatani, J. Levesque, D. Zeidler, H. Niikura, H. Pepin, J. Kieffer, P. Corkum, and D. Villeneuve, Nature (London) **432**, 867 (2004).

[13] S. Baker, J. S. Robinson, C. A. Haworth, H. Teng, R. A. Smith, C. C. Chiril, M. Lein, J. W. G. Tisch, and J. P. Marangos, Science **312**, 424 (2006).

[14] A. L. Cavalieri, N. Mueller, T. Uphues, V. S. Yakovlev, A. Baltuska, B. Horvath, B. Schmidt, L. Bluemel, R. Holzwarth, S. Hendel, M. Drescher, U. Kleineberg, P. M. Echenique, R. Kienberger, F. Krausz, and U. Heinzmann, Nature (London) **449**, 1029 (2007).

[15] D. Shafir, Y. Mairesse, H. J. Wrner, K. Rupnik, D. M. Villeneuve, P. B. Corkum, and N. Dudovich, New J. Phys. **12**, 073032 (2010).

[16] M. Drescher, M. Hentschel, R. Kienberger, M. Uiberacker, V. Yakovlev, A. Scrinzi, T. Westerwalbesloh, U. Kleineberg, U. Heinzmann, and F. Krausz, Nature (London) **419**, 803 (2002).

[17] H. J. Woerner, J. B. Bertrand, D. V. Kartashov, P. B. Corkum, and D. M. Villeneuve, Nature (London) **466**, 604 (2010).

[18] E. Goulielmakis, Z.-H. Loh, A. Wirth, R. Santra, N. Rohringer, V. S. Yakovlev, S. Zherebtsov, T. Pfeifer, A. M. Azzeer, M. F. Kling, S. R. Leone, and F. Krausz, Nature (London) **466**, 739 (2010).

[19] A. Wirth, M. Th. Hassan, I. Grguraš, J. Gagnon, A. Moulet, T. T. Luu, S. Pabst, R. Santra, Z. A. Alahmed, A. M. Azzeer, V. S. Yakovlev, V. Pervak, F. Krausz, and E. Goulielmakis, Science **334**, 195 (2011).

[20] M. Lewenstein, P. Balcou, M. Y. Ivanov, A. L'Huillier, and P. B. Corkum, Phys. Rev. A **49**, 2117 (1994).

[21] P. B. Corkum, Phys. Rev. Lett. **71**, 1994 (1993).

[22] K. J. Schafer, B. Yang, L. F. DiMauro, and K. C. Kulander, Phys. Rev. Lett. **70**, 1599 (1993).

[23] A. Gordon, F. X. Kärtner, N. Rohringer, and R. Santra, Phys. Rev. Lett. **96**, 223902 (2006).

[24] V.-M. Gkortsas, S. Bhardwaj, E. L. Falco-Filho, K.-H. Hong, A. Gordon, and F. X. Krtner, J. Phys. B **44**, 045601 (2011).

[25] A.-T. Le, R. R. Lucchese, S. Tonzani, T. Morishita, and C. D. Lin, Phys. Rev. A **80**, 013401 (2009).

[26] L. Landau and E. Lifschitz, *Quantum Mechanics Non-Relativistic* (Pergamon Press, New York, 1965).

[27] C. D. Lin, A.-T. Le, Z. Chen, T. Morishita, and R. Lucchese, J. Phys. B **43**, 122001 (2010).

[28] T. Morishita, A.-T. Le, Z. Chen, and C. D. Lin, Phys. Rev. Lett. **100**, 013903 (2008).

[29] C. Vozzi, F. Calegari, E. Benedetti, J.-P. Caumes, G. Sansone, S. Stagira, M. Nisoli, R. Torres, E. Heesel, N. Kajumba, J. P. Marangos, C. Altucci, and R. Velotta, Phys. Rev. Lett. **95**, 153902 (2005).

[30] M. Y. Emelin, M. Y. Ryabikin, and A. M. Sergeev, New J. Phys. **10**, 025026 (2008).

[31] W. Boutu, S. Haessler, H. Merdji, P. Breger, G. Waters, M. Stankiewicz, L. J. Frasinski, R. Taieb, J. Caillat, A. Maquet, P. Monchicourt, B. Carre, and P. Salieres, Nat. Phys. **4**, 545 (2008).

[32] B. A. Sickmiller and R. R. Jones, Phys. Rev. A **80**, 031802 (2009).

[33] J. Z. Kamiński and F. Ehlotzky, Phys. Rev. A **54**, 3678 (1996).

[34] O. Smirnova, A. S. Mouritzen, S. Patchkovskii, and M. Y. Ivanov, J. Phys. B **40**, F197 (2007).

[35] A. Abdurrouf and F. H. M. Faisal, Phys. Rev. A **79**, 023405 (2009).

[36] K. C. Kulander, K. J. Schafer, and J. L. Krause, Int. J. Quantum Chem. **40**, 415 (1991).

[37] J. Higuet, H. Ruf, N. Thiré, R. Cireasa, E. Constant, E. Cormier, D. Descamps, E. Mével, S. Petit, B. Pons, Y. Mairesse, and B. Fabre, Phys. Rev. A **83**, 053401 (2011).

[38] M. Awasthi, Y. V. Vanne, A. Saenz, A. Castro, and P. Decleva, Phys. Rev. A **77**, 063403 (2008).

[39] I. A. Ivanov and A. S. Kheifets, Phys. Rev. A **79**, 053827 (2009).

[40] B. K. McFarland, J. P. Farrell, P. H. Bucksbaum, and M. Ghr, Science **322**, 1232 (2008).

[41] O. Smirnova, Y. Mairesse, S. Patchkovskii, N. Dudovich, D. Villeneuve, P. Corkum, and M. Y. Ivanov, Nature (London) **460**, 972 (2009).

[42] A. D. Shiner, B. E. Schmidt, C. Trallero-Herrero, H. J. Worner, S. Patchkovskii, P. B. Corkum, J. Kieffer, F. Legare, and D. M. Villeneuve, Nat. Phys. **7**, 464 (2011).

[43] H. J. Wörner, H. Niikura, J. B. Bertrand, P. B. Corkum, and D. M. Villeneuve, Phys. Rev. Lett. **102**, 103901 (2009).

[44] J. P. Farrell, L. S. Spector, B. K. McFarland, P. H. Bucksbaum, M. Gühr, M. B. Gaarde, and K. J. Schafer, Phys. Rev. A **83**, 023420 (2011).

[45] A. F. Starace, in *Handbuch der Physik*, Vol. **31**, edited by W. Mehlhorn (Springer, Berlin, 1980), pp. 1–121.

[46] N. Rohringer, A. Gordon, and R. Santra, Phys. Rev. A **74**, 043420 (2006).

[47] L. Greenman, P. J. Ho, S. Pabst, E. Kamarchik, D. A. Mazziotti, and R. Santra, Phys. Rev. A **82**, 023406 (2010).

[48] N. Rohringer and R. Santra, Phys. Rev. A **79**, 053402 (2009).

[49] S. Pabst, L. Greenman, P. J. Ho, D. A. Mazziotti, and R. Santra, Phys. Rev. Lett. **106**, 053003 (2011).
[50] P. J. Mohr, B. N. Taylor, and D. B. Newell, Rev. Mod. Phys. **80**, 633 (2008).
[51] A. Gordon and F. Kärtner, Opt. Express **13**, 2941 (2005).
[52] E. Seres, J. Seres, F. Krausz, and C. Spielmann, Phys. Rev. Lett. **92**, 163002 (2004).
[53] A. E. Rothman and D. A. Mazziotti, J. Chem. Phys. **132**, 104112 (2010).
[54] D. A. Mazziotti, Phys. Rev. Lett. **106**, 083001 (2011).
[55] R. Santra and A. Gordon, Phys. Rev. Lett. **96**, 073906 (2006).
[56] S. Patchkovskii, Z. Zhao, T. Brabec, and D. M. Villeneuve, Phys. Rev. Lett. **97**, 123003 (2006).
[57] S. Sukiasyan, C. McDonald, C. Destefani, M. Y. Ivanov, and T. Brabec, Phys. Rev. Lett. **102**, 223002 (2009).

5.5 Theory of Attosecond Transient Absorption Spectroscopy of Krypton for Overlapping Pump and Probe Pulses

Stefan Pabst, Arina Sytcheva, Antoine Moulet, Adrian Wirth, Eleftherios Goulielmakis, and Robin Santra

Published in Phys. Rev. A **86**, 063411 (2012)

Original publication: http://dx.doi.org/10.1103/PhysRevA.86.063411
Free preprint version: http://arxiv.org/abs/1212.1589

Statement of Contributions

I performed all calculations except the calculations of the polarizabilities with the program DALTON, which has been done by Arina Sytcheva. The interpretation of the results has been done by Antoine Moulet, Robin Santra, and myself. I wrote the manuscript and generated all figures.

PHYSICAL REVIEW A **86**, 063411 (2012)

Theory of attosecond transient-absorption spectroscopy of krypton for overlapping pump and probe pulses

Stefan Pabst,[1,2] Arina Sytcheva,[1] Antoine Moulet,[3] Adrian Wirth,[3] Eleftherios Goulielmakis,[3] and Robin Santra[1,2]
[1]*Center for Free-Electron Laser Science, DESY, Notkestrasse 85, 22607 Hamburg, Germany*
[2]*Department of Physics,University of Hamburg, Jungiusstrasse 9, 20355 Hamburg, Germany*
[3]*Max-Planck-Institut für Quantenoptik, Hans-Kopfermann-Str. 1, D-85748 Garching, Germany*
(Received 19 September 2012; published 17 December 2012)

We present a fully *ab initio* calculations for attosecond transient absorption spectroscopy of atomic krypton with overlapping pump and probe pulses. Within the time-dependent configuration interaction singles (TDCIS) approach, we describe the pump step (strong-field ionization using a near-infrared pulse) as well as the probe step (resonant electron excitation using an extreme-ultraviolet pulse) from first principles. We extend our TDCIS model and account for the spin-orbit splitting of the occupied orbitals. We discuss the spectral features seen in a recent attosecond transient absorption experiment [A. Wirth *et al.*, Science **334**, 195 (2011)]. Our results support the concept that the transient absorption signal can be directly related to the instantaneous hole population even during the ionizing pump pulse. Furthermore, we find strong deformations in the absorption lines when the overlap of pump and probe pulses is maximum. These deformations can be described by relative phase shifts in the oscillating ionic dipole. We discuss possible mechanisms contributing to these phase shifts. Our finding suggests that the nonperturbative laser dressing of the entire N-electron wave function is the main contributor.

DOI: 10.1103/PhysRevA.86.063411 PACS number(s): 32.80.Rm, 42.65.Re, 31.15.A−

I. INTRODUCTION

The interaction of matter with light is a key process in physical systems on any length scale. The fundamentals of matter-light interaction can be best studied in atomic systems due to their relative simplicity. The absorption of light promotes electrons into excited states. If enough energy is absorbed by the system, one or more electrons can leave the atom (i.e., ionization takes place) [1–3]. The most common types of ionization are single-photon and few-photon ionizations [4–6], above-threshold ionization [7–11], and tunnel ionization [12–17].

Recently, high-order-harmonic generation (HHG) has become a major tool in attosecond physics, allowing one to generate ultrashort light pulses with broad spectral bandwidths [18,19]. From the ability to generate attosecond pulses [20], an entire new research area has emerged [21] focusing on electronic dynamics [22–28] and molecular motion [29–32] on their fundamental time scale. A particularly interesting aspect is the electron motion and the corresponding hole-creation dynamics during the ionization process [33–35]. The high pulse intensities used in these experiments distort significantly the potential of the electrons such that it is possible for the electron to tunnel through or even travel over the barrier out of the system (i.e., tunnel-ionization or barrier-suppression regime, respectively).

A well-known model to describe tunnel ionization in atomic systems is the Ammosov, Delone, and Krainov (ADK) model [36,37]. It applies to intense low-frequency fields, where a quasistatic approximation can be made, meaning electrons follow adiabatically the external field. In these kinds of fields, tunneling rates and final ion populations can be well reproduced by the ADK model [38]. Short, few-cycle pulses give access to instantaneous rather than cycle-averaged quantities and reveal the nonadiabatic behavior of the electronic motion. In this case, an explicit time-dependent treatment of the ionization process is advantageous. In combination with a multichannel theory, the dynamics in the relative phases between generated ionic states can be captured; something that cannot be done by the ADK model. In the past, the state of the ion (after ionization) has not been of high interest, since it was not experimentally accessible.

Such a technique does now exist: attosecond transient absorption spectroscopy [39–42]. Transient absorption spectroscopy has been used for years to study chemical reactions on the femtosecond time scale [43]. However, just recently this technique has been extended to the attosecond regime [39], where it is possible to probe the diagonal and off-diagonal elements of the ion density matrix (IDM) of the generated ion. From the off-diagonal IDM elements, the relative phase and the degree of coherence between the ionic states can be extracted, which are highly sensitive to the multichannel interactions occurring during the ionization process [44]. Attosecond transient absorption spectroscopy has also been used to study the dynamics of autoionizing states [45–48] and to study the motion of an electron wave packet during ionization [49].

The rapid technical advances in synthesizing light pulses made it possible to generate subcycle near-infrared (NIR) pulses lasting no longer than a few femtoseconds and to reduce the jitter (time-delay fluctuation) between the NIR pump pulse and the extreme ultraviolet (XUV) probe pulse to tens of attoseconds [35]. This time delay stability allows one to reliably probe the NIR-driven tunnel ionization dynamics within an optical cycle (approx. 2 fs) as a function of the pump-probe delay. For nonoverlapping pump and probe pulses, transient absorption spectroscopy can be used to determine the instantaneous IDM at the time of the probe pulse [40].

The aim of this study is to investigate the ion population dynamics in krypton within the pump pulse. We show that the instantaneous ionic-state population can be well captured by the transient absorption spectrum even for overlapping pump and probe pulses. Furthermore, we observe strong

modifications of the absorption lines in the transient absorption spectroscopy when pump and probe pulses have the maximum overlap.

We show that these deformations can be understood by relative phase shifts in the ionic dipole. We identify that the highly nonperturbative dressing of the N-electron states (particularly with the neutral ground state) is responsible for the phase shift. Also the dressing of the ionic [$(N-1)$-electron] states, which leads to energy shifts in the ionic states, contributes to the phase shift. The latter, however, is much weaker than the first dressing mechanism. Note that these two dressing mechanisms are quite different in nature. The first mechanism dresses N-electron states and the second mechanism dresses $(N-1)$-electron states.

To capture these dressing mechanisms during ionization, a description of the entire N-electron system is required. We describe the dynamics of the full N-body wave function with a time-dependent configuration interaction singles (TDCIS) approach [50]. The description of the pump and the probe steps of Refs. [35,39] requires at least two active electrons, since the pump pulse ionizes an outer-valence electron and the probe pulse resonantly excites an inner-shell electron into the generated hole. Therefore, it is crucial to use a multichannel model, which goes beyond the single-active-electron (SAE) approximation, to describe the pump-probe process.

The paper is structured as follows: In Sec. II, we give an overview of our TDCIS method and describe the theory of attosecond transient absorption for overlapping pump and probe pulses. The results are discussed in detail in Sec. III. In Sec. IV we draw our conclusions. Atomic units [51] are employed throughout unless otherwise noted.

II. THEORETICAL METHODS

A. Equations of motion

The time-dependent Schrödinger equation of an N-electron system exposed to linearly polarized electric fields is given by

$$i\frac{\partial}{\partial t}|\Psi(t)\rangle = \hat{H}(t)|\Psi(t)\rangle, \tag{1a}$$

$$\hat{H}(t) = \hat{H}_0 + \hat{H}_1 - E(t)\hat{z}, \tag{1b}$$

where $|\Psi(t)\rangle$ is the full N-electron wave function and $\hat{H}(t)$ is the exact N-body Hamiltonian, which can be partitioned into three main parts: (1) $\hat{H}_0 = \hat{F} - i\eta\hat{W}$ is the sum of the time-independent Fock operator $\hat{F}$ and a complex absorbing potential (CAP), which reads $W(r) = [r - r_{\mathrm{CAP}}]^2\Theta(r - r_{\mathrm{CAP}})$, where r is the radius, and $\Theta(r)$ is the Heaviside step function; (2) the electron-electron interactions that cannot be captured by the mean-field potential in $\hat{H}_0$ are captured by $\hat{H}_1$ ($=\hat{V}_C - \hat{V}_{\mathrm{HF}} - E_{\mathrm{HF}}$; for a detailed description of these quantities see Refs. [50,52]); and (3) the term $E(t)\hat{z}$ is the laser-matter interaction in the electric dipole approximation using the length form. The CAP within $\hat{H}_0$ prevents artificial reflections of the ionized photoelectron from the radial grid boundary and is located far from the atom such that all processes close to the atom are unaffected by the CAP. This is controlled by the parameter r_{CAP}.

By allowing only one electron to get excited or ionized out of the ground-state configuration, we strongly reduce the complexity of solving Eq. (1a). A suitable way to achieve this goal is by exploiting the configuration interaction (CI) language and describing the N-body wave function in terms of the Hartree-Fock ground state $|\Phi_0\rangle$ and singly excited configurations $|\Phi_i^a\rangle$. This approximation is known as CI singles (CIS). The corresponding TDCIS N-electron wave function reads

$$|\Psi(t)\rangle = \alpha_0(t)|\Phi_0\rangle + \sum_{i,a}\alpha_i^a(t)\big|\Phi_i^a\big\rangle, \tag{2a}$$

$$\big|\Phi_i^a\big\rangle = \hat{c}_a^\dagger\hat{c}_i|\Phi_0\rangle, \tag{2b}$$

where i,j and a,b refer to occupied orbitals and unoccupied (virtual) orbitals, respectively, in the Hartree-Fock ground state $|\Phi_0\rangle$. Indices p,q are used when no distinction is made between occupied and virtual orbitals. The operators $\hat{c}_p^\dagger$ and $\hat{c}_p$ create and annihilate, respectively, an electron in the spin orbital $|\varphi_p\rangle$. The equations of motion (EOMs) for the expansion coefficients $\alpha_0(t)$ and $\alpha_i^a(t)$ read

$$i\dot{\alpha}_0(t) = -E(t)\sum_{i,a}\big(\Phi_0|\hat{z}|\Phi_i^a\big)\alpha_i^a(t), \tag{3a}$$

$$\begin{aligned} i\dot{\alpha}_i^a(t) = {} & (\varepsilon_a - \varepsilon_i)\alpha_i^a(t) + \sum_{b,j}\big(\Phi_i^a|\hat{H}_1|\Phi_j^b\big)\alpha_j^b(t) \\ & - E(t)\left(\big(\Phi_i^a|\hat{z}|\Phi_0\big)\alpha_0(t) + \sum_{b,j}\big(\Phi_i^a|\hat{z}|\Phi_j^b\big)\alpha_j^b(t)\right), \end{aligned} \tag{3b}$$

where ε_p are the orbital energies of the orbitals $|\varphi_p\rangle$, which are eigenstates of the modified, time-independent Fock operator (i.e., $\hat{H}_0|\varphi_p\rangle = \varepsilon_p|\varphi_p\rangle$). The operator $\hat{H}_1$ is the residual electron-electron interaction, which goes beyond the mean-field potential. The parentheses $|\cdot)$ and $(\cdot|$ stand for the vector and dual vector with respect to the symmetric inner product required because of the non-Hermiticity of $\hat{H}_0$. The dipole interaction between singly excited configurations reduces to transitions between states of the excited electron and transitions between ionic states:

$$\big(\Phi_i^a|\hat{z}|\Phi_j^b\big) = (\varphi_a|\hat{z}|\varphi_b)\delta_{i,j} - (\varphi_j|\hat{z}|\varphi_i)\delta_{a,b}. \tag{4}$$

A detailed description of our implementation of the TDCIS method can be found in Refs. [50,53].

From the full N-body wave function one can construct the ion density matrix (IDM) $\hat{\rho}^{\mathrm{IDM}}(t)$ by tracing over the excited electron. The matrix elements are given by

$$\begin{aligned} \rho_{i,j}^{\mathrm{IDM}}(t) = \sum_{a,b}\Bigg(\alpha_i^a(t)\big[\alpha_j^b(t)\big]^* o_{b,a} + 2\eta\, e^{i(\varepsilon_i-\varepsilon_j)t} \\ \times\int_{-\infty}^{t}dt' w_{b,a}\,\alpha_i^a(t')\big[\alpha_j^b(t')\big]^* e^{-i(\varepsilon_i-\varepsilon_j)t'}\Bigg), \end{aligned} \tag{5}$$

where $w_{b,a}$ are the matrix elements of the CAP in the virtual orbital basis, and $o_{b,a}$ are the overlap matrix elements between virtual orbitals. The second term in Eq. (5) corrects the loss of norm in the IDM due to the absorption of the excited electron by the CAP. The CAP is placed far away from the atom such that an electron so far out does not affect the ion, specifically the ionic states. Therefore, the absorption of an electron by the CAP results only in an artificial loss of norm

that is compensated by the second term in Eq. (5). To keep the notation compact, we use the notation $\rho_i^{\mathrm{IDM}}(t) := \rho_{i,i}^{\mathrm{IDM}}(t)$ for ionic state populations.

B. Spin-orbit splitting

In order to include the effect of spin-orbit splitting in the occupied orbitals, we follow the logic of Ref. [54], where we account for spin-orbit splitting with degenerate-state perturbation theory within the (n,l) orbital manifold. The occupied orbital i is, then, characterized by the quantum numbers n_i,l_i,j_i,m_i^J, where n_i is the principal quantum number, l_i is the orbital angular momentum, j_i is the total angular momentum, and m_i^J is the projection of the total angular momentum onto the polarization direction of the external laser field. The occupied spin orbitals read

$$|\varphi_i\rangle = \begin{pmatrix} C^{j_i,m_i^J}_{l_i,m_i^J-\frac{1}{2};s_i,\frac{1}{2}} & |n_i,l_i,m_i^J-\frac{1}{2}\rangle \\ C^{j_i,m_i^J}_{l_i,m_i^J+\frac{1}{2};s_i,-\frac{1}{2}} & |n_i,l_i,m_i^J+\frac{1}{2}\rangle \end{pmatrix}, \tag{6}$$

where the Clebsch-Gordan coefficient is given by $C^{l_3,m_3}_{l_1,m_1;l_2,m_2} = \langle l_1,m_1;l_2,m_2|l_3,m_3\rangle$, $s_i = \frac{1}{2}$ is the spin of the electron, and $|n,l,m\rangle$ are the one-particle orbitals obtained from a nonrelativistic Hartree-Fock calculation. The orbital energies ε_i are taken from experimental ionization potentials. For the virtual orbitals, we can neglect spin-orbital splitting and use the quantum numbers n_a,l_a,σ_a,m_a^L to classify the orbitals, where σ_a is the spin component in the laser polarization direction and m_a^L is the projection of the orbital angular momentum onto the laser polarization direction. The virtual orbitals read

$$|\varphi_a\rangle = |n_a,l_a,m_a^L\rangle \begin{pmatrix} \delta_{\sigma_a,\frac{1}{2}} \\ \delta_{\sigma_a,-\frac{1}{2}} \end{pmatrix}. \tag{7}$$

The use of linearly polarized light leads to the condition $m_i^J = m_a^L + \sigma_a$ for each singly excited configuration $|\Phi_i^a\rangle$, which is conserved by $\hat{H}(t)$. After the introduction of spin-orbit splitting for the occupied orbitals, we cannot make use of the σ and m^L symmetries independently to reduce the number of singly excited configurations, $|\Phi_i^a\rangle$, as done in Ref. [53]. However, not all symmetries are lost and we find that Eq. (3b) is (up to a global phase) invariant under the parity transformation $(m_i^J,m_a^L,\sigma_a) \to (-m_i^J,-m_a^L,-\sigma_a)$. The new parity-adapted, singly excited configurations $|\Phi_i^a\rangle_\pi$ read

$$|\Phi_i^a\rangle_\pi = \frac{1}{\sqrt{2}}\left[|\Phi_i^a\rangle_+ + (-1)^{l_i+s_i-j_i+\pi}|\Phi_i^a\rangle_-\right], \tag{8}$$

where the configurations $|\Phi_i^a\rangle_\pm$ stand for singly excited configurations with $m_i^J \gtrless 0$, respectively. States with $\pi = 0$ are *gerade* parity state and $\pi = 1$ states are *ungerade* parity state. All *ungerade* configurations $|\Phi_i^a\rangle_{\pi=1}$ will never get populated and we can exclude them from our further investigations. Note that the factor $(-1)^{l_i+s_i-j_i}$ comes from the symmetry $C^{l_3,m_3}_{l_1,m_1;l_2,m_2} = (-1)^{l_1+l_2-l_3}C^{l_3,-m_3}_{l_1,-m_1;l_2,-m_2}$.

C. Matrix elements

The matrix elements, which are needed for Eqs. (3), must be evaluated in the parity-adapted $|\Phi_i^a\rangle_\pi$ configuration basis. The dipole matrix elements with respect to the symmetric inner product read

$$\pi_1\left(\Phi_i^a|\hat{z}|\Phi_j^b\right)_{\pi_2} = \left(\delta_{i,j}\delta_{\sigma_a,\sigma_b}z^{m_a^L}_{(A,B)} - \delta_{a,b}\delta_{m_i^J,m_j^J}\sum_\sigma z^{m_i^J-\sigma}_{(J,I)}\,C^{j_i,m_i^J}_{l_i,m_i^J-\sigma;s_i,\sigma}\,C^{j_j,m_j^J}_{l_j,m_j^J-\sigma;s_j,\sigma}\right)\delta_{\pi_1,\pi_2}, \tag{9a}$$

$$\left(\Phi_0|\hat{z}|\Phi_i^a\right)_\pi = \sqrt{2}\,\delta_{\pi,0}\delta_{m_i^J,m_a^L+\sigma_a}\,z^{m_a^L}_{(A,I)}C^{j_i,m_i^J}_{l_i,m_i^J-\sigma_a;s_i,\sigma_a}, \tag{9b}$$

where we used the notation $i = (I,j_i,m_i^J)$ with $I = (n_i,l_i)$ and $a = (A,m_a^L,\sigma_a)$ with $A = (n_a,l_a)$. The dipole matrix elements in the original, non-parity-adapted basis are given by $z^m_{(P,Q)} := (n_p,l_p,m|\hat{z}|n_p,l_q,m)$. The matrix elements of $\hat{H}_1$ read

$$\begin{aligned}\pi_1\left(\Phi_i^a|\hat{H}_1|\Phi_j^b\right)_{\pi_2} = {} & 2\delta_{\pi_1,0}\delta_{\pi_2,0}C^{j_i,m_i^J}_{l_i,m_i^J-\sigma_a;s_i,\sigma_a}\,C^{j_j,m_j^J}_{l_j,m_j^J-\sigma_b;s_j,\sigma_b}\,v^{M_1}_{(AJIB)} - \delta_{\pi_1,\pi_2}\delta_{\sigma_a,\sigma_b}\sum_\sigma C^{j_i,m_i^J}_{l_i,m_i^J-\sigma;s_i,\sigma}\,C^{j_j,m_j^J}_{l_j,m_j^J-\sigma;s_j,\sigma}\,v^{M_1^\sigma}_{(AJBI)} \\ & - (-1)^{\pi_1}\delta_{\pi_1,\pi_2}\delta_{\sigma_a,-\sigma_b}\sum_\sigma C^{j_i,m_i^J}_{l_i,m_i^J-\sigma;s_i,\sigma}\,C^{j_j,m_j^J}_{l_j,m_j^J+\sigma;s_j,-\sigma}\,v^{M_2^\sigma}_{(AJBI)},\end{aligned} \tag{10}$$

where $M_1 = (m_a^L,m_b^L,m_a^L,m_b^L)$, $M_1^\sigma = (m_a^L,m_j^L-\sigma,m_b^L,m_i^J-\sigma)$, and $M_2^\sigma = (m_a^L,-m_j^L-\sigma,-m_b^L,m_i^J-\sigma)$. The Coulomb matrix elements in the non-parity-adapted basis read $v^M_{(PQRS)} := (n_p,l_p,m_p;n_q,l_q,m_q|\hat{r}_{12}^{-1}|n_r,l_r,m_r;n_s,l_s,m_s)$ with $M = (m_p,m_q,m_r,m_s)$.

D. Transient absorption for overlapping pulses

The transient absorption signal is a direct measure of the cross section of the system. In Ref. [40] the transient absorption signal was derived for the case of nonoverlapping pump and probe pulses. The probe pulse was treated in first-order perturbation theory such that it was possible to give an analytic expression for the transient absorption signal as a function of the instantaneous IDM $\hat{\rho}^{\mathrm{IDM}}(t)$. The pump pulse, usually a strong-field NIR pulse, which ionizes the atom by tunnel ionization, was treated nonperturbatively.

For overlapping pump and probe pulses, the influence of the probe pulse does not decouple from the impact of the pump pulse. Therefore, it is not clear to which extent $\hat{\rho}^{\mathrm{IDM}}(t)$

can be extracted from the transition absorption spectrum like for nonoverlapping pulses. In order to fully capture the overall effect of pump and probe pulses, both pulses are treated nonperturbatively, meaning the TDCIS equations of motion [see Eq. (3)] are solved for an electric field $E(t) = E_{\text{pump}}(t) + E_{\text{probe}}(t)$. Note that the probe step could also be treated perturbatively by introducing a two-time IDM, which depends on two different time arguments. In our nonperturbative approach only the one-time IDM $\hat{\rho}^{\text{IDM}}(t)$ needs to be constructed for each pump-probe configuration. From $\hat{\rho}^{\text{IDM}}(t)$ the ionic dipole moment,

$$\langle z\rangle_{\text{ion}}(t) = \text{Tr}[\hat{z}\hat{\rho}^{\text{IDM}}(t)] \tag{11}$$

and the atomic cross section

$$\sigma_a(\omega) = 4\pi\frac{\omega}{c}\text{Im}\left[\frac{\langle z\rangle_{\text{ion}}(\omega)}{E_{\text{probe}}(\omega)}\right] \tag{12}$$

can be calculated. By performing the trace over $\hat{\rho}^{\text{IDM}}(t)$ and not over the full N-body density matrix $\hat{\rho}(t)$, we consider only dipole transitions between ionic states. Transitions between virtual orbitals can be neglected, since the XUV probe pulse interacts only weakly with the excited electron. Transitions between occupied and virtual orbitals describe stimulated emission and photoionization processes. Both mechanism do not lead to sharp features in $\sigma_a(\omega)$ around the bound-bound transition energies. Therefore, we ignore these contributions, which lead to background signals we are not interested in.

The detector, where the transient absorption spectrum is measured, does not record the atomic response but rather a damped spectrum of the form

$$|E_{\text{probe}}(L,\omega)|^2 = |E_{\text{probe}}(0,\omega)|^2\, e^{-Ln_{\text{AT}}\sigma_a(\omega)}, \tag{13}$$

where $E_{\text{probe}}(0,\omega)$ is the incoming probe electric field, L is the length of the medium, $E_{\text{probe}}(L,\omega)$ is the probe electric field at the end of the medium, and n_{AT} is the atomic number density. In Eq. (13) Beer's law is used, which assumes a homogeneous medium and that the ratio $\langle z\rangle_{\text{ion}}(\omega)/E_{\text{probe}}(\omega)$ is independent of $E_{\text{probe}}(\omega) := E_{\text{probe}}(0,\omega)$. In Sec. III B the validity of Beer's law is discussed.

Due to the finite energy resolution of the detector, the transient absorption signal in Eq. (13) has to be convolved with a Gaussian mask function, where the full width at half maximum (FWHM) width is given by the energy resolution of the detector. The cross section $\sigma_m(\omega)$ measured at the detector can be related to the atomic cross section and is given by

$$\sigma_m(\omega) = -\frac{1}{n_{\text{AT}}L}\ln(e^{-n_{\text{AT}}L\sigma_a(\omega)} * G_{\delta E}(\omega)), \tag{14}$$

where $G_{\delta E}(\omega)$ is the area-normalized Gaussian with the FWHM width of δE, and the symbol $*$ stands for the frequency convolution. The dependence on the pump-probe configuration, specifically the pump-probe delay τ, enters parametrically in Eqs. (11)–(14) such that the atomic and the measured cross sections read $\sigma_a(\omega;\tau)$ and $\sigma_m(\omega;\tau)$, respectively.

E. Oscillating dipole model

In the following, we develop a general expression for the transient absorption spectrum, which is based on a simple model. Later in Sec. III we use this generalized expression to discuss the features of the transient absorption spectrum for overlapping pulses obtained from our TDCIS calculations described in Sec. II A-II C.

First, we reduce the description of the ion to a two-level system. The ground state $|g\rangle$ can only be accessed by the pump pulse via tunnel ionization and the excited state $|e\rangle$ can only be accessed by the probe pulse via resonant excitation out of $|g\rangle$. The probe pulse, which may be approximated by a delta pulse [i.e., $E_{\text{probe}}(t;\tau) = E_0\delta(t-\tau)$], creates a coherent superposition $|\Psi(t>\tau)\rangle = a_0|g\rangle + a_1 e^{-i(\omega_0 - i\Gamma/2)(t-\tau)}|e\rangle$, where ω_0 is the positive energy difference between the two states, $1/\Gamma$ is the lifetime of the excited state, and $a_1 = -iE_0a_0\langle e|z|g\rangle$ results from the excitation by the probe pulse. This superposition leads to an oscillating dipole

$$\begin{aligned}\langle z\rangle_{\text{ion}}(t>\tau) &= \langle\Psi(t)|z|\Psi(t)\rangle \\ &= -2E_0|\langle e|z|g\rangle|^2|a_0|^2\sin[\omega_0(t-\tau)]e^{-\frac{\Gamma}{2}(t-\tau)}.\end{aligned} \tag{15}$$

Inserting Eq. (15) into Eq. (12) and using $E_{\text{probe}}(\omega;\tau) = E_0e^{-i\omega\tau}$, the final expression for the cross section reads

$$\sigma(\omega;\tau) = \frac{4\pi\omega}{c}z_0\frac{\Gamma/2}{(\omega-\omega_0)^2+\frac{\Gamma^2}{4}}, \tag{16}$$

where $z_0 = |a_0|^2|\langle e|z|g\rangle|^2$ determines the transition strength. We see that for a simple two-level system the cross section is purely Lorentzian and directly proportional to the ground-state population $|a_0|^2$ at the time of the probe step.

Adiabatic energy shifts in the ionic states during the intense NIR pulse result in a phase shift in the oscillating ionic dipole [i.e., $\langle z\rangle_{\text{ion}} \propto \sin[\omega_0(t-\tau)+\phi(\tau)]$]. Here, we assume the ionic state and the dipole oscillation live for a long time after the NIR pulse is over such that the entire dipole dynamics can be approximated by a phase-shifted oscillation. The phase shift $\phi(\tau)$ has a dramatic influence on the shape of the transition line, which reads

$$\sigma(\omega;\tau) = \frac{4\pi\omega}{c}z_0\frac{\frac{\Gamma}{2}\cos[\phi(\tau)] + (\omega-\omega_0)\sin[\phi(\tau)]}{(\omega-\omega_0)^2+\frac{\Gamma^2}{4}}. \tag{17}$$

Note that the phase shift $\phi(\tau)$ affects only the shape of the transition but not the strength z_0.

In Fig. 1 $\sigma(\omega;\tau)$ is shown for specific values of ϕ. The transition line is purely Lorentzian for $\phi = 0$. In the case $\phi = \pi/2$, the cross section shows a dispersive behavior and has equally negative and positive regions that lie symmetrically around the field-free transition energy $\omega_0(0)$. For all other phases, the cross section is a sum of these two scenarios and becomes asymmetric around ω_0. A phase shift by π changes the sign of the cross section. For $-\pi/2 \leqslant \phi \leqslant \pi/2$, the system shows an absorbing behavior whereas for $\pi/2 \leqslant \phi \leqslant 3/2\pi$ the system is rather emitting. A similar scenario has been discussed in atomic helium, where neutral excited states are dressed by an IR pulse leading to emitting and absorbing patterns depending on the pump-probe delay [55].

Similarly to the dressing of the ionic states, the influence of the excited electron on the ion via the residual Coulomb interaction and via the pump field can lead to additional phase shifts in the oscillating dipole (see Sec. II F). Furthermore,

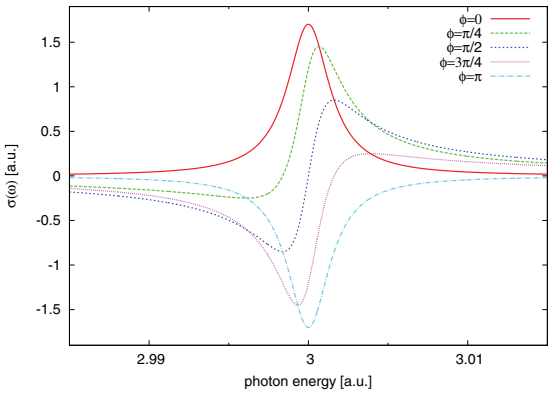

FIG. 1. (Color online) Cross section $\sigma(\omega)$ of Eq. (17) for several values of $\phi(\tau)$. The transition energy is $\omega_0 = 3$ a.u., $\Gamma = 3.2 \times 10^{-3}$ a.u., and the transition strength is given by $z_0 = 0.01$.

corrections to the transition strength z_0 can occur, which may cause z_0 to be no longer directly proportional to the instantaneous hole population. In order to capture these effects, we parametrize not only the phase $\phi(\tau)$ but also the transition strengths $z_0 \to z_0(\tau)$. Our generalized version of Eq. (17) for a multilevel ion reads

$$\sigma_{\text{dipole}}(\omega;\tau) = \frac{4\pi\omega}{c}\sum_T z_T(\tau)\frac{\frac{\Gamma_T}{2}\cos[\phi_T(\tau)] + (\omega-\omega_T)\sin[\phi_T(\tau)]}{(\omega-\omega_T)^2 + \frac{\Gamma_T^2}{4}}, \tag{18}$$

where we sum over all possible ionic transitions T. Note that Eq. (18) is designed to capture the influence of all these effects that go beyond our simple two-level model [see Eq. (16)]. However, Eq. (18) cannot explain why these changes occur and where they come from.

F. Mechanisms leading to phase shift

As discussed in Sec. II E, the dressing of the ion can induce a phase shift in the ionic dipole. In the following, we discuss in the language of TDCIS how the dressing by the field and the coupling of the excited electron to the ionic subsystem can influence the phases $\phi_T(\tau)$ of Eq. (18). First, we analyze the scenario where the time evolutions of the excited electron (a index) and the ionic states (i index) are decoupled. This is the case when the terms $(\Phi_i^a|\hat{H}_1|\Phi_j^b)$ and $(\Phi_i^a|\hat{z}|\Phi_0)$ are switched off in Eq. (3b). The resulting EOM can be written as

$$i\dot{\alpha}_i^a(t) = \sum_b H^{\text{elec}}_{(a,b)}(t)\alpha_i^b(t) + \sum_j H^{\text{ion}}_{(i,j)}(t)\alpha_j^a(t), \tag{19}$$

where $H^{\text{elec}}_{(a,b)}(t) := \varepsilon_b\delta_{a,b} + E(t)(\varphi_a|\hat{z}|\varphi_b)$ affects only the excited electron, and $H^{\text{ion}}_{(i,j)}(t) := -\varepsilon_j\delta_{i,j} - E(t)(\varphi_j|\hat{z}|\varphi_i)$ affects only the ionic states. $\hat{H}^{\text{elec}}$ and $\hat{H}^{\text{ion}}$ can be viewed as Hamiltonians of the two subsystems. Note that the Hamiltonians of both subsystems commute; that is, $[\hat{H}^{\text{elec}}(t), \hat{H}^{\text{ion}}(t)] = 0$. To confirm that Eq. (19) leads to decoupled EOMs for the excited electron and the ion, we make the product ansatz $\alpha_i^a(t) = \chi_a(t)\kappa_i(t)$, where the EOMs of the separated electronic and ionic wave functions are given by

$$i\dot{\chi}_a(t) = \sum_b H^{\text{elec}}_{(a,b)}(t)\chi_b(t), \tag{20a}$$

$$i\dot{\kappa}_i(t) = \sum_j H^{\text{ion}}_{(i,j)}(t)\kappa_j(t). \tag{20b}$$

We find that the product ansatz with the decoupled EOMs of Eqs. (20) solves Eq. (19). This shows that Eq. (19) is the overall EOM of the full N-electron system, which consists of two totally separated subsystems. Note that the term $(\Phi_i^a|\hat{z}|\Phi_j^b)$ [cf. Eq. (4)] does affect the excited electron and the ion but it does not lead to interactions between the two. Enforcing a normalized electron wave function, we find from Eq. (20b) that the IDM is given by

$$\rho^{\text{IDM}}_{i,j}(t) = \kappa_j^*(t)\kappa_i(t) = e^{i\omega_T(t-\tau)}\rho^{\text{IDM}}_{i,j}(\tau)e^{i\phi_T^{\text{ion}}(t,\tau)}, \tag{21}$$

where $T = i \to j$ denotes the ionic transition. If $E(t) = 0$ for all times t, we find $\phi_T^{\text{ion}}(t,\tau) = 0$ for all t and τ. Hence, the additional phase $\phi_T^{\text{ion}}(t,\tau)$ enters only due to the term $-E(t)(\varphi_j|\hat{z}|\varphi_i)$ in $\hat{H}^{\text{ion}}$. This is exactly the field-driven dressing of the ionic system. After the pulse is over [$E(t) = 0$], the phase $\phi_T^{\text{ion}}(t,\tau)$ becomes independent of t and depends only on the probe time τ [i.e., $\phi_T^{\text{ion}}(t,\tau) \to \phi_T^{\text{ion}}(\tau)$]. In Sec. III D 1, we show how the field-driven dressing of the ionic system can be analytically analyzed with the help of the polarizability of the ion. It is interesting to note that the influence of the electric field on the excited electron [i.e., $E(t)(\varphi_a|\hat{z}|\varphi_b)$] does not influence the IDM and subsequently the ionic dipole oscillation.

Additional phase shifts similar to $\phi_T^{\text{ion}}(\tau)$ can also occur due to the coupling between the ion and the excited electron. There exist two kinds of mechanism that can couple these two subsystems: (1) the residual Coulomb interaction [the $(\Phi_i^a|\hat{H}_1|\Phi_j^b)$ in Eq. (3b) are the corresponding matrix elements], and (2) the field-driven mixing of the excited N-electron states with the neutral ground state [the $(\Phi_i^a|\hat{z}|\Phi_0)$ in Eq. (3b) are the corresponding matrix elements]. Both terms were ignored in Eq. (19), which led to two decoupled subsystems. To distinguish the phase shifts induced by the two different mechanisms, we introduce $\phi_T^{\text{residual}}(\tau)$ and $\phi_T^{\text{ground}}(\tau)$. The phase shift due to the residual Coulomb interaction is denoted by $\phi_T^{\text{residual}}(\tau)$, and $\phi_T^{\text{ground}}(\tau)$ denotes the phase shift due to the field-driven mixing to the neutral ground state.

Adding up all three phase shifts we find that the total phase shift for the transition T is given by

$$\phi_T(\tau) = \phi_T^{\text{ion}}(\tau) + \phi_T^{\text{residual}}(\tau) + \phi_T^{\text{ground}}(\tau). \tag{22}$$

In Sec. III D we discuss which of the three phase shifts gives the dominant contribution.

III. RESULTS

A. System, pulse, and numerical parameters

All presented results were calculated with the XCID package [56]. All calculations were performed with 600 radial grid points, a maximum radius $r_{\max} = 150$, and a nonlinear grid

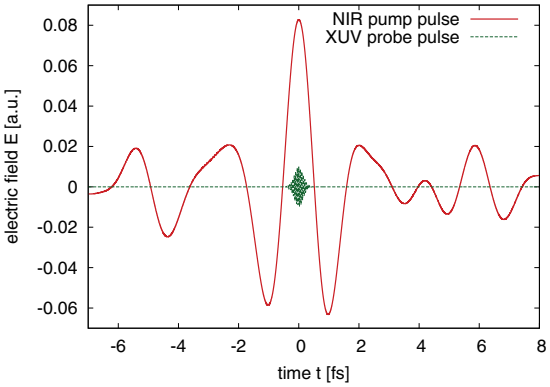

FIG. 2. (Color online) NIR pump (solid red line) and XUV probe pulses (green dashed line) used for transient absorption spectroscopy are shown separately. The peaks of both pulses are centered at $t = 0$.

mapping parameter $\zeta = 1.0$. The CAP starts at a radius $r_{\mathrm{CAP}} = 130$ and has a strength $\eta = 0.003$. The maximum angular momentum employed was $l_{\max} = 30$. Furthermore, if the orbital angular momentum of any one-particle orbital $|\varphi_p\rangle$ appearing in the matrix elements of $\hat{H}_1$ exceeded 4, then only the monopole term of $\hat{H}_1$ was considered. With these parameters, our results are converged. A detailed explanation about the parameters of the grid, of the CAP, and of the residual Coulomb interaction can be found in Ref. [50].

The NIR pulse profile measured in Ref. [35] is used as the pump pulse in all the following results and is shown in Fig. 2. The pump pulse is approximately 2 fs long with one main peak and two side peaks. The maximum electric field strength of the pump pulse is ≈0.08 a.u. (corresponding to an instantaneous intensity of 4.8×10^{14} W/cm^2). For the probe pulse (also shown in Fig. 2) a Gaussian pulse profile is used with a central frequency of 3 a.u. (≈81 eV), a FWHM width of the intensity profile of 10 a.u.(≈240 as), a carrier envelope phase of zero, and a maximum field strength of 10^{-2} a.u. (≈3.4 TW/cm^2).

As in Refs. [35,39], we choose atomic krypton as our system of interest. The spin-orbit coupling within the occupied orbitals is accounted for in first-order perturbation theory, as described in Sec. II B. The energies of the singly ionized ionic states $[NL_J^M]^{-1}$ with respect to the Hartree-Fock ground-state energy are given by the negative orbital energies (i.e., Koopmans' theorem). Here, N is the principal quantum number, L is the orbital angular momentum, J is the total angular momentum, and M is the projection of J. Since we are using linearly polarized light, the values for M and $-M$ states are always the same. Therefore, we refer always to a sum of both $|M|$ contributions (i.e., $[NL_J^M]^{-1} = [NL_J^{+M}]^{-1} + [NL_J^{-M}]^{-1}$).

The orbital energies of the $4p$ orbitals are replaced by experimental values taken from Ref. [57] in order to match the experimental ionization potentials. The orbital energies of the $4p$ shell are given by $\varepsilon_{4p_{1/2}} = -0.5389$ (= − 14.67eV) and $\varepsilon_{4p_{3/2}} = -0.5148$ (= − 14.00eV). The orbital energies of the $3d$ shell are taken from Ref. [58]. In addition, we account for the finite lifetime of all $3d^{-1}$ configurations of 7.5 fs (Γ = 88 meV) [39]. Hence, the $3d$ orbital energies become complex and read $\varepsilon_{3d_{3/2}} = -3.5 - i\Gamma/2$ (= − 95.24 − i0.044 eV) and $\varepsilon_{3d_{5/2}} = -3.4525 - i\Gamma/2$ (= − 93.95 − i0.044 eV).

B. Transient absorption spectrum

In a recent experiment [35] attosecond transient absorption spectroscopy has been used to investigate the hole production dynamics in atomic krypton during a subcycle NIR pump pulse. The theory described in Ref. [40] was used to analyze the transient absorption spectrum and to connect the spectrum to the instantaneous IDM $\rho_{i,j}^{\mathrm{IDM}}(t)$. Propagation effects and the finite energy resolution of the detector were accounted for as described in Eq. (14). The macroscopic propagation is captured by Beer's law. Previous studies [40] have shown that Beer's law is valid for the pump-probe scenario investigated here. Similar conclusions have been found in Ref. [41] when the probe pulse is much shorter than the pump pulse (as in our case). For probe pulses longer than the pump pulse, the macroscopic propagation can quite strongly deviate from Beer's law.

The theory developed in Ref. [40] is, strictly speaking, only valid when pump and probe pulses do not overlap and the tunnel-ionized electron is far from the parent ion. In this case, the ionic subsystem [i.e., $\hat{\rho}^{\mathrm{IDM}}(t)$] reduces to a simple multilevel system without any kinds of interactions with the environment and between levels. Hence, the entire dynamics of the ion is analytically known and reads $\rho_{i,j}^{\mathrm{IDM}}(t) = \rho_{i,j}^{\mathrm{IDM}}(t_0)e^{i(\varepsilon_i-\varepsilon_j)(t-t_0)}$. For overlapping pulses, the dynamics of $\hat{\rho}^{\mathrm{IDM}}(t)$ becomes more complex. Therefore, it is not clear to which extent the transient absorption spectrum for a given pump-probe delay can be related to $\rho_{i,j}^{\mathrm{IDM}}(t)$ when pump and probe pulses do overlap.

In Fig. 3 the calculated transient absorption spectrum $\sigma_m(\omega;\tau)$ is shown as a function of photon energy ω and pump-probe delay τ. The three main transition lines [i.e., $4p_{3/2}^{-1} \rightarrow 3d_{5/2}^{-1}$ (79.95 eV), $4p_{1/2}^{-1} \rightarrow 3d_{3/2}^{-1}$ (80.57 eV), and $4p_{3/2}^{-1} \rightarrow 3d_{3/2}^{-1}$ (81.24 eV)] are clearly visible. To shorten the notation we refer to these three transition lines as T_1,T_2, and T_3, respectively.

The cross section shown in Fig. 3 is in agreement with experimental observations [35]. The transition strengths increase mainly around $\tau \approx 0$, when the krypton atom is being probed within the main peak of the pump pulse. It is also during this main peak of the pump pulse where the atom gets mainly

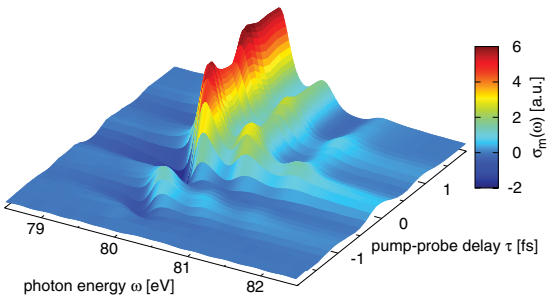

FIG. 3. (Color online) Attosecond XUV transient absorption spectrum $\sigma_m(\omega;\tau)$ [see Eq. (14)] of krypton as a function of energy ω and pump-probe delay τ.

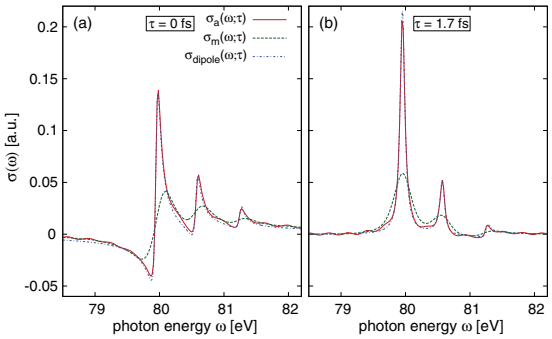

FIG. 4. (Color online) Transient absorption spectra for the pump-probe delay $\tau = 0$ and $\tau = 70$ ($\approx$1.7 fs) are shown in panels (a) and (b), respectively. The atomic cross section σ_a (solid red line), the measured cross section σ_m (green dashed line), and $\sigma_{\rm dipole}$ (blue dotted line) are shown for each τ.

ionized. Simultaneously during the hole creation, the transition lines in the transient absorption spectrum change dramatically their shapes, resulting in negative cross sections for energies just below the field-free transition energies. Negative cross sections can be only seen here for the T_1 transition, because a detector resolution of $\approx$300 meV let these features disappear for the transitions T_2 and T_3 (cf. Fig. 4).

Similar to $\tau \approx 0$, line deformations and negative cross sections do also occur at $\omega \approx 80$ eV for $\tau \approx \pm 1$ fs, where the probe pulse coincide with the side peaks of the pump pulse (cf. Fig. 2). The side peaks of the pump pulse are strong enough to lead to tunnel ionization as well (cf. Fig. 5). In particular, the ionization and the deformation caused by the first side peak of the pump pulse ($\tau \approx -1$ fs) can be nicely seen in Fig. 3 for the transition line T_1. As will become clear in the discussion in

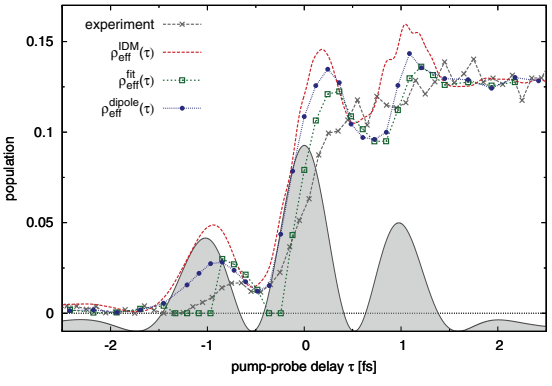

FIG. 5. (Color online) Instantaneous hole population $\rho_{\rm eff}^{\rm IDM}(\tau)$ (solid red line) together with reconstructed populations $\rho_{\rm eff}^{\rm dipole}(\tau)$ (blue dotted line) and $\rho_{\rm eff}^{\rm fit}$ (green dashed line). The experimental population (grey dashed line) is taken from Ref. [35]. The reconstructed and experimental populations are scaled such that all have the same value at $t = 2.4$ fs. The NIR pulse intensity is highlighted (gray area) in the background.

Sec. III D, the mechanism behind the deformations in all three cases ($\tau \approx 0, \pm 1$ fs) is the same.

For $\tau > 2$ fs, the dynamics of the hole populations is barely affected by the pump pulse and behaves as if they were field-free. At these time delays, the intensity of the pump pulse is also strongly reduced (by more than a factor 10) compared to the peak intensity at $\tau = 0$, thus supporting the observation of field-free behavior for larger pump-probe delays. Field-free behavior means, for the main transition line T_1, that it becomes stationary and does not change anymore in shape and strength. The other two transition lines show interference effects from the coherent superposition of $4p_{3/2}^{-1}$ and $4p_{1/2}^{-1}$ [39,40].

Large negative time delays ($\tau < -2$ fs) are not of interest and, therefore, they are not shown in Fig. 3 for two reasons: First, the ionic cross section [see Eqs. (12) and (14)] is zero for large negative time delays because only neutral krypton atoms exist prior to the NIR pulse. Second, no electronic dynamics can be probed before the NIR pulse, since the neutral krypton atoms are in the electronic ground state.

In Fig. 4 the transient absorption spectra $\sigma_a(\omega;\tau)$, $\sigma_m(\omega;\tau)$, and $\sigma_{\rm dipole}(\omega;\tau)$ are shown for $\tau = 0$ and $\tau = 70$($\approx$1.7 fs). The transition lines in $\sigma_m(\omega;\tau)$ are broadened with respect to the atomic cross section $\sigma_a(\omega;\tau)$ due to the propagation effect and the finite detector resolution ($\approx$300 meV), which is wider than the natural transition widths ($\Gamma_i = 88$ meV). The cross section $\sigma_{\rm dipole}(\omega;\tau)$ is obtained by fitting Eq. (18) to $\sigma_a(\omega;\tau)$ obtained from the TDCIS calculations. The energies ω_{T_i} and the natural widths Γ_{T_i} of all transition lines T_i are kept fixed (see Sec. III A) and only the magnitudes $z_{T_i}(\tau)$ and the phases $\phi_{T_i}(\tau)$ are fit to $\sigma_a(\omega;\tau)$. The features of $\sigma_a(\omega;\tau)$ are well captured by $\sigma_{\rm dipole}(\omega;\tau)$ for all τ. At $\tau = 70$, the two strongest transition lines are Lorentzian shaped as expected for nonoverlapping pump and probe pulses. The second (T_2) and especially the third (T_3) transition lines do not have a Lorentzian shape due to the coherent superposition of $4p_{3/2}^{-1}$ and $4p_{1/2}^{-1}$.

The success of $\sigma_{\rm dipole}(\omega;\tau)$ in capturing all features of $\sigma_a(\omega;\tau)$ shows that the influence of all terms in Eq. (3), which go beyond a simple two-level model (see Sec. II F), can be understood by phase shifts $\phi_{T_i}(\tau)$ and changes in the oscillating dipole strengths $z_{T_i}(\tau)$.

However, the oscillating dipole model cannot explain what is the physical origin of $\phi_{T_i}(\tau)$ or whether or not $z_{T_i}(\tau)$ can be related to $\rho^{\rm IDM}(\tau)$. The answers to these questions are discussed in the following.

C. Population dynamics

First, we turn our focus to the population dynamics of the ionic states. In particular, we investigate the hole-creation dynamics in the $4p_{3/2}$ orbitals during the pump pulse. In order to do so, we need to focus only on the main transition T_1. For nonoverlapping pulses, the transition strength is proportional to the instantaneous population

$$\rho_{\rm eff}^{\rm IDM}(\tau) := \rho_{4p_{3/2}^{1/2}}^{\rm IDM}(\tau) + \tfrac{2}{3}\rho_{4p_{3/2}^{3/2}}^{\rm IDM}(\tau),$$

where $\rho_i^{\rm IDM}(\tau)$ are the hole populations of the ionic states $i = [4p_{3/2}^{1/2}]^{-1}$ and $i = [4p_{3/2}^{3/2}]^{-1}$ (for details on the notation see Sec. III A), respectively. In Fig. 5, we compare $\rho_{\rm eff}^{\rm IDM}(\tau)$ (solid red line) with the transition strength $\rho_{\rm eff}^{\rm dipole} := z_{T_1}(\tau)$

(blue dotted line), with the reconstructed population $\rho_{\rm eff}^{\rm fit}$ (green dashed line) obtained by applying the same fitting procedure as in Ref. [35] to $\sigma_m(\omega;\tau)$, and with the experimental data of Ref. [35].

In all three theoretical curves, oscillatory behavior can be seen during buildup of the hole populations. The features of $\rho_{\rm eff}^{\rm IDM}(\tau)$ are well captured by $\rho_{\rm eff}^{\rm dipole}(\tau)$ and by $\rho_{\rm eff}^{\rm fit}(\tau)$. It shows that $\rho_{\rm eff}^{\rm IDM}(\tau)$ can be quite well reconstructed from the transient absorption spectrum even though pump and probe pulses do strongly overlap. Note, however, that at the major peak ($\tau \approx 0$) a delay of about ≈200 as occurs in $\rho_{\rm eff}^{\rm fit}(\tau)$. The deviations from $\rho_{\rm eff}^{\rm IDM}(\tau)$ are a measure of the influence of the excited electron on the ionic states, since the adiabatic dressing of the ionic states does not affect the transition strength. As described in Sec. II E, if the evolution of the excited electron decouples directly after the probe step from the evolution of the ion, $\rho_{\rm eff}^{\rm dipole}(\tau)$ coincides with $\rho_{\rm eff}^{\rm IDM}(\tau)$.

In the experiment, this oscillatory behavior was not seen and the transition strengths increased monotonically with τ. The reason for this discrepancy might lie in the strong restriction of the CIS space for the ionic degree of freedom. Within the CIS space generated from the neutral ground state of the atom, the ion is described exclusively by one-hole configurations.

D. Line deformations and phase shifts

As we have seen in Sec. III B the oscillating dipole model is able to describe all features of the transient absorption spectra by only adjusting the strengths $z_T(\tau)$ and the phases $\phi_T(\tau)$ of the three transitions. The strengths $z_T(\tau)$ are in close connection to the instantaneous populations of the ionic states even for overlapping pulses [cf. Sec. III C]. The correct values of $\phi_T(\tau)$ are important to capture the shapes of the transition lines, which can change significantly during the pump pulse [cf. Fig. 4].

In Fig. 6, $\phi_{T_1}(\tau)$ and $\phi_{T_3}(\tau)$ are shown. The phase $\phi_T(\tau)$ is chosen such that the strengths z_T are always positive. The region $\tau < -1.5$ fs is not shown, since the strengths of the transitions are of the same order as the numerical background noise, which leads to large uncertainties in ϕ_T. The last peak of the pump field at $\tau = 1$ fs has only a small effect on ϕ_T whereas the first peak at $\tau = -1$ fs has a strong influence on the phases. This is an interesting observation, since both peaks have the same intensity.

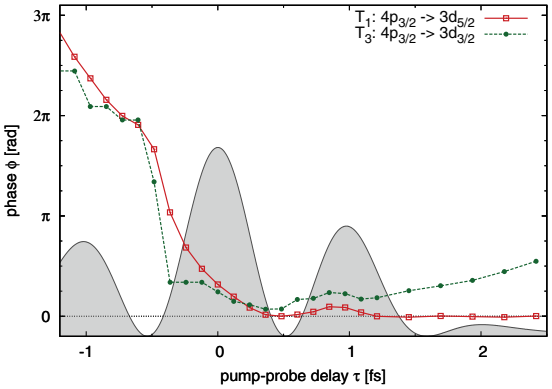

FIG. 6. (Color online) Phase shift $\phi_{T_1}(\tau)$ of strongest transition line and phase shift $\phi_{T_3}(\tau)$ of weakest transition line.

As mentioned earlier, the coherent superposition of the ionic states $4p_{1/2}^{-1}$ and $4p_{3/2}^{-1}$ results in a phase shift $(\varepsilon_{4p_{3/2}} - \varepsilon_{4p_{1/2}})\tau$, which is particularly dominant in transition T_3 [40] and has been observed in previous experiments [39]. This coherence-induced phase shift is also visible in $\phi_{T_3}(\tau)$ for $\tau >$ 1 fs (see Fig. 6). The slope of $\phi_{T_3}(\tau)$ is approx. 0.023 a.u., which is in good agreement with $\varepsilon_{4p_{3/2}} - \varepsilon_{4p_{1/2}} = 0.024$. The main transition line T_1 is not affected by this coherent superposition and, therefore, goes over into a Lorentzian shape (i.e., $\phi_{T_1} = 0$) for large τ (cf. Fig. 6).

We have seen in Fig. 6 that the phase shift ϕ_T can be quite large. However, what has not been answered yet is the origin of ϕ_T. As discussed in Sec. II F, there are three main contributions to $\phi_T(\tau)$ [cf. Eq. (22)]: (1) $\phi_T^{\rm ion}(\tau)$ induced by the NIR-driven dressing of the ionic system [the $(\varphi_j|\hat{z}|\varphi_i)$ are the corresponding matrix elements]; (2) $\phi_T^{\rm residual}(\tau)$ induced by the residual Coulomb interaction; and (3) $\phi_T^{\rm ground}(\tau)$ induced by the NIR-driven mixing of the excited N-electron system with the neutral ground state [the $(\Phi_i^a|\hat{z}|\Phi_0)$ are the corresponding matrix elements]. Particularly, in order to account for $\phi_T^{\rm residual}(\tau)$ and $\phi_T^{\rm ground}(\tau)$, it is important to have a multielectron picture which can describe the degrees of freedom of the ionized electron and of the ion.

The strong line deformations, if only the positive part of the cross section is considered, appear as if the transition energies have moved. This energy shift we call apparent energy shift. In Fig. 7, we make a direct comparison between calculated (red and green lines) and experimentally obtained (blue dashed line) [35] energy shifts of the strongest transition line, T_1. In the calculations yielding the red line (with crosses), no approximation is made in the TDCIS calculations. For the green line (with asterisks), all couplings to the 4s orbital are turned off. The procedure used to extract the apparent energy shift is described in Ref. [35].

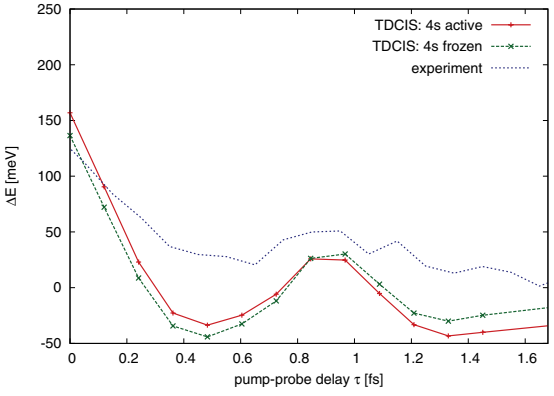

FIG. 7. (Color online) Apparent energy shifts of strongest transition line T_1 for calculated cross sections with (red line with crosses) and without (green line with asterisks) the 4s orbital active, and for the experimentally obtained cross sections (blue dotted line). The experimental values are taken from Ref. [35].

The magnitude of the apparent energy shifts are correctly reproduced by the calculations. Ignoring the $4s$ orbitals makes no significant difference. Particularly in the theoretical results, the second pump peak is clearly visible. For $\tau > 1.4$ fs, the energy shifts go as expected to zero, indicating that influence of the pulse decreases and the krypton ion can be treated as a field-free ion. Negative pump-probe delays are not shown because the transition strengths are too weak to obtain reliable results.

In the following, we discuss each mechanism which can lead to the strong line deformations seen in Fig. 3. We discuss each mechanism in terms of $\phi_T(\tau)$, since the oscillating dipole model showed that these deformations can be fully understood by a phase shift.

1. *Field dressing of ionic system and polarizability of Kr$^+$*

In the presence of a strong external field, the energies of the ionic state become modified [i.e., $\varepsilon_i \to \varepsilon_i(E)$]. If the photon energy is much smaller than the ionization potential, the influence of the field on the ionic state can be described adiabatically. This is the case for Kr^+, where the ionization potential is 24 eV [59] and the photon energy of the pump pulse is 1.4 eV and, therefore, far off-resonance with any ionic transition. Hence, the energy corrections $\Delta\varepsilon_i(E) = \varepsilon_i(E) - \varepsilon_i(0)$ of the dressed ionic states i are well captured by the quadratic Stark effect

$$\Delta\varepsilon_i[E_{\text{pump}}(t)] = \frac{\alpha(i)}{2} E^2_{\text{pump}}(t), \tag{23}$$

where $\alpha(i)$ is the polarizability of the ionic state i, and the pump electric field is linearly polarized. Note that the energy of the ionic state i is $-\varepsilon_i$. After the pulse is over, $\Delta\varepsilon_i(0) = 0$ and the ion is back in its field-free state with the ionic energies $\varepsilon_i(0)$. If an oscillating dipole (coherent superposition of two states i and j) is present while the energy of the ionic states get shifted, the dipole oscillates after the pulse with the field-free transition energy $\omega_{i\to j}(0) = \varepsilon_i(0) - \varepsilon_j(0)$ but phase shifted by [35]

$$\phi^{\text{ion}}_{i\to j}(t) = \int_t^\infty dt' \Delta\omega_{i\to j}[E_{\text{pump}}(t')], \tag{24a}$$

$$\Delta\omega_{i\to j}(E) = \Delta\varepsilon_i(E) - \Delta\varepsilon_j(E) = \frac{\alpha(i) - \alpha(j)}{2} E^2, \tag{24b}$$

where $\Delta\omega_{i\to j}[E_{\text{pump}}(t)]$ is the instantaneous shift in the transition energy between the states i and j. The phase shift $\phi^{\text{ion}}_{i\to j}(t)$ is exactly the ionic phase shift $\phi^{\text{ion}}_T(\tau)$ with $T = i \to j$, which originates from the field-dressing of the ionic system.

In order to estimate $\phi^{\text{ion}}_T(t)$ we use the quantum chemistry code DALTON [60] to calculate exact polarizabilities of the ionic states. Furthermore, we can clarify to which extent our TDCIS calculation can correctly describe the polarizability of the ion and subsequently $\phi^{\text{ion}}_{i\to j}(t)$. The polarizabilities were calculated with a complete active space self-consistent field (CASSCF) wave function and with a CIS wave function. Here, CIS means that Kr^+ is described in the space of one-hole configurations, which is consistent without TDCIS configuration space. In CASSCF calculations, spatial deformations of the ionic states are included that would require CISD and higher-order configuration excitations with respect to the ground configuration of the neutral atom. These deformations are not included in CIS.

TABLE I. Static dipole polarizabilities $\alpha_{x,x} = \alpha_{y,y}$ and $\alpha_{z,z}$ of several states of Kr^+ are shown. Polarizabilities obtained by the CIS and CASSCF methods are compared. The CIS and CASSCF calculations are done with DALTON. All values are given in atomic units and with a precision up to the second digit.

	CIS		CASSCF	
	$\alpha_{x,x}$	$\alpha_{z,z}$	$\alpha_{x,x}$	$\alpha_{z,z}$
$[4p^{3/2}_{3/2}]^{-1}$	1.57	0.01	10.62	10.77
$[4p^{1/2}_{3/2}]^{-1}$	0.53	2.09	10.72	10.57
$[4p^{1/2}_{1/2}]^{-1}$	1.05	1.05	10.67	10.67
$[3d^{5/2}_{5/2}]^{-1}$	−0.01	0.00	9.57	9.71
$[3d^{3/2}_{5/2}]^{-1}$	0.00	0.00	9.63	9.60
$[3d^{1/2}_{5/2}]^{-1}$	0.00	−0.01	9.65	9.54
$[3d^{3/2}_{3/2}]^{-1}$	0.00	0.00	9.58	9.68
$[3d^{1/2}_{3/2}]^{-1}$	0.00	−0.01	9.65	9.55

In Table I, we summarize the results of the static dipole polarizabilities for several states of Kr^+ with holes in the $4p$ or the $3d$ orbital manifolds. For more details about the polarizability calculations see Appendix. The CASSCF calculations are in good agreement (±2% accuracy) with the static polarizabilities in Ref. [61]. Polarizabilities obtained with the CASSCF method are in very good agreement (<2%) with experimental results [62,63] for neutral krypton atoms. For ionic krypton the correlation effects are reduced in comparison to neutral krypton, thus making the CASSCF calculations even more accurate. Hence, we may assume that the CASSCF results for Kr^+ are practically exact.

The polarizabilities obtained with CASSCF have values around 10.7 for $4p_j^{-1}$ ionic states and values around 9.6 for $3d_j^{-1}$ ionic states. In both cases, the anisotropy $(\alpha_{z,z} - \alpha_{x,x})$ is small. This stands in contrast to the CIS results, where a high anisotropy in the polarizabilities of $4p^{-1}$ is found. Furthermore, the polarizabilities of the ionic states $3d^{-1}$ are basically zero with the CIS basis set. The only contribution to $\alpha(3d^{-1})$ comes from the weak coupling between the $3d$ and $4p$ orbitals. Within CIS, the polarizabilities for $4p^{-1}$ are determined by the coupling to the $4s^{-1}$ state. Ionic states with two or more holes in the initially occupied orbitals do not exist in CIS and, therefore, cannot contribute to the polarizabilities. This restriction in the CIS space limits the ability of the ionic states to respond to the external field and leads to much smaller polarizabilities (as seen in Table I).

The quantity that determines $\phi^{\text{ion}}_T(t)$ is the difference in the polarizabilities, not the polarizabilities themselves [see Eq. (24)]. We are only interested in the α_{zz} component, since we use light linearly polarized along the z axis. For the strongest transition line $4p^{-1}_{3/2} \to 3d^{-1}_{5/2}$, we need to look at the differences $\alpha([4p^m_{3/2}]^{-1}) - \alpha([3d^m_{5/2}]^{-1})$ for the ionic states with $m = 1/2$ and $m = 3/2$.

In Table II theses differences are shown. The strong m dependence of the CIS results is due to the high anisotropy of the polarizabilities. The accurate CASSCF results show almost

TABLE II. Differences between static dipole polarizabilities $\alpha_{z,z}$ of states involved in the main transition line $4p_{3/2}^{-1} \rightarrow 3d_{5/2}^{-1}$. The values are given in atomic units.

$\alpha([4p_{3/2}^{m}]^{-1}) - \alpha([3d_{5/2}^{m}]^{-1})$	CIS	CASSCF
$m = \frac{1}{2}$	2.10	1.03
$m = \frac{3}{2}$	0.01	1.17

no dependence on m. Since the $[4p_{3/2}^{m=3/2}]^{-1}$ population is, in our calculation, much smaller than the $[4p_{3/2}^{1/2}]^{-1}$ population, we focus only on the $m = \frac{1}{2}$ results. Contrary to the results of the polarizabilities, where the CIS approach underestimates the values, the difference $\alpha([4p_{3/2}^{1/2}]^{-1}) - \alpha([3d_{5/2}^{1/2}]^{-1})$ is overestimated by CIS. The maximum energy shifts in the transition for the given pump parameters [cf. Fig. 2] are 183 meV (CIS) and 102 meV (CASSCF), respectively. Assuming the maximum energy shifts persist over 2 fs, the resulting phase shifts are 0.56 rad (CIS) and 0.31 rad (CASSCF), respectively. This approximation can be nicely verified by a three-level Bloch model describing only the $(N-1)$-electron ionic states $3d^{-1}$,$4s^{-1}$, and $4p^{-1}$.

The phase shift $\phi_{T_1}^{\text{ion}}$ is, however, much smaller than ϕ_{T_1} [see Fig. 8]. Hence, $\phi_{T_1}^{\text{ion}}(t)$ cannot be the main contribution to $\phi_{T_1}(t)$. Furthermore, when the coupling to the $4s^{-1}$ ionic state is switched off and $\alpha(i) \approx 0$ within TDCIS, the phase shift $\phi_{T_1}(t)$ is almost unchanged. Note that in this case, the ionic states cannot be dressed and $\phi_{T_1}^{\text{ion}} = 0$.

2. *Residual Coulomb interaction*

Here, we discuss the influence of the residual Coulomb interaction—specifically $\phi_T^{\text{residual}}(\tau)$. First, we simplify the krypton atom to a two-level system with the states $[4p_{3/2}^{1/2}]^{-1}$ and $[3d_{5/2}^{1/2}]^{-1}$ such that no dressing of the ionic states can occur ($\phi_T^{\text{ion}} = 0$). The total phase shift reads now $\phi_T(\tau) = \phi_T^{\text{residual}}(\tau) + \phi_T^{\text{ground}}(\tau)$. Second, we also ignore $\hat{H}_1$ such that the ionized electron can have no influence on the remaining ion via $\hat{H}_1$—this means we set $\phi_T^{\text{residual}} = 0$. In Fig. 9, we compare $\phi_{T_1}(\tau)$ obtained from the full TDCIS model including $\hat{H}_1$ and all ionic states of Kr^+ (solid red line) and that obtained from the simplified two-channel TDCIS model (green dashed line) just described. Whether or not $\hat{H}_1$ is included makes no significant difference in the behavior of $\phi_{T_1}(\tau)$. Hence, residual Coulomb interaction between the ionized electron and the ion has almost no effect [i.e., $\phi_T^{\text{residual}}(\tau) \approx 0$].

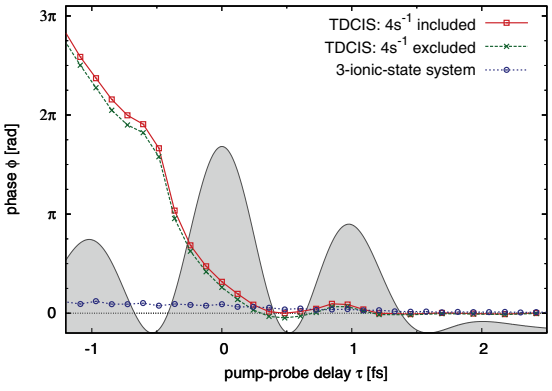

FIG. 8. (Color online) The phase shifts $\phi_{T_1}(\tau)$ of the transition line $T_1(4p_{3/2}^{-1} \rightarrow 3d_{5/2}^{-1})$ are shown for TDCIS calculations with (solid red line) and without (green dashed line) the ionic state $4s^{-1}$. Additionally, the phase shift $\phi_{T_1}^{\text{ion}}(\tau)$ (blue dotted line) is shown for a Bloch model describing three ionic states (see text for details). Here, $\phi_{T_1}^{\text{ion}}(\tau)$ originates solely from the dressing of the ionic state $[4p_{3/2}^{1/2}]^{-1}$ through the coupling to $4s^{-1}$.

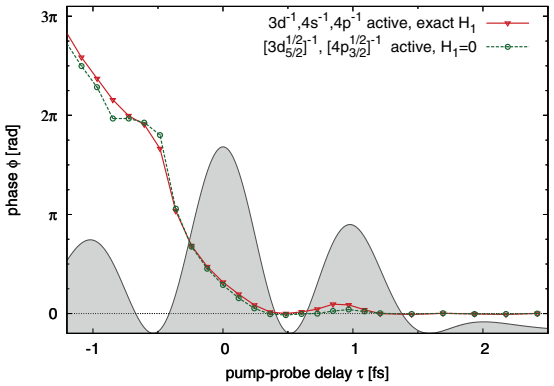

FIG. 9. (Color online) Phase shifts $\phi_{T_1}(\tau)$. The TDCIS calculations were done on the one side (solid red line) with the full electron-ion interaction and all $3d^{-1}$,$4s^{-1}$,$4p^{-1}$ ionic states active, and on the other side (green dashed line) with a simplified two-level TDCIS model without residual Coulomb interaction ($\hat{H}_1 = 0$).

3. *Field-induced mixing with the neutral ground state*

The discussions in Secs. III D 1 and III D 2 have shown that $\phi_T^{\text{ion}} \ll \phi_T$ and $\phi_T^{\text{residual}} \ll \phi_T$. Hence, we must conclude that the main reason for the phase shift comes from the field-driven mixing with neutral ground state [i.e., $\phi_T(\tau) \approx \phi_T^{\text{ground}}(\tau)$; cf. Eq. (22)]. Remember that the mixing to the ground state is captured by the terms $(\Phi_0|\hat{z}|\Phi_i^a)$, $(\Phi_i^a|\hat{z}|\Phi_0)$ [cf. Eq. (3)]. These terms are also responsible for describing tunnel ionization. To verify that the field-induced mixing of the excited N-electron states Φ_i^a with Φ_0 is indeed the main reason for the observed phase shift, we perform calculations where we once switch off the field-driven mixing to Φ_0 after the probe step and once where we leave it on. The probe pulse is here delta like [i.e., $E_{\text{probe}}(t) \propto \delta(t-\tau)$]. We again reduce krypton to a two-level atom (excluding the $4s$ orbital) as described in Sec. III D 2. In this two-level system $\phi_T^{\text{ion}}(\tau) = \phi_T^{\text{residual}}(\tau) = 0$ such that the only phase shift that can occur is $\phi_T^{\text{ground}}(\tau)$.

In Fig. 10, the phase $\phi_T(\tau)$ is shown with and without the mixing to the neutral ground state. If we set $(\Phi_0|\hat{z}|\Phi_i^a) = 0$ (i.e., $\phi_T^{\text{ground}} = 0$) after the probe step, the phase shift totally disappears for all pump-probe delays. When including the ground-state mixing, we obtain again the usual behavior of $\phi_T(\tau)$. Hence, we conclude that the main source of $\phi_T(\tau)$, which deforms the transition lines in the transient absorption spectrum (cf. Fig. 3), is the field-induced dressing of the entire

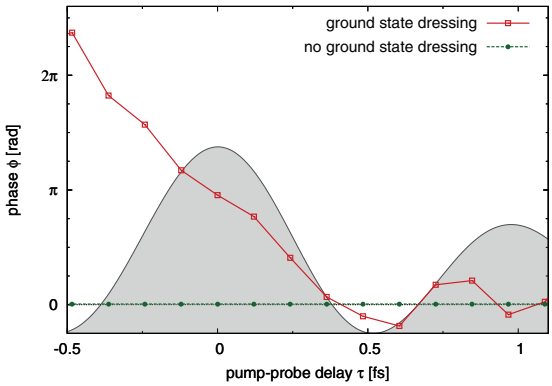

FIG. 10. (Color online) Phase shifts $\phi_T(\tau)$ for transition $T = [4p_{3/2}^{1/2}]^{-1} \rightarrow [3d_{5/2}^{1/2}]^{-1}$. The TDCIS calculations were done once with (solid red line) and once without (green dashed line) field-driving mixing with the neutral ground state Φ_0 after the probe pulse. In both cases, no dressing of the ionic states can occur (see text for details).

N-electron system—particularly the mixing with the neutral ground state.

IV. CONCLUSION

We have described our theoretical model, namely a time-dependent configuration-interaction singles (TDCIS) approach, which has been implemented in the software package XCID. We extended our method and included spin-orbit splitting for the occupied orbitals. This extension leads to new symmetry classes and, therefore, new matrix elements. With the help of this multielectron approach, we are able to study attosecond transient absorption experiments for overlapping pump and probe pulses from first principles. The pump pulse as well as the probe pulse are treated nonperturbatively.

Transient absorption spectroscopy with overlapping pulses makes it possible to study the tunnel ionization dynamics with subcycle resolution. We find that the hole populations extracted from the transient absorption spectrum are in close connection to the instantaneous hole populations even though this relationship is, strictly speaking, only true for nonoverlapping pump and probe pulses.

The strong deformations in the transient absorption lines, which appear during the ionization process, can be fully understood by phase shifts in the induced ionic dipole oscillations. We find that the phase shift due to the dressing of the ion by the pump pulse is not sufficient to account for the observed line deformations. We also excluded the residual Coulomb interaction between the ionized electron and the remaining ion as a possible source.

The main contribution to the phase shift comes from field-induced mixing of the excited N-electron states with the neutral ground state, which is highly nonperturbative. This dressing mechanism creates a coupling between the ionized electron and the ion, which makes the ionic subsystem dependent on the state of the ionized electron and vice versa. This dressing mechanism is quite peculiar, since the ionized electron was believed to be a spectator, since the probe pulse does only affect the ionic states.

The nonperturbative mixing to the neutral ground state affects also the phase relations between ionic states. These phase relations are particularly important for the hole dynamics in an atom or molecule [64]. By varying the pump-probe delay, the phases between ionic states can be influenced, and transient absorption spectroscopy provides a way to "read out" these phases.

ACKNOWLEDGMENTS

This work has been supported by the Deutsche Forschungsgemeinschaft (DFG) under Grant No. SFB 925/A5. We thank Jan Malte Slowik for helpful discussions.

APPENDIX: DIPOLE POLARIZABILITY

The dipole polarizability of a system that is in state S can be obtained within perturbation theory and reads [65]

$$\alpha_{m,n}(S) = 2\sum_I \frac{\langle S|x_m|I\rangle\langle I|x_n|S\rangle}{E_I - E_S}, \tag{A1}$$

where E_S and E_I are the energies of the states S and I, respectively, and $\sum_I$ stands for the sum over all intermediate states. If S is an eigenstate with magnetic quantum number M_J, the polarizability entries $\alpha_{x,x}(S)$ and $\alpha_{y,y}(S)$ are equal $[\alpha_{x,x}(S) = \alpha_{y,y}(S)]$ [66]. The formulas for $\alpha_{x,x}(S)$ and $\alpha_{z,z}(S)$ read [66]

$$\alpha_{x,x}(S) = A_J\big[J(J-1) + M_J^2\big] + B_J\big[J(J+1) - M_J^2\big] + C_J\big[(J+1)(J+2) + M_J^2\big], \tag{A2a}$$

$$\alpha_{z,z}(S) = 2A_J\big[J^2 - M_J^2\big] + 2B_J M_J^2 + 2C_J\big[(J+1)^2 - M_J^2\big], \tag{A2b}$$

where the constants A_J, B_J,and C_J stand for specific sums over intermediate states I with $J_I = J_S - 1$, $J_I = J_S$,, and $J_I = J_S + 1$, respectively.

For singly ionized atomic krypton, we are interested in the polarizabilities for ionic states with a hole in the $4p$ or the $3d$ orbital manifolds. Using DALTON, we calculated polarizabilities that do not include spin-orbit coupling. In order to obtain polarizabilities for the spin-orbit-coupled ionic states $[4p_j^{m_j}]^{-1}$ and $[3d_j^{m_j}]^{-1}$ we perform first-order perturbation theory for degenerate states. The diagonal polarizability entries of the spin-orbit-coupled ionic states $[NL_J^{M_J}]^{-1}$ expressed with the polarizabilities of the nonrelativistic states $[NL_{M_L}]^{-1}$

TABLE III. Static dipole polarizabilities $\alpha_{x,x}$ and $\alpha_{z,z}$ are shown for two Kr^+ states. All other polarizabilities can be deduced from these values. Polarizabilities obtained by the CIS and CASSCF methods are compared. All values are given in atomic units with a precision up to the second digit.

	CIS		CASSCF	
	$\alpha_{x,x}$	$\alpha_{z,z}$	$\alpha_{x,x}$	$\alpha_{z,z}$
$[4p_0]^{-1}$	0.01	3.13	10.77	10.46
$[3d_0]^{-1}$	0.00	0.00	9.66	9.52

read

$$\alpha_{n,n}\left(\left[NL_J^{M_J}\right]^{-1}\right)=\sum_{\sigma,M_L}\left[C^{J,M_J}_{L,M_L;1/2,\sigma}\right]^2\alpha_{n,n}([NL_{M_L}]^{-1}). \quad \text{(A3)}$$

With the help of Eqs. (A2) and (A3) only two polarizability entries $\alpha_{n,n}(S), n \in \{x,y,z\}$ from states with the same N and L quantum numbers are needed and all other diagonal polarizability entries of any state S' can be obtained as long as S' has the same N and L quantum numbers. In Table III the calculated polarizabilities are shown that are used to obtain all polarizabilities in Table I. For the CASSCF and CIS calculations we obtained converged results with the augmented correlation-consistent quintuple-zeta basis set including polarization functions (aug-cc-pV5Z) [67].

[1] A. F. Starace, in *Handbuch der Physik*, edited by W. Mehlhorn (Springer, Berlin, 1980), Vol. 31, pp. 1–121.
[2] M. R. H. Rudge, Rev. Mod. Phys. **40**, 564 (1968).
[3] T. Brabec and F. Krausz, Rev. Mod. Phys. **72**, 545 (2000).
[4] M. Schultze, M. Fiess, N. Karpowicz, J. Gagnon, M. Korbman, M. Hofstetter, S. Neppl, A. L. Cavalieri, Y. Komninos, T. Mercouris *et al.*, Science **328**, 1658 (2010).
[5] K. Klünder, J. M. Dahlström, M. Gisselbrecht, T. Fordell, M. Swoboda, D. Guénot, P. Johnsson, J. Caillat, J. Mauritsson, A. Maquet *et al.*, Phys. Rev. Lett. **106**, 143002 (2011).
[6] G. Sansone, F. Kelkensberg, J. F. Perez-Torres, F. Morales, M. F. Kling, W. Siu, O. Ghafur, P. Johnsson, M. Swoboda, E. Benedetti *et al.*, Nature (London) **465**, 763 (2010).
[7] K. J. Schafer, B. Yang, L. F. DiMauro, and K. C. Kulander, Phys. Rev. Lett. **70**, 1599 (1993).
[8] M. Lein, J. P. Marangos, and P. L. Knight, Phys. Rev. A **66**, 051404 (2002).
[9] M. Busuladžić, A. Gazibegović-Busuladžić, D. B. Milošević, and W. Becker, Phys. Rev. Lett. **100**, 203003 (2008).
[10] M. Busuladžić, A. Gazibegović-Busuladžić, and D. B. Milošević, Phys. Rev. A **80**, 013420 (2009).
[11] A. Gazibegović-Busuladžić, E. Hasović, M. Busuladžić, D. B. Milošević, F. Kelkensberg, W. K. Siu, M. J. J. Vrakking, F. Lépine, G. Sansone, M. Nisoli *et al.*, Phys. Rev. A **84**, 043426 (2011).
[12] V. P. Krainov, W. Xiong, and S. L. Chin, Laser Phys. **2**, 467 (1992).
[13] T. Brabec, M. Côté, P. Boulanger, and L. Ramunno, Phys. Rev. Lett. **95**, 073001 (2005).
[14] C. I. Blaga, F. Catoire, P. Colosimo, G. G. Paulus, H. G. Muller, P. Agostini, and L. F. DiMauro, Nat. Phys. **5**, 335 (2009).
[15] A. Fleischer, H. J. Wörner, L. Arissian, L. R. Liu, M. Meckel, A. Rippert, R. Dörner, D. M. Villeneuve, P. B. Corkum, and A. Staudte, Phys. Rev. Lett. **107**, 113003 (2011).
[16] R. Murray, M. Spanner, S. Patchkovskii, and M. Y. Ivanov, Phys. Rev. Lett. **106**, 173001 (2011).
[17] A. N. Pfeiffer, C. Cirelli, M. Smolarski, R. Dorner, and U. Keller, Nat. Phys. **7**, 428 (2011).
[18] P. B. Corkum and F. Krausz, Nat. Phys. **3**, 381 (2007).
[19] A.-T. Le, R. D. Picca, P. D. Fainstein, D. A. Telnov, M. Lein, and C. D. Lin, J. Phys. B **41**, 081002 (2008).
[20] E. Goulielmakis, M. Schultze, M. Hofstetter, V. S. Yakovlev, J. Gagnon, M. Uiberacker, A. L. Aquila, E. M. Gullikson, D. T. Attwood, R. Kienberger *et al.*, Science **320**, 1614 (2008).
[21] F. Krausz and M. Ivanov, Rev. Mod. Phys. **81**, 163 (2009).
[22] O. Smirnova, S. Patchkovskii, Y. Mairesse, N. Dudovich, and M. Y. Ivanov, Proc. Natl. Acad. Sci. USA **106**, 16556 (2009).
[23] O. Smirnova, Y. Mairesse, S. Patchkovskii, N. Dudovich, D. Villeneuve, P. Corkum, and M. Y. Ivanov, Nature (London) **460**, 972 (2009).
[24] M. Vrakking, Nature (London) **460**, 960 (2009).
[25] S. Haessler, J. Caillat, W. Boutu, C. Giovanetti-Teixeira, T. Ruchon, T. Auguste, Z. Diveki, P. Breger, A. Maquet, B. Carre *et al.*, Nat. Phys. **6**, 200 (2010).
[26] O. Smirnova and M. Ivanov, Nat. Phys. **6**, 159 (2010).
[27] H. J. Wörner, J. B. Bertrand, B. Fabre, J. Higuet, H. Ruf, A. Dubrouil, S. Patchkovskii, M. Spanner, Y. Mairesse, V. Blanchet *et al.*, Science **334**, 208 (2011).
[28] P. Hockett, C. Z. Bisgaard, O. J. Clarkin, and A. Stolow, Nat. Phys. **7**, 612 (2011).
[29] S. Baker, J. S. Robinson, C. A. Haworth, H. Teng, R. A. Smith, C. C. Chiril, M. Lein, J. W. G. Tisch, and J. P. Marangos, Science **312**, 424 (2006).
[30] M. Lein, Phys. Rev. Lett. **94**, 053004 (2005).
[31] H. J. Woerner, J. B. Bertrand, D. V. Kartashov, P. B. Corkum, and D. M. Villeneuve, Nature (London) **466**, 604 (2010).
[32] X. Zhou, P. Ranitovic, C. W. Hogle, J. H. D. Eland, H. C. Kapteyn, and M. M. Murnane, Nat. Phys. **8**, 232 (2012).
[33] P. Eckle, A. N. Pfeiffer, C. Cirelli, A. Staudte, R. Dörner, H. G. Muller, M. Büttiker, and U. Keller, Science **322**, 1525 (2008).
[34] A. N. Pfeiffer, C. Cirelli, M. Smolarski, D. Dimitrovski, M. Abusamha, L. B. Madsen, and U. Keller, Nat. Phys. **8**, 76 (2012).
[35] A. Wirth, M. T. Hassan, I. Grgura, J. Gagnon, A. Moulet, T. T. Luu, S. Pabst, R. Santra, Z. A. Alahmed, A. M. Azzeer *et al.*, Science **334**, 195 (2011).
[36] M. Ammosov, N. Delone, and V. Krainov, Zh. Eksp. Teor. Fiz. **91**, 2008 (1986).
[37] C. Z. Bisgaard and L. B. Madsen, Am. J. Phys. **72**, 249 (2004).
[38] A. Saenz, Phys. Rev. A **66**, 063408 (2002).
[39] E. Goulielmakis, Z. Loh, A. Wirth, R. Santra, N. Rohringer, V. S. Yakovlev, S. Zherebtsov, T. Pfeifer, A. M. Azzeer, M. F. Kling *et al.*, Nature (London) **466**, 739 (2010).
[40] R. Santra, V. S. Yakovlev, T. Pfeifer, and Z.-H. Loh, Phys. Rev. A **83**, 033405 (2011).
[41] M. B. Gaarde, C. Buth, J. L. Tate, and K. J. Schafer, Phys. Rev. A **83**, 013419 (2011).
[42] J. C. Baggesen, E. Lindroth, and L. B. Madsen, Phys. Rev. A **85**, 013415 (2012).
[43] M. Dantus, M. J. Rosker, and A. H. Zewail, J. Chem. Phys. **87**, 2395 (1987).
[44] S. Pabst, L. Greenman, P. J. Ho, D. A. Mazziotti, and R. Santra, Phys. Rev. Lett. **106**, 053003 (2011).
[45] H. Wang, M. Chini, S. Chen, C.-H. Zhang, F. He, Y. Cheng, Y. Wu, U. Thumm, and Z. Chang, Phys. Rev. Lett. **105**, 143002 (2010).

[46] Z.-H. Loh, C. H. Greene, and S. R. Leone, Chem. Phys. **350**, 7 (2008).
[47] M. Tarana and C. H. Greene, Phys. Rev. A **85**, 013411 (2012).
[48] W.-C. Chu and C. D. Lin, Phys. Rev. A **85**, 013409 (2012).
[49] M. Holler, F. Schapper, L. Gallmann, and U. Keller, Phys. Rev. Lett. **106**, 123601 (2011).
[50] L. Greenman, P. J. Ho, S. Pabst, E. Kamarchik, D. A. Mazziotti, and R. Santra, Phys. Rev. A **82**, 023406 (2010).
[51] P. J. Mohr, B. N. Taylor, and D. B. Newell, Rev. Mod. Phys. **80**, 633 (2008).
[52] N. Rohringer, A. Gordon, and R. Santra, Phys. Rev. A **74**, 043420 (2006).
[53] S. Pabst, L. Greenman, D. A. Mazziotti, and R. Santra, Phys. Rev. A **85**, 023411 (2012).
[54] N. Rohringer and R. Santra, Phys. Rev. A **79**, 053402 (2009).
[55] J. Herrmann, M. Weger, R. Locher, M. Sabbar, P. Riviére, U. Saalmann, J.-M. Rost, L. Gallmann, and U. Keller, arXiv:1206.6208.
[56] S. Pabst, L. Greenman, and R. Santra, XCID program package for multichannel ionization dynamics, DESY, Hamburg, Germany (2011), Rev. 534, with contributions from P. J. Ho.
[57] National Institute of Standards and Technology, http://www.nist.gov/pml/data/atomspec.cfm
[58] A. Thompson, X-Ray Data Booklet, http://xdb.lbl.gov
[59] J. Sugar and A. Musgrove, J. Phys. Chem. Ref. Data **20**, 859 (1991).
[60] DALTON—A Molecular Electronic Structure Program, Release Dalton2011 (2011); http://daltonprogram.org
[61] M. Medveď, P. Fowler, and J. Hutson, Mol. Phys. **98**, 453 (2000).
[62] A. Kumar and W. J. Meath, Can. J. Chem. **63**, 1616 (1985).
[63] U. Hohm and K. Kerl, Mol. Phys. **69**, 803 (1990).
[64] S. Lünnemann, A. I. Kuleff, and L. S. Cederbaum, J. Chem. Phys. **130**, 154305 (2009).
[65] J. Mitroy, M. S. Safronova, and C. W. Clark, J. Phys. B **43**, 202001 (2010).
[66] B. Bederson and E. J. Robinson, *Beam Measurements of Atomic Polarizabilities* (John Wiley & Sons, Inc., Hoboken, NJ, USA, 2007), pp. 1–27.
[67] A. K. Wilson, D. E. Woon, K. A. Peterson, and J. Thom H. Dunning, J. Chem. Phys. **110**, 7667 (1999).

5.6 Enhanced Nonlinear Response of Ne^{8+} to Intense Ultrafast X-rays

Arina Sytcheva, Stefan Pabst, Sang-Kil Son, and Robin Santra

Published in Phys. Rev. A **85**, 023414 (2012)

Original publication: http://link.aps.org/doi/10.1103/PhysRevA.85.023414
Free preprint version: http://arxiv.org/abs/1202.6277

Statement of Contributions

Arina Sytcheva, Robin Santra and I developed the concept of using our TDCIS program to calculate resonant two-photon cross sections of Ne^{+8}. Arina Sytcheva and I extented the program accordingly.

PHYSICAL REVIEW A **85**, 023414 (2012)

Enhanced nonlinear response of Ne^{8+} to intense ultrafast x rays

Arina Sytcheva,[1,*] Stefan Pabst,[1,2] Sang-Kil Son,[1] and Robin Santra[1,2,†]
[1]*Center for Free-Electron Laser Science, DESY, DE-22607 Hamburg, Germany*
[2]*Department of Physics, University of Hamburg, DE-20355 Hamburg, Germany*
(Received 30 November 2011; published 21 February 2012)

We investigate the possible reasons for the discrepancy between the theoretical two-photon ionization cross section, $\sim 10^{-56}$ cm^4 s, of Ne^{8+} obtained within the perturbative nonrelativistic framework for monochromatic light [S. Novikov and A. Hopersky, J. Phys. B **34**, 4857 (2001)] and the experimental value, 7×10^{-54} cm^4 s, reported in [G. Doumy *et al.*, Phys. Rev. Lett. **106**, 083002 (2011)] at a photon energy of 1110 eV. To this end, we consider Ne^{8+} exposed to deterministic and chaotic ensembles of intense x-ray pulses. The time-dependent configuration interaction singles (TDCIS) method is used to quantitatively describe nonlinear ionization of Ne^{8+} induced by coherent intense ultrashort x-ray laser pulses. The impact of the bandwidth of a chaotic ensemble of x-ray pulses on the effective two-photon ionization cross section is studied within the lowest nonvanishing order of perturbation theory. We find that, at a bandwidth of 11 eV, the effective two-photon ionization cross section of Ne^{8+} at a photon energy of 1110 eV amounts to 5×10^{-57} and 1.6×10^{-55} cm^4 s for a deterministic ensemble and a chaotic ensemble, respectively. We show that the enhancement obtained for a chaotic ensemble of pulses originates from the presence of the one-photon $1s^2$-$1s4p$ resonance located at 1127 eV. Using the TDCIS approach, we also show that, for currently available radiation intensities, two-photon ionization of a $1s$ electron in neutral neon remains less probable than one-photon ionization of a valence electron.

DOI: 10.1103/PhysRevA.85.023414 PACS number(s): 32.80.Rm, 42.50.Ar, 31.15.−p, 02.70.−c

I. INTRODUCTION

Modern highly intense x-ray free-electron lasers (XFELs), such as the Linac Coherent Light Source (LCLS) at SLAC National Accelerator Laboratory, Stanford, USA [1], and the SPring-8 Ångström Compact Free-Electron Laser (SACLA), Harima, Japan [2], deliver both soft and hard x-ray radiation. FLASH at DESY, Hamburg, Germany [3], operates in the VUV and soft x-ray regimes, and the European XFEL [4], which is under construction, is planned to deliver photon energies up to 12 keV. These facilities offer possibilities to explore inner-shell electron dynamics and nonlinear response of atoms and molecules to intense x-ray radiation (see, for example, Refs. [5–10]).

The present theoretical work is triggered by a recent experiment on nonlinear ionization of neon atoms performed at the LCLS [6]. The experiment utilized the capability of the LCLS to produce unprecedentedly intense x-ray beams, with up to $\sim 10^{12}$ x-ray photons in a $\sim$100 fs pulse with a peak intensity of $\sim 10^{17}$ W/cm^2. Within a single pulse the initially neutral target absorbed multiple photons yielding a variety of ion species in different electronic configurations. At a photon energy of 1110 eV, which is below the K-shell threshold of Ne^{8+}, Doumy *et al.* [6] observed production of hydrogenlike neon, Ne^{9+}. The Ne^{9+}/Ne^{8+} ratio was observed to depend quadratically on the peak intensity, which is consistent with nonlinear two-photon ionization of Ne^{8+}. Nevertheless, the two-photon ionization cross section, deduced from this experimental observation with the help of a rate-equation model, is 7×10^{-54} cm^4 s, which is two orders of magnitude higher than the value obtained within perturbation theory [11,12].

In the present paper, we focus on the following points: (i) the discrepancy between the observed [6] and theoretically predicted [11] two-photon ionization cross-section values of Ne^{8+} and (ii) the possibility of two-photon ionization of a $1s$ electron in neutral neon below the K-shell threshold of neon.

To describe the nonlinear interaction of Ne^{8+} and neutral neon with an intense coherent ultrashort x-ray pulse, we adopt the time-dependent configuration interaction singles (TDCIS) method—a nonperturbative *ab initio* multichannel approach [13–16]. TDCIS allows for pulses of arbitrary shape and peak intensity, and provides an intuitive picture of the electron dynamics induced by a light pulse of finite duration. Correlation effects between the ejected photoelectron and the remaining ion are included via exact treatment of the Coulomb interaction [15]. Going beyond the standard single-active electron approximation [13,17], the TDCIS model accounts for the coupling between different excitation (ionization) channels.

In our study, we employ the TDCIS method implemented in the XCID code [18]. To eliminate spurious reflections, which appear when the electronic wave packet reaches the boundary of the numerical grid, we apply absorbing boundaries through the inclusion of a complex absorbing potential (CAP) [19,20]. Implemented within the framework of TDCIS, the CAP provides a measure for the ionization probability for the outgoing electron. The ionization probability, given by the diagonal components of the reduced ion density matrix (IDM), is used in this work for calculating the generalized two-photon ionization cross section.

For nonlinear light-matter interaction the spectral and temporal shape of the pulse is a crucial factor [21,22]. The rate of simultaneous absorption of two photons depends on the statistics of the exciting field [23–25]. Present XFELs have a coherence time that is much shorter than the pulse duration and can be considered as chaotic [26,27]. For a chaotic ensemble of pulses [25] with a finite bandwidth and

*arina.sytcheva@cfel.de
†robin.santra@cfel.de

a short coherence time [28], within the lowest nonvanishing order of perturbation theory (LOPT), the effective two-photon ionization cross section can be written as a convolution of the monochromatic two-photon cross section and the spectral distribution function. We investigate the effect of finite coherence time on the two-photon ionization cross section by using a Gaussian spectral distribution function. The monochromatic two-photon ionization cross section we calculate within the Hartree-Fock-Slater (HFS) model [29], implemented within the XATOM code [30,31]. The results to be presented here indicate that the treatment of XFEL radiation as a chaotic finite-bandwidth ensemble of pulses, rather than a deterministic ensemble of pulses, is likely to be capable of explaining the enhanced two-photon ionization cross section reported in Ref. [6].

The paper is organized as follows: we outline the theoretical approaches in Sec. II, present details on the numerical implementation and the obtained results in Sec. III, and draw conclusions in Sec. IV. Atomic units are used throughout, unless otherwise noted.

II. THEORY

A. Two-photon ionization cross section for a coherent finite pulse

A detailed description of our implementation of the TDCIS method can be found in Ref. [14]. Briefly, we construct the electronic wave packet in an atom as a linear combination of the Hartree-Fock ground state $|\Phi_0\rangle$ and one-particle–one-hole (1p-1h) excitations $|\Phi_i^a\rangle$,

$$|\Psi,t\rangle = \alpha_0(t)|\Phi_0\rangle + \sum_i \sum_a \alpha_i^a(t)\big|\Phi_i^a\big\rangle, \tag{1}$$

where

$$\big|\Phi_i^a\big\rangle = \frac{1}{\sqrt{2}}\{\hat{c}_{a\uparrow}^\dagger \hat{c}_{i\uparrow} + \hat{c}_{a\downarrow}^\dagger \hat{c}_{i\downarrow}\}|\Phi_0\rangle. \tag{2}$$

Here, $i,j,\ldots$ label orbitals occupied in $|\Phi_0\rangle$, whereas unoccupied (virtual) orbitals are marked by $a,b,\ldots$. The operators $\hat{c}_{p\sigma}^\dagger$ and $\hat{c}_{p\sigma}$ create and annihilate, respectively, electrons in a spin orbital of the modified Fock operator $\hat{F}_{\rm CAP} = \hat{F} - i\eta\hat{W}$, which consists of the Fock operator $\hat{F}$ and the CAP in the form $-i\eta\hat{W}$. The spin states are designated with σ. In the electric dipole approximation, the nonrelativistic Hamiltonian of the atom interacting with the x-ray field is given by

$$\hat{H} = \hat{F}_{\rm CAP} + \hat{V}_C - \hat{V}_{\rm HF} - E_{\rm HF} - \mathcal{E}(t)\hat{z}, \tag{3}$$

where $\hat{V}_C$ stands for the electron-electron Coulomb interaction, $\hat{V}_{\rm HF}$ and $E_{\rm HF}$ are the Hartree-Fock mean-field potential and ground-state energy, respectively, $\hat{z}$ is the dipole operator, and $\mathcal{E}(t)$ is the electric field of the intense ultrashort laser pulse, which is assumed to be linearly polarized along the z axis. By substituting the wave function given by Eq. (1) into the time-dependent Schrödinger equation, one gets a set of coupled ordinary differential equations for the coefficients $\alpha_0(t)$ and $\alpha_i^a(t)$.

Using the state $|\Psi,t\rangle$, we construct the reduced density matrix of the residual ion produced in the photoionization process,

$$\hat{\rho}(t) = {\rm Tr}_a[|\Psi,t\rangle\langle\Psi,t|], \tag{4}$$

$$\rho_{ij}(t) = \sum_{a,b} \alpha_i^a(t)\big[\alpha_j^b(t)\big]^* o_{ab}, \tag{5}$$

where o_{ab} stands for the overlap between eigenfunctions of $\hat{F}_{\rm CAP}$. The CAP is only active at large distances from the atom, and hence, affects only virtual orbitals. Application of the CAP is equivalent to attenuation of the wave packet when it reaches the boundary of the numerical grid [32]. Because of the CAP, the norm of the wave packet from Eq. (1) as well as the norm of the reduced ion density matrix (4), are not conserved and decrease as ionization proceeds. In order to compensate for this loss of norm in the IDM, one has to introduce a correction [14,33]:

$$\delta\rho_{ij}(t) = 2\eta e^{i(\varepsilon_i-\varepsilon_j)t}\int_{-\infty}^{t} dt' \sum_{a,b} w_{ba}\alpha_i^a(t')\big[\alpha_j^b(t')\big]^* \times e^{-i(\varepsilon_i-\varepsilon_j)t'}, \tag{6}$$

with ε_i being the orbital energies and w_{ba} the matrix elements of the CAP operator $\hat{W}$. In the limit $t\to\infty$, i.e., after the ionizing pulse is over, a diagonal component of the corrected IDM, $\rho_i + \delta\rho_i (\equiv \rho_{ii} + \delta\rho_{ii})$, can be thought of as the excitation probability from an occupied orbital i. Under the conditions considered here, the uncorrected ρ_i vanishes for a sufficiently long time after the pulse is over, indicating that the photoelectron is completely absorbed by the CAP. Conversely, the IDM correction $\delta\rho_i$ approaches a constant value at $t\to\infty$ and can be interpreted as the ionization probability of an electron from orbital i.

The ionization probability per unit time due to direct absorption of N photons (in s^{-1}) is given by $\sigma^{(N)}J^N$, where J is the photon flux in the number of photons $\mathrm{cm}^{-2}\mathrm{s}^{-1}$. This allows for a definition of an effective two-photon ionization cross section for a coherent pulse centered at a mean photon energy $\omega_{\rm in}$ with a bandwidth of $\Delta\omega_{\rm p}$,

$$\sigma_{\rm coh}^{(2)}(\omega_{\rm in},\Delta\omega_{\rm p}) = \frac{\lim\limits_{t\to\infty}\delta\rho_i(t)}{\int_{-\infty}^{\infty} dt\, J(t)^2}. \tag{7}$$

The quantities $\omega_{\rm in}$ and $\Delta\omega_{\rm p}$ enter the right-hand side of Eq. (7) implicitly through the IDM correction $\delta\rho_i$, obtained using the Hamiltonian from Eq. (3), and the flux $J(t)$. The definition of Eq. (7) is valid provided the ground state is not depleted, i.e., in the perturbative limit.

B. Two-photon ionization cross section for chaotic fields

When defining the cross section in Eq. (7) we assume that the x-ray pulse is well defined (deterministic). In general, the radiation produced by an XFEL operating in the self-amplified spontaneous emission (SASE) regime is chaotic with respect to fluctuations in the electric field. The simplest way to account for the XFEL chaoticity is to recall that the N-photon ionization rate, within the LOPT, is proportional to $N!J^N$, which amounts to effective doubling (2!) of the cross-section value for two-photon ionization [21]. This factor of 2 cannot explain the discrepancy found in Ref. [6]. The most rigorous and accurate way to simulate the experimental situation would

be by introducing an appropriate stochastic model [34,35] for the radiation and solving the TDCIS equations many times using an ensemble of realistic pulses. Afterward one would have to average the results over all members of the ensemble. However, this approach is computationally very costly.

Here, we follow the result of Mollow [25] who showed that within the second-order perturbation theory for a field consisting of finite chaotic pulses, the transition rate due to two-photon absorption during the pulse can be expressed in terms of the spectral first-order field correlation function. In the case of a finite-bandwidth field and near an intermediate resonance of the target atom the two-photon ionization cross section for an incoherent pulse can be cast in the form

$$\sigma^{(2)}_{\rm incoh}(\omega_{\rm in},\Delta\omega_{\rm p}) = 2\int_{-\infty}^{\infty} d\omega\, \sigma^{(2)}_{\rm LOPT}(\omega) F(\omega,\omega_{\rm in},\Delta\omega_{\rm p}), \quad (8)$$

where $F(\omega,\omega_{\rm in},\Delta\omega_{\rm p})$ is the normalized spectral distribution function and $\sigma^{(2)}_{\rm LOPT}$ is the result of the LOPT for monochromatic radiation [11,12,36]:

$$\sigma^{(2)}_{\rm LOPT}(\omega) = \pi(4\pi\alpha\omega)^2 \sum_f \delta(\omega_f - \omega_g - 2\omega) \times \left| \sum_l \frac{\langle f|z|l\rangle\langle l|z|g\rangle}{\omega_g + \omega - \omega_l + i\Gamma_l/2} \right|^2, \quad (9)$$

with α being the fine-structure constant. In Eq. (9), $|f\rangle$, $|l\rangle$, and $|g\rangle$ stand for final, intermediate, and ground states, respectively. Γ_l accounts for the natural linewidth of the intermediate states $|l\rangle$; ω_g and ω_l denote energies of the ground and intermediate states, respectively. Note that the factor of 2 in Eq. (8) accounts for the enhancement of two-photon absorption from a single-mode chaotic field [21].

The spectral distribution of a single XFEL pulse is very spiky and random [22,37]. Averaged over many shots the spectral distribution can be taken as a normalized Gaussian [38,39],

$$F(\omega,\omega_{\rm in},\Delta\omega_{\rm p}) = \frac{2\sqrt{\ln 2}}{\sqrt{\pi}\,\Delta\omega_{\rm p}} \exp\left[-4\ln 2\left(\frac{\omega-\omega_{\rm in}}{\Delta\omega_{\rm p}}\right)^2\right]. \quad (10)$$

The result given by Eq. (8) can be understood as a nonlinear atomic response to a spectral range of uncorrelated modes. Here, the atomic response to the individual frequencies is summed incoherently. In contrast, Eq. (7) represents nonlinear atomic response to a coherent pulse. In the next section, we apply Eqs. (7) and (8) to calculate effective two-photon ionization cross sections of Ne^{8+} in the photon-energy range below its K edge.

III. RESULTS AND DISCUSSION

We start our numerical study with the nonlinear atomic response of Ne^{8+} to a deterministic coherent pulse using TDCIS implemented in the XCID code [18]. We obtain converged results by using a nonuniform radial grid extending from $r = 0$ to $r = 80$ a.u. with 1000 grid points and a pseudospectral-grid parameter $\zeta = 0.461$ [14]. Under these conditions, there is an almost uniform orbital energy spacing of about 0.3 a.u. across a wide energy range (up to 150 a.u.) for the final states of the outgoing electron. The CAP starts at $r = 50$ a.u. We use a CAP strength $\eta = 0.002$ a.u., which makes the energy levels broad enough to describe the quasicontinuum. In this range of η, we satisfy the stationarity condition with respect to η: $\partial[\lim_{t\to\infty}\delta\rho_{1s}(t)]/\partial\eta = 0$, where ρ_{1s} denotes the diagonal component of the IDM corresponding to the $1s$ orbital. The positions of $1s^2$-$1s\,np$ resonances are obtained with an accuracy of 0.03 a.u. and the one-photon ionization potential of Ne^{8+} equals 43.9 a.u. (1194.1 eV). For the comparison, the experimental value of the ionization potential of Ne^{8+} is 1195 eV [40]. We account for angular momenta of the outgoing electron up to $l_{\rm max} = 2$. The laser pulse is given by $\mathcal{E}(t) = \mathcal{E}_0 \exp\{-2\ln 2(t/\tau_{\rm p})^2\}\cos(\omega_{\rm in}t)$, where $\tau_{\rm p}$ is the FWHM duration of the pulse intensity[1] and $\mathcal{E}_0$ is the peak electric field.

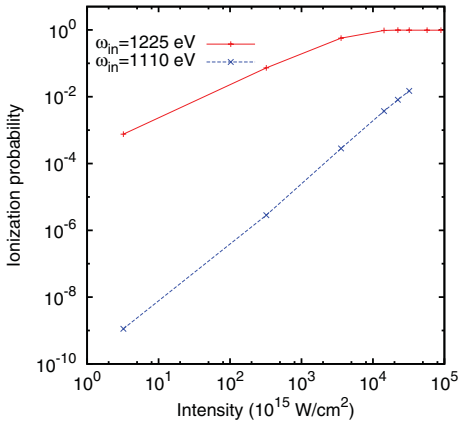

FIG. 1. (Color online) Intensity dependence of the ionization probability of Ne^{8+}, given by the diagonal IDM correction $\delta\rho_{1s}$, at photon energies of 1225 eV (above the single-photon ionization threshold) and 1110 eV (below the single-photon ionization threshold). A deterministic pulse of 6-eV bandwidth (FWHM) is used.

In Fig. 1, we show how the $1s$ ionization probability depends on intensity at two different photon energies used in the experiment [6], below (1110 eV) and above (1225 eV) the one-photon ionization threshold. For the calculation we use a coherent pulse with a FWHM bandwidth of 6 eV. We can see that in double logarithmic scale the slope of the curve corresponding to 1110 eV is 2, while that for 1225 eV, the slope below saturation, is 1. This reflects the fact that at 1225 eV, $1s$ ionization is a one-photon process, whereas at 1110 eV, it is a two-photon process. Above $\sim 3\times 10^{18}$ W/cm^2, depletion of the ground state becomes substantial.

Doumy *et al.* [6] measured the mean photon energy with an uncertainty of several tenths of an electron volt and the pulse spectral width was 10 ± 1 eV. [2] In Fig. 2, we show the two-photon ionization cross section, calculated using Eq. (7) for several pulse durations corresponding to the FWHM bandwidths of 20, 15, 11, 8, and 6 eV. The peak electric

[1] The pulse duration given in femtoseconds is inversely related to the bandwidth of the pulse given in eV as $\Delta\omega_{\rm p} = 1.8/\tau_{\rm p}$.

[2] G. Doumy (private communication).

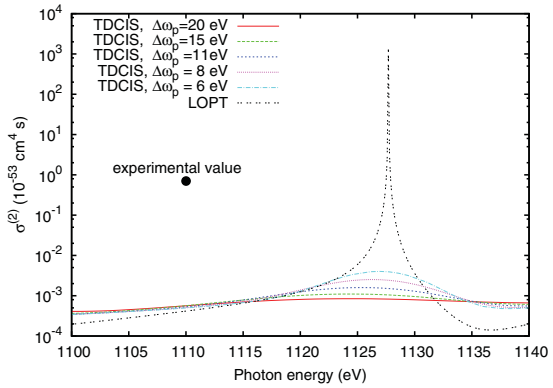

FIG. 2. (Color online) Effective two-photon ionization cross section for Ne^{8+}. The TDCIS results are given by Eq. (7) for several different pulse bandwidths (FWHM). The LOPT result is obtained using Eq. (9). The point at 1110 eV corresponds to the experimental value of 7×10^{-54} cm^4 s reported in Ref. [6].

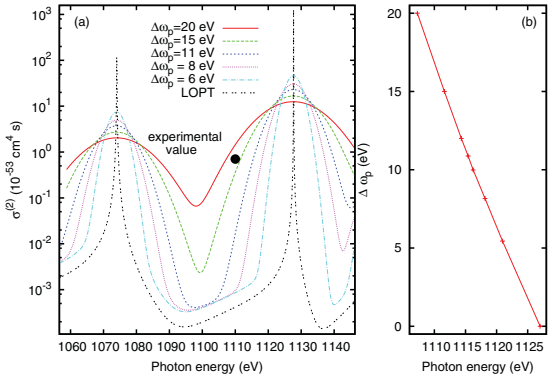

FIG. 3. (Color online) (a) Two-photon ionization cross section for Ne^{8+}, given by Eq. (8). The perturbative result $\sigma^{(2)}_{\rm LOPT}$ of Eq. (9) (dotted line) is taken as a reference signal for averaging over different bandwidths (FWHM) of the pulses. The point at 1110 eV corresponds to the experimental value of 7×10^{-54} cm^4 s reported in Ref. [6]. (b) Relation between the bandwidth $\Delta\omega_{\rm p}$ and the mean photon energy $\omega_{\rm in}$ for which the two-photon ionization cross section $\sigma^{(2)}_{\rm incoh}$ is fixed at 7×10^{-54} cm^4 s.

field $\mathcal{E}_0 = 0.03$ a.u. was used. Also shown is the cross section $\sigma^{(2)}_{\rm LOPT}(\omega)$ given by Eq. (9). For the latter, we use the HFS model [29], implemented within the XATOM code [30,31]. The HFS model positions the intermediate resonances at lower energies than those obtained in TDCIS, therefore we shifted the curve $\sigma^{(2)}_{\rm LOPT}(\omega)$ such that the $1s^2$-$1s4p$ resonance is at the right position of 1127.1 eV. Doumy *et al.* [6] noticed that in a similar perturbative calculation [11] the authors did not account for the $1s^2$-$1s4p$ resonance. We have included this resonance in both TDCIS and LOPT calculations. However, as we see from Fig. 2, neither the inclusion of this resonance nor the finite bandwidth of the radiation pulse taken into account in TDCIS can explain the discrepancy of several orders of magnitude between the theoretical and experimental values.

Now, we use Eq. (8) to convolve the monochromatic two-photon ionization cross section obtained with Eq. (9), with the spectral distribution function given by Eq. (10), and show the results in Fig. 3(a). One can see that within the bandwidth, off from the resonances, the cross section is substantially enhanced, because the main contribution to the convolution in Eq. (8) comes from the resonance peaks. Indeed, for a bandwidth of 11 eV the cross section at 1110 eV is 1.6×10^{-55} cm^4 s, thus is enhanced by at least one and one-half orders of magnitude with respect to the perturbative result (4×10^{-57} cm^4 s). In Fig. 3(b), we show the relation between the pulse bandwidth $\Delta\omega_{\rm p}$ and mean photon energy $\omega_{\rm in}$, which is needed for the calculated two-photon ionization cross section to reach the experimentally found value of 7×10^{-54} cm^4 s. For a bandwidth of 17 eV, the calculated cross section increases up to this value at the photon energy of 1110 eV used in the experiment. Thus, our findings suggest that the main reasons for the enhanced two-photon ionization cross section of Ne^{8+} at 1110 eV originate from the proximity of the $1s^2$-$1s4p$ resonance, the chaoticity of the LCLS radiation, and the finite bandwidth of its pulses.

In connection with the study of two-photon ionization of core electrons, it is worth mentioning another recent experiment of Young *et al.* [5], where direct multiphoton ionization of neon was completely shadowed by a sequence of one-photon ionization events. One of the measurements has been done at the photon energy of 800 eV, just below the K edge, 870 eV, of neutral neon. In this case, one x-ray photon carries enough energy to ionize valence electrons, and therefore the valence-shell electrons are stripped in a sequence of one-photon absorption processes. Creation of a $1s$-shell vacancy is possible only through the absorption of two photons. No evidence for this process was detected.

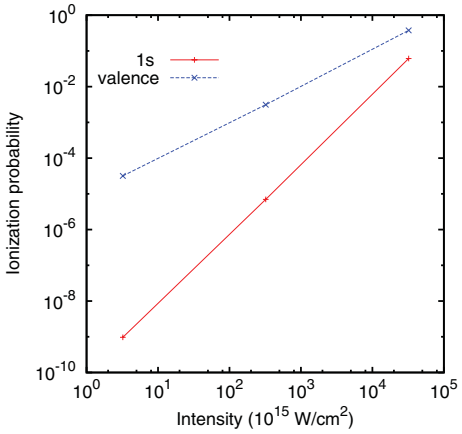

FIG. 4. (Color online) Intensity dependence of the ionization probability of neutral neon, given by the IDM corrections $\delta\rho_{1s}$ for $1s$ electrons and $\delta\rho_{2s} + \sum_m \delta\rho_{2p_m}$ for valence electrons, at a photon energy of 800 eV (below the one-photon ionization threshold for the K shell, but above the one-photon ionization threshold for the valence shells). A deterministic pulse of 6-eV bandwidth (FWHM) is used.

Using the TDCIS model, we study the possibility of creating a core hole in Ne via simultaneous absorption of two 800-eV photons. The converged result is obtained by using a maximum radius of 90 a.u. with 1000 grid points and $\zeta = 0.461$. A CAP of strength $\eta = 0.002$ starts at 60 a.u. Accounting for angular momenta of the ionized electron up to $l_{\max} = 3$ is sufficient. In Fig. 4, we show the ionization probabilities of valence and core electrons for neutral neon as a function of peak intensity. One can see that at the intensity of 3×10^{17} W/cm^2 the probability of ejecting a $1s$ electron is more than 10^2 times smaller than that of ejection of a valence electron. With increasing intensity, the relative probability of $1s$ ionization with respect to valence ionization grows. Nevertheless, this calculation shows that direct two-photon processes with ejection of an inner-shell electron never dominate the one-photon ionization of valence electrons, even for a pulse as short as $\tau_p = 300$ as (corresponding to a bandwidth of 6 eV). We confirm the observation of Young *et al.* [5] that multiphoton processes involving inner-shell electrons are overshadowed by valence ionization as long as the valence electrons are not stripped away.

IV. CONCLUSION

In conclusion, we investigated the two-photon ionization cross section of Ne^{8+} in the vicinity of the $1s^2$-$1s4p$ resonance. We presented a strategy for calculating the two-photon ionization cross section within the TDCIS framework. However, the TDCIS model, which allows for a perfectly coherent radiation pulse, does not explain the enhanced two-photon ionization cross section, obtained by Doumy *et al.* [6] at 1110 eV, in spite of the inclusion of the $1s^2$-$1s4p$ resonance which was missing in Ref. [11]. The inclusion of the $1s^2$-$1s4p$ resonance within the LOPT approach for monochromatic light does not explain the experimental result either. Chaoticity and short coherence time of the XFEL radiation, taken into account through the spectral distribution function in the cross-section expression obtained within LOPT, partially explain the observed enhancement. For the bandwidth of 10 $\pm$1 eV, estimated in the experiment, we obtained an increase of the effective two-photon cross section by a factor of 40 with respect to the perturbative result for monochromatic radiation. To explain the experimentally observed value of 7×10^{-54} cm^4 s within this framework one would need a broader spectral bandwidth ($\sim$17 eV) or a mean photon energy tuned closer to the $1s^2$-$1s4p$ resonance. It is also worth noting that some indirect pathways that avoid production and two-photon ionization of ground-state Ne^{8+} have not been included in the rate-equation model used in Ref. [6]. This might have caused the experimental $\sigma^{(2)}$ to be overestimated. Nevertheless, we believe the $1s^2$-$1s4p$ resonance is the key to explain the enhanced two-photon ionization cross section of Ne^{8+} at 1110 eV, but its influence depends strongly on the XFEL spectral density and uncertainties in its mean photon energy.

From the study of neutral neon performed within the TDCIS framework, we also infer that, when available, valence electron stripping due to one-photon ionization dominates over two-photon ionization of inner-shell electrons even at intensities far beyond current experimental possibilities.

ACKNOWLEDGMENTS

We gratefully acknowledge helpful discussions with Joe Frisch and Linda Young. We thank Alexandro Saenz for e-mail communication regarding Ref. [36], and Gilles Doumy for providing important details on the experiment. A.S. is thankful to Gopal Dixit for his useful comments and Otfried Geffert for his help in software development.

[1] P. Emma, R. Akre, J. Arthur, R. Bionta, C. Bostedt, J. Bozek, A. Brachmann, P. Bucksbaum, R. Coffee, F. Decker *et al.*, Nat. Photonics **4**, 641 (2010).
[2] D. Pile, Nat. Photonics **5**, 456 (2011).
[3] W. Ackermann, G. Asova, V. Ayvazyan, A. Azima, N. Baboi, J. Bähr, V. Balandin, B. Beutner, A. Brandt, A. Bolzmann *et al.*, Nat. Photonics **1**, 336 (2007).
[4] *The European X-Ray Free-Electron Laser Technical Design Report*, edited by M. Altarelli *et al.* (DESY, Hamburg, Germany, 2007), [http://xfel.desy.de/technical_information/tdr/tdr/].
[5] L. Young, E. Kanter, B. Krässig, Y. Li, A. March, S. Pratt, R. Santra, S. Southworth, N. Rohringer, L. DiMauro *et al.*, Nature (London) **466**, 56 (2010).
[6] G. Doumy, C. Roedig, S.-K. Son, C. Blaga, A. DiChiara, R. Santra, N. Berrah, C. Bostedt, J. Bozek, P. Bucksbaum *et al.*, Phys. Rev. Lett. **106**, 083002 (2011).
[7] M. Richter, M. Y. Amusia, S. V. Bobashev, T. Feigl, P. N. Juranić, M. Martins, A. A. Sorokin, and K. Tiedtke, Phys. Rev. Lett. **102**, 163002 (2009).
[8] A. Rudenko, L. Foucar, M. Kurka, T. Ergler, K. Kühnel, Y. Jiang, A. Voitkiv, B. Najjari, A. Kheifets, S. Lüdemann *et al.*, Phys. Rev. Lett. **101**, 073003 (2008).
[9] R. Moshammer, Y. Jiang, L. Foucar, A. Rudenko, T. Ergler, C. Schröter, S. Lüdemann, K. Zrost, D. Fischer, J. Titze *et al.*, Phys. Rev. Lett. **98**, 203001 (2007).
[10] Y. Liu, S. Tschuch, A. Rudenko, M. Dürr, M. Siegel, U. Morgner, R. Moshammer, and J. Ullrich, Phys. Rev. Lett. **101**, 053001 (2008).
[11] S. Novikov and A. Hopersky, J. Phys. B **34**, 4857 (2001).
[12] P. Koval, Ph.D. thesis, Universität Kassel, 2004.
[13] N. Rohringer, A. Gordon, and R. Santra, Phys. Rev. A **74**, 043420 (2006).
[14] L. Greenman, P. J. Ho, S. Pabst, E. Kamarchik, D. A. Mazziotti, and R. Santra, Phys. Rev. A **82**, 023406 (2010).
[15] S. Pabst, L. Greenman, P. J. Ho, D. A. Mazziotti, and R. Santra, Phys. Rev. Lett. **106**, 053003 (2011).
[16] P. Krause, T. Klamroth, and P. Saalfrank, J. Chem. Phys. **127**, 034107 (2007).
[17] K. Kulander, K. Schafer, and J. Krause, Int. J. Quantum Chem. **40**, 415 (1991).
[18] S. Pabst and R. Santra, XCID—A program package for multi-channel ionization dynamics, Rev. 314, with contributions from P. J. Ho, CFEL, DESY, Hamburg, Germany, 2011.
[19] U. Riss and H.-D. Meyer, J. Phys. B **26**, 4503 (1993).

[20] R. Santra and L. Cederbaum, Phys. Rep. **368**, 1 (2002).
[21] R. Loudon, *The Quantum Theory of Light* (Oxford University Press, Oxford, 1983).
[22] E. Saldin, E. Schneidmiller, and M. Yurkov, *The Physics of Free Electron Lasers* (Springer-Verlag, Berlin, 2000).
[23] P. Lambropoulos, Phys. Rev. **168**, 1418 (1968).
[24] P. Lambropoulos, C. Kikuchi, and R. K. Osborn, Phys. Rev. **144**, 1081 (1966).
[25] B. R. Mollow, Phys. Rev. **175**, 1555 (1968).
[26] G. Dattoli and M. Richetta, Opt. Commun. **50**, 165 (1984).
[27] E. Saldin, E. Schneidmiller, and M. Yurkov, New J. Phys. **12**, 035010 (2010).
[28] P. J. Ho and R. Santra, Phys. Rev. A **78**, 053409 (2008).
[29] J. Slater, Phys. Rev. **81**, 385 (1951).
[30] S.-K. Son, L. Young, and R. Santra, Phys. Rev. A **83**, 033402 (2011).
[31] S.-K. Son and R. Santra, XATOM—An integrated toolkit for x-ray and atomic physics, Rev. 354, CFEL, DESY, Hamburg, Germany, 2011.
[32] R. Kosloff and D. Kosloff, J. Comput. Phys. **63**, 363 (1986).
[33] N. Rohringer and R. Santra, Phys. Rev. A **79**, 053402 (2009).
[34] S. Reiche, C. Pellegrini, J. Rosenzweig, P. Emma, and P. Krejcik, in *Proceedings of the 2001 Particle Accelerator Conference,* (IEEE, New York, 2001), Vol. 4, pp. 2751–2753.
[35] T. Pfeifer, Y. Jiang, S. Düsterer, R. Moshammer, and J. Ullrich, Opt. Lett. **35**, 3441 (2010).
[36] A. Saenz and P. Lambropoulos, J. Phys. B **32**, 5629 (1999).
[37] S. Krinsky and R. Gluckstern, Phys. Rev. ST Accel. Beams **6**, 050701 (2003).
[38] I. A. Vartanyants, A. Singer, A. P. Mancuso, O. M. Yefanov, A. Sakdinawat, Y. Liu, E. Bang, G. J. Williams, G. Cadenazzi, B. Abbey *et al.*, Phys. Rev. Lett. **107**, 144801 (2011).
[39] J. Galayda, J. Arthur, D. Ratner, and W. White, J. Opt. Soc. Am. B **27**, 106 (2010).
[40] A. Thompson *et al.*, *X-Ray Data Booklet* (Lawrence Berkeley National Laboratory, University of California Berkeley, CA, 2009).

Part III

Conclusion

Chapter 6

Conclusions and Outlook

6.1 Conclusions

Ultrafast sciences are young and rapidly developing. The characteristic time scales of electronic and nuclear dynamics range from picoseconds (10^{-12} s) to attoseconds (10^{-18} s). No mechanical and electronic devices operate on such time scales. Therefore, the only way to investigate this nanoworld is by literately shining light on it. Within the last decade tremendous technological progress has been made in generating short and shorter pulses, and at the same time possessing better control of their shape and timing with respect to other pulses. These are essential prerequisites for watching and controlling ultrafast motions of atoms and molecules. Along with the reduction in the pulse duration comes a steady increase in the photon energy of these pulses. This wide tunability makes it possible to study a vast range of motions spanning from molecular rotations and vibrations to electronic dynamics of outer-valence, inner-shell, or even core electrons.

On the theoretical side, much progress has also been made in tackling the challenges that emerge in the ultrafast world. Many dynamics triggered by light pulses lead to complex motions requiring a large configuration space in order to fully capture the motion. Laser alignment of molecules or the high-harmonic generation (HHG) process are two examples where high rotational states with angular momenta $J > 50$ are needed to accurately describe the underlying dynamics. The large variety of pulse durations, intensities, and photon energies make it difficult to develop a theoretical model that can cope with all the possible kinds of dynamics that can be triggered by such a large range of pulse parameters. Particularly challenging are laser-matter interactions that cannot be treated perturbatively, such as strong-field ionization or non-adiabatic alignment of molecules in three dimensions.

In this thesis, two prominent classes of ultrafast dynamics have been discussed:

- laser-alignment dynamics of molecules,
- ultrafast ionization dynamics of noble gas atoms,

where the characteristic time scale of molecular rotations is in the picosecond range, and ionization dynamics happens on the scale of attoseconds to a few femtoseconds. For both areas of ultrafast dynamics, I have developed programs that solve the time-dependent Schrödinger equation for any type of pulse shape. Solving numerically the time-dependent Schrödinger equation is computationally demanding but, therefore, also more general. Exploiting the underlying symmetries has proven to be essential in making these calculations more feasible and pushing them even further. Often speed-ups of a factor 2 or more can be easily achieved.

Laser Alignment of Molecules

The rotational motion of molecules is triggered by non-resonant laser pulses. The induced dipole moment in the molecule interacts with the electric field of the pulse and creates an angle-dependent potential, which forces the molecules to be aligned in the polarization direction(s) of the pulse. Using pulses that are short or long with respect to the rotational dynamics allows the generation of complex rotational motions. Combinations of several short pulses, long and short pulses, or static and optical fields are also exploited. This is often done to maximize the degree of alignment without ionizing the molecule. Multi-pulse methods have been predominantly used to study impulsive alignment dynamics of linear or symmetric-top molecules due to their unique alignment dynamics. Impulsive alignment offers the possibility to study these aligned molecules under field-free conditions. This is particularly interesting for strong-field or attosecond experiments on molecular systems where the alignment is needed but the subsequent processes should not be disturbed by the presence of an aligning laser pulse.

In the case of asymmetric-top molecules, my findings suggest that standard multi-pulse schemes, which are used to align symmetric-top molecules in 1D, cannot be easily applied to 3D alignment. Just replacing elliptically polarized pulses with linearly polarized pulses is not enough to impulsively align asymmetric-top molecules in 3D. Particularly, the rotational revival feature of linear and symmetric-top molecules does not exist in asymmetric-top molecules. Even though asymmetric-top molecules can show some kind of revival behavior, the dephasing between rotational states is too rapid to be recoverable by a subsequent pulse. The only promising multi-pulse approach that can overcome the rapid dephasing is a fast sequence of pulses very closely spaced to each other. The number of pulses is unfortunately limited because the spacing between them has to decrease with every pulse since the rotational dynamics becomes faster and faster. My studies on SO_2 have shown that the alignment of the most and the second most polarizable axes increases

with the number of pulses. The degree of alignment of the third axis is, however, almost unchanged from its initial isotropic value.

Aligning molecules is not done out of self-interest. Aligning molecules is essential for many experiments. Hence, the understanding of alignment motion is crucial to find new ways of improving the alignment even further. All kinds of laser-matter interactions are highly dependent on the relative alignment/orientation of the molecule. This can be seen in the alignment dependence of the HHG spectrum, and also in x-ray diffraction studies of laser-aligned molecules. My investigations of x-ray diffraction from laser-aligned naphthalene molecules have shown that the degree of 3D alignment is essential for getting useful, high-Q diffraction information needed to reconstruct the molecular structure with atomic resolution. For naphthalene, degrees of alignment of $\langle\cos^2\theta\rangle > 0.9$ are needed to resolve atomic positions. This can only be achieved with adiabatic alignment at the moment, since impulsive alignment schemes for asymmetric molecules do not reach this high degree of alignment.

Finite rotational temperatures of the gas phase molecules are the main cause of a reduced alignment quality. Temperatures below 1 K are required to achieve the necessary alignment, since the maximum intensity of the adiabatic alignment pulse cannot be arbitrarily high. If the pulse intensity exceeds the tunnel ionization threshold, naphthalene molecules start to get ionized. As long as the x-ray pulse duration is comparable or shorter than the alignment dynamics, the effective resolution in the reconstruction is not affected by the finite pulse duration. My studies have shown that at rotational temperatures of 1 K it is possible to image molecular structure with a resolution such that the two-ring structure of naphthalene is visible. At temperatures of $T = 10$ mK, the position of the individual carbon atoms starts to emerge.

Ultrafast Ionization Processes in Noble Gas Atoms

When the pulse intensity reaches values of $10^{13} - -10^{14}$ W/cm^2, the electric field is so strong that an electron can be ripped out from an atom. This ionized electron can strongly interact with the ion and changes its state as long as it is in the vicinity of the ion. Studying these types of effects requires a multichannel theory such as time-dependent configuration-interaction singles (TDCIS). TDCIS combines the one-electron nature of many strong-field processes with electronic structure theory, where correlation effects between electrons are included that go beyond the independent particle model.

HHG is a very prominent mechanism connecting strong-field physics with attosecond physics. Nowadays, HHG is not just used as a tool to produce UV attosecond pulses; the HHG spectrum itself has moved into the scientific focus. It can provide information about the electronic structure and electronic motion. To successfully investigate the electronic structure, it is essential that correlation effects are included in the theoretical analyses. Our findings on the HHG spectrum of argon demonstrate that multi-orbital and multipole

effects have to be included in the theory. Not doing so can lead to HHG yields that are up to one order of magnitude off. The HHG cut-off region seems to be quite robust to these effects but at lower energies the changes can be significant. In argon, the benchmark was the position and the shape around the characteristic Cooper minimum. Similar to the giant dipole resonance in xenon, the existence of the Cooper minimum is not a multielectron effect. But its strength, shape, position, and indirect side effects in neighboring subshells depend strongly on multielectron and correlation effects.

Ultrafast correlation dynamics have been investigated in my studies of decoherences in attosecond photoionziation. The photoelectron (particularly the slower ones) interacts with the parent ion during its detachment—a process neglected in the sudden approximation. The energy gained by the photoelectron due to absorption of a photon can be redistributed between the electron and the ion via the residual Coulomb interaction. Such an energy exchange (known as interchannel effects) leads subsequently to an entanglement between the photoelectron and the ion. If at some later stage only the ionic subsystem is probed (e.g., with transient absorption spectroscopy), one finds that the ionic state is not in a pure state—meaning it cannot be described by a coherent ionic wavefunction and is only fully characterized by a density matrix description. The entanglement between the photoelectron and the ion naturally results in a reduction in the coherences of the subsystems. Particularly slow photoelectrons do strongly interact with the ion. Ultrashort pulses with broad spectral bandwidths create both slow and fast photoelectrons. The increase in slow photoelectrons with broader spectral bandwidths reduces the decoherence in the ionic subsystem despite the fact that the broad spectrum is favorable for the creation of a coherent hole wavepacket in the ion. If no interchannel effects occur during ionization, the electron-ion entanglement is strongly reduced and the ultrashort pulse triggers an almost perfectly coherent hole motion.

The possible degree of coherence that can be generated via photoionization is highly interesting. Photoionization is the first step in launching a hole wavepacket. In molecular systems, the hole dynamics can be quite complex and are not restricted to the atomic site where it was initiated. After some time, the ionic hole may have traveled to a different atomic site in the molecule where it can influence site-specific chemical reactions; a situation which has already been observed in recent experiments.

The preparatory ionization process as well as the subsequent hole motion in the ion can be investigated by transient absorption spectroscopy. Not only can the ionic population be studied time-dependently, but also the phase relations between ionic states can be measured. My studies on atomic krypton have shown that access to the relative phase makes it possible to directly probe field-driven interactions. During the tunnel ionization of krypton, the field-driven interaction between the ion and the freed electron via the neutral ground state results in strong deformations in the shapes of the absorption lines in the transient absorption spectrum.

Transient absorption spectroscopy, together with complementary techniques such as streaking, opens the door to the ultrafast world of both partners—the photoelectron and the ion—and the interaction between them. Combined with the control of molecular alignment, not just atomic but also molecular dynamics can be studied.

6.2 Outlook

Ultrafast Ionization Processes in Noble Gas Atoms

The rapid progress in the last years of strong-field and attosecond physics can be expected to continue in the next years to come. The steady push towards shorter pulses and higher photon energies from the HHG side as well as from big facilities, namely the development of free-electron lasers (FELs) in the UV (e.g., FLASH) and in the x-ray regime (e.g., LCLS, SACLA, and the European XFEL), pave the way for a wide range of coherent pump-probe experiments on femtosecond and attosecond time scales.

Transient absorption spectroscopy with femtosecond x-ray pulses would allow the probing of delocalized valence hole dynamics in molecules at specific atom sites by tuning the x-ray energy near element-specific absorption edges. Also nuclear motion and its interplay with electronic excitations, leading to non-Born-Oppenheimer dynamics, can be studied on a few femtosecond time scale. On a picosecond time scale, structural deformations have already been measured in metal-ligand complexes. Here, additional dynamics in the spin degrees of freedom occur that are less common in closed-shell systems.

The theoretical, or more precisely the numerical, demand in solving a molecular system is much more challenging than for an atomic closed-shell system. The great advantage that comes with a spherically symmetric object is then lost and the angular part of the wavefunction no longer factorizes from the radial part. For elliptically polarized pulses, this radial-angular factorization is lost as well, regardless of the system symmetry. Elliptically or circularly polarized light introduces new dynamics in the angular projection M. Particularly for magnetic (open-shell) systems, circularly polarized light is ideal for studying magnetic and spin dynamics. Therefore, the extension of the XCID package to circularly and elliptically polarized pulses opens the possibility of studying new classes of motion that are not possible in the current version of the program.

Molecular systems, however, offer a much richer electronic motion, potentially coupled to vibrational or rotational degrees of freedom. The single-active electron picture, which works quite well for closed-shell atoms, becomes less and less appropriate for larger molecular systems. A theoretical description of a dynamical process with several active electrons (e.g., TDCISD) is on the other hand very challenging. Therefore, most studies that included rigorously multi-electron dynamics focus on the smallest two-electron system—helium.

In strong-field processes, it is necessary on the one side to describe delocalized continuum states. On the other side, it is not always necessary to include high order correlations, as done in higher order configuration-interaction (CI) approaches. The idea of reducing the correlation dynamics but leaving the degrees of freedom for the spatial and momentum dynamics untouched can be realized in a multi-configuration time-dependent Hartree-Fock (MCTDHF) ansatz. In MCTDHF, configuration coefficients as well as one-particle orbitals are time-dependent. The advantage of time-dependent orbitals is that the configuration space is dynamically optimized, which keeps the number of needed configurations small. Within this smaller dynamical configuration space, a full CI (FCI) is performed.

Instead of performing a FCI within this dynamics subspace, which might be quite challenging for ultrafast scenarios, it seems more attractive to do a lower order CI like CIS. This idea of merging the MCTDHF logic with a TDCIS ansatz seems to be more promising and especially a much more feasible approach for extending the current XCID package. In addition to the common set of equations of motion for the configuration coefficients, a new set of equations emerges for the time-dependent orbitals. With such an approach, the remaining electrons in an ion are now allowed to adjust to the removal of the N^{th} electron without the need to introduce higher-order correlation classes. Already the polarizability studies of Kr^+ have shown that the spatial adjustments of the orbitals rather than higher correlation effects are crucial for obtaining more reliable results.

Laser Alignment of Molecules

For strong-field and attosecond experiments with molecular systems, the alignment or even the orientation of the molecule becomes an important aspect. Unfortunately, despite the fact that the polarizability increases with system size, larger molecules become more and more difficult to align. The growing negative influence of the finite rotational temperature outpaces the positive effect of the polarizability. Larger molecular are also less stiff than smaller ones. This means that larger molecules more easily get deformed by an external field making the rigid-rotor approximation questionable.

Furthermore, the polarizability tensor is generally not diagonal in the principal axes of inertia. Only for small molecules with high internal symmetries (e.g., SO_2 or naphthalene) are the polarizability tensor and the moment of inertia tensor diagonal in the same body-fixed frame. The larger the molecules, the less likely it is that these two sets of reference frames coincide. This creates two kinds of challenges for larger molecules. First, the alignment dynamics becomes more challenging, since the molecule rotates around the moment of inertia axes but the aligning field forces the molecule to align to the polarizability axes. Therefore, it is not clear to which extent current techniques are still suitable for large molecules. Second, the computational challenge grows as well. The increased complexity in the alignment dynamics gets reflected onto the more complex dynamics of the angular momentum projection K, which no longer changes in steps of 2 but rather of 1, doubling the number of accessible rotational states.

Another interesting extension for the XALMO package is the possibility to treat longer wavelengths, where the alignment motion cannot be averaged over a cycle period of the aligning laser pulse. Such pulses can orient polar molecules. From the numerical point of view, this leads to another loss of symmetry in the angular projection M, which would not change in steps of 2 anymore. Together with the loss in symmetry of the K quantum number for large molecules, the numerical demand is significantly increased in comparison to the alignment studies presented in this thesis. Despite the challenges, this extension would offer new opportunities to discover novel alignment dynamics schemes that boost the efficiency of aligning and/or orienting molecules.

Overall Perspective

From rotational motion of molecules down to single electronic excitations, a wide range of nanoscale dynamics can nowadays be probed and controlled by ultrafast pulses, and the possibilities continue to expand to even more complicated systems. With the advent of FELs, intense femtosecond UV and x-ray (short wavelength) pulses became available. Pump-probe experiments in the UV and x-ray regimes can target atom-specific electronic dynamics. Particularly for molecules, this raises the tantalizing prospect of controlling chemical reactions by triggering the break-up and formation of bonds. Optical and NIR (long wavelength) pulses, on the other hand, provide unmatched spatial and temporal coherence properties. Due to the high degree of coherence, electron motion on an attosecond scale can be revealed with techniques like attosecond streaking. Optical pulses can also be used to probe structural information via high harmonic generation. With more moderate intensities, optical pulses control the rotational dynamics of molecules. By continuing the rapid progress experimentally and theoretically, the dream of making a molecular movie and watching electrons and atoms move might become a reality sooner than we think.

Acknowledgement

First of all, I am very grateful to Prof. Robin Santra for accepting the risk of taking me as his first Ph.D. student and guiding me safely through the vibrant fields of strong-field and attosecond physics. His inspiring enthusiasm and his great devotion to answer every little question I had in great detail made the three years of my Ph.D. the most educational and most productive period of my life.

I want to express my deepest gratitude to my diploma supervisor Prof. Paul-Gerhard Reinhard for preparing me for life as a Ph.D. student. Without Prof. Reinhard's help and connections to Argonne National Laboratory, I would not have met Robin. Here, I also want to use the change to thank Teng Lek Khoo at Argonne for introducing me to Robin. Furthermore, Prof. Reinhard made it possible that I could start my Ph.D. with Robin by formally being my Ph.D. supervisor for the time I worked at Argonne.

My first year I worked with Robin at Argonne. There, I had the pleasure to work together with wonderful people—namely, Linda Young, Steve Southworth, Bertold Krässig, Elliot Kanter, Anne-Marie March, and Phay Ho. Since most of the group members were experimentalists, I had very fruitful discussions that prevented me from getting lost in the world of equations. I realized how joyful it is to work on "real world problems" that can potentially turn into real experiments. I will never forget the time I spent in Argonne. I also want to mention here Bob Bell, the best landlord I can imagine. His lively spirit and his overwhelmingly active lifestyle made me think that it is I, not he, who is the seventy-year old man.

Robin made my Ph.D. not just scientifically eventful. After a little more than a year in Argonne, Robin became a professor at the University of Hamburg. In summer 2010, Robin and I moved to Hamburg where we joined the Center for Free-Electron Laser Science (CFEL). Soon, Robin's group grew in size and became as international as a group can be. Now, I can proudly say: I have friends from all around the world, and I hope that these friendships will never break. The wide range of personalities working in the group creates a wonderful atmosphere—and not just during working hours. For this, I want to thank every single one in the group.

A special thanks goes to Sang-Kil Son, Jan Malte Slowik, Gopal Dixit, and Oriol Vendrell for the most interesting scientific discussions. Another thank you goes to all the

Ph.D. students who joined Robin's group, creating a more student-like atmosphere between all the post-docs. I also want to use this chance to apologize to Antonia Karamatskou, Dietrich Krebs, Yi-Jen Chen, and particularly to Arina Sytcheva who had to suffer with the programs I have written. Please be assured, I really did not intended to punish you. I want to say thank you to Zheng Li and Zoltan Jurek for volunteering to play Frisbee with me when the sun occasionally came out. Also a thanks to El-Amine Madjet, Gopal, Sang-Kil, and Oriol for the nice coffee break discussions.

On the personal side, I have experienced great support from my parents, Hartmut and Anita Pabst, and from my brother, Christian Pabst. I am deeply indebted to my father, who ignited my scientific interest. Without his passion for showing his son the amazing world physics, I would not writing a Ph.D. thesis in physics at the moment.

And most importantly, I want to thank my girlfriend Cassandra Hunt for so many things. Without her, I would have never considered the possibility of doing a Ph.D. in the United States and specifically at Argonne. I am most greatly honored by her decision to come with me to Hamburg and to continue her Ph.D. here at CFEL. Lastly, I want to thank Cassi for her steady support and understanding during the entire time of my Ph.D.